Theoretical investigations of the electronic spectroscopy and ultrafast photochemistry of binary transition metal carbonyl complexes

Russell G. McKinlay

Submitted for the degree of Doctor of Philosophy (Chemistry)

Heriot-Watt University

School of Engineering and Physical Sciences

December 2011

Abstract

This thesis is concerned with the electronic absorption spectroscopy and photochemical relaxation mechanisms of binary metal carbonyl complexes. These paradigm complexes exhibit a wide range of photoinduced vibronic coupling related phenomena that are only recently beginning to be understood with the development of modern experimental and computational techniques. These experiments have shown that after irradiation using ultrafast (femtosecond) laser pulses an unsaturated photoproduct is produced, and possibly relaxes through a conical intersection at a Jahn-Teller active geometry, on the same ultrafast timescale. However while experiment can imply the presence of conical intersection, only theoretical methods can confirm this and accurately probe the appropriate part of the potential energy surfaces relevant to this mechanism. The accurate assignment of the electronic excited states of these carbonyls is also a matter of debate with different theoretical and experimental techniques applied to these systems over the years. The large density of excited states of different character within a small energy range and the high computational expense of studying transition metal complexes with highly correlated methods presents a considerable challenge to the theoretical chemist.

The research presented in this thesis falls into two main parts, firstly the electronic excited states of the binary transition metal carbonyl complexes $Fe(CO)_5$, $Cr(CO)_6$ and $Ni(CO)_4$ were studied with highly correlated coupled cluster methods as well as their one-photon and two-photon absorption spectra. These results were compared with previous experimental and theoretical results. The electronic excited states and one-photon absorption spectra were also studied for the group 7 mixed-metal bimetallic carbonyls ($MnTc(CO)_{10}$, $MnRe(CO)_{10}$ and $TcRe(CO)_{10}$) for the first time with time-dependent density functional theory (TD-DFT), the ability of TD-DFT methods to describe charge-transfer states was also investigated here.

The second part of this thesis focussed on the relaxation pathways of the $^2Mn(CO)_5$ and $^1Fe(CO)_4$ initial photoproducts of the photodissociation of $Mn_2(CO)_{10}$ and $Fe(CO)_5$ respectively using CASSCF. Both were found to relax to their lowest energy state through a Jahn-Teller induced conical intersection at a Jahn-Teller active geometry in agreement with experimental observation.

Acknowledgements

I would like to express my sincere and heartfelt thanks to everyone who has helped and assisted me in producing the research presented in this thesis over the last three and a half years, but to mention everyone individually would be an almost impossible task. However, to everyone who has helped or assisted me in any small way, I thank-you.

The person whom I wish to thank in particular is Dr. Martin Paterson, my supervisor. Without his seemingly endless knowledge, energy and enthusiasm, completing the work presented here would have not been possible and I will always be grateful to him.

I would also like to single out the theoretical chemistry section of Heriot-Watt University for gratitude. I could not wish to work with a better group of people, and through our regular meetings and discussions have formed a very open and friendly group of young scientists with whom it is a joy to work with.

The EPSRC is also thanked for funding through grant number EP/F01709X.

Last but not least my thanks goes to my family and my wife, Justyna. I would be nothing without them.

List of Papers

[1] R.G. McKinlay and M.J. Paterson, The Jahn-Teller Effect in Binary Transition Metal Carbonyl Complexes, in *"The Jahn-Teller Effect: Fundamentals and Implications for Physics and Chemistry"*, Eds. H. Köppel, D.R. Yarkony and H. Barentzen, Heidleberg, **2009**, p. 311-344.

[2] R.G. McKinlay, J.M. Żurek and M.J. Paterson, Vibronic Coupling in Systems: Photochemistry, Conical Intersections and the Jahn-Teller and pseudo-Jahn-Teller effects, *Adv. Inorg. Chem*, 62, **2010**, p. 351-390.

Table of Contents

Chapter 1

Introduction

1.1 Structural aspects and importance of binary transition metal carbonyls

The chemical species studied in this thesis are binary transition metal carbonyl complexes. The word 'binary' means made up of two parts and in all cases discussed here the molecules studied are made up of one or two transition metal atoms, and a number of carbonyl ligands sufficient to satisfy the 18-electron rule in each case, which is discussed below. Such complexes were first discovered in 1890 [1] and have been one of the most investigated series of transition metal complexes of the last one hundred years or so. The binary carbonyls and substituted carbonyls have found many applications in research as model complexes for the way they bind to carbonyl ligands, which will be discussed in detail below, and many well-known transition metal complexes contain a carbonyl ligand, such as Vaska's complex (*trans*-chlorocarbonylbis(triphenylphosphine)iridium(I)) which is a well-known catalyst that can reversibly bind an oxygen molecule [2]. Binary metal carbonyls can also be used to make other compounds as carbonyl ligands can be replaced by other ones [3], a process known as ligand substitution, where the metal carbonyls can be oxidised, reduced or broken up entirely. Such processes can be achieved thermally, photochemically, or with a suitable oxidising agent or reducing agent. What is important to note here in a general sense is that once one of these binary carbonyls has lost one carbonyl ligand the resulting fragment is often very reactive, and generally exists only for a short period of time before reacting further. This thesis is concerned with the photochemistry of binary metal carbonyls in which the reactive photoproduct is an unsaturated metal carbonyl obtained via photodissociation of the parent carbonyl.

The so-called covalent model can determine the number of ligands these metal carbonyls have (an alternative ionic model also exists that also reaches the same conclusion using a different system of electron counting; this will not be discussed further). In this model the neutral transition metal may bond to one or more ligands also in their neutral states. Ligands are classed as either *x*-type or *l*-type according to their electronic structure, or they can be a mixture of *x*-or *l*-type depending on how they bond to the metal, e.g., l_2x. An *x*-type ligand will coordinate to the metal via a covalent bond where one electron is donated to the metal and one electron is accepted from the metal,

so that the bonding atom of the ligand completes its octet. An *l*-type ligand usually already has a complete octet so coordinates to the metal in other ways. Examples of this are through a lone pair of electrons, or through a π-bond. *x*-type ligands can also have a lone pair of electrons, or π-bonds, but they coordinate as *x*-type ligands as this is energetically more favourable. The carbonyl ligand which is the only ligand discussed in this thesis is an *l*-type ligand, bonding to the metal through a lone pair of electrons on carbon. The valence electrons (primarily the *n*d-shell but also the (*n*+1)s- and (*n*+1)p-shells to a certain extent, see later) of the metal chiefly govern how it coordinates to ligands. A complex ML_n is formed and the total number of electrons around the metal centre is then counted. Firstly the electrons in the d-shell are counted and to this the number of electrons donated to the metal from each ligand is added. Each *x*-type ligand donates one electron and each *l*-type ligand two electrons, finally the overall charge of the complex ML_n is taken into account. The total number of electrons around the metal can then be counted using the formula:

$$N_e = N_m + 2N_l + N_x - q \qquad (1.1)$$

In the equation above N_m is the metal electron count, N_l is the number of any *l*-type ligands multiplied by two as they each contribute two electrons, N_x is the number of *x*-type ligands and *q* the overall charge on the complex. The 18-electron rule mentioned above states that in general stable low oxidation state transition metal complexes will have N_e = 18, since for the metal this would correspond to a filled Noble gas-like spd shell. If a complex has a count less than this then they are generally very reactive, such as $Fe(CO)_4$ or $Cr(CO)_5$ which both have 16 electrons. In carbonyl complexes such as these, which are co-ordinately unsaturated, then the 18-electron rule is not obeyed. The stability of these carbonyls can be therefore greatly reduced by the application of heat or increased pressure, for example $Cr(CO)_6$ will decompose at 573K, or the application of a pulse of light from a laser at suitable wavelength will cause these carbonyls to break down very quickly, due to the dissociation of one or more carbonyl ligands and the creation of very reactive unsaturated species. It is this feature that is a focal point of this thesis and will be highlighted in section 1.2.

From a perspective of models that predict the bonding properties of molecules, such as ligand field theory, then the bonding of stable 18-electron saturated transition

metal complexes can be predicted. This model is effectively an extension of crystal field theory. Crystal field theory looks at bonding in transition metal complexes concentrating on electrostatic interaction only. Ligands surround the metal centre and are treated as point charges that create an electric field around the metal centre. If these point charges are placed around the metal centre in different ways they can interact with the metal d orbitals causing them to increase or decrease in energy and the interaction can be attractive, repulsive or there can be no interaction. For example if the point charges were arranged around the metal in an octahedral arrangement on Cartesian axes relatie to spherically symmetric field then the $d_{xy,}$ d_{xz} and d_{yz} orbitals would point away from the ligands and would be stabilized by the same amount but the d_z^2 and $d_{x^2-y^2}$ orbitals would point directly at the ligands and would be destabilized by the same amount. This causes a crystal field splitting of these orbitals with a parameter, Δ, which states the energy separation between the two sets of orbitals. Examples of these splittings are shown in figure 2.7 as ligand field splittings of three carbonyl complexes.

Ligand field theory goes further than crystal field theory to describe bonding in d-block metal complexes and includes electrostatic interactions between metal and ligand electrons whilst still focusing on the role of the d orbitals of the metal in a complex. Experimental spectroscopic data is used in ligand field theory, namely the splitting of the metal d orbitals in the ligand field and Racah parameters that will not be discussed further here. What is important from the point of view of this discussion and later chapters is that the transition of electron density from the metal d orbitals to higher energy metal d orbitals or to higher energy ligand orbitals when a complex absorbs light can provide clues as to the structure of the complex prior to absorbing light. Transitions between metal d orbitals are called ‘metal-centred’ (MC) or ‘ligand field’ (LF) transitions and transitions between metal d orbitals and ligand orbitals are called charge transfer (CT) transitions. It is because metal complexes undergo electronic transitions when they absorb light in the visible region of the spectrum that cause them to be coloured. CT transitions are usually very intense absorptions and occur at higher energy than weaker intensity LF transitions. These features will be discussed in detail when the electronic spectroscopy of metal carbonyls is examined in chapters 3-5.

The geometrical shapes of transition metal complexes, ML_n, can be predicted by using a model such as the Kepert model [4], which predicts the shapes of metal

complexes by the number of ligands around the metal centre and the repulsion between them. Non-bonding electrons on the metal centre such as lone pairs are ignored (unlike in VSEPR theory which is an alternative model that predicts the geometry of molecules which does include the influence of such electrons and is not suitable for metal complexes so is not discussed further here) so each ligand will repel the other equally. For example, $Fe(CO)_5$ has five ligands so it would be a trigonal bipyramid or a square-based pyramid, $Cr(CO)_6$ would be an octahedron and $Ni(CO)_4$ a tetrahedron. The real challenge for inorganic chemists is: what are the structures of the reactive, unsaturated metal complexes? This is important when trying to understand the photoreactivity of these metal carbonyls. Table 1.1 shows examples of such saturated and unsaturated carbonyl complexes with their associated electron counts and their ground state structures are shown in figure 1.1.

Figure 1.1 Ground state structures of three binary transition metal carbonyls with the point group of each structure in italics.

It can be observed that in the case of manganese a monometallic complex is not stable and instead forms a dimer. This is because manganese has an odd number of electrons in its valence shell, i.e. it is d^7. So after the coordination of five carbonyl ligands giving ten electrons to the total electron count and with the seven electrons from the manganese valence shell the total electron count for $Mn(CO)_5$ would only be seventeen. An extra electron is gained when two $Mn(CO)_5$ fragments come together and form a covalent bond, each giving the other manganese an extra electron which fulfils the 18-electron rule, N_{m-m} in table 1.1.

Table 1.1 Covalent electron counting in a number of examples of saturated and unsaturated binary transition metal carbonyls, ML_n.

ML_n	N_m	$2N_l$	N_{m-m}	q	N_e
$Ni(CO)_4$	10	8	0	0	18
$Ni(CO)_3$	10	6	0	0	16
$Fe(CO)_5$	8	10	0	0	18
$Fe(CO)_4$	8	8	0	0	16
$Mn_2(CO)_{10}$	7	10	1	0	18
$Mn(CO)_5$	7	10	0	0	17
$Cr(CO)_6$	6	12	0	0	18
$Cr(CO)_5$	6	10	0	0	16

From a ligand field perspective, carbonyl ligands donate a lone pair of electrons that reside in a σ bond on carbon to an empty d orbital on the metal, this is called a *donation interaction*. At the same time the metal donates electron density back to the ligand from a d orbital to a higher lying π antibonding orbital on the carbonyl ligand, this is called a *back-donation interaction*. Through this interaction the metal is classed as a σ acceptor and π donor, and the carbonyl ligand conversely a σ donor and π acceptor. This type of bond where electrons are donated from one atom only to another instead of one atom each providing an electron to form a bond is called a *dative* bond. π Interactions are not required for a dative bond. These two complementary interactions strengthen the metal-carbon bond, but weaken the carbon-oxygen bond due to population of the π antibonding orbital which reduces the bond order. A qualititative molecular orbital diagram for CO is shown in figure 1.2.

Some other features of the carbonyl ligand that are also worth noting are that in the complexes that are studied here each carbonyl group bonds to the metal atom through the carbon. It is also possible for a carbonyl ligand to bond to the metal centre through the oxygen atom. This carbonyl ligand has been given the name 'isocarbonyl'. Though it has been found from theoretical study using density functional theory (DFT), a method discussed in chapter 2, that isomers of metal carbonyls such as $Cr(CO)_6$ including one isocarbonyl ($Cr(CO)_5(OC)$) unit are usually much higher in energy (>30kcal mol^{-1} for $Cr(CO)_5(OC)$ compared to $Cr(CO)_6$) and this was also found to be true for structures where the carbonyl unit acts a Cr-C-O-Cr 'bridging' unit compared to

a Cr-Cr bond in bimetallic systems (>22±5 kcal mol^{-1}) like $Cr_2(CO)_6(\mu\text{-}CO)_3$ where (μ-$CO)_3$ indicates the bridging ligands [5].

Carbonyls can act as 'bridging' ligand between two metal atoms. An example of this is the structure of $Fe_2(CO)_9$ which is composed of two $Fe(CO)_3$ units joined by three bridging carbonyl ligands, although the presence of an Fe-Fe bond in this complex is somewhat controversial [6, 7], highlighting the complexity of the structures of some of these binary carbonyls. The electronic structure of the free carbon monoxide molecule is also unusual, with a dipole moment of 0.122 Debye [8], a slight positive charge on the oxygen atom, and slight negative charge on the carbon atom. This is counterintuitive as oxygen has a higher electronegativity than carbon so one would expect the charges on the atoms to be the other way around. This is because the free carbon monoxide has a triple bond between carbon and oxygen to complete the octet of electrons around carbon. The means oxygen has donated a lone pair of electrons to carbon. Therefore there is a lot of electron density between carbon and oxygen and a slight positive charge on oxygen.

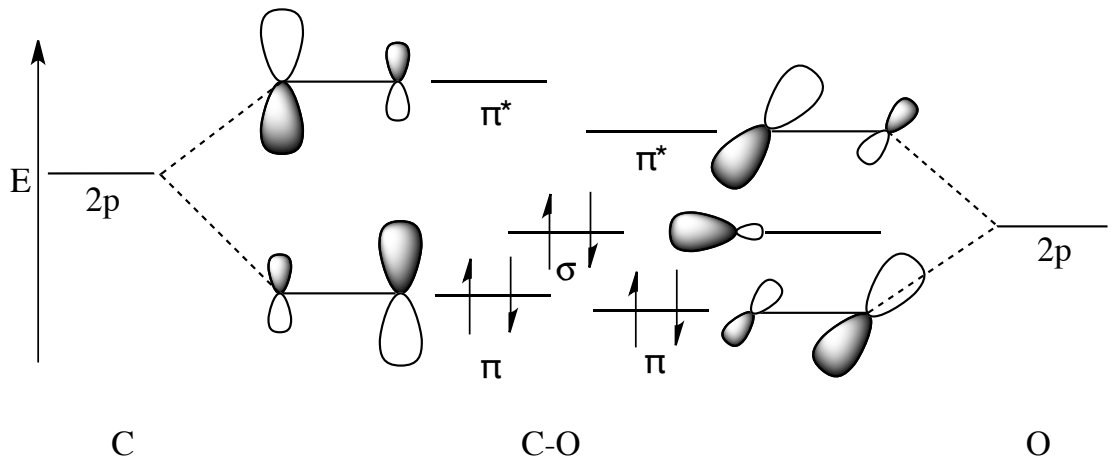

Figure 1.2 Schematical representation of the frontier molecular orbitals of the carbonyl ligand illustrating the low lying π* orbitals. The occupied σ orbital is nonbonding [9].

A central concept in this thesis is how would the stability of such binary carbonyls be affected by the loss of a carbonyl ligand? From simple structural considerations if one carbonyl is removed then the 18-electron rule is no longer obeyed and the unsaturated fragments would be very reactive. The position of the coordination

'hole', which is determined by the leaving ligand, would make several structural models possible. Among those structural models are highly symmetric models that could give rise to degenerate electronic states that will be Jahn-Teller active. This means that the system will distort along a non-totally symmetric vibration to break its symmetry and lower the energy of the system from being in a degenerate electronic state. These Jahn-Teller active states are not often found in classical inorganic chemistry, as they would require the system to be in a higher energy low-spin manifold, for example, an open-shell singlet manifold. The population of these degenerate states in such spin manifolds can cause these photofragments to undergo radiationless decay to a lower electronic state on an ultrafast (femtosecond) timescale. It will be shown in future chapters that these degenerate states and spin manifolds can only be reached photochemically using state-of-the-art laser-based experimental techniques. These Jahn-Teller (degenerate) states are essential to explain these experimental findings.

1.2 Background to metal carbonyl photochemistry

The motivation primarily for this thesis is to investigate and interpret some surprising experimental results from the group of Fuβ *et al*. They have studied the photodissociation of metal carbonyls and found this occurred on an ultrafast (femtosecond) timescale. Mainly they have studied the initial photodissociation process of a range of carbonyls using state-of-the-art femtosecond pump-probe laser techniques with transient ionisation spectroscopy [10, 11, 12, 13, 14, 15]. Effectively with such experiments one gives the system energy that excites the system. The nuclei will then respond and this can be probed to answer the question of where the energy goes in the system. A clue to this is given when the time-resolved transient ionisation spectra are studied, for example for the group 6 hexacarbonyls ($M(CO)_6$, M=Cr, Mo, W), coherent oscillations are observed for the various unsaturated ion fragments of the dissociation process $M(CO)_n$ (n=5,4,3,2,1,0). Examples of such spectra are given later in chapter 6. A Fourier transform of time gives frequency (i.e. energy domain) information and when these spectra are formed the spectra are all dominated by one large peak at the same position, which relates to a specific molecular vibration, possibly relating to an L-M-L bending vibration. This result leads to another question: Why are the reactive photoproducts focusing most of their energy into only one molecular vibration? A

possible answer is that there must be some feature on the excited state potential energy surfaces that would allow these fragments to relax in a very efficient manner on an ultrafast timescale. This is indicative of a conical intersection such as a Jahn-Teller type conical intersection [16, 17]. Indeed, the initial photoproduct of these reactions ML_{x-1} is formed on a femtosecond timescale and luminescence or indications of other long lived excited state behaviour is generally not observed. A schematical representation of this process is shown in figure 1.3.

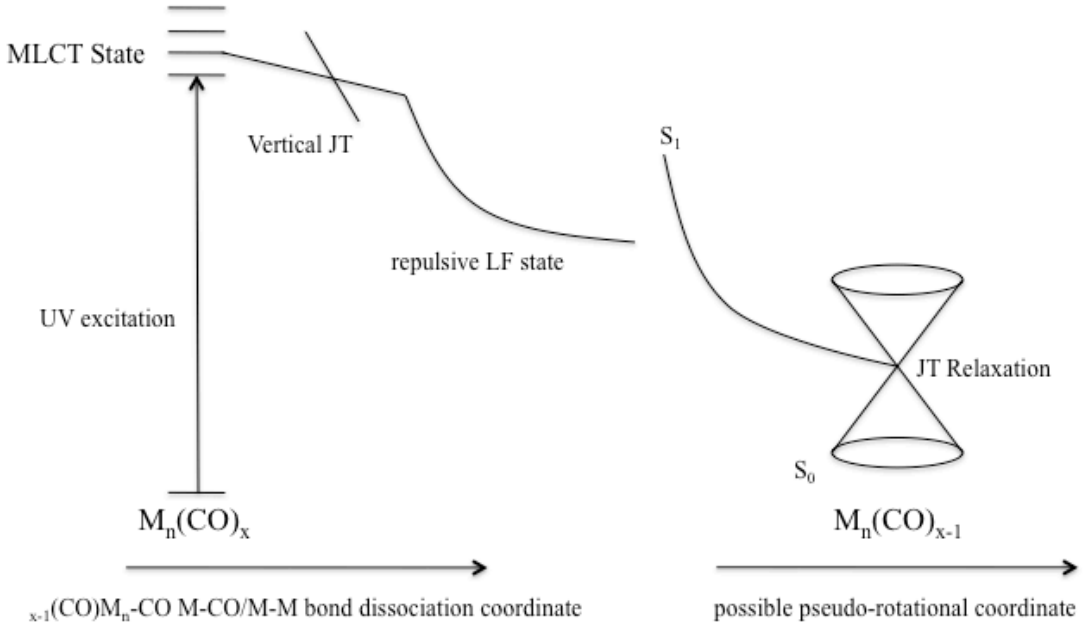

Figure 1.3 Schematical representation of the dissociation process of the transition metal complexes discussed.

The initial photoproducts of these carbonyls ($Cr(CO)_5$ and $Fe(CO)_4$ in the singlet spin manifold and $Mn(CO)_5$ in the open-shell doublet spin manifold) can adopt symmetric structures that are Jahn-Teller active, i.e. a Jahn-Teller geometry that will be the apex of a conical intersection. Potentially the photodissociation process of these carbonyls could therefore provide a link between conical intersections, which are common in organic photochemistry, and Jahn-Teller theory. These experimental studies will be discussed fully in chapters 6, 7 and 8.

A theoretical study is needed of these processes because whilst experiment can indicate the presence of a conical intersection, only theoretical methods can accurately probe the excited states and coupled potential energy surfaces. It is the purpose of this thesis to carry out this task; to theoretically investigate the excited states and structures

of the initial photoproducts of the laser-induced photodissociation of two carbonyls, $Fe(CO)_5$ and $Mn_2(CO)_{10}$, which will complement the work already performed on $Cr(CO)_6$, which we have additionally reported further advanced studies of its photodissociation.

This thesis consists of two main parts. Firstly an investigation of the electronic spectroscopy of a range of metal carbonyls, itself a challenge due to the large number of states of different chemical character within the given spectral range, to see where the energy goes in the system, which state is initially populated and what states could be responsible for the initial photoreaction. Most importantly it should be noted that the assignment of the spectra of these binary carbonyls is still somewhat controversial. Different theoretical and experimental studies have been carried out in the past and these will be reviewed later in this thesis but currently no total agreement has been reached regarding the assignment of the electronic excited states of this important class of transition metal complexes. Other aspects looked at in terms of electronic spectroscopy include the differences between one and two photon absorption spectroscopy in $Fe(CO)_5$, $Cr(CO)_6$ and $Ni(CO)_4$. Two photon absorption has been used to initiate the photodissociation process for $Fe(CO)_5$ [18], but so far no experimental or theoretical reports are available in the literature for the other binary carbonyls in this subject. The spectroscopic properties of more unusual carbonyls such as the group 7 mixed metal carbonyls will also be discussed. This will be presented in chapters 3-5.

Secondly a study of the coupled potential energy surfaces of $Fe(CO)_4$ and $Mn(CO)_5$ around the Jahn-Teller geometry and the topology of the surface around the lower half of the conical intersection formed from the Jahn-Teller geometry or indeed a general conical intersection if one is present will be discussed. If the lower surface topology is known then a hypothesis can be made as to the motion of the system on the surface after moving through the intersection. This will be presented in chapters 6,7 and 8. State-of-the-art theoretical tools are needed to carry out this work and these will be fully discussed in chapter 2 along with a discussion of the appropriate electronic structure theory required. One theme that will continue through this thesis and will be discussed is that the complex photochemistry of these complexes can only now start to be theoretically studied with any degree of accuracy. As already discussed, theoretical investigations are needed to answer the questions which experimental studies have

raised regarding the spectroscopy and initial photochemistry of these carbonyls and the latest theoretical methods will be used that have already been successfully used in recent years in organic photochemistry [19, 20, 21, 22].

Lastly it should also be noted that there are very few theoretical works in the literature regarding the photochemistry and spectroscopy of these metal carbonyls compared to organic systems. The computational expense of studying transition metal complexes with highly accurate theoretical methods and the potential number of different excited states and photoproducts marks the topics studied in this thesis as very challenging but equally worthwhile.

The discussions in chapters 3-8 are arranged such that all relevant original research already carried out relating to the subject of the chapter will be reviewed first. This will be followed by the contribution to that body of original research carried out by this thesis and any conclusions drawn from the assembled data.

1.3 References

[1] Mond, L.; Langer, C.; Quincke, F., Action of carbon monoxide on nickel. *J. Chem. Soc.* **1890**, 749.

[2] Vaska, L.; DiLuzio, J. W., Carbonyl and hydrido-carbonyl complexes of iridium by reaction with alcohols. Hydrido complexes by reaction with acid. *J. Am. Chem Soc.* **1961,** 83, 2784-2785.

[3] Geoffroy, G. L.; Wrighton, M. S., *Organometallic photochemistry*. Academic Press Inc.: London, 1979; Vol. 1.

[4] Housecroft, C. E.; Sharpe, A. G., *Inorganic chemistry*. 1st ed.; Pearson Education: Harlow, 2001.

[5] Zhang, Z.; Qian-shu, L.; Xie, Y.; King, R. B.; Schaefer III, H. F., Binuclear and trinuclear chromium carbonyls with linear bridging carbonyl groups: Isocarbonyl versus carbonyl bonding of carbonyl monoxide ligands. *J. Phys. Chem. A* **2010,** 114, 4627-4672.

[6] Bauschlicher, C. W., On the bonding in $Fe_2(CO)_9$. *J. Chem. Phys.* **1986,** 84, 872-876.

[7] Reinhold, J.; Kluge, O.; Mealli, C., Integration of electron density and molecular orbital techniques to reveal questionable bonds: The test case of the direct fe-fe bond in $Fe_2(CO)_9$. *Inorg. Chem.* **2007,** 46, 7142-7147.

[8] Scuseria, G. E.; Miller, M. D.; Jensen, F.; Geertsen, J., The dipole mement of carbon monoxide. *J. Chem. Phys.* **1991,** 94, 6660-6663.

[9] Jean, Y., *Molecular orbtials of transition metal complexes*. Oxford University Press: Oxford, 2005.
[10] Trushin, S. A.; Fuss, W.; Schmid, W. E.; Kompa, K. L., Femtosecond dynamics and vibrational coherence in gas-phase ultraviolet photodecomposition of $Cr(CO)_6$. *J. Phys. Chem. A* **1998,** 102, 4129-4137.
[11] Trushin, S. A.; Fuss, W.; Schmid, W. E., Conical intersections, pseudorotation and coherent oscillations in ultrafast photodissociation of group-6 metal hexacarbonyls. *Chem. Phys.* **2000,** 259, 313-330.
[12] Fuss, W.; Trushin, S. A.; Schmid, W. E., Ultrafast photochemistry of metal carbonyls. *Res. Chem. Intermed.* **2001,** 27, 447-457.
[13] Trushin, S. A.; Kosma, K.; Fuss, W.; Schmid, W. E., Wavelength-independent ultrafast dynamics and coherent oscillation of a metal-carbon stretch vibration in photodissociation of $Cr(CO)_6$ in the region of 270-345 nm. *Chem. Phys.* **2008,** 347, 309-323.
[14] Fuss, W.; Schmid, W. E.; Trushin, S. A., Ultrafast photodissociation dynamics of $Ni(CO)_4$. *J. Phys. Chem. A* **2001,** 105, 333-339.
[15] Trushin, S. A.; Fuss, W.; Kompa, K. L.; Schmid, W. E., Femtosecond dynamics of $Fe(CO)_5$ photodissociation at 267 nm studied by transient ionization. *J. Phys. Chem. A* **2000,** 104, 1997-2006.
[16] Paterson, M. J.; Hunt, P. A.; Robb, M. A.; Takahashi, O., Non-adiabatic direct dynamics study of chromium hexacarbonyl photodissociation. *J. Phys. Chem. A* **2002,** 106, 10494-10504.
[17] Worth, G. A.; Welch, G.; Paterson, M. J., Wavepacket dynamics study of $Cr(CO)_5$ after formation by photodissociation: Relaxation through an (e $\oplus$ a) $\otimes$ e Jahn-Teller conical intersection. *Mol. Phys.* **2006,** 104, 1095-1105.
[18] Banares, L.; Baumert, T.; Bergt, M.; Kiefer, B.; Gerber, G., Femtosecond photodissociation dynamics of $Fe(CO)_5$ in the gas phase. *Chem. Phys. Lett.* **1997,** 267, 141-148.
[19] Bernardi, F.; Olivucci, M.; Robb, M. A., Potential energy surface crossings in organic photochemistry. *Chem. Soc. Rev.* **1996,** 25, 321.
[20] Paterson, M. J.; Bearpark, M. J.; Robb, M. A.; Blancafort, L.; Worth, G. A., Conical intersections: A perspective on the computation of spectroscopic Jahn-Teller parameters and the degenerate 'intersection space'. *Phys. Chem. Chem. Phys.* **2005,** 7, 2100-2115.
[21] Piechowska-Strumik, K.; Lauvergnat, D.; Bacchus-Montabonel, M. C.; Desouter-Lecomte, M., Quantum dynamics around a non planar conical intersection in vinoxy radical relaxation. *Chem. Phys. Lett.* **2006,** 425, 16-21.
[22] Klessinger, M., Conical intersections and the mechanism of singlet photoreactions. *Angew. Chem.-Int. Ed. Eng.* **1995,** 34, 549-551.

Chapter 2

Theory and Methods

2.1 Perspective on excited state potential energy surfaces and the breakdown of the Born-Oppenheimer approximation

The world of photochemistry is large, when light interacts with matter the range of effects and processes that occur is staggering and many such processes are fundamental in our everyday lives. When molecules interact with photons and become photochemically excited, different electronic configurations are generated and the "products" from such configurations can differ greatly from a ground state reaction. Mixing of electronic excited states gives these electronic configurations. For any given molecule there is in theory a vast array of possible excited states, each relating to every possible distribution of electrons within the molecular orbitals of the system. Theoretically studying the processes resulting from electronic excited states is widely regarded as a challenge because of the intense effort these often-large calculations put on computational resources.

When understanding chemical reactivity possibly the most famous and successful tool in this field is that of the Born-Oppenheimer approximation. Its roots lie in the fact that the electron is 1836 times lighter than the lightest possible nucleus, i.e. the proton. Because of this it can be argued that the nuclear dynamics are much, much slower than the electronic dynamics. The electronic and nuclear motions can then be decoupled and the potential energy of the system can be calculated as a function of the nuclear geometry. This function is also known as a potential energy surface (PES). Conceptually we can think of the nuclei moving in a potential over the averaged electronic motion, where the electrons will instantly respond to any displacement of the nuclei. Chemical reactions take place on potential energy surfaces. Thermal reactions generally include the ground state of the PES with exceptions to this trend being chemilluminescence and gas phase electron transfer processes, whereas a photochemical reaction includes the ground state PES and any possible number of excited states that are each represented by their own PES. A potential energy surface is a function of 3N-6 variables, where N refers to the number of atoms. These numbers come from the fact that three coordinates are needed to specify the locations of N atoms i.e. the x, y and z coordinates in coordinate space. This 3N number is then reduced by six to account for the specification of a centre of mass of the molecule and translation of

the whole molecule and internal rotations. The dimensionality of real potential energy surfaces can be very large as the variables can relate to normal bond vibrations, lengths or any combination of these. Figure 2.1 shows a schematical representation of two potential energy surfaces plotted over just one reaction coordinate *r*. A Jablonski diagram can also schematically show transitions between different electronic and vibrational states, which is shown on the right of figure 2.1.

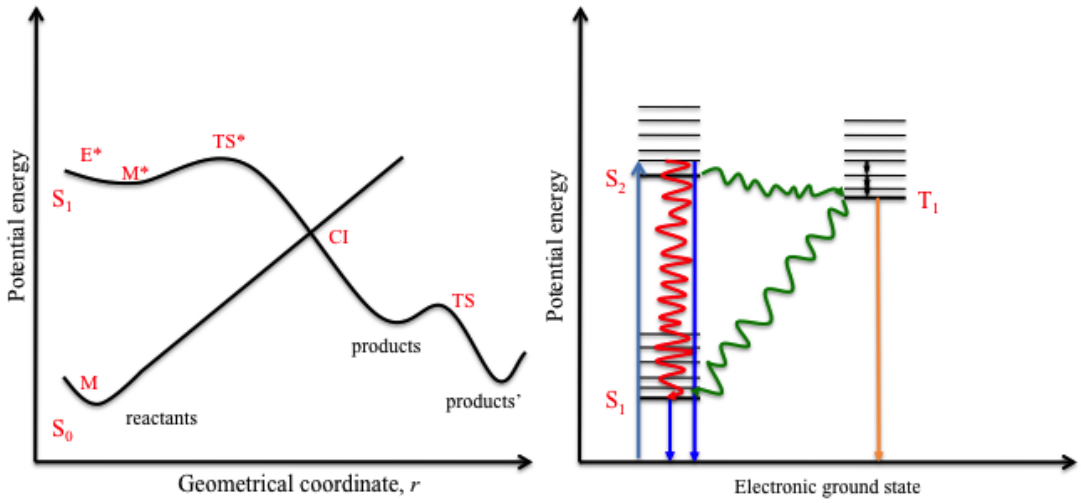

Figure 2.1 Schematical representations of ground and excited state potential energy surfaces connected by a conical intersection plotted against one geometrical coordinate, *r*. A Jablonski diagram for another hypothetical system is on the right.

Here the general features of PESs can be seen with respect to a photochemical reaction between two states in a singlet spin manifold, S_0 and S_1 (other spin states are possible like a triplet state T_1 in the Jablonski diagram). On the right of this figure a photochemical reaction occurs when the system at the ground state minimum energy geometry, M, absorbs a photon and is excited onto the excited state PES, S_1, to a structure in the Franck-Condon region, E*. This region is a region of vertical excitation from the lower to upper states that obeys the Franck-Condon principle that states what electronic transitions the system can take before the nuclei can respond because of the mass difference, so the upper state will closely resemble the lower state. This is conceptually similar to the Born-Oppenheimer approximation. From here the system will follow a minimum energy path to the excited energy minimum structure M*. Direct radiative decay can occur from this point back to the ground state PES. If the two points are of the same multiplicity like they are here then this decay is called fluorescence. The system from M* can also switch to a state of different multiplicity at the same point,

called intersystem crossing, to a triplet state for example and then decay radiatively from here back to point M. This process is much slower than fluorescence as transitions between states of different multiplicity are formally spin forbidden and are called phosphorescence.

On the right of figure 2.1 is the Jablonski diagram. This is a schematical representation of the excited electronic and vibrational states of a system. Thick black horizontal lines represent electronic states and thin lines vibrational states of that electronic state. Here states of different multiplicity are present but any energy difference between states separated along the x-axis is purely schematical. Different photochemical processes are represented with lines of different colours. The light blue arrow is the absorption of a photon (or more than one) and an excitation from the ground electronic state (of singlet spin) to a vibrational state of the second singlet spin electronic excited state. From here the system may undergo a non-radiative process such as internal conversion represented by the red line where the excess energy of the system is redistributed to some vibrational state in a lower electronic state of the same spin, here the first singlet spin excited electronic state. The same thing can also happen to a state of different spin, here the first triplet spin electronic excited state. This is intersystem crossing and is represented by the green arrow. Radiative processes can occur where the system can directly relax from the initially populated state of the same spin down to the ground state or from a state populated after interconversion. This is fluorescence and is represented by dark blue arrow. Radiative relaxation after intersystem crossing to the triplet state to the ground state is phosphorescence and is represented by the orange arrow. The timescales of all these processes shown in figure 2.1 varies quite considerably. A molecular vibration takes place on the order of a few femtoseconds and motion through a conical intersection is on the same timescale. This shows the system often cannot vibrate many times before passing to the lower state. Fluorescence can take place on a nanosecond time scale so a system can vibrate many times before the system relaxes to the lower state. Phosphorescence can take place on a time scale of seconds or even longer.

In this thesis however we are primarily concerned with examples of systems where instead of merely fluorescing or phosphorescing back to the ground state the system can follow a minimum energy path, which may or may not include more than

one excited state, and decay in a radiationless manner through a point on both PESs where the energies of states are degenerate; a conical intersection, labelled CI on figure 2.1. There may be some energy barrier on the excited PES in the form of a transition state geometry, TS*, where its imaginary frequency relates to a vibrational mode leading to a region of conical intersection. Decay through a conical intersection is very fast, in order of a few vibrational periods so on an ultrafast or femtosecond timescale. The presence of conical intersections can be inferred by experimental observation and the lack of any fluorescence or phosphorescence. Such conical intersections are prevalent in organic photochemistry as they provide very fast and efficient photochemical 'funnels' to the ground state. They are thought to be part of many light-induced processes in the human body such as the ultrafast *cis-trans* isomerisation in the central motif of the rhodopsin protein in the eye, so giving us vision[1-3]. Early work in this field was conducted by groups of Robb[4-10] and Yarkony[11-14] and Ruendenberg[15-18] on small systems and organic molecules. Advances in computer hardware and theoretical methods means that conical intersections have increased in prominence and are now ubiquitous in photochemistry in general.

Theoretically modelling structures on the ground state PES can be done relatively straightforwardly by using any of a number of so-called *ab initio* methods, which are designed to solve the Schrödinger equation, or density functional theory (DFT) which is conceptually different. These methods are discussed in further detail later in this chapter. However attempting to model PESs around the point of a conical intersection presents a challenge. This is because at the point of a conical intersection vibrational motion of the nuclei can change the nature of the electronic wavefunction. The nuclear and electronic motions are coupled and can no longer be separated and the Born-Oppenheimer approximation breaks down. This type of coupling is called vibronic coupling. This represents two general challenges from the point of view of designing theoretical methods to account for such behaviour. The first challenge is developing methods that can calculate many-electronic states of molecular systems. The second challenge is to develop methods which can describe non-Born-Oppenheimer behaviour on these surfaces i.e. regions of conical intersection.

This breakdown of the Born-Oppenheimer effect can be seen symbolically. Firstly consider ab initio methods in quantum chemistry, which look to solve the time independent Schrödinger equation;

$$\widehat{H}_i \Psi_i = E_i \Psi_i \tag{2.1}$$

Where Ψ_i is the total wavefunction for the *i*-th state of the system and E_i is the total energy of the *i*-th state of the system. Practically this equation cannot be solved when the system is made up of more than two particles so further approximation must be made here and there is a disparity between types of particle, here the types of particle discussed are nuclei and electrons and are treated differently so the Hamiltonian operator is separated into nuclear and electronic parts.

$$\widehat{H}_T(\mathbf{R},\mathbf{r}) = \widehat{T}_N(\mathbf{R}) + \widehat{H}_e(\mathbf{r};\mathbf{R}) \tag{2.2}$$

The nuclear kinetic energy operator $\widehat{T}_N$ only acts on the nuclear coordinates $(\mathbf{R})$. The second term is known as the electronic Hamiltonian and acts on both nuclear and electronic coordinates $(\mathbf{r};\mathbf{R})$ and results from the 'clamping' of the nuclei to fixed positions. A range of eigenvalue equations can now be solved of the form

$$\widehat{H}_e \Psi_i^e(\mathbf{r};\mathbf{R}) = V_i(\mathbf{R}) \Psi_i^e(\mathbf{r};\mathbf{R}) \tag{2.3}$$

Where any state *i* of the system has its own wavefunction, which is called the adiabatic wavefunction for state *i*, $\Psi_i^e(\mathbf{r};\mathbf{R})$ which depends parametrically on both electronic and nuclear coordinates and each eigenvalue $V_i(\mathbf{R})$ is dependent only on the nuclear coordinates. Solved for different arrangements of the nuclei these equations provide the adiabatic potential energy surface for state *i* and there is an infinite number of states which can be associated to the ground and excited states of the system. The electronic eigenfunctions are not allowed to mix under the nuclear coordinates and so are kept independent of one-another under this adiabatic approximation.

If the total molecular wavefunction is expanded using as a basis the adiabatic eigenfunctions of a Hermitian (symmetric) matrix.

$$\Phi_T(\mathbf{r},\mathbf{R}) = \sum_{i=1}^{\infty} \chi_i^n(\mathbf{R})\Psi_i^e(\mathbf{r};\mathbf{R}) \tag{2.4}$$

This expression can then be inserted into the total molecular Shrödinger equation that gives the following equation

$$\nabla_n^2\chi_i^n + E_j\chi_i^n + \sum_{i=1}^{\infty} -\frac{1}{M}\left[\left\langle \Psi_j^e \middle| \nabla_n \middle| \Psi_i^e \right\rangle \left(\nabla_n \chi_i^n\right) + \left\langle \Psi_j^e \middle| \nabla_n^2 \middle| \Psi_i^e \right\rangle\right]\chi_i^n = E_{tot}\chi_i^n \tag{2.5}$$

This is possible as the electronic eigenfunctions are eigenfunctions of a Hermitian (symmetric) operator and so are orthogonal and normalized, 'orthonormal' see equation (2.13). Rectilinear coordinates are used for $\hat{T}_N$, M is a mass scale (here the average nuclear mass using a standard scale and the mass of an electron is one atomic unit) and *i* and *j* are different states of the system. The Born-Oppenheimer approximation neglects the first- and second-order nonadiabatic coupling terms that are the nondiagonal $(i \neq j)$ terms in equation (2.5) and the diagonal term $\left\langle \Psi_j^e \middle| \nabla_n^2 \middle| \Psi_i^e \right\rangle$, the second-order nonadiabatic coupling terms. This results in the nuclear Shrödinger equation

$$\nabla_n^2\chi_i^n + E_i\chi_i^n = E_{tot}\chi_i^n \tag{2.6}$$

Where all states are thought of being completely decoupled from one another. Coupling between states can be very small due to the inverse mass dependence but the first-order nonadiabatic coupling term can also be written so that it depends inversely on the difference in energy between electronic states (electronic eigenvalues of states *i* and *j*).

$$\left\langle \Psi_j^e \middle| \nabla_n \middle| \Psi_i^e \right\rangle = \frac{\left\langle \Psi_j^e \middle| \dfrac{\partial \hat{H}_e}{\partial \mathbf{R}} \middle| \Psi_i^e \right\rangle}{V_j - V_i} \tag{2.7}$$

This quantity is called the first order non-adiabatic coupling, a non-Born-Oppenheimer term and is not calculated directly by modern electronic structure software, instead the numerator on the right hand side is calculated which is called the derivative coupling.

This equation is fully derived in appendix 1 to show how it comes about. It can be seen from this equation that in the area of degeneracy or near-degeneracy between these two states that the term on the bottom becomes zero and the whole term has a singularity at this point. Therefore this coupling becomes more important than any mass difference and the nuclear and electronic motions can no longer be separated. This can also be seen in equation (2.5) where there are terms which are inversely proportional to mass meaning they are usually very small but in a non-Born-Oppenheimer problem the first order non-adiabatic coupling becomes very large and cannot be ignored anymore irrespective of its inverse proportionality to mass. In order to model such topological PES features as conical intersections we must go further than the Born-Oppenheimer approximation.

Equation (2.7) is very important when one looks to find a conical intersection on a PES. The history of conical intersections goes back many years to the earlier part of the 20th century. In 1929 von-Neumann and Wigner[19, 20] proved mathematically that two independent parameters have to be varied to get a degeneracy of eigenvalues of a real symmetric matrix such as a real Hamiltonian matrix. This Hamiltonian matrix depends on a set of nuclear coordinates so when these coordinates are changed then the matrix elements will also change. Here the Von-Neumann Wigner parameters are the vibrational degrees of freedom of a system. Applying this to vibrational degrees of freedom in molecules it was realised that the non-crossing rule for diatomics, with their one vibrational degree of freedom, that two electronic states cannot cross if they are of the same symmetry, is not valid for polyatomic molecules. This was realised by Edward Teller in 1969[21]. Instead electronic state PESs of a polyatomic molecule can cross in a space of M-2, where M is the number of vibrational degrees of freedom in the molecule. It is important here to note the timescale between these two reports. The von-Neumann Wigner theorem was very abstract when it was first introduced where the parameters discussed were not explicitely defined. It took forty years for Edward Teller to show this theorem held true for vibrational degrees of freedom.

Considering the conical intersection point CI in figure 2.1 for small displacements, the degeneracy is maintained for molecular displacements along any of the M-2 vibrational coordinates. This is called the intersection space and is formally 3N-8 in dimension. The remaining two vibrational coordinates therefore lift the

degeneracy and allows passage through the conical intersection. These two coordinates together form a two dimensional plane which is known as the branching space here, but has other names with varying notation[22-27]. These two vibrational coordinates are better known as the gradient difference and derivative coupling vectors which are respectively shown in equations (2.8) and (2.9).

$$\bar{x}_1 = \frac{\partial(E_1 - E_2)}{\partial \mathbf{R}} \tag{2.8}$$

$$\bar{x}_2 = \left\langle \Psi_i \middle| \left(\frac{\partial \hat{H}_e}{\partial \mathbf{R}} \right) \middle| \Psi_j \right\rangle \tag{2.9}$$

In the above equations **R** is a vector of nuclear Cartesian coordinates, E_1 and E_2 are the eigenvalues of the two electronic states and Ψ_i and Ψ_j are solutions of the electronic Schrödinger equation for states *i* and *j*. If these two vector coordinates are plotted against the potential energy of the two degenerate states then the result is the conical intersection takes the form of a double cone. This is shown schematically in figure 2.2 along with two types of conical intersection. There is a great variety in the upper and lower surface topology around the point of a conical intersection and indeed this point is but a single point on a degenerate seam that spans the intersection space and can be highly curved through the nuclear configuration space[28]. The work of Ruedenberg on the variety of surface topologies around a point of intersection is important here, see for example This means searching for a conical intersection geometry and accurately deciphering the topology of the surfaces around it is a challenging task both in terms of using chemical intuition to decide which geometries are important for the problem and the theoretical methods used to describe such geometries. Molecular symmetry can often be used to predict the presence of an electronic degeneracy and so a conical intersection. This was a result of the pioneering work of Hermann Jahn and Edward Teller, known as the Jahn-Teller effect.

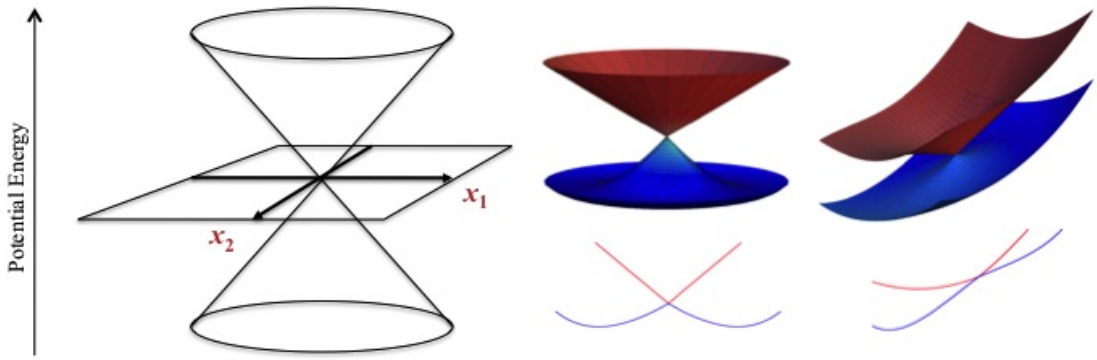

Figure 2.2 A schematic description of a conical intersection with the branching space included on the left and two conical intersection topologies on the right. The first one is circular cone which can be present in a Jahn-Teller problem and the second a sloped conical intersection which can be present in more general vibronic coupling problems involving organic molecules. These are further described in[29].

2.2 The Jahn-Teller and pseudo Jahn-Teller effects

In 1937 Hermann Jahn and Edward Teller proved by thoroughly studying all molecular point groups that any chemical structure in an orbitally (electronic) degenerate state will be unstable to linear displacement along some non-totally symmetric vibrations. This displacement causes the lower adiabatic PES to be stabilized[30]. The symmetry of the vibrational coordinates that cause this effect can be determined by the symmetric square of the irreducible representation of the degenerate electronic state with itself. Because of molecular symmetry, as worked out by Jahn and Teller, there will always be a non-totally symmetric vibration which will remove the electronic degeneracy and lower the symmetry and energy of the system. The geometrical coordinates that lead to the degenerate state is called the Jahn-Teller geometry and is a conical intersection point such as the point CI in figure 2.1.

One can express the nature of a Jahn-Teller distortion in a standard way. An E symmetry degenerate electronic state interacting with a doubly degenerate vibrational modes of e symmetry can be written as $E \otimes e$. These vibrational modes will lift the E symmetry degeneracy at first-order. So if the derivative coupling and gradient difference vectors are calculated then they will have symmetries as predicted by the Jahn-Teller theorem and will always transform to be a totally-symmetric and non totally-symmetric irreducible representation of an Abelian (no degenerate irreducible

representations) subgroup of the higher symmetry non-Abelian symmetry group that contains the degeneracy. The Jahn-Teller and pseudo Jahn-Teller effects, which will be discussed later, have been used to interpret many experimental observations most notably high T_c (critical temperature) superconductivity. Jahn-Teller geometries are the same as the conical intersections that are common in organic chemistry and if they can be reached on the upper PES then they provide an efficient chemical funnel to the lower state, and as will be discussed later the structures that are found around the point of a Jahn-Teller geometry are often non-classical inorganic structures. They differ from those intersections found in organic chemistry because their presence can always be predicted from symmetry arguments. Indeed diagnostic tools have been developed in order to predict which structures result from a Jahn-Teller distortion. One such tool is the epikernel principle of Ceulemas and Vanquickenborne[31]. In order to understand this theorem kernels and epikernels must be introduced. These are calculated for any irreducible representation in a point group. Kernels (K_i) are groups of symmetry elements that are preserved when a system distorts along a vector that spans some irreducible representation (Λ). Epikernels (E_i) are groups of higher symmetry elements that are only selectively preserved in part of the degenerate distortion space. The shorthand nomenclature here considers the i-th kernel or epikernel for some irreducible representation in some symmetry point group (G). so giving $K_i(G, \Lambda)$ and $E_i(G, \Lambda)$. The theorem states that after linear distortion from some Jahn-Teller geometry the point groups of the resulting minima will be the highest ranking epikernels and the point groups of saddle points will be the lower ranking epikernels and kernels.

Certain topological features of PESs such as local curvature and areas where two or more surfaces are close in energy but do not cross (avoided crossing) can be attributed to another type of Jahn-Teller effect, the pseudo-Jahn-Teller effect. This effect can explain such topological features that cause molecules to spuriously break symmetry when not in a degenerate electronic state. It differs from the Jahn-Teller effect as it describes the vibronic coupling between two or more non-degenerate electronic states and a non-totally symmetric vibrational mode, this can be either degenerate or non-degenerate. What is important to the work herein described and the pseudo-Jahn-Teller effect in particular is how two different degenerate states that can each show a Jahn-Teller effect can also vibronically couple. The energy difference at

some common Jahn-Teller geometry can become vanishingly small but non-zero, indicating an avoided crossing. Radiationless decay can occur through an avoided crossing like through a conical intersection however the timescale for decay may be longer as more than one vibrational oscillation may be needed around the point where the energy difference is smallest before the system can pass to the lower surface. Figure 2.3 shows the differences between radiationless decay through a conical intersection and through an avoided crossing.

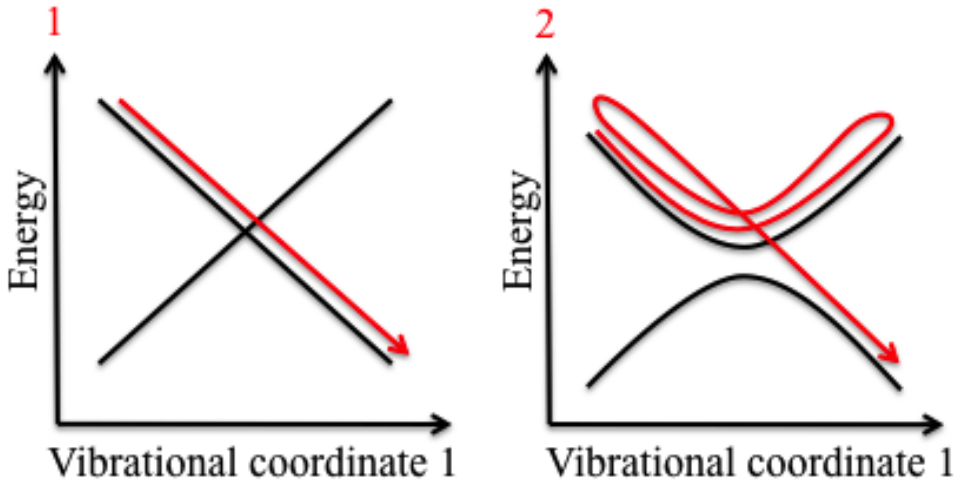

Figure 2.3 Schematical differences between the radiationless decay though a conical intersection (1) and an avoided crossing (2). Decay through an avoided crossing may take longer as the system may oscillate many times on the upper surface first.

Longuet-Higgins and Coulson[32, 33] were the first to call this effect the pseudo-Jahn-Teller effect in 1950 after studying the lowest singlet states of cyclobutadiene. This effect however must not be confused with another type of Jahn-Teller effect that some authors refer to as the second order Jahn-Teller effect. The effect is defined here as Jahn-Teller coupling at second order with respect to nuclear displacements. Where the Jahn-Teller effect and pseudo-Jahn-Teller effects are the result of molecules where their shells of frontier molecular orbitals are unfilled. The second order Jahn-Teller effect is the result from a molecule with a filled shell of frontier molecular orbitals but a very small energy gap between highest occupied molecular orbital (HOMO) and lowest unoccupied (LUMO) molecular orbital. The difference between the Jahn-Teller and second order Jahn-Teller effect can most clearly be seen in the size of molecular distortion that can results from these effects, where the Jahn-Teller and pseudo-Jahn-Teller effects cause small distortions such as symmetry breaking but the product of the distortion would still belong to a familiar symmetry

point group. The distortion that is caused by the second order Jahn-Teller effect is much bigger and can lead to distortion of the molecule. The symmetry rules are also different between these two effects. The rule for the Jahn-Teller and pseudo Jahn-Teller effects, as previously mentioned, is that the vibrational coordinates, Q, that cause these effects can be determined by the symmetric square of the irreducible representation of the degenerate electronic state with itself. The selection rule of the second order Jahn-Teller effect is that the symmetry of Q is the direct product of the symmetries of the ground and low-lying excited states. The mathematical formulation of these effects is complex and particularly for the pseudo Jahn-Teller effect many formulations have been published. Perhaps the easiest to understand is the one suggested by Pearson[34]. This has the form of a perturbative expansion for the energy E of an electronic state Ψ_0 that is a function of some vibrational normal coordinate Q_i;

$$E(Q_i) = E_0 + Q_i \left\langle \Psi_0 \left| \frac{\partial V}{\partial Q_i} \right| \Psi_0 \right\rangle + \frac{Q_i^2}{2} \left\langle \Psi_0 \left| \frac{\partial^2 V}{\partial^2 Q_i} \right| \Psi_0 \right\rangle + Q_i^2 \sum_j \frac{\left[\left\langle \Psi_0 \left| \frac{\partial V}{\partial Q_i} \right| \Psi_j \right\rangle \right]^2}{E_0 - E_j} + \ldots . \quad (2.10)$$

In this expansion E_0 is the energy of the optimized geometry from which the distortion occurs, Ψ_0 and Ψ_j are two electronic wavefunctions that usually represent ground and excited states but can be any state, V is the electronic potential and E_j the energy of the *j*-th excited state. The Jahn-Teller effect comes from the terms that are linear in Q_i and the pseudo- and second order Jahn-Teller effects come from terms that are quadratic in Q_i. The first of these terms is the gradient of an electronic state and by its own definition will be zero for the optimized geometry in a non-degenerate electronic state. The second of these terms is more challenging to describe but one can think of it as an increase in energy due to distortion using the fixed wavefunction that was optimized at the reference geometry. This term is always positive, which was proved by Bersuker and co-workers[35]. The third term is always negative and is the mixing of adiabatic electronic states under a nuclear perturbation. It allows for the electronic wavefunction to relax at distorted geometries. From the definitions of these two second order terms it can be seen that the stability of a molecule with respect to

distortion along the vibrational coordinate Q_i is determined by the relative magnitudes of the two terms. The molecular geometry will be unstable and the potential energy surface will have negative curvature for Q_i if the distortion term has a larger magnitude than the relaxation term.

Bersuker and co-workers have rigorously investigated the commonality of the pseudo-Jahn-Teller effect and it has been shown that it is responsible for instabilities of high symmetry molecular systems that are in non-degenerate electronic states. Examples of such systems are NH_3, CH_4, BH_3, BH_4^- and a series of octahedral metal complexes. Theoretical study of such effects requires state-of-the art theoretical methods, such as multi-configurational electronic structure methods which will be discussed later in this chapter.

2.3 Electronic structure theory

2.3.1 The wavefunction and Hamiltonian operator

The systems discussed in this thesis and their photochemistry have been investigated by a wide range of methods that are part of the wider field of electronic structure theory. Some methods used for spectroscopy, surfaces and dynamics are very specialised.

The starting point of this discussion is perhaps the principal postulate of electronic structure theory, the wavefunction, Ψ. A wavefunction exists for any chemical system and can be described using quantum mechanics. The beauty of a wavefunction from the point of a theoretical chemist is that it will give back any observable property of its chemical system if it is operated upon by the correct operator in an eigenfunction equation. The wavefunction is also governed by some rules. When a wavefunction for a one particle system is multiplied by its complex conjugate the product will have units of probability density which is probability per unit distance.

$$\int |\Psi|^2 \, dr = 1 \tag{2.11}$$

So the normalized integral of the wavefunction over all space being equal to one shows that the probability of finding the particle at $r \pm dr$ is one. Because of this the wavefunction must also be single-valued, continuous and quadratically integrable. The eigenvalue that is most commonly sought by the theoretical chemist is the energy of the chemical system. The appropriate operator, which returns the energy of the system when applied to the wavefunction, is the Hamiltonian operator in the Schrödinger equation. The Hamiltonian can be written generally as

$$\widehat{H} = -\sum_i \frac{1}{2m_e}\nabla_i^2 - \sum_i \frac{1}{2m_k}\nabla_k^2 - \sum_i \sum_k \frac{Z_k}{r_{ik}} + \sum_{i<j} \frac{1}{r_{ij}} + \sum_{k<l} \frac{Z_k Z_l}{r_{kl}} \qquad (2.12)$$

Where the first two terms relate to the respective kinetic energies of the electrons and nuclei, the third term is the attraction between the nuclei and electrons and the last two terms are the repulsive interactions between electrons and the repulsive interactions between the nuclei respectively. Here i and j are electrons, k and l are nuclei, m_e and m_k are the respective masses of the electrons and nuclei and ∇^2 is the kinetic energy Laplacian in three dimensional Cartesian coordinates. A point to note here is that the Schrödinger equation can have an infinite number of acceptable solutions so there can be an infinite set of orthonormal wavefunctions Ψ_α that will each have their own respective eigenvalues, E_∞. Orthonormality is defined as

$$\int\int\int \Psi_i \Psi_j d\vec{r}_1 \vec{r}_2 .. \vec{r}_n = \delta_{ij} \qquad (2.13)$$

For a one-particle system where the wavefunction depends on three dimensional coordinates. So for a one-particle system with a specific wavefunction in mind, say Ψ_i then the energy can be calculated

$$\int \Psi_i \widehat{H} \Psi_i dr = \int \Psi_i E_i \Psi_i dr \qquad (2.14)$$

In which the energy for that specific wavefunction is produced and i and j are identical and index the wavefunction that is chosen. Equation (2.14) can now be simplified by

taking the energy outside the integral on the right hand side as it is a scalar value and taking equation (2.13) in account this leaves

$$\int \Psi_i \widehat{H} \Psi_i dr = E_i \tag{2.15}$$

The energy of the system can be determined if one has a suitable molecular wavefunction and applies the Hamiltonian.

2.3.2 The variational principle

The system can have many eigenfunctions that can form an infinite set, however equation (2.15) does not explain how to obtain this set. So a logical starting place could be to define some function Φ that is composed of all Ψ_i in some combination whose contributions are determined by some coefficients c_i. So the energy of the system with this function would be

$$\int \Phi \widehat{H} \Phi dr = \sum_i c_i^2 E_i \tag{2.16}$$

Where the sum of all the coefficients and their associated energies will give the energy of Φ. Quantum mechanics states that the energy must be bound from below so there must be a lowest energy value of the system, the ground state. Even though one may not know any of the values of the coefficients or energy value of that coefficient the total energy must be equal to or greater than zero

$$\int \Phi \widehat{H} \Phi dr - E_0 \int \Phi^2 dr \geq 0 \tag{2.17}$$

Where E_0 is the energy of the ground state. If the multiplier of the ground state energy is equal to one the chosen function Φ is normalized by definition. A simple rearrangement of equation (2.17) gives the following equation

$$\frac{\int \Phi \widehat{H} \Phi dr}{\int \Phi^2 dr} \geq 0 \tag{2.18}$$

What equation (2.18) shows is that a wavefunction can be constructed in any way and its suitability to mimic the ground state of the true system can be judged by how low its energy is. One gets better values by constructing better wavefunctions. This is called the variational principle.

2.3.3 Hartree-Fock theory

Now the energy of a trial wavefunction can be determined by constructing a trial wavefunction and then improving it with the variational principle in mind. As previously discussed the trial wavefunction can be constructed in any way one wishes but because the systems under study are chemical, for convenience this could be the linear combination of atomic orbitals (LCAO) approach, where the guess is constructed as a linear combination of atomic wavefunctions.

$$\phi = \sum_{i=1}^{N} a_i \varphi_i \tag{2.19}$$

Here there is a set of N φ_i functions that forms a basis set where each function φ_i is called a basis function and each of these has associated with it some coefficent a_i. Some issues arise from this approximation such as where the basis functions should be positioned around the chemical system being studied and what they should look like but for simplicity it can be thought that the basis functions are centred on the nuclei. The energy of the guess wavefunction can be computed by combining equations (2.18) and (2.19) which results in the equation

$$E = \frac{\int \left(\sum_i a_i \varphi_i \right) \widehat{H} \left(\sum_j a_j \varphi_j \right) dr}{\int \left(\sum_i a_i \varphi_i \right) \left(\sum_j a_j \varphi_j \right) dr} \tag{2.20}$$

Which can be rearranged to give;

$$E = \frac{\sum_{ij} a_i a_j H_{ij}}{\sum_{ij} a_i a_j S_{ij}} \tag{2.21}$$

Two new integrals appear now, H_{ij} is known as the resonance integral and S_{ij}, which is the overlap integral and can be thought of as the level of overlap between two basis functions in space in a phase-matched fashion. To minimise the energy of the wavefunction values must be chosen for the basis set coefficients a_i to minimise the energy for all possible linear combinations of basis functions. Considering mathematics the energy can be considered as a function and therefore its energy is to be at a minimum when its derivatives are zero with respect to all free variables, in this case the basis set coefficients. This gives rise to N equations, which must be solved for this to be true.

$$\sum_{i=1}^{N} a_i (H_{ki} - ES_{ki}) = 0 \tag{2.22}$$

Where all N equations are over all k. Each equation here has an unknown, a_i, and if the determinant formed from the coefficients of all a_i is equal to zero then the entire set of N equations will have a non-trivial solution. This set can be expanded into a matrix representation, the so-called secular equation.

$$\begin{vmatrix} H_{11} - ES_{11} & \cdots & H_{1N} - ES_{1N} \\ \vdots & \ddots & \vdots \\ H_{N1} - ES_{N1} & \cdots & H_{NN} - ES_{NN} \end{vmatrix} = 0 \tag{2.23}$$

This representation will have N energies E_j which will permit this equation to be true. Each E_j will produce its own individual set of coefficients a_{ij} which can be found by solving the linear set of equations (2.22) with E_j. The optimal wavefunction within the given basis set, ϕ_j will be defined by a_{ij}.

$$\phi_j = \sum_{i=1}^{N} a_{ij} \varphi_i \tag{2.24}$$

Everything discussed in this section so far is for a one-electron system so in the chosen basis the ground state would simply refer to the only occupied molecular orbital with the excited states being the higher lying molecular orbitals. Naturally matters become much more complicated for many-electron systems.

The overall goal is to successfully apply the Schrödinger equation to a many-electron wavefunction that describes a chemically interesting system. Perhaps the simplest starting point when moving from a one-electron system to a many-electron system is to imagine the many-electron system being made up of many one-electron wavefunctions. The energy of each can then be determined by solving a series of one-electron Schrödinger equations of the form

$$\hat{h}_i \psi_i = \varepsilon_i \psi_i \tag{2.25}$$

Where electron i is in the orbital ψ. The Hamiltonian in this case contains terms relating to the one-electron kinetic energy and the term relating to electron-nuclei attraction

$$\hat{h}_i = -\frac{1}{2}\nabla_i^2 - \sum_{k=1}^{M} \frac{Z_k}{r_{ik}} \tag{2.26}$$

Where all electrons in the system are non interacting. The Hamiltonian of the total system is therefore the sum of all one -electron Hamiltonians

$$\widehat{H} = \sum_{i=1}^{N} h_i \tag{2.27}$$

So the total electronic Schrödinger equation for this system will have the form

$$\widehat{H}\Psi_{HP} = \left(\sum_{i=1}^{N} \varepsilon_i \right) \Psi_{HP} \tag{2.28}$$

Where the subscript 'HP' stands for 'Hartree-product' and this well known result is known as a Hartree-product wavefunction. This is a very simplistic formulation as it does not account for the in distinguishability of electrons and interelectronic repulsion. This feature can be included into the Hamiltonian by adding a term to the Hamiltonian already defined in equation (2.26).

$$\hat{h}_i = -\frac{1}{2}\nabla_i^2 - \sum_{k=1}^{M}\frac{Z_k}{r_{ik}} + V_i\{j\} \tag{2.29}$$

Where the new term $V_i\{j\}$ describes the average potential experienced by electron i with all other electrons in orbitals $\{j\}$. This term is defined as

$$V_i\{j\} = \sum_{j\neq i}\int\frac{\rho_j}{r_{ij}}d\vec{r} \tag{2.30}$$

Integration over all space is needed as the nuclei are treated as point charges in this description and electrons are treated as wavefunctions so their charge spreads out, and ρ_j is the probability density associated with electron j. At this point it is worth mentioning the dilemma that is created by looking for optimum wavefunctions for all the occupied molecular orbitals of the system that can then be used in one-electron Hamiltonians, but they cannot be used if they are not used in the first instance. The solution to this is to bring in the idea mentioned earlier about firstly generating a guess. Hartree[36] was the first to try this in 1928 when dealing with atomic orbitals on atoms. A series of guess wavefunctions are used to construct all one-electron Hamiltonians. All one-electron Schrödinger equations are then solved to produce a new set of one-electron wavefunctions that can be used to produce a new set of one- electron Hamiltonians. This new set produced should be different from the initial guess and perhaps closer to the best possible description of the system using this method. This process can be repeated to produce, presumably, increasingly accurate wavefunctions. This process can be artificially ended by imposing a condition where the difference between a new set of wavefunctions and the former set is within a set threshold level. This final set of wavefunctions is the *converged* set. This total process is called the 'self-consistent-field' (SCF) procedure and the converged orbitals are called the SCF orbitals. There are

many caveats to this process such as getting the correct balance between the number of SCF cycles and the convergence threshold as large numbers of cycles can be computationally expensive but a low threshold will lead to a poorly converged wavefunction.

The addition of $V_i\{j\}$ improves upon the Hamiltonian used in the Hartree product wavefunction but has a weakness that in part causes it to fail to accurately describe the true Hamiltonian of the system, namely that electron-electron repulsion is double counted because if all one-electron eigenvalues were summed up from equation (2.28) then it can be seen that all one-electron Hamiltonians include the repulsion of their associated electrons with all other electrons in the system in a average way. So h_j would include the repulsion of electron *j* with electron *i*, but h_i would also include the same repulsive contribution. This can be corrected by calculating the energy as

$$E = \sum_i \varepsilon_i - \frac{1}{2}\sum_{i \neq j} \int\int \frac{|\psi_i|^2 |\psi_j|^2}{r_{ij}} d\vec{r}_i d\vec{r}_j \tag{2.31}$$

In this equation the double integral over all space is again included as all electrons are treated as wavefunctions, this integral is also referred to as the Coulomb integral that will be discussed later. The energy of a molecular orbital is given by ε_i, *i* and *j* run over all electrons where the probability densities of electrons *i* and *j* are expressed in their true form as

$$\rho_j = |\psi_j|^2 \tag{2.32}$$

With this correction in place this description is still short of a few chemically relevant properties of electrons in orbitals that are necessary to describe a many-electron system, most importantly the Pauli exclusion principle and through this the spin of electrons.

Due to the Born–Oppenheimer approximation the electronic Hamiltonian is reliant only on the spatial coordinates of electrons but a description of the spin of each

electron is needed for a complete description. This satisfies the Pauli exclusion principle that states that no two electrons can have the exact same set of quantum numbers. Perhaps the simplest remedy to this is to add a spin coordinate, ω to the existing three spatial coordinates, *r*. Together they can be called *x*. This alone makes no difference at all but does make a difference when another postulate is taken into account, antisymmetry. Antisymmetry, or the antisymmetry principle states that a wavefunction must change sign if the coordinates of two electrons are interchanged, i.e.

$$\Psi(x_1....,x_i,....,x_j,....x_N) = -\Psi(x_1....,x_j,....,x_i,....x_N) \tag{2.33}$$

It is worth noting that antisymmetry is also an independent postulate of quantum mechanics from the Schrödinger equation meaning that a suitable wavefunction must satisfy both. For example the antisymmetric wavefunction for a two-electron system with two one-electron orbitals the wavefunction would look like

$$\Psi(x_1,x_2) = 2^{-1/2}(\psi_i(x_1)\psi_j(x_2) - \psi_j(x_1)\psi_i(x_2)) \tag{2.34}$$

Where the prefactor $2^{-1/2}$ is for normalization. Writing out antisymmetric wavefunctions for such simple systems is quite straightforward however this quickly becomes rather time consuming for bigger systems but equation (2.34) can be written as a determinant

$$\Psi(x_1,x_2) = 2^{-1/2}\begin{vmatrix} \psi_i(x_1) & \psi_j(x_1) \\ \psi_i(x_2) & \psi_j(x_2) \end{vmatrix} \tag{2.35}$$

For this two-electron example writing it as a determinant makes little difference than writing it out in long hand notation but for *N* electron systems writing a determinant allows for the wavefunction to be written in a reasonably manageable form.

$$\Psi(x_1,x_2,....,x_N) = (N!)^{-1/2}\begin{vmatrix} \chi_i(x_1) & \cdots & \chi_k(x_1) \\ \vdots & \ddots & \vdots \\ \chi_i(x_N) & \cdots & \chi_k(x_N) \end{vmatrix} \tag{2.36}$$

Here χ now appears and this is called a 'spin orbital'. This takes into account the spin of electrons, as spin orbitals are the product of a spatial orbital ψ and an electron spin eigenfunction. It was first realised by Slater in 1930[37] that antisymmetric wavefunctions can be written as a determinant. Interchanging two rows will cause the determinant to change sign. Antisymmetric wavefunctions are large and time-intensive to write down as quantum particles are truly indistinguishable and so every electron appears in every spin orbital. A feature of Slater-determinants that is important for density functional theory (DFT) is a correlation effect of electrons of the same spin, quantum mechanical exchange. Exchange describes the reduced probability of finding two electrons close to one another with spins parallel and its effect on the Coulomb repulsion. The concept of the 'Fermi-hole' applies here, conceptually surrounding each electron.

This all leads onto the benchmark method of electronic structure theory for calculating the energy of many-electron wavefunctions – Hartree-Fock theory. This method blends together the ideas already discussed in the variational principle, the secular equation, the SCF procedure and Slater determinants. A Slater determinant can be used to describe an antisymmetric wavefunction and the ground state of the system under study will be given by the best wavefunction from this determinant. Minimizing such a wavefunction, using the variational principle, with respect to the spin orbitals derives the Hartree-Fock equation.

$$\hat{f}(i)\chi(x_i) = \varepsilon\chi(x_i) \tag{2.37}$$

Where $\hat{f}(i)$ in the above equation is a one-electron operator called the Fock operator which has a form very similar to that of the one-electron Hamiltonian of a Hartree product wavefunction.

$$\hat{f}_i = -\frac{1}{2}\nabla_i^2 - \sum_k^{nuclei} \frac{Z_k}{r_{ik}} + V_i^{HF}\{j\} \tag{2.38}$$

Electron-electron repulsion is accounted for in the third term in an average way in which it is the average potential experienced by the *i*-th electron because of all other electrons in the system. Accounting for electron correlation in an average manner rather than an instantaneous one is central to Hartree-Fock theory. The third term is called the Hartree-Fock potential and the potential of electron *i* depends on the spin orbitals of all other electrons. It is defined as

$$2J_i - k_i \tag{2.39}$$

Where J_i and k_i are operators that relate to the Coulomb and exchange integrals respectively. At this point it can be argued that the molecular orbitals of the system must be determined, i.e. a basis set is needed. Roothaan[38] in 1951 came up with a procedure to determine the basis set of molecular orbitals effectively by introducing a set of known spatial basis functions that allows the differential Hartree-Fock equations to be solved using matrix algebra. So a set of *K* known basis functions are introduced and expand the (at the moment) unknown molecular orbitals in the linear combination such as in equation (2.24). Where a_{ij} are a set of expansion coefficients that need to be calculated to obtain the Hartree-Fock molecular orbtials. By substituting this linear expansion into the Hartree-Fock equation a matrix representation can be obtained. This leads onto the Roothaan equations which are written as

$$\hat{f}(1)\sum_v C_{vi}\phi_v(1) = \varepsilon_i \sum_v C_{vi}\phi_v(1) \tag{2.40}$$

$$\mathbf{FC = SCe} \tag{2.41}$$

This is an equation made up of different matrices where **F** is the Fock matrix, which is the matrix representation of the Fock operator with the set of basis functions that were introduced earlier. **S** is known as the overlap matrix and is a positive-definite matrix, which is to say the eigenvalues of the matrix are necessarily positive numbers. The basis functions in the overlap matrix are not orthogonal to each other despite being thought of as normalized and linearly independent and so can overlap. Both of these matrices are *K* x *K* Hermitian (this means it is a square complex matrix equal to its own conjugate transpose) and can be diagonalised by a unitary matrix. The matrix **C** is the matrix of

expansion coefficients and is a K x K square matrix. Finally **e** is the matrix of orbital energies and is diagonal.

So with a basis set of K functions now in hand the secular equation is solved to find all the roots E_j.

$$\begin{vmatrix} F_{11} - ES_{11} & \cdots & F_{1N} - ES_{1N} \\ \vdots & \ddots & \vdots \\ F_{N1} - ES_{N1} & \cdots & F_{NN} - ES_{NN} \end{vmatrix} = 0 \qquad (2.42)$$

Where matrix elements S are the overlap matrix elements already discussed and F has matrix elements of the form

$$F_{\mu\nu} = \langle \mu | -\frac{1}{2}\nabla^2 | \nu \rangle - \sum_{k}^{nuclei} Z_k \langle \mu | \frac{1}{r_k} | \nu \rangle + \sum_{\lambda\sigma} P_{\lambda\sigma}[(\mu\nu \mid \lambda\sigma) - \frac{1}{2}(\mu\nu \mid \lambda\sigma)] \quad (2.43)$$

Here basis functions are indexed by lower-case Greek letters and molecular orbitals are indexed by lower-case Roman letters.

The last term in the equation for the Fock matrix elements involves P, the density matrix. This in abstract determines how important the Coulomb and exchange integrals are energetically to the many-electron wavefunction. The notation of the last term relates to a double integral with four indices

$$(\mu\nu \mid \lambda\sigma) = \int\int \phi_\mu(1)\phi_\nu(1)\frac{1}{r_{12}}\phi_\lambda(1)\phi_\sigma(1)d\bar{r}(1)d\bar{r}(2) \qquad (2.44)$$

Where the basis functions ϕ_λ and ϕ_σ are the probability density of one-electron and ϕ_μ and ϕ_ν are the density of the other. The factor of one half appears in the last term before the exchange term to account for the fact that exchange only occurs when two electrons of the same spin interact, which has already been mentioned. This is naturally not needed for $(\mu\nu \mid \lambda\sigma)$ which is the Coulomb interaction and applies to all electron interactions. This process is used to calculate the orbital coefficients to form a density

matrix that will then be used for the Fock matrix elements. However a secular equation is being used to find those orbital coefficients. This then brings in the idea of an SCF cycle.

So to talk through this process in a closed shell case one would first choose a geometry for the system under study and a suitable basis set. All one-electron, overlap and two-electron integrals would then be calculated and stored. An initial guess density matrix would then be constructed and with all this information then the Hartree-Fock secular equation can be built and solved. An SCF procedure can then proceed until a suitable threshold is met relating to the difference between recurring density matrices. The energy for this chosen geometry within the given basis set is then known. The molecular geometry can then be optimized if desired.

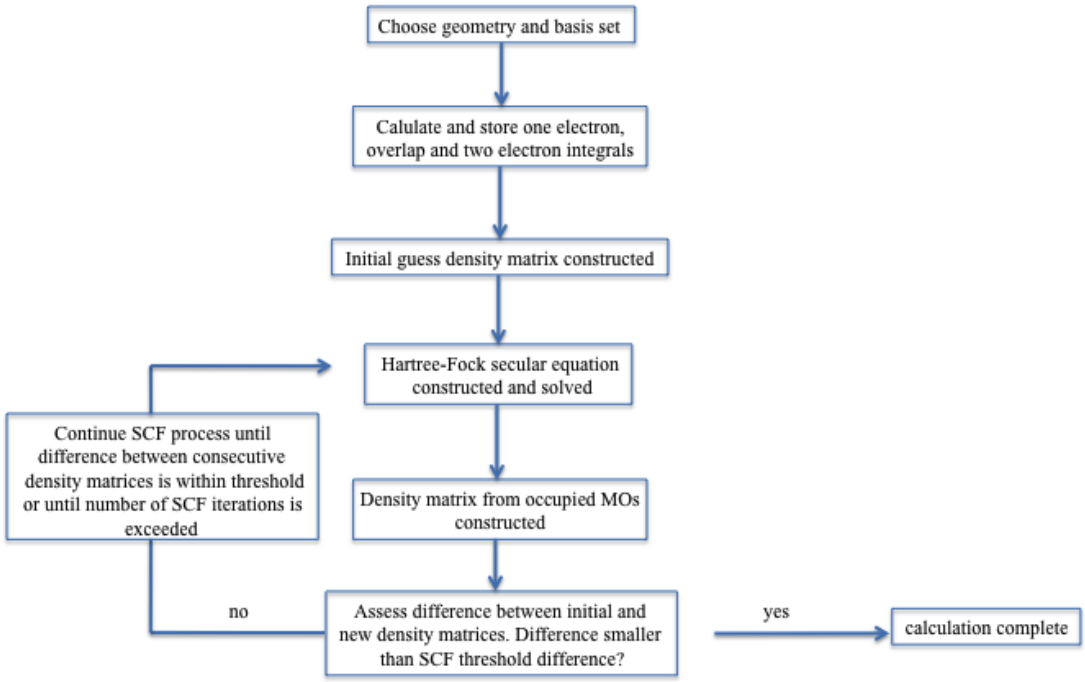

Figure 2.4 Schematic flow chart of the SCF process in Hartree-Fock theory.

Up to now only systems with no unpaired electrons have been studied i.e. they are called ‘closed-shell’. But some of the systems discussed in later chapters of this thesis have unpaired electrons so are ‘open-shell’. So it would be logical at this point to consider how Hartree-Fock theory can be applied to open-shell systems. Hartree- Fock theory applied to closed-shell systems is called restricted Hartree-Fock theory. When an open-shell wavefunction is used then two types of Hartree-Fock are available, restricted

open-shell Hartree-Fock (ROHF) and unrestricted open-shell Hartree-Fock (UOHF) more commonly shortened to simply unrestricted Hartree-Fock (UHF). In ROHF all electrons occupy closed-shell orbitals apart from those which are unpaired. This has a disadvantage however in that the variational energy increases by constraining the paired electrons to closed shell orbtials. So here only UHF will be discussed. The general Hartree-Fock eigenvalue equation with restricted Hartree-Fock spin orbtials is equation (2.37). But for UHF we define two analogous equations with respect to either the α or β spin of an electron

$$\hat{f}^{\alpha}(x_i)\psi_j^{\alpha}(x_i) = \varepsilon_j^{\alpha}\psi_j^{\alpha}(x_i) \tag{2.45}$$

$$\hat{f}^{\beta}(x_i)\psi_j^{\beta}(x_i) = \varepsilon_j^{\beta}\psi_j^{\beta}(x_i) \tag{2.46}$$

With spatial orbitals ψ_j^{α} and ψ_j^{β} describing electrons that have α or β spins respectively. These spatial orbtials come from an unrestricted set of spin orbitals

$$\chi(x_i) = \begin{cases} \psi_j^{\alpha}(r)\alpha(\omega) \\ \psi_j^{\beta}(r)\beta(\omega) \end{cases} \tag{2.47}$$

Where ω is a spin function. In RHF $\psi_j^{\alpha} \equiv \psi_j^{\beta} \equiv \psi_j$ (they are equivalent). If the spatial orbitals are separated according to spin so too must be the Fock operators

$$\hat{f}^{\alpha}(x_i) = h(x_i) + \sum_{a}^{N\alpha}\left[J_a^{\alpha}(x_i) - k_a^{\alpha}(x_i)\right] + \sum_{a}^{N\beta} J_a^{\beta}(x_i) \tag{2.48}$$

$$\hat{f}^{\beta}(x_i) = h(x_i) + \sum_{a}^{N\beta}\left[J_a^{\beta}(x_i) - k_a^{\beta}(x_i)\right] + \sum_{a}^{N\alpha} J_a^{\alpha}(x_i) \tag{2.49}$$

In which the sums in the above equations are over N^{α} orbitals ψ_a^{α} occupied with electrons of α spin with an analogous case for electrons of β spin. The first term $h(x_i)$ is identical to the Fock operator for RHF. Electrons of spin α have Coulomb and exchange potentials coming from all other α spin electrons in ψ_a^{α} orbitals and a Coulomb potential only from electrons of β spin in ψ_a^{β} orbitals. As $f^{\alpha}(x_i)$ depends on β spin orbitals and

$f^{\beta}(x_i)$ depends on α spin orbitals both eigenvalue equations are coupled and must be solved simultaneously in an iterative process. The total electronic energy for this unrestricted case is thus analogous to the restricted case but includes the separation of spins

$$E_0 = \sum_{a}^{N\alpha} h_{aa}^{\alpha} + \sum_{a}^{N\beta} h_{aa}^{\beta} + \frac{1}{2}\sum_{a}^{N\alpha}\sum_{a}^{N\alpha}(J_{ab}^{\alpha\alpha} - k_{ab}^{\alpha\alpha}) + \frac{1}{2}\sum_{a}^{N\beta}\sum_{a}^{N\beta}(J_{ab}^{\alpha\alpha} - k_{ab}^{\alpha\alpha}) + \sum_{a}^{N\alpha}\sum_{b}^{N\beta} J_{ab}^{\alpha\beta} \quad (2.50)$$

Similar to RHF with the Roothaan equations these differential equations can be converted into a matrix representation and a basis set is introduced within which the unrestricted molecular orbitals can be expanded.

$$\psi_i^{\alpha} = \sum_{\mu=1}^{K} C_{\mu i}^{\alpha}\phi_{\mu} \quad (2.51)$$

With an analogous basis set for β spin electrons. A procedure similar to that of Roothan is then carried out but with spins separated to produce to Pople-Nesbet equations

$$\mathbf{F}^{\alpha}\mathbf{C}^{\alpha} = \mathbf{S}\mathbf{C}^{\alpha}\mathbf{e}^{\alpha} \quad (2.52)$$

$$\mathbf{F}^{\beta}\mathbf{C}^{\beta} = \mathbf{S}\mathbf{C}^{\beta}\mathbf{e}^{\beta} \quad (2.53)$$

These equations must be solved simultaneously as both Fock matrices depend on both C^{α} and C^{β} but can be solved in a similar way to the Roothan equations. Now if one were to consider the total charge density for the electrons it would simply be the sum of the individual charge densities of the electrons with α or β spins.

$$\rho^{T}(r) = \rho^{\alpha}(r) + \rho^{\beta}(r) \quad (2.54)$$

However electrons of different spin have different spatial distributions so a spin density is defined

$$\rho^{S}(r) = \rho^{\alpha}(r) - \rho^{\beta}(r) \quad (2.55)$$

Where the individual spin densities are positive everywhere. Substituting the basis set expansions into the expressions for the individual charge densities can then produce the density matrices.

$$\rho^{\alpha}(r) = \sum_{a}^{N\alpha} \left| \psi_a^{\alpha}(r)^2 \right| = \sum_{\mu} \sum_{\nu} P_{\mu\nu}^{\alpha} \phi_{\mu}(r) \phi_{\nu}^{*}(r) \tag{2.56}$$

With an equivalent equation for electrons of β spin. So the unrestricted density matrices will be defined as

$$P_{\mu\nu}^{\alpha} = \sum_{a}^{N\alpha} C_{\mu a}^{\alpha} (C_{\nu a}^{\alpha}) * \tag{2.57}$$

Again, with an analogous equation for electrons of β spin. The total density matrix and spin density are given respectively as

$$P^{T} = P^{\alpha} + P^{\beta} \tag{2.58}$$

$$P^{S} = P^{\alpha} - P^{\beta} \tag{2.59}$$

The elements of the Fock matrices are

$$F_{\mu\nu}^{\alpha} = H_{\mu\nu}^{core} + \sum_{\lambda} \sum_{\sigma} P_{\lambda\sigma}^{T} (\mu\nu \mid \sigma\lambda) - P_{\lambda\sigma}^{\alpha} (\mu\lambda \mid \sigma\nu) \tag{2.60}$$

$$F_{\mu\nu}^{\beta} = H_{\mu\nu}^{core} + \sum_{\lambda} \sum_{\sigma} P_{\lambda\sigma}^{T} (\mu\nu \mid \sigma\lambda) - P_{\lambda\sigma}^{\beta} (\mu\lambda \mid \sigma\nu) \tag{2.61}$$

The HF SCF equations can then be solved in a similar way to the restricted case but with the main difference being that two coupled matrix eigenvalue equations are solved simultaneously.

Hartree-Fock theory contains one hundred per cent of the exchange interaction but all other electron correlation is treated in an average way, as the Fock operator is a one-electron operator. While this theory was a large step forward towards accurately calculating molecular wavefunctions, accurate treatment of the correlated motion of

electrons is needed to describe chemically interesting properties of such molecules. One way to improve upon this situation is to reach the HF limit for the system under study, which is to say solve the Hartee-Fock SCF equations with an infinite basis set. From here the difference between the true energy of the system and the energy produced from the HF limit is simply the correlation energy – the contribution to the total energy of the system by electron correlation. With the idea of an infinite basis set in mind a discussion of basis sets will now be given.

2.3.4 Polyatomic basis sets

Basis sets as briefly mentioned in section 2.3.3 are the collective name for the group of basis functions that are used to construct each molecular orbital for the system under study and so construct the molecular wavefunction. In Hartree-Fock theory the wavefunction is a Slater determinant formed from the individual occupied molecular orbitals. These molecular orbitals are linear combinations of basis functions, each of which has a coefficient that is determined by the solution of the Hartree-Fock SCF equations. The Hartree-Fock limit previously mentioned is a very useful idea but requires an infinite basis set which is not practically computable for anything other than the smallest of chemical systems i.e. one or two light atoms. So 'finite' basis sets must be used that can be increased in size that can effectively approach the Hartree-Fock limit for the respective system. When using finite basis sets one must consider such factors as selecting basis functions that have a chemically relevant form, in that they have large amplitudes where the electron probability density is large and small amplitudes where it is small or zero. Other factors are to select basis functions that allow the various integrals that appear in Hartree-Fock theory to be calculated as effectively as possible and finally one must be aware that amongst these integrals are the two-electron integrals previously discussed which increase in number by N^4 where N is the number of basis functions so it would also be beneficial to keep the number of basis functions to a practical minimum. These factors when obeyed may dictate what is considered to be a good quality basis set.

Many types of basis function are mathematically possible but in modern electronic structure theory only two types are commonly used. One type is a Slater type orbital (STO) which has the general form in atom-centred Cartesian coordinates

$$\phi(x,y,z,a,i,j,k) = \left(\frac{\zeta^3}{\pi}\right)^{1/2} \left[\frac{(8\zeta)^{i+j+k} i!\,j!\,k!}{(2i)!(2j)!(2k)!}\right] x^i y^j z^k e^{-\zeta(x+y+z)} \qquad (2.62)$$

The other type is called a Gaussian type orbital (GTO) where the difference in form between the two is e^{-r} to e^{-r^2} respectively i.e. to go from an STO to a GTO you effectively change the atomic orbital like functions to the form of Gaussian functions. The equivalent form of a GTO is

$$\phi(x,y,z,a,i,j,k) = \left(\frac{2\alpha}{\pi}\right)^{3/4} \left[\frac{(8\alpha)^{i+j+k} i!\,j!\,k!}{(2i)!(2j)!(2k)!}\right]^{1/2} x^i y^j z^k e^{-\alpha(x^2+y^2+z^2)} \qquad (2.63)$$

Where ζ and α are the respective STO and GTO orbital exponents. These are positive numbers that are larger than zero, in essence they determine the 'diffuseness' or 'size' of the basis function, *i*, *j* and *k* are non-negative integers that determine the nature of the orbitals as defined here in a Cartesian coordinate sense. GTOs were introduced by S.F. Boys[39] to make up for quite a significant weakness in the implementation of STOs to larger systems. STOs actually have a number of attractive features such as they are able to closely describe the qualitative features of molecular orbitals. Therefore fewer STOs than GTOs would be needed in the basis function expansion of a molecular orbital. For example if one considers the radial behaviour of a atomic orbital: at r=0 where r is the distance between the nuclei and electrons, an STO will have a finite slope whereas a GTO will have zero slope. With increasing distance from the nuclei, real atomic orbitals decay in a manner that is exponential in *r* like an STO whereas GTOs decay in manner that is exponential squared meaning they decay much more rapidly than an STO or a real orbital, so the 'tail' of the wavefunction is not well described. So why not use STOs all the time? This brings the subject back to the reason for S.F. Boys introducing the use of GTOs because when calculating the molecular orbtials in an HF SCF calculation the number of two–electron four-index integrals already discussed in equation (2.44) is N^4 where N is the number of basis functions. Evaluation of these integrals with Slater type

basis functions is difficult and time-consuming as they cannot be solved analytically. However with Gaussian-type basis functions these integrals can be calculated analytically in a much faster and more efficient manner. The next logical step, then, might be to try and combine the proper radial shape of an STO with the computational efficiency of a GTO. This can be done by mimicking the shape of an STO using linear combinations of 'primitive' GTOs (PGTO), collectively this linear combination is known as a contracted GTO (CGTO) and is defined as

$$\varphi(x,y,z;\{a\},i,j,k) = \sum_{a=1}^{M} C_a \phi(x,y,z;\alpha_a,i,j,k) \tag{2.64}$$

Where M is the number of primitive Gaussians used and C_a are fixed contraction coefficients. By proper choice of the number of primitive Gaussians, contraction coefficients and contraction exponents α then the CGTO can assume any functional form one wishes within the limitation of the PGTOs used. If the PGTOs reside on different centres then the resulting CGTO could have the form of any basis function. So the strategy to implement this contraction is to firstly choose the values for M, C_a and α that would fit the right-hand side of equation (2.64) to the desired set of basis functions. Over the course of an HF SCF calculation the values of M, C_a and α do not change so the two-electron integrals can be computed very quickly as sums of very quickly calculated two-electron integrals over the PGTOs i.e. the CGTOs will resemble the radial shape of an STO but the four-indexed integrals can be computed analytically. So if one selects proper contraction parameters M, C_a and α then basis functions will be produced with integrals evaluated from PGTOs but can resemble any type of basis function.

The first procedure to fit a linear combination of M=1,2,3… PGTOs to an STO that found widespread use was the STO-MG procedure of Hehre, Stewart and Pople[40]. This nomenclature means 'Slater type orbitals approximated by M-Gaussians'. Obviously the higher the value of M the higher the accuracy of calculation but with increasing M comes increasing computational cost as each individual basis function is made up from increasing number of PGTOs so the number of two-electron four index integrals become increasingly complicated. The optimum value of M was

found to be 3 and the product is the well-known STO-3G basis set. The contraction coefficients can have positive or negative sign in order to mimic the radial nodal behaviour of a number of orbitals. In modern electronic structure theory the STO-3G basis set is known as a 'minimal' basis set. It is referred to as a 'minimal' basis set as only one contracted basis function is used as defined by the valence for every orbital core in the system under study. For example, hydrogen and helium have only one 1s function, lithium to neon second row elements will have one each of 1s,2s,$2p_x$,$2p_y$ and $2p_z$ orbitals etc. This is the minimum number of orbitals needed to describe each element. Of course this is nowhere near the HF limit defined earlier that used an infinite basis set so the next logical question is how to increase the size of the basis set while still keeping the basis set computationally efficient?

Logically one would answer this question by simply adding more basis functions. Here the common convention when increasing the number of basis functions is to use the zeta (ζ) name after the exponent of an STO where if one were to double the number of basis functions this would be called a double zeta (DZ) basis set. So hydrogen and helium would have two 1s functions and lithium to neon elements would have two sets of 1s and 2s functions and two sets of 2p functions etc. Multiple zeta basis sets immediately increase the quality of the description of the electronic distribution of different systems that can be studied as electron distribution can vary in different directions like in systems with π bonds. Simply doubling the number of basis functions indiscriminately can increase the computational cost with little improvement to the description of the system because the core orbitals rarely change but valence orbitals can change markedly due to their contribution to different types of chemical bonding. To account for this special types of basis sets are known as 'split-valence' and for a split–valence double zeta basis set this would denoted as 'VDZ'. Possibly the most well-known family of split valence basis sets are those of Pople and co-workers which have a naming structure that acts as a guide to the contraction scheme, i.e. 3-21G, 6-21G, 4-31G, 6-31G and so on. The first number in the nomenclature signifies the number of PGTOs that are used for the contracted core functions. The numbers after the hyphen refer to the PGTOs used for the valence functions. Here, two numbers after the hyphen signify a double zeta basis set, three numbers means a triple zeta basis set. For example, for a carbon atom with a 3-21G basis set would have the primitive functions

6s3p which contracts to 3s2p. The same carbon atom with a bigger 6-31G basis set would have the primitive functions 10s4p which contracts to 3s2p. This is known as the degree of contraction. Another well-known series of basis sets are the basis sets of Dunning of co-workers that include cc-pVDZ, cc-pVTZ and cc-pVQZ where the 'cc' stands for 'correlation consistent' that means that the basis is designed to account for correlation energy in the valence electrons. The 'p' stands for 'polarization functions', which are features of this series of basis sets that will be discussed later. Once one moves away from the minimal basis set the way the exponents and coefficients are chosen for the contracted functions must be considered. Fitting to STOs is no longer of any great advantage with larger basis sets as they are considered to be the optimal approximation to an atomic orbital with a single function. A popular way to start is to use the variational principle to provide the optimum coefficients. With the example of carbon still in mind if a number of basis functions are used in the basis set for carbon and the exponent for each function is calculated using the variational principle it is often the case that most of the functions will describe the core orbitals which as previously discussed will change very little due to their proximity to the nucleus. The real chemistry happens in the outer valence that will change depending on the chemical environment. This means that most of the computational cost has gone into describing orbitals that behave in an almost constant manner. To improve this the coefficients that describe the core orbitals are fixed, reducing the number of coefficients that need to be evaluated using the variational principle. This means the core orbitals will be described by a fixed linear combination of basis functions. This decreases the computational cost but also decreases the number of variational parameters and so increases the energy.

Two main strategies for contraction have been used; the first one discussed here is the system used by Pople and co-workers called segmented contraction. This means that the PGTOs used on one basis function are not used on another of the same angular momentum. PGTOs are divided into sets where their coefficients determine how they should be converted to CGTOs. This type of contraction is an older type of contraction used in the Pople basis sets mentioned above. The other type of contraction strategy is called general contraction in which there is only one set of PGTOs on any given atom, which enter all CGTOs, but with different coefficients. Such basis sets are the ones developed by Dunning also mentioned above.

A practical consideration when constructing basis sets for chemical systems is making sure that the chemical system has the correct bonding character and a structure that is chemically sensible. Using large basis sets with s functions for hydrogen and s and p functions for second row (heavy) elements can often lead to incorrect structures and bonding in molecules such as ammonia or some phosphates. This is because there is not enough mathematical flexibility to describe the wavefunction for their 'real' geometries, i.e. the molecular orbitals need to be accurately described using a more flexible basis set than those that are perfectly fine for isolated atoms. This extra flexibility is gained by adding another set of basis functions to each atom one angular momentum quantum number higher than the current highest basis function. These are called polarization functions. So for hydrogen in a molecular structure a set of p functions would be added and for heavier elements a set of d functions. For example the bonding molecular orbitals between oxygen and hydrogen is better described by adding a little bit of the appropriate d orbital on oxygen. With increasing size of basis set i.e. from double zeta to triple zeta then the number of polarization functions can also increase. For the Dunning basis sets a double zeta basis set will have one set of p functions for hydrogen and one set of d functions for second row elements. A triple zeta basis set will have two sets of p functions on hydrogen and one set of d functions and second row elements will have one set of f functions and two sets of d functions. For the Dunning basis sets polarization functions are noted by the presence of a lower-case 'p' in the basis set name mentioned above. Polarization functions are noted by stars (*) for the Pople basis sets. A 6-31G* basis set will polarization functions on heavier elements and a 6-31G** basis set will have polarization functions on both heavier atoms and hydrogen. Pople basis sets can also show the presence of polarization functions explicitly such as 6-31G(d) that is equivalent to 6-31G*.

Another feature of basis sets that are designed to increase their accuracy are the diffuse functions. Many systems require a basis set to account for a loosely bound electron far from the nucleus and the bulk of the electron density. This is especially true for anions and when calculating properties such as electron affinities and Rydberg states in electronic spectroscopy. So basis functions that are spatially diffuse can be added, basis sets can also be said to be 'augmented'. The Pople basis sets indicate the presence of diffuse functions by the use of a plus (+) sign in the basis set name. For example the 6-31++G* basis set will have one set of diffuse s and p functions on second row

elements and diffuse s functions on hydrogen. The Dunning basis sets add ‘aug’ to the beginning of the basis set name to show that the basis set has been augmented with diffuse functions, with diffuse functions on all atoms e.g. aug-cc-pVDZ.

Another type of basis set that will be used a lot in the following chapters of this thesis is the so-called atomic natural orbital basis set (ANO). ANO basis sets use natural orbitals to contract the PGTOs to CGTOs. Natural orbitals diagonalise the density matrix of the system and determine the occupation number of each orbital, as these are the eigenvalues of the diagonalised density matrix. The natural orbitals are produced from an initial correlated calculation of the free atoms. When a correlated wavefunction is used (methods for including electron correlation in the wavefunction are discussed in section 2.3.5) then the occupation numbers can have any value between zero, not occupied, or two, fully doubly occupied. If an HF wavefunction was used on a closed shell system then the occupation number would have a value of only zero or two. From the magnitude of the occupation numbers the best possible combination of PGTOs are selected for contraction. With a lower threshold value of occupation number then gradually smaller sets of CGTOs can be produced in a series as the same set of PGTOs are used for each.

So far only hydrogen, helium and the heavier atoms of the second row of the periodic table up to neon have been discussed in terms of possible basis sets. However in this thesis all species that have been studied are transition metal carbonyls of various sizes and different metallic centres. Metals have large number of core electrons, which means a large number of basis functions are needed to describe them, and there will also be increased contribution to the total energy from electron correlation. Even though these electrons are mostly core electrons the computational cost with a standard basis set such as the ones of Pople and Dunning will be very high. So ‘effective core potentials’ or ‘pseudopotentials’ as they are also called are used, which are mathematical functions that can efficiently describe the core electrons and nucleus of each metallic centre with reasonable accuracy. Basis sets of such types used for the work in this thesis are the Los Alamos double zeta basis set (LANL2DZ)[41] and the Stuttgart-Dresden basis set (SDD)[42]. Peterson and co-workers have also developed a series of all-electron basis sets for the first row transition metals that do not have effective core potentials[43] and these are also used in this thesis.

2.3.5 Correlated methods, configuration interaction, multiconfigurational methods, perturbation theory and coupled cluster

A brief account of methods that look to improve upon the Hartree-Fock method will now be given. While the Hartree-Fock method has been very successful, as already mentioned, it has one large drawback in that each electron interacts with all others in an average way and not instantaneously. The difference between the total energy of the system and the energy of the system within the Hartree-Fock limit is the electron correlation energy, E_{corr}

$$E_{corr} = E_{HF} - E_0 \tag{2.65}$$

This instantaneous correlation is called dynamic correlation. This correlation energy commonly represents around one per cent of the total energy however it is perhaps the most important energy contribution needed for describing chemically interesting properties of molecules e.g. barrier heights. So the Hartree-Fock method can be improved upon using different methods to estimate E_{corr}.

The first method to be discussed is conceptually the simplest, the full configuration interaction (CI). A full CI calculation with an infinite basis set will give full solution to the non-relativistic time-dependent Schrödinger equation. A full CI wavefunction is made up firstly of a linear combination of determinants that relate to different 'configuration state functions' or CSFs as so

$$\Psi_{CI} = c_0\Psi_{HF} + \sum_{i}^{occ}\sum_{r}^{vir} c_i^r\Psi_i^r + \sum_{i<j}^{occ}\sum_{r<s}^{vir} c_{ij}^{rs}\Psi_{ij}^{rs} + \sum_{i<j<k}^{occ}\sum_{r<s<t}^{vir} c_{ijk}^{rst}\Psi_{ijk}^{rst} + ... \tag{2.66}$$

Where Ψ_{HF} is the 'reference' wavefunction and in the later terms *i*,*j* and *k* are occupied molecular orbitals in that reference wavefunction and *r*,*s* and *t* are virtual orbitals in that same reference wavefunction. The remaining terms represent the excitation of electrons from occupied orbitals to virtual ones. So the second term represents all possible single electron excitations, the third term all double electron excitations and so on. A CSF is a linear combination of determinants that are spin-adapted. For a singlet closed shell case

then only one determinant will be required for the CSF. Each term in the expansion is one CSF and each has associated with it an expansion coefficient, *c*. The energies of equation (2.66) can be determined by forming a matrix representation for the basis of the *N*-electron functions of the equation and calculating from this the eigenvalues of the equation using the linear variational method. This matrix is referred to as the full CI matrix, which has the general form

(2.67)

$$\begin{bmatrix} \langle \Psi_{HF} | H | \Psi_{HF} \rangle & 0 & \langle \Psi_i^r | H | \Psi_{ij}^{rs} \rangle & 0 & \\ \vdots & \langle \Psi_i^r | H | \Psi_i^r \rangle & \langle \Psi_i^r | H | \Psi_{ij}^{rs} \rangle & \langle \Psi_i^r | H | \Psi_{ijk}^{rst} \rangle & \cdots \\ \vdots & \vdots & \langle \Psi_{ij}^{rs} | H | \Psi_{ij}^{rs} \rangle & \langle \Psi_{ij}^{rs} | H | \Psi_{ijk}^{rst} \rangle & \cdots \\ \vdots & \vdots & \vdots & \langle \Psi_{ijk}^{rst} | H | \Psi_{ijk}^{rst} \rangle & \cdots \\ & & & & \cdots \\ & & & & \langle \Psi_{ijkl}^{rstv} | H | \Psi_{ijkl}^{rstv} \rangle \end{bmatrix}$$

Some general features can be taken from the structure of this matrix: for example due to Brillouin's theorem[44] there will be no coupling between the ground state and single excitations. Also matrix elements of the Hamiltonian will be zero if they differ by more than two orbitals so there will be no coupling between the ground state and triple excitations upwards. Because of this the full CI matrix is rather sparse. In order to calculate the wavefunction of the whole system and its eigenvalues the full *N*-electron Hamiltonian must be diagonalized or equivalently find the *N* roots of the CI secular equation that is analogous to the HF secular equation. The form of this is

$$\begin{vmatrix} H_{00} - E & H_{SS} & \cdots & H_{0N} \\ H_{S0} & H_{SS} - E & \cdots & H_{SN} \\ \vdots & \vdots & \ddots & \vdots \\ H_{M0} & H_{MS} & \cdots & H_{MN} - E \end{vmatrix} = 0 \qquad (2.68)$$

Where 0 is the ground state HF wavefunction, *S* are all singlet excitations and so on. Each *H* in this matrix corresponds to a matrix element similar to equation (2.67), from this the values of the CI coefficients can be deduced for all CSFs that are in the expansion of equation (2.66), which for a full CI could be all possible terms within the

limit of the basis set. A CI will commonly use the MOs from the precuring HF SCF calculation so they are held fixed. A full CI calculation will deliver the exact value for E_{corr} within the given basis set which is called the basis set correlation energy. If a complete infinite basis set is used then E_{corr} will be calculated exactly and thus, previously mentioned, the exact solution the non-relativistic time-dependent Schrödinger equation. A full CI calculation may be quite simple theoretically and will give an exact result to the Schrödinger equation but in practise a full CI calculation is too computationally expensive for anything but the smallest of molecules. One can of course truncate the expansion in equation (2.66) to include only one or two types of excitations, so for example truncating the expansion to only include single excitations will result in CI singles (CIS), only including doubles will produce a CI doubles (CID) calculation. In the full CI matrix there is no coupling between the ground state and singlet excitations so in a CIS calculation the ground state is unaffected by the introduction of single excitations, so a CIS calculation would only be useful in the calculation of excited states because the CSF corresponding to single excitations represents an upper bound to the first excited state of the system just as the first term will be an upper bound to the ground state energy. This general feature of CI methods is called 'variational' as the variational method is used. Double excitations do affect the ground state of the system so it is advantageous to include them. However with inclusion of all double excitations can make the size of the CI matrix very large indeed with large systems but for smaller systems with a smaller basis set the matrix is small enough to be diagonalized with little computational expense. Including triples can affect the ground state albeit indirectly as they do not directly couple to the ground state but do couple to double excitations which in turn couple to the ground state but there are a huge amount of triple excitations for larger systems meaning inclusion of any excitations bigger than doubles makes the size of the matrix very big and time-consuming to diagonalize even when using sophisticated methods to perform this task. There are, however, comparatively few single excitations that can affect the ground state in a similar way that triple excitations can, through coupling to double excitations, so heralding the CI singles and doubles (CISD) method. Which terms can couple to others obeys the Slater-Condon rules. The 'variational' feature that CISD possesses means that the energy produced by this method will be an upper bound to the exact energy within the limits of the basis set. One feature that truncated CI methods do not possess is that they are not 'size consistent'. This feature ensures that the ability of the

method to describe the energy of the system is always consistent even when interaction between parts of the system is removed, for example by physical separation to great distances. Therefore the total energy of the system should be equal to the sum of the energies of the constituent parts at infinite separation. Size consistency is a desirable feature of electronic structure methods and can be added into the CISD method in various ways, which will not be discussed here.

One other type of CI calculation that should be mentioned at this stage is so-called multireference CI (MRCI). This is analogous to the CI method already discussed but instead of using an HF reference wavefunction an MCSCF (discussed below) reference wavefunction is used instead. There is a very big improvement in the structure of the optimized orbitals, meaning the CI can converge must faster. A price must be paid for this advantage though in that an MCSCF reference wavefunction is harder to construct than an HF one and the size of the CI matrix and number of elements involved in the calculation can become enormous so again this method is only suitable for small systems. Truncated variants of MRCI also lack size consistency.

Hartree-Fock theory already discussed accounts for electron correlation effects in an average way, so HF can also be called a mean field theory. In HF theory each electron experiences an electric field created by all other electrons and each electron is placed in an MO that is optimised using an SCF cycle obeying the variational principle. This forms a single determinantal wavefunction, which the Hamiltonian will act upon to give the energy of the many-
electron system. However what about cases when the system cannot be described accurately by only one determinant and others have to be considered equally? Methods that account for this are the next to be discussed.

In a very general way an improvement can be made over the HF wavefunction by writing the total wavefunction as a linear combination of more than one Slater determinant each of which has an associated weight.

$$\Psi = c_1\Psi_{HF} + c_2\Psi_2 + c_3\Psi_3 + ... \qquad (2.69)$$

Perhaps the simplest example where this kind of treatment is advantageous is that of the hydrogen molecule where HF theory will place both electrons in the bonding MO. However by including an extra configuration, $c_2\Psi_2$ where both electrons are in the antibonding orbital and the total wavefunction is a linear combination of the two and the coefficients c of each determinant are determined variationally, an improvement over the HF energy can be gained. Obviously if all configurations are included this will be the full CI method discussed earlier and the value of one coefficient will be bigger than the other but crucially both will have a non-zero value showing each configuration contributes meaningfully to the total wavefunction. The situation can become more complex if the frontier molecular orbitals occupy two or more degenerate orbitals such as π orbitals in organic systems or metal d orbitals in symmetric transition metal complexes and there is at least one-electron hole. For a molecule with a triplet ground state over doubly degenerate frontier molecular orbitals, HF theory would put two electrons in one of the degenerate orbitals and the MOs will be optimised for that configuration. However an equally good representation would be from doubly occupying the other degenerate frontier MO and then optimising all MOs for that configuration. Putting both configurations in the total wavefunction and variationally optimising the coefficients of each they should have the same value.

This idea splits electron correlation effects into two types. The type describing the instantaneous correlation of electrons with each other that is known as ‘dynamic’ correlation and the type which arises from the need to treat two or more configurations equally in the total wavefunction is called ‘non-dynamic’ or ‘static’ correlation. It is a lack of static correlation that also shows that HF theory is not a flexible enough method to describe excited state problems and Jahn-Teller degeneracies. It is worth mentioning that ROHF theory discussed earlier can account for multiple determinants but cannot account for multiple configurations of CSFs (configuration state functions) that relate to both the spin state and occupation number of the MOs.

The first method to be discussed that can account for multiple configurations is the ‘multi-configuration’ SCF (MCSCF) method that can basically be thought of as an SCF calculation that can handle more that one determinant. The MCSCF wavefunction has the form of equation (2.69) in that it is constructed of multiple configurations each

with its own coefficient or weight, which are constructed at the guess stage of the calculation. This is so that the MOs can be optimised for multiple configurations in the SCF cycle. It also finds the optimum value of the coefficient of each CSF in the expansion variationally. So the MCSCF wavefunction can account for multiple configurations but also for any multi-determinantal character of any configurations. Orbitals in an MCSCF wavefunction are described by their occupation number rather than their eigenvalues and can have any value between zero (not occupied) and two (fully doubly occupied). The occupation number can be expressed as

$$(occupation\,number)_{i,MCSCF} = \sum_{n}^{CSF} (occupation\,number)_{i,n} a_n^2 \qquad (2.70)$$

CSFs are orthogonal so the sum of the squares of all CSF coefficients will be one and the sum above runs over all CSFs. A percentage contribution of a particular CSF to the total wavefunction multiplies the occupation number of the orbital of that CSF. One large limiting factor with MCSCF theory is that the user determines the configurations that are included in the total wavefunction so a great deal of chemical knowledge is required when using this method. As a result MCSCF, wavefunctions though maybe a good starting point for multi-configurational problems, can be inflexible and not provide a good enough description of the system if not enough or correct configurations are included. In conjugated organic systems all the π orbitals or all d orbitals for transition metal complexes should be included if they are close in energy as they could produce configurations which contribute meaningfully to the static correlation effects. So one can include more electrons and orbitals into an 'active space' of *m* electrons in *n* orbitals and then decide which configurations within are important. This though can be improved further by simply computing all CSFs within the active space (i.e. carrying out a full CI calculation within the active space), this forms another method which is called the complete active space SCF (CASSCF) method. The total number of CSFs in the active space increases exponentially according to the formula

$$N = \frac{n!(n+1)!}{\left(\frac{m}{2}\right)!\left(\frac{m}{2}+1\right)!\left(n-\frac{m}{2}!-\right)!\left(n-\frac{m}{2}+1\right)!} \qquad (2.71)$$

So the number of CSFs to be computed will be too expensive for any system that requires a large active space. Outside the active space all orbitals are split into occupied orbitals which have an occupation number of two and virtual orbitals which have an occupation number of zero. Similar to the MCSCF method a great deal of care and chemical knowledge is required when selecting orbitals and the number of electrons for the active space. Guess orbitals can first be generated at any level of theory and then inspected for inclusion into the active space. Once suitable orbitals have been chosen and included in the active space the wavefunction can then be optimised and the resulting orbitals and occupation numbers can then be inspected again to make sure they are correct. Generally if an orbital in the optimised active space has an occupation number greater than 1.998 or lower than 0.020 then it can be taken out of the active space as it may not contribute to the static electron correlation in any meaningful way. The orbital shapes can also be inspected to make sure they are resemble what is expected.

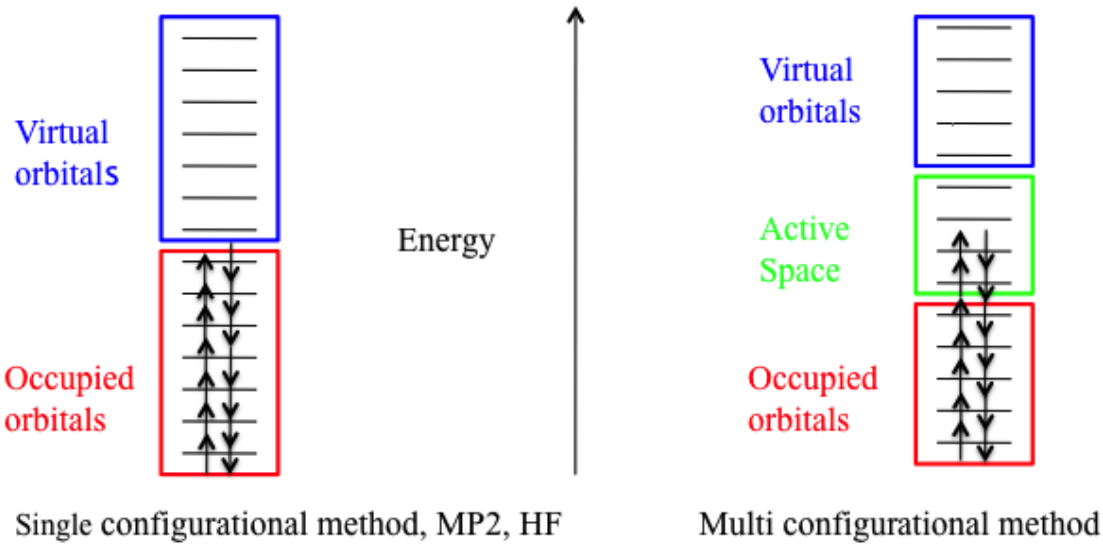

Figure 2.5 Illustration of molecular orbitals and their classifications for single configurational methods and multi configurational methods

With a converged CASSCF wavefunction in hand the molecular geometry can then be optimised over one or multiple electronic states for a range of points on coupled or uncoupled potential energy surfaces of different character. For example a point of conical intersection can be computed by state averaging over two or more PESs, which the conical intersection connects. The gradient difference and derivative coupling vectors can then be generated and analytical gradients used to search the whole of the

3N-8 dimensional intersection space seam for the lowest energy point. Ground and excited state minima and saddle points can also be computed which shows that CASSCF is a very flexible method in theoretical chemistry if used with care and can be applied to a wide range of problems, allowing for system size and basis set specification. One feature that CASSCF lacks is dynamic electron correlation. Though once an optimised wavefunction or geometry has been produced other methods in theoretical chemistry can be utilized to correct for this. Perhaps the most well known method is CASSCF with a second order perturbation correction to the total energy to account for dynamic correlation effects, the CASPT2 method[45], although other methods have also been developed which will not be discussed further here.

The second method that looks to include electron correlation is perturbation theory. Although this method is not used directly for any of the calculations presented in this thesis a brief discussion of the basic concepts of this method will be of benefit when discussing the more advanced methods discussed later in this chapter. A big advantage that perturbation theory has over truncated CI methods is that it is size consistent at each level of termination but is not variational. As the name suggests perturbation theory essentially splits the Hamiltonian of the total system under study into a zeroeth-order part, H_0, and a perturbation, ϑ. The Schrödinger equation for the total system could then be written as

$$\widehat{H}\Psi_i = (\widehat{H}_0 + \vartheta)\Psi_i = \varepsilon_i \Psi_i \tag{2.72}$$

H_0 has exact eigenfunctions and eigenvalues. Commonly and in MØller-Plesset perturbation theory[46] H_0 is the HF Hamiltonian i.e. a non-interacting sum of one-electron Fock operators

$$\widehat{H}_0 = \sum_{i=1}^{n} f_i \tag{2.73}$$

The exact energy is then expressed as an infinite sum of contributions, the expressions of which contain both eigenvalues of H_0 and matrix elements of the perturbation between eigenfunctions of H_0. The so-called '*n*th-order' perturbation theory will contain

products of n such matrix elements between eigenfunctions of H_0 and are grouped together.

In a practical sense in the methods of electronic structure theory used today the most common perturbation theory are the MØller-Plesset (MPn, n=1,2,3…) series of perturbation theories. These methods use as H_0 the HF Hamiltonian and $\Psi_i^{(0)}$ is the HF wavefunction so it is a Slater determinant from the occupied MOs of the system. The zeroeth-order energy is simply the sum of occupied orbital energies which themselves are eigenvalues of specific one-electron Fock operators. One facet to this is that the perturbation term of MPn theory includes the Coulomb and exchange operators already seen in section 2.3.3 as they are not included in the HF wavefunction so electron-electron repulsion is double counted without this perturbation. MP2, the second-order correction to the zeroeth-order eigenvalue is the common starting point in the use of the MPn methods as MP1 is simply the HF energy itself. The sum of the zeroeth-, first- and second-order energies defines the MP2 energy. MP2 has proved successful in the past for exploring PESs. Higher order versions of MP theory such as MP3 and MP4 have problems such as a lack of analytical gradients and MP4 being much more expensive than MP2 while offering little improvement in the energy over MP2. What is important to this thesis is that MPn methods account for dynamic electron correlation effects and can be used in conjunction with multireference methods that account for static electron correlation effects to offer the best possible description of E_{corr}. These multireference methods such as CASSCF are used in this thesis to investigate coupled potential energy surfaces that does not include dynamic electron correlation. A method that combines CASSCF and MP2 is CASPT2. CASPT2 methods have been successfully applied to molecular systems for the investigation of structure and spectroscopy, with most papers in this area by Roos and co-workers which are reviewed in[47].

The last group of methods that estimate E_{corr} that will be discussed here are the coupled cluster (CC) series of methods. The full CI wavefunction within a given basis set would be

$$\Psi = e^{T}\Psi_{HF} \tag{2.74}$$

Where the '*T*' is known as the coupled cluster operator and is defined as

$$\hat{T} = T_1 + T_2 + T_3 + ... + T_N \tag{2.75}$$

Here '*N*' is the total number of electrons in the system. Each individual term in the coupled cluster operator expansion will produce every possible determinant with *i* excitations from the reference wavefunction e.g.

$$T_3 = \sum_{i<j<k}^{occ} \sum_{a<b<c}^{vir} t_{ijk}^{abc} \Psi_{ijk}^{abc} \tag{2.76}$$

In this way it is similar to the terms in a CI expansion, the 't' terms are called the coupled cluster amplitudes that are calculated with the condition that equation (2.74) holds true. Similar to CI the application of *T* to the reference wavefunction is equivalent to a full CI calculation. This means this calculation is far too expensive for any chemically interesting system so *T* is truncated in a similar way to truncated CI methods. So rather simply in CCS theory *T* is truncated to T_1 only so only single excitations are included. In CCD theory *T* is truncated to T_2 to include only double excitations. At the CCD level, for example, the CCD wavefunction can be expressed with a Taylor expansion

$$\Psi_{CCD} = \left(1 + T_2 + \frac{T_2^2}{2!} + \frac{T_2^3}{3!} + ... \frac{T_2^N}{N!}\right) \Psi_{HF} \tag{2.77}$$

If only $1+T_2$ were included in the above expansion this would be the CID method discussed earlier. However CCD has an advantage here over the CID method in that as well as the contribution of 'connected' double excitations the extra terms in the Taylor expansion relate to higher order excitations that are 'unconnected' i.e. the square of T_2 gives quadruple excitations, the cube of T_2 gives hex tuple excitations and so on. This also ensures that truncated CC methods are size consistent but not variational just like the MP*n* methods. These 'unconnected' excitation terms all contribute to the total coupled cluster energy and increase its accuracy. Amongst the most well-known truncated coupled cluster theories are so-called CCSD [48] with 'connected' single and

double excitations and CCSDT[49] which includes full 'connected' single, double and triple excitations. CCSD has proved to be very popular in modern electronic structure theory due to its relative accuracy with reasonable computational expense. CCSDT is desirable as it improves upon the CCSD energy in a size-consistent manner but for many chemically interesting systems it is too expensive. With this in mind the CCSD(T) model was developed to estimate the effect of connected triples with little increase in computational expense over CCSD by inclusion of a coupling term between single and triple excitations, as such CCSD(T) is now regarded to be the flagship CC model and has been widely used in many areas of computational chemistry.

The real computational challenge with CC theory that accounts for the increased cost over the Hartree-Fock method is evaluating the CC amplitudes, *t*, the number of which will vary depending on the level of truncation of *T*. Very generally they can be determined by multiplying the Schrödinger equation on the left by trial wavefunctions, which are expressed as determinants of the HF orbitals. From this a set of coupled non-linear equations is produced and an iterative process is then used to solve these equations and determine the amplitudes. With the values of the coupled cluster amplitudes calculated the coupled cluster energy can then be determined.

2.3.6 Density functional theory

The next group of methods to be discussed here move away from the HF and post-HF methods discussed in sections 2.3.4 and 2.3.5 that utilise a wavefunction, density functional theory (DFT) methods. These methods are perhaps the most widely used methods in modern computational chemistry due to their low computational cost but relative accuracy when compared to coupled cluster or MP*n* methods whilst returning energies that are equivalent to these methods or sometimes better and their inclusion in the most common electronic structure codes. The key difference between density functional methods and the methods in sections 2.3.4 and 2.3.5 is that the wavefunction is replaced with the electronic density. This is a physical observable (it can be measured by X-ray diffraction) which like the Hamiltonian depends on the total number of electrons and positions and atomic numbers of the nuclei. If one knows the electronic density of a system then a Hamiltonian can be constructed and the energy of a system can be calculated using an analogous Schrödinger equation. The electronic density is the

square of the wavefunction (as a probability density) and when integrated over all space will give the total number of electrons in the system.

$$\int \rho(r)\,dr = N \tag{2.78}$$

Nuclei will correspond to 'cusps' that are local maxima in the electronic density due to the attractive force between electrons and the nuclei. There is a singularity in the gradient of the density at these points and a cusp is the result. The nuclear charge is also related to the cusps in the density

$$\lim_{r_A \longrightarrow 0}\left[\frac{\partial}{\partial r} + 2Z_A\right]\bar{\rho}(r) = 0 \tag{2.79}$$

Here Z is the atomic number of nucleus A, $\bar{\rho}$ is the spherically averaged density and r_A is the radial distance from A. So with all this information theoretically present a Hamiltonian can be constructed. Early versions of DFT were implemented in the field of solid-state physics due to their simplicity such as the quantum statistical method developed by Thomas and Fermi[50, 51]. Early methods such as this approximated the system to be classical for simplicity because the electron density was the only variable when computing the energy of the system. One may then separate the energy into potential energy (nuclear-electron (attractive) and electron-electron (repulsive)) and kinetic energy parts similar to the structure of a Hamiltonian. Therefore the potential and kinetic energies are functions of the density. The naming of DFT can therefore be explained here as the potential and kinetic energy parts of the system are functions of the density but the density itself is a function of the three-dimensional spatial coordinates of electrons and nuclei. So the density is a functional as it is a function whose argument is also a function, so the potential and kinetic energy parts of the system are 'density functionals'. The potential energy parts of the system can be simply expressed as

$$V_{nuc-elec}\left[\rho(r)\right] = \sum_{k}^{nuclei} \frac{Z_k}{\left|r - r_k\right|}\rho(r)dr \tag{2.80}$$

$$V_{elec-elec}[\rho(r)] = \frac{1}{2}\int\int \frac{\rho(r_1)\rho(r_2)}{|r_1 - r_2|} dr_1\, dr_2 \qquad (2.81)$$

Where r_1 and r_2 are integration variables that run over all space, however the kinetic energy is harder to understand. To get round this problem a model system is introduced thought of having a 'sea' of electrons of non-zero density moving in infinite space with an overall positive charge that is distributed evenly over the 'sea'. This model is known as a uniform electron gas or 'jellium'. Thomas and Fermi derived the kinetic energy of this uniform electron gas to be

$$T_{jellium}[\rho(r)] = \frac{3}{10}(3\pi^2)^{2/3}\int \rho^{5/3}(r)\, dr \qquad (2.82)$$

The energy of an atom can now be expressed by combining the three previous equations

$$E_{TF}[\rho(r)] = \frac{3}{10}(3\pi^2)^{2/3}\int \rho^{5/3}(r)\, dr - \sum_{k}^{nuclei}\int \frac{Z_k}{|r - r_k|} + \frac{1}{2}\int\int \frac{\rho(r_1)\rho(r_2)}{|r_1 - r_2|} dr_1 dr_2 \quad (2.83)$$

This early method is rather crude as crucially it does not take into account electron correlation or quantum mechanical exchange. However with an assumed variational principle it provides a method to get the energy of a system without having to refer to a wavefunction. Hole functions can be added to this model to account for electron correlation but these methods rarely find use in modern computational chemistry.

More improved DFT methods will now be outlined that facilitated the success of DFT. A major step forward came in 1964 when Hohenberg and Kohn[52] proved their existence and variational theorems that moved DFT closer to the form it is seen in today. The existence theorem effectively proves that the ground-state density is sufficient to determine the Hamiltonian and so the energy depends on the density. The second theorem was to prove that the variational theorem exists for DFT just as with molecular orbital theory. This is because a Hamiltonian and wavefunction can be determined from the density. Elegant as this theorem is, it seems to be a bit of a pointless exercise as HF and post-HF methods already utilise a wavefunction, Hamiltonian and the variational principle without needing to consult the density. There

is also no clear way to improve upon the density within this variational theorem. To improve matters what is needed is a method to determine the variational energy without the need of a wavefunction, which is what Kohn and Sham in 1965[53] developed.

They decided to approximate the real system under study with a hypothetical system with non-interacting electrons but their ground state densities are identical. The Hamiltonian operator is therefore also for a system with non-interacting electrons so it has a form similar to that in equation (2.73) i.e. a sum of one-electron operators. The eigenfunctions it will operate on will be Slater determinants of each one-electron operator and the resulting eigenvalues will be the sum of one-electron eigenvalues as in

$$\widehat{H}_{GS}\Psi_{GS} = \sum_{i}^{occ}\varepsilon_i\Psi_{GS} \tag{2.84}$$

The energy functional can then be expressed in terms of spin orbitals and separated into its constituent parts

$$E[\rho(r)] = \sum_{i}^{N}\left(\langle\chi_i|-\frac{1}{2}\nabla_i^2|\chi_i\rangle - \langle\chi_i|\sum_{k}^{nuclei}\frac{Z_k}{|r_i-r_k|}|\chi_i\rangle\right) + \sum_{i}^{N}\langle\chi_i|\frac{1}{2}\int\frac{\rho(r')}{|r_i-r'|}dr'|\chi_i\rangle + E_{xc}[\rho(r)] \tag{2.85}$$

In which the first term corresponds to the kinetic energy of the non-interacting system, the second is the attractive potential between nuclei and electrons and the third term the repulsive classical interaction between electrons. The last term incorporates quantum mechanical exchange, electron correlation, the difference in the kinetic energy between the non-interacting system suggested by Kohn and Sham and the real one and the correction for the classical self-interaction term. This self-interaction and exchange are both accounted for in HF theory. Having obtained a way of using the density to describe the system and a suitable Hamiltonian, a method to choose spin orbitals χ that will result in the minimum energy like in HF theory is needed. Therefore an SCF process similar to HF theory can be implemented. There are indeed a number of similarities between a Kohn-Sham SCF and HF SCF such as the orbitals obey a pseudoeigenvalue equation

$$\hat{h}_i^{KS}\chi_i = \varepsilon_i\chi_i \tag{2.86}$$

And these orbitals are expanded into a basis set and a secular equation is used to compute the individual orbital coefficients that is analogous to HF theory. The main difference is that the Fock matrix elements are replaced by matrix elements $K_{\mu\nu}$

$$K_{\mu\nu} = \left\langle \phi_\mu \left| -\frac{1}{2}\nabla^2 - \sum_k^{nuclei} \frac{Z_k}{r_{ik}} + \int \frac{\rho(r')}{|r-r'|} dr' + V_{xc} \right| \phi_\nu \right\rangle \tag{2.87}$$

But even here there are many similarities such as the first two terms of the one-electron Fock operator in equation (2.38) relating to the kinetic energy and nuclear attraction are identical to the first two terms operator used in equation (2.87). The two-electron four index integrals will also be the same between HF and Kohn-Sham DFT and the interelectronic repulsion operator is expressed in the same basis used for the orbitals in Kohn-Sham DFT. Furthermore the orbitals will describe the exact density because the energy in equation (2.85) is exact and the separable noninteracting Hamiltonian will operate on a Slater-determinantal eigenfunction that is formed from these orbitals.

$$\sum_{i=1}^{N} \hat{h}_i^{KS} \left| \chi_1\chi_2\chi_3\cdots\chi_N \right\rangle = \sum_{i=1}^{N} \varepsilon_i \left| \chi_1\chi_2\chi_3\cdots\chi_N \right\rangle \tag{2.88}$$

This type of DFT is variational and exact as long as the exchange correlation term in equation (2.85) is accounted for exactly and size-consistent regardless of how E_{xc} is treated. It is also interesting that while HF theory in inherently approximate within an infinite basis set, DFT is the opposite and within the same infinite basis set it is exact. The main problem with DFT occurs in that the form of E_{xc} as a function of the density is not intuitive. Thus most modern methods account for this in different ways, such as the local density approximation (LDA) or generalized gradient approximation (GGA) but these methods are not used in this thesis so are not discussed further.

The last feature of DFT methods to be discussed is the inclusion of varying amounts of HF exchange in the exchange correlation energy. One may see this as an

improvement in principle as HF theory accounts for the exchange in a system exactly. One would think this a logical step to take to move forward with the accuracy of DFT methods as exchange effects are much bigger than correlation effects. A general equation to illustrate this would be

$$E_{xc} = (1-a)E_{xc}^{DFT} + aE_{x}^{HF} \tag{2.89}$$

Where E_x^{HF} is the HF exchange term and a is some variable (also called a 'parameter') that can be altered in order to 'tune' the accuracy of the method. This type of procedure is called the 'adiabatic connection method' because it looks to control amount of electron-electron interactions in the system. In other words it tries to connect the Kohn-Sham noninteracting system with the real one. These density functionals that incorporate a portion of HF exchange are called 'hybrid' functionals and can have more than one parameter meaning their exchange correlation energies are made up of contributions of exchange and correlation from different areas of density functional theory like LDA and GGA methods and HF exchange in varying ratios. These contributions are governed by the values and number of parameters. Hybrid functionals are perhaps the most widely used variants of DFT with a particular example being the B3LYP 3-parameter hybrid functional which is perhaps the most well known. Many different hybrid functionals have been developed for different purposes such as the study of excited states (time-dependent DFT or TD-DFT and CAM-B3LYP for the study of charge transfer states) or DFT with inclusion of dispersion effects (DFT-D) and this is an on-going field of research.

One last point to note is that with the exception of B3LYP and CAM-B3LYP no specific DFT methods have been discussed, only the general features of various methods. This is because unlike the post-HF methods above there is no systematic naming system for DFT methods just as there is no real systematic way of improving them. Many DFT functionals are named with the initials of the people who developed them and numbers that mean the year they were developed or the number of parameters they have or both. This means it can be unclear how a certain DFT functional is composed simply from its name or how it could perform against another functional. Therefore a certain amount of knowledge is needed when choosing a particular

functional for a particular task or how to choose a subsequent functionals to increase the accuracy of the result (if needed). DFT methods have been used in this thesis mostly for the study of electronic absorption spectra using functionals such as CAM-B3LYP in chapters 3,4 and 5. B3LYP has also been used briefly in chapter 7 and M06L in chapter 8, so only a somewhat brief discussion of the basics of DFT has been given.

2.4 Geometry optimisation methods

The methods discussed above describe how to obtain the energy of a chemical system with increasing accuracy but an equally important part of theoretical chemistry is determining where on a potential energy surface does that system exist with the geometry it possesses, i.e. is it at a minimum, saddle point of point of conical intersection? Finding minima, saddle points and conical intersection points are very important in theoretical chemistry and to the work discussed in this thesis as they allow the theoretical chemist to understand a chemical process or discover new reaction pathways, decide whether a molecule at a certain geometry should be stable and how molecules with the same geometries but exist on neighbouring potential energy surfaces affect one another, for example at a point of avoided crossing. In order to find a stationary point or point of conical intersection a method of geometry optimisation must be used. To calculate a minimum energy point the energy and gradient (i.e. the first-order derivative which point in the negative direction with respect to forces on atoms) for the initial geometry used are calculated. The positions of the atoms are then altered slightly in the direction of the gradient, and then the energy is calculated once again. This process can then be repeated until the lowest energy point possible is found and the geometry is optimised. There are a number of different methods that modern electronic structure codes use to calculate how the gradient is reduced such as conjugate gradient or Newton-Raphson methods, which are the most popular, and steepest descent however these methods will not be discussed in further detail here. In practise the system will be considered optimised when under some convergence limit value because stationary points cannot be located exactly. This is because the gradient can only be reduced to a certain value that can cause some numerical inaccuracies.

As already discussed for polyatomic molecules a potential energy surface is 3N-6 dimensional where N is the number of atoms and this number also equals the number of vibrational normal modes the system possesses. In order to calculate a minimum energy point of such a potential energy surface the gradient must be zero or within the convergence limit of the code used and the matrix of second derivatives, also called the Hessian, must also be calculated. The Hessian gives information of the curvature of the surface and at a minimum energy point all curvatures are positive. All normal vibrational modes are eigenvectors of the Hessian so at a minimum energy point they are said to all have positive eigenvalues. The harmonic vibrational frequency for the normal mode is related to the Hessian eigenvalue.

To calculate an n-th order saddle point there will be n negative eigenvalues of the Hessian matrix so for a transition state that would connect reactants to products for a ground state chemical reaction this would be a first order saddle point so there would be only one negative eigenvalue of the Hessian matrix. To locate a transition state structure the highest energy point along the path of the potential energy surface connecting reactants to products needs to be maximised in the direction of the transition vector i.e. the vibrational mode with the negative eigenvalue of the Hessian matrix and the energy needs to be minimised in all other 3N-7 directions on the surface. Many modern electronic structure codes contain algorithms to optimise transitions state points but these calculations can be expensive for larger systems as a Hessian needs to be calculated many times.

Optimising a point of conical intersection is different again to optimising a transition state or minimum energy point because the energy needs to be minimised in the N-2 directions of the intersection space to preserve the degeneracy between electronic states. The two remaining vibrational coordinates form the branching space vectors already discussed in this chapter. The energy gap has to be minimised in the direction of the branching space vectors, and for the optimised point of intersection the energy difference must be zero. This results in two conditions that must be fulfilled for successful completion of a conical intersection optimisation.

$$\frac{\delta E}{\delta x_3} = \frac{\delta E}{\delta x_4} = \ldots = \frac{\delta E}{\delta x_n} \tag{2.90}$$

$$E_j - E_i = 0 \tag{2.91}$$

The work discussed in this thesis uses the Gaussian code[54, 55] to optimise conical intersection points and in this code the program for minimising the energy difference E_j-E_i in the branching space uses the condition:

$$\frac{\partial}{\partial q}\left(E_j - E_i\right)^2 = 2(E_j - E_i)x_1 = 0 \tag{2.92}$$

Here x_1 is the gradient difference vector. The size of the step taken along the surface is dependent on the difference between the electronic states studied and the gradient is taken along where this energy difference adopts a minimum value. The gradient of a conical intersection point is non-zero because of the surface topology as it is the apex of a cone. The gradient of a conical intersection point is then calculated as a projection of the gradient of E_j along the 3N-8 intersection space seam which goes to zero when the geometry of the conical intersection point is optimised. So to optimise a point of conical intersection a point on the intersection space is firstly found and then the code will move the system around the intersection space vectors until a minimum energy point is found. This procedure is more complicated than searching for points on a single potential energy surface, and when using CASSCF previously discussed, optimising a point of conical intersection is challenging task.

2.5 Spectroscopy; theoretical methods

2.5.1 Basic principles of electronic spectroscopy

Much of this thesis is concerned with the processes that occur after a transition metal carbonyl complex has absorbed one or more photons and enters an electronic excited state. A natural question would be what are the excitation energies associated with these excited states and what are their nature? This is the purpose of spectroscopy for this

thesis; to measure or 'map' out the excited states of selected binary transition metal carbonyls and find out which ones can be populated after photoexcitation.

Before even considering how theoretical methods can model such spectra an introduction to the basic ideas of electronic spectroscopy will be given. Vibrational and rotational spectra can also be produced for such complexes but will not be considered here. A molecule will absorb a photon or photons of some frequency (or total frequency if more than one-photon) if it has a transition dipole that will oscillate at the same frequency as the photon (or photons) it has absorbed. Intense transitions are caused by the interaction of the electric dipole of a certain transition interacting with a certain part of an applied electric field, and a measure of how intense a transition will be is proportional to the square of the electric dipole moment μ_{elec}. Transitions are 'allowed' when the electric dipole moment for a transition is non-zero, where so-called 'selection rules' govern which transitions are allowed. There are two types of selection rule – specific selection rules that describe possible transitions from changes in the quantum number of states and gross selection rules that will describe possible transitions from the geometrical properties of the molecule under study. Physically μ_{elec} describes the magnitude of the migration of charge over the dipole during a transition. Selection rules and types of transitions for transition metal carbonyls will be discussed later. We also define at this point the polarizability of a molecule α, which measures the response of some molecule to the applied electric field. As we are discussing electronic spectroscopy only this is called the electric polarizability. So when an electric field is applied to a molecule the polarizability of that molecule will provide information on how it will respond to the electric field and could also have an electric dipole moment. If rectilinear Cartesian coordinates are used to describe the molecule being studied and an electric field is applied along the *z*-direction then an expression for the polarizability of the molecule in terms of integrals over its wavefunctions between ground and higher lying state *i* will be

$$\alpha_{zz} = -2\sum_{i}{}' \frac{\langle 0|\mu_z|i\rangle\langle i|\mu_z|0\rangle}{E_0^{(0)} - E_i^{(0)}} \tag{2.93}$$

This is called the static polarizability for the *z*-direction and there will be analogous expressions for the *x*- and *y*-directions and the mean polarizability will be the sum of all

three contributions. In moving on to discuss the role of polarizability and the electric dipole moment in the calculation of electronic spectra it is worthwhile to note some interesting features of these two properties of a molecule. One such feature is the fluctuation of the electric dipole moment $\Delta\mu$ that is the root mean square deviation of the electric dipole moment from the mean value of μ_{elec}. $\Delta\mu$ is non-zero even for molecules with $\mu_{elec}=0$ which are non-polar, where

$$\alpha \approx \frac{2\Delta\mu^2}{3\Delta E} \tag{2.94}$$

Where ΔE is the mean value of all excitations of the molecule and it is shown that the polarizability is proportional to the square of $\Delta\mu$. This provides a basic argument that an applied electric field can distort the electronic distribution of a molecule if the electrons are not too close to the nuclei. The further away the electrons are from the nucleus then the higher the value of the polarizability. So larger molecules with large number of electrons such as transition metal complexes will have larger polarizabilities and large number of electronic excited states.

Now considering electronic molecular spectroscopy in terms of μ_{elec} and α it can be said that α depends on the square of μ_{elec}. For an electronic spectrum produced from the absorption of one-photon the measure of intensity of an allowed transition in the spectrum is the oscillator strength *f*. The oscillator strength for a transition between the ground state 0 and some arbitrary excited state *i* is defined as

$$f_{i0} = \left(\frac{4\pi m_e}{3e^2\hbar}\right)\nu_{i0}\left|\mu_{i0}\right|^2 \tag{2.95}$$

Where the oscillator strength is related to the polarizability by

$$\alpha = \frac{\hbar^2 e^2}{m_e}\sum_i{}' \frac{f_{i0}}{\Delta E_{i0}^2} \tag{2.96}$$

If the sum over all oscillator strengths by the Kuhn-Thomas rule[56, 57] is equal to the number of (valence) electrons in the system N_V and we will have the following expression

$$\alpha \approx \frac{\hbar^2 e^2 N_V}{m_e \Delta E^2} \tag{2.97}$$

Which shows again that molecules with heavier atoms with large number of electrons e.g. transition metals, to be highly polarizable as the polarizability will increase with increasing numbers of valence electrons. Here a connection is established between electronic spectra and polarizabilities. Many high intensity transitions at low frequencies in the visible part of the spectrum contribute to this high polarizability and also shows why so many transition metal complexes are coloured.

One aspect of spectroscopy that is investigated in this thesis is the difference between spectra that are produced from the absorption of one-photon and the absorption of two photons. Figure 2.6 shows qualitatively the difference between one and two-photon absorption processes

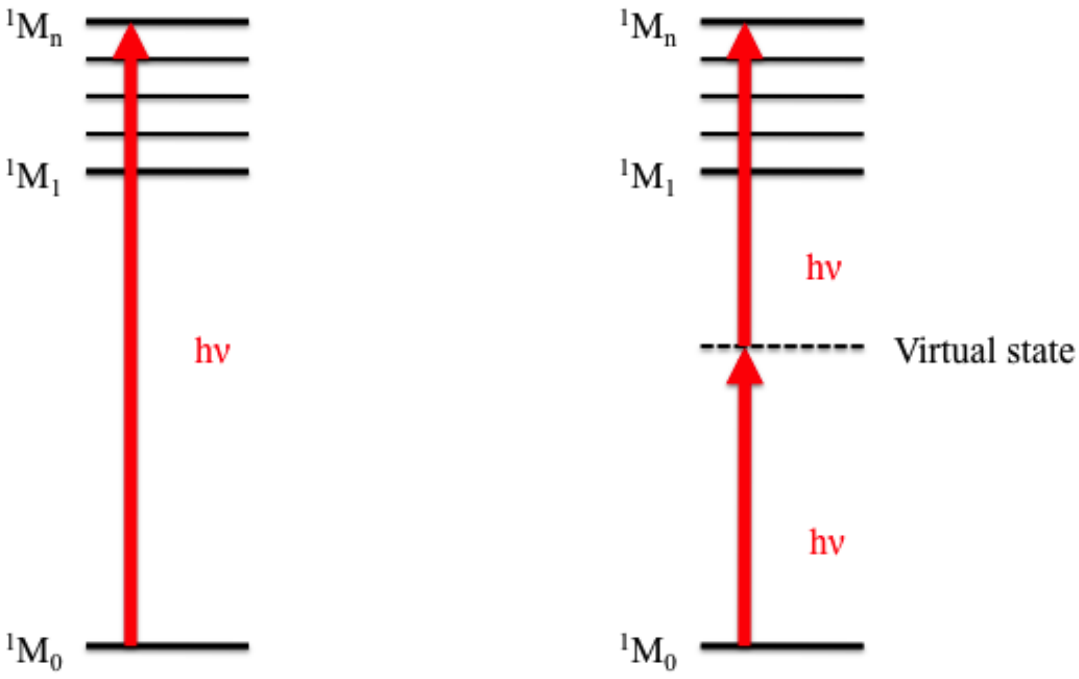

Figure 2.6 Schematic differences between one- and two-photon absorption processes between ground and excited electronic states.

In two-photon absorption spectroscopy the molecule simultaneously absorbs two photons that results in an electronic transition which correspond to the combined energy of the photons involved. The system goes through a so-called 'virtual state' that is a

superposition of the real states of the molecule, and through this virtual state different states can be populated and so one and two-photon absorption spectra can be different. This is especially true for transition metal complexes that are highly symmetrical and have excited states of different symmetry because the spectroscopic selection rules are different. Equally the same states could be allowed for both processes meaning spectral 'overlap' may be observed.

The next logical question to ask is what are the selection rules that govern which excited states can be populated? Two main rules are well known in this respect, namely that the overall spin state must not change and that for molecules that are centrosymmetric (i.e. have an inversion centre or 'i' symmetry element in their molecular point groups) the transition must involve a change in parity (the Laporte rule). This means that transitions between orbitals of the same type are not allowed. Table 2.1 presents the symmetries for allowed states for one and two-photon absorption for three binary transition metal carbonyls for which two-photon absorption spectra are calculated in chapters 3 and 4.

Table 2.1 Symmetries of allowed states from either one-photon or two-photon absorption for three binary metal carbonyls. Red indicates that the state is allowed in both cases and there is a possibility of spectral overlap

		Symmetry of allowed states	
Binary Carbonyl	**Point Group**	**One-photon**	**Two-photon**
$Cr(CO)_6$	O_h	T_{1u}	A_{1g}, E_g, T_{2g}
$Fe(CO)_5$	D_{3h}	A_2'', E'	A_1', E', E''
$Ni(CO)_4$	T_d	T_2	A_1, E, T_2

The electronic spectra of polyatomic molecules containing transition metals can be a challenge to resolve due to the number of electronic states available. The d orbitals in the transition metal are no longer all degenerate due to the presence of ligands so there can be transitions between the d orbitals as well as transitions between the ligands and the metal in either direction. With respect to transitions between the d orbitals the ligands cause the d orbitals to no longer be degenerate and how they split is determined by how the ligands coordinate to the metal and the overall symmetry of the complex. With symmetric complexes the d orbitals can split into two or more groups of

degenerate orbitals that are separated in energy by the ligand field splitting parameter, Δ. This splitting is usually small enough to allow transitions between these orbitals, the d orbital splitting for three common symmetrical structures of transition metal complexes studied in chapters 3 and 4 are shown in figure 2.7.

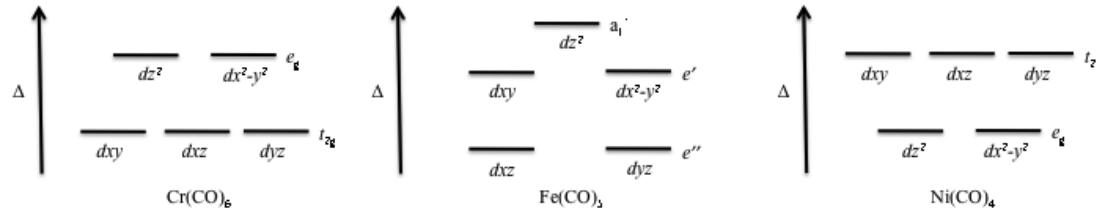

Figure 2.7 Ligand field splitting of the d orbitals only for three binary metal carbonyls

The other main type of transition occurs between the transition metal and the ligands. These are called charge transfer transitions and can include a transfer of electron density from the metal d orbitals to the ligand (MLCT), from the ligand to the metal (LMCT) or even from one ligand to another (LLCT). Carbonyl ligands have low-lying π anti-bonding orbitals that can accept an electron from the d orbitals so it can be assumed that the electronic spectra of binary metal carbonyl complexes will have many charge transfer states. Theoretical methods designed to measure the spectra of these complexes and other transition metal complexes are state-of-the-art and two such types of method that have been used in this thesis are discussed in section 2.5.2 below.

2.5.2 Propagator and coupled cluster response methods

Theoretical methods that look to describe the excited states and transition moments of binary transition metal carbonyls as used in this thesis are based broadly on either so-called propagator methods, or response theory. The general idea behind a propagator is that it is the probability amplitude that a particle at some point, r_1, at some time, t_1, will proceed to the point r_2 at time t_2 later. A propagator for the time-dependent functions $P(t_1)$ and $Q(t_2)$ would have the form

$$\left\langle\left\langle P(t_1);Q(t_2)\right\rangle\right\rangle = -i\theta(t_1-t_2)\left\langle\Psi_0\left|P(t_1)Q(t_2)\right|\Psi_0\right\rangle \pm i\theta(t_2-t_1)\left\langle\Psi_0\left|P(t_1)Q(t_2)\right|\Psi_0\right\rangle \quad (2.98)$$

Where θ is a step function ($\theta(x)$=0 for x<0, $\theta(x)$=1 for x>0) and a $\pm$ sign is inserted to account for both cases if P and Q are number-conserving operators or not. What is important from the point of spectroscopy is that the Fourier transform of the propagator form of equation (2.98) has the following form

$$\langle\langle P;Q\rangle\rangle = \sum_{i\neq 0} \frac{\langle \Psi_0 | P | \Psi_i \rangle \langle \Psi_i | Q | \Psi_0 \rangle}{\omega - E_i + E_0 + i\eta} \pm \frac{\langle \Psi_0 | P | \Psi_i \rangle \langle \Psi_i | Q | \Psi_0 \rangle}{\omega - E_i - E_0 - i\eta} \qquad (2.99)$$

Which is called the spectral or frequency representation. Here ω is the frequency of an applied field and to ensure this representation is valid when ω is equal to the difference in energy between states 0 and i in the denominator η is an infinitesimally small number. If P and Q are number conserving operators (i.e. they do not correspond to adding or removing electrons from the system under study) this expression is called a polarization propagator. If the frequency of the applied field is equal to the difference in energy between states 0 and i and η is not present then there will be a pole. The poles in a polarization propagator relate to the excitation energies of the system under study and the numerator where there is a pole is called the residue and will determine the transition moments (oscillator strength for one-photon absorption) between the reference state 0 any other excited state under study, i.

These general features can be better appreciated by relating them to commonly used electronic structure methods that calculate electronic excited states. Propagator methods as with other advanced electronic1 structure methods require a reference from which electrons can be excited, be it a wavefunction or Kohn-Sham orbital energies. If a CCSD reference is used this will be the so-called equation of motion CCSD (EOM-CCSD) method[58] that is used in later chapters. If DFT energies from a large choice of DFT functionals are used such as DFT this is known as time-dependant density functional theory (TD-DFT). TD-DFT has been used at great length for the study of one-photon electronic spectroscopy in a range of compounds and its usefulness in this area is beyond doubt, however there is one shortcoming with TD-DFT, which is that it cannot properly describe charge transfer states. The main reason for this is to do with how TD-DFT treats short and long-range quantum mechanical exchange. Because as previously discussed in section 2.3.6 hybrid functionals contain different amounts of exchange and dynamic electron correlation from different places i.e. their level of

parameterisation. Typically exchange from exchange DFT functionals are used for exchange at short range like with DFT that uses exchange from the Becke88 (B88)[59] exchange functional like B3LYP or similar, which is effective at short range and some exchange from HF that is better for describing long range exchange. More exchange is used from B88 than HF in B3LYP and this does not change so for electronic transitions where the charge travels over a longer distance like in a charge transfer state. And so charge transfer states are not properly described with TD-DFT because these methods do not give a suitable description of long range exchange. One method that looks to improve on this is the CAM-B3LYP hybrid functional of Handy and co-workers[60]. This functional looks to improve on standard TD-DFT with B3LYP by altering the ratio between B88 and HF exchange at short or long range according to a Coulomb type behaviour. This means more B88 exchange is used at short range but more HF exchange is used at long range when needed. This functional will be used in later chapters to test to see if it can indeed describe charge transfer states better than TD-B3LYP.

The other range of methods used are the coupled cluster response range of methods. Response theory measures the response of a molecular property to a time-dependent perturbation. In theory any molecular property can be studied so if one can use a wavefunction to make an approximate description of the system then response theory can be used to calculate the desired property, but in the context of electronic spectroscopy the molecular property studied is the electric polarizability and the perturbation is an electric field. For an oscillating electric field this can be expressed as

$$V(t) = \sum_k e^{-i\omega_k t} U F_k \tag{2.100}$$

Where U is the perturbation operator, ω_k is the frequency of the applied field and F_k is the field strength. In a general case the molecular property W has an expectation value that can be expanded according to some perturbations, say R and S

$$\langle W \rangle(t) = \langle W \rangle(0) + \sum_k e^{-i\omega_k t} \langle\langle W;R \rangle\rangle_{\omega_k} F_k + \frac{1}{2}\sum_{k,l} e^{-i(\omega_k-\omega_l)t} \langle\langle W;R,S \rangle\rangle_{\omega_k,\omega_l} F_k F_l + \ldots \quad (2.101)$$

This expansion represents response theory where the molecular property *W* responds to the operators *R* and *S*, where the first, second and third order terms are respectively the linear, quadratic and cubic response terms. For electronic spectroscopy the molecular property is the expectation value of the dipole operator and the perturbation is the electric field. The equation used to determine the frequency dependence of the response function is used to determine the excited states and transition moments of the response function. This equation is similar to equation (2.99) above

$$\langle\langle \mu,\mu \rangle\rangle_{\omega_y} = \alpha(\omega) = 2\sum_k \frac{\langle \Psi_0 | \mu | \Psi_k \rangle \langle \Psi_k | \mu | \Psi_0 \rangle}{(\omega_y - \omega_k)} \quad (2.102)$$

The quantity $\langle\langle \mu,\mu \rangle\rangle_{\omega_y}$ is called the dipole-dipole polarisability and $\alpha(\omega)$ is the frequency dependent polarisability. The energy difference between the two states 0 and *k* is given by ω_k and the frequency of the applied electric field is ω_y so as with the spectral representation (Fourier transform) of a propagator above the electronic excitation energies of the system under study will correspond to the poles which occur when the frequency of the applied field is equal to them, and the residue at these poles is related to the square of the transition dipole moment so will determine the oscillator strength of that transition. The above equation is for the linear response function that will simulate a one-photon absorption spectrum. Use of the analogous quadratic response function will give the two-photon absorption spectrum. A pole search is carried out to find as many excited states as required. As with propagator methods a reference is required and the work described in later chapters uses coupled cluster theory for this, so-called coupled cluster response theory. A coupled cluster response calculation firstly calculates the coupled cluster energy and amplitudes for the ground state then calculates the excitation energies of the system directly using the response eigenvalue equations, so ground and excited state wavefunctions do not need to be independently optimised. The initial ground state calculation requires the ground state

to be composed of primarily only one configuration of electrons but the excited states calculated with response theory do not have to be composed of primarily only one configuration so they are able to freely mix at the correlated level. This means that coupled cluster response theory treats all excited states of the system in an equal and balanced way regardless of their character.

One final consideration with coupled cluster response theory is the coupled cluster reference used. Coupled cluster models such as CCSD and CCSD(T) have already been mentioned in section 2.3.5 but other truncated coupled cluster models have been developed that fit into a hierarchy of coupled cluster models for molecular response properties[61]. How these models fit together can best been seen by discussing briefly their amplitude equations for different levels of excitation e.g. singles and doubles excitations. To start the Hamiltonian is partitioned into the Fock operator, a fluctuation operator, U and V, a one-electron external perturbation.

$$\widehat{H} = F + U + V \tag{2.103}$$

Where V is not included in F, this is known as the orbital unrelaxed approach. The amplitude equations can then be written in terms of a Baker-Campbell-Hausdorff expansion and with so-called similarly transformed operators of the type

$$\widehat{O} = e^{-T_1} O e^{T_1} \tag{2.104}$$

From this the coupled cluster response methods all approximate the singles contributions from the CCS method to first order, the contributions from doubles to second order and so on. What this means is that in a standard coupled cluster calculation the contributions of singles are minimal but in a response calculation they are included as well as doubles and triples and so on. The first model to be discussed is CC2[42] that sets the contributions of singles from the CCS method to first order and doubles to second order but the doubles contributions are simplified over those from the CCSD response method. The next level up from CCSD is the CC3[62] approximate model that approximates the triples equations from the CCSDT in the same way that CC2 approximates the doubles equations of CCSD. The computational cost of each

method and to what order it calculates excitation energies and transition states is shown in table 2.2.

Table 2.2 Computational cost and ordering of coupled cluster response methods

Method	**Computational cost/N^x (N=number of basis functions)**	**Excitation energy/correct to given order in electron correlation**	**Transition moments/ correct to given order in electron correlation**
CCS	N^4	1	0
CC2	N^5	2	1
CCSD	N^6	2	2
CC3	N^7	3	2
CCSDT	N^8	4	3

The computational cost for these approximate models go from N^5 for CC2 and N^7 where N is the number of basis functions for CC3 and while they give no significant improvement over CCSD or CCSD(t) for ground state problems they fit into a size-consistent heriarchy of CC models that will eventually converge towards the full CI limit and can be used with response theory for the study of electronic spectroscopy, which is discussed in chapters 3 and 4. The accuracy of these methods is shown graphically in figure 2.8 against the size of basis set. It can also be seen that figure 2.8 relates to the pioneering work of Pople in relation to increasingly accurate levels of theory (theoretical models) in electronic structure theory. The work of Pople in relation to electronic structure theory and the hierarchy in figure 2.8 can be seen in [63-65].

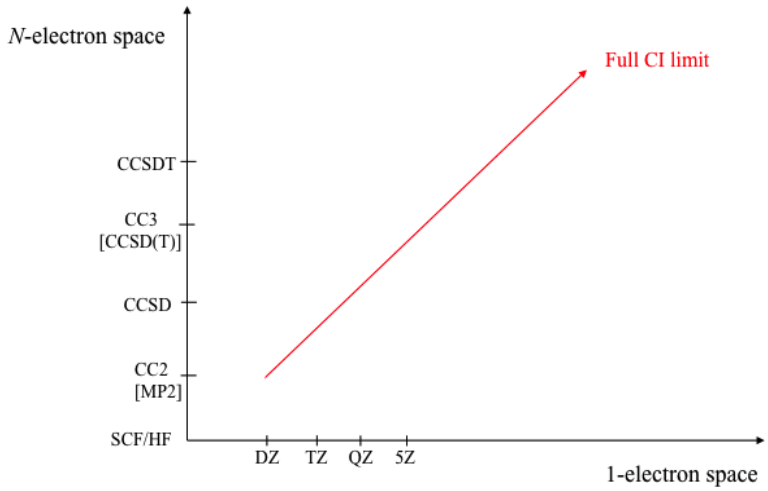

Figure 2.8 Graphical illustration of the relative cost of various *ab initio* methods against the quality of basis set from double zeta (DZ) to an infinite basis set and the full CI limit for the energy of a system or molecular property of that system.

2.6 Computational details

All results presented in this thesis were carried out using one of two commercial electronic structure codes. The Gaussian 03 and 09 codes[54, 55] were used to produce all results presented here as these codes have the CASSCF method needed for the potential energy surface studies within them with the exception of the results produced in chapters 3 and 4 using coupled cluster response methods. These results were produced using the Dalton code[66] as this code is the only one available with the full hierarchy of coupled cluster response methods.

2.7 References

[1] Kotzian, M.; Rosch, N.; Schroder, H.; Zerner, M. C., Optical spectra of transition metal carbonyls - $Cr(CO)_6$, $Fe(CO)_5$, and $Ni(CO)_4$. *J. Am. Chem Soc.* **1989,** 111, 7687-7696.

[2] Koerting, C. F.; Walzl, K. N.; Kuppermann, A., The spectroscopy of the group VI transition-metal hexacarbonyls using the electron-impact method. *J. Chem. Phys.* **1987,** 86, 6646-6653.

[3] Li, J.; Schreckenbach, G.; Ziegler, T., A reassessment of the first metal-carbonyl dissociation energy in $M(CO)_4$ (M=Ni, Pd, Pt), $M(CO)_5$ (M=Fe, Ru, Os), and $M(CO)_6$ (M=Cr, Mo, W) by a quasi relativistic density functional method. *J. Am. Chem Soc.* **1995,** 117, 486-494.

[4] Bernardi, F.; Olivucci, M.; Ragazos, I. N.; Robb, M. A., A new mechanistic scenario for the photochemical transformation of ergosterol - an MC-SCF and MM-VB study. *J. Am. Chem Soc.* **1992,** 114, 8211-8220.

[5] Palmer, I. J.; Olivucci, M.; Bernardi, F.; Robb, M. A., An MC-SCF study of the thermal and photochemical cycloaddition of dewar benzene. *J. Org. Chem.* **1992,** 57, 5081-5087.

[6] Olivucci, M.; Ragazos, I. N.; Bernardi, F.; Robb, M. A., A conical intersection mechanism for the photochemistry of butadiene - a MC-SCF study. *J. Am. Chem Soc.* **1993,** 115, 3710-3721.

[7] Palmer, I. J.; Ragazos, I. N.; Bernardi, F.; Olivucci, M.; Robb, M. A., An MC-SCF study of the S_1 and S_2 photochemical-reactions of benzene. *J. Am. Chem Soc.* **1993,** 115, 673-682.

[8] Olivucci, M.; Bernardi, F.; Celani, P.; Ragazos, I.; Robb, M. A., Excited state cis-trans isomerization of cis-hexatriene - a CAS-SCF computational study. *J. Am. Chem Soc.* **1994,** 116, 1077-1085.

[9] Yamamoto, N.; Bernardi, F.; Bottoni, A.; Olivucci, M.; Robb, M. A.; Wilsey, S., Mechanism of carbene formation from the excited states of diazirine and diazomethane - an MC-SCF study. *J. Am. Chem Soc.* **1994,** 116, 2064-2074.

[10] Bernardi, F.; Olivucci, M.; Robb, M. A., Potential energy surface crossings in organic photochemistry. *Chem. Soc. Rev.* **1996,** 25, 321.

[11] Yarkony, D. R., On the role of conical intersections in photodissociation .4. Conical intersections and the geometric phase in the 2^3a" and 3^3a" states of CH_2. *J. Chem. Phys.* **1996,** 104, 2932-2939.

[12] Yarkony, D. R., On the role of conical intersections in photodissociation .5. Conical intersections and the geometric phase in the photodissociation of methyl mercaptan. *J. Chem. Phys.* **1996,** 104, 7866-7881.

[13] Gordon, M. S.; Glezakou, V. A.; Yarkony, D. R., Systematic location of intersecting seams of conical intersection in triatomic molecules: The 1^2a '-2^2a ' conical intersections in BH_2. *J. Chem. Phys.* **1998,** 108, 5657-5659.

[14] Young, R. A.; Yarkony, D. R., A novel conical intersection topography and its consequences: The 1, 2 ^{2}a conical intersection seam of the vinoxy radical. *J. Chem. Phys.* **2005,** 123, 9.

[15] Atchity, G. J.; Xantheas, S. S.; Ruedenberg, K., Potential energy surfaces near intersections. *J. Chem. Phys.* **1991,** 95, 1862-1876.

[16] Atchity, G. J.; Ruedenberg, K., Strong shifts in diabatic nondynamic electron correlations cause conical intersection between low-lying closed-shell adiabatic singlets of like symmetry in ozone. *J. Chem. Phys.* **1993,** 99, 3790-3798.

[17] Atchity, G. J.; Ruedenberg, K.; Nanayakkara, A., The intersection seam between the 1^1a' and 2^1a' states of ozone. *Theor. Chem. Acc.* **1997,** 96, 195-204.

[18] Atchity, G. J.; Ruedenberg, K., A local understanding of the quantum chemical geometric phase theorem in terms of diabatic states. *J. Chem. Phys.* **1999,** 110, 4208-4212.

[19] Mckinlay, R. G.; Paterson, M. J., The Jahn-Teller effect in binary transition metal carbonyl complexes. In *The Jahn-Teller effect: Fundamentals and implications for physics and chemistry*, Koppel, H.; Barentzen, H.; Yarkony, D. R., Eds. Springer-Verlag: Heidelberg, 2009.

[20] Mond, L.; Langer, C.; Quincke, F., Action of carbon monoxide on nickel. *J. Chem. Soc.* **1890**, 749.

[21] Noga, J.; Bartlett, R. J., The full CCSDT model for molecular electronic-structure. *J.Chem. Phys.* **1987,** 86, 7041-7050.

[22] Yarkony, D. R., Conical intersections and the spin-orbit interaction: A new dimension in conical intersections. *Abstr. Pap. Am. Chem. Soc.* **2002,** 223, 220.

[23] Yarkony, D. R., Conical intersections: Topography, connectivity, and nuclear dynamics. *Abstr. Pap. Am. Chem. Soc.* **2001,** 221, 392.
[24] Yarkony, D. R., Conical intersections: The new conventional wisdom. *J. Phys. Chem. A* **2001,** 105, 6277-6293.
[25] Yarkony, D. R., Conical intersections: Diabolical and often misunderstood. *Accounts Chem. Res.* **1998,** 31, 511-518.
[26] Yarkony, D. R., Diabolical conical intersections. *Rev. Mod. Phys.* **1996,** 68, 985-1013.
[27] Matsika, S.; Yarkony, D. R., Conical intersections and the spin-orbit interaction. *Role. Degen. States. Chem.* **2002,** 124, 557-581.
[28] Paterson, M. J.; Bearpark, M. J.; Robb, M. A.; Blancafort, L.; Worth, G. A., Conical intersections: A perspective on the computation of spectroscopic Jahn-Teller parameters and the degenerate 'intersection space'. *Phys. Chem. Chem. Phys.* **2005,** 7, 2100-2115.
[29] McKinlay, R. G.; Zurek, J. M.; Paterson, M. J., Vibronic coupling in inorganic systems: Photochemistry, conical intersections, and the Jahn-Teller and pseudo-Jahn-Teller effects. *Adv. Inorg. Chem.* **2010,** 62, 351-390.
[30] Rosch, N.; Kotzian, M.; Jorg, H.; Schroder, H.; Rager, B.; Metev, S., On visible transients in gas-phase UV photolysis of transition-metal compounds - experimental and theoretical results for $Ni(CO)_4$. *J. Am. Chem Soc.* **1986,** 108, 4238-4239.
[31] Schlenker, F. J.; Bouchard, F.; Waller, I. M.; Hepburn, J. W., State resolved photofragmentation of Ni(CO)4 at 193, 248, and 308 nm - a detailed study of the photodissociation dynamics. *J. Chem. Phys.* **1990,** 93, 7110-7118.
[32] Thomsen, C. L.; Madsen, D.; Keiding, S. R.; Thogersen, J.; Christiansen, O., Two-photon dissociation and ionization of liquid water studied by femtosecond transient absorption spectroscopy. *J. Chem. Phys.* **1999,** 110, 3453-3462.
[33] Seder, T. A.; Church, S. P.; Weitz, E., Wavelength dependence of excimer laser photolysis of $Cr(CO)_6$ in the gas-phase - a study of the infrared-spectroscopy and reactions of the $Cr(CO)_5$, $Cr(CO)_4$, $Cr(CO)_3$, $Cr(CO)_2$ fragments. *J. Am. Chem Soc.* **1986,** 108, 4721-4728.
[34] Schreiner, A. F.; Brown, T. L., A semiempirical molecular orbital model for $Cr(CO)_6$, $Fe(CO)_5$, and $Ni(CO)_4$. *J. Am. Chem Soc.* **1968,** 90, 3366-3374.
[35] Trushin, S. A.; Fuss, W.; Schmid, W. E., Conical intersections, pseudorotation and coherent oscillations in ultrafast photodissociation of group-6 metal hexacarbonyls. *Chem. Phys.* **2000,** 259, 313-330.
[36] Ehlers, A. W.; Frenking, G., Structures and fond energies of the transition-metal carbonyls $M(CO)_5$ (M=Fe, Ru, Os) and $M(CO)_4$ (M=Ni, Pd, Pt). *Organometallics* **1995,** 14, 423-426.
[37] Church, S. P.; Grevels, F. W.; Hermann, H.; Schaffner, K., Structures and kinetics of $Cr(CO)_5$ and $Cr(CO)_5.H_2O$ in cyclohexane solution - flash-photolysis study of $Cr(CO)_6$ with infrared and visible detection. *Inorg. Chem.* **1985,** 24, 418-422.
[38] Fletcher, T. R.; Rosenfeld, R. N., Photofragmentation dynamics of $Cr(CO)_6$ in the gas-phase. *J. Am. Chem Soc.* **1983,** 105, 6358-6359.
[39] Daniel, C., Electronic spectroscopy and photoreactivity in transition metal complexes. *Coord. Chem. Rev.* **2003,** 238, 143-166.
[40] Paterson, M. J.; Hunt, P. A.; Robb, M. A.; Takahashi, O., Non-adiabatic direct dynamics study of chromium hexacarbonyl photodissociation. *J. Phys. Chem. A* **2002,** 106, 10494-10504.

[41] Barnes, L. A.; Rosi, M.; Bauschlicher, C. W., An abinitio study of $Fe(CO)_1$, $Fe(CO)_5$, and $Cr(CO)_6$. *J. Chem. Phys.* **1991,** 94, 2031-2039.

[42] Banares, L.; Baumert, T.; Bergt, M.; Kiefer, B.; Gerber, G., Femtosecond photodissociation dynamics of $Fe(CO)_5$ in the gas phase. *Chem. Phys. Lett.* **1997,** 267, 141-148.

[43] Arnbjerg, J.; Jimenez-Banzo, A.; Paterson, M. J.; Nonell, S.; Borrell, J. I.; Christiansen, O.; Ogilby, P. R., Two-photon absorption in tetraphenylporphycenes: Are porphycenes better candidates than porphyrins for providing optimal optical properties for two-photon photodynamic therapy? *J. Am. Chem Soc.* **2007,** 129, 5188-5199.

[44] Paterson, M. J.; Kongsted, J.; Christiansen, O.; Mikkelsen, K. V.; Nielsen, C. B., Two-photon absorption cross sections: An investigation of solvent effects. Theoretical studies on formaldehyde and water. *J. Chem. Phys.* **2006,** 125.

[45] Koch, H.; Christiansen, O.; Jorgensen, P.; deMeras, A. M. S.; Helgaker, T., The CC3 model: An iterative coupled cluster approach including connected triples. *J. Chem. Phys.* **1997,** 106, 1808-1818.

[46] Persson, B. J.; Roos, B. O.; Pierloot, K., A theoretical-study of the chemical bonding in $M(CO)_x$ (M=Cr, Fe, and Ni). *J. Chem. Phys.* **1994,** 101, 6810-6821.

[47] Pierloot, K., Transition metals compounds: Outstanding challenges for multiconfigurational methods. *Int. J. Quan. Chem.* **2011,** in press.

[48] Ben Arnor, N.; Villaume, S.; Maynau, D.; Daniel, C., The electronic spectroscopy of transition metal carbonyls: The tough case of $Cr(CO)_6$. *Chem. Phys. Lett.* **2006,** 421, 378-382.

[49] Pierloot, K.; Tsokos, E.; Vanquickenborne, L. G., Optical spectra of $Ni(CO)_4$ and $Cr(CO)_6$ revisited. *J. Phys. Chem.* **1996,** 100, 16545-16550.

[50] Purvis, G. D.; Bartlett, R. J., A full coupled-cluster singles and doubles model - the inclusion of disconnected triples. *J. Chem. Phys.* **1982,** 76, 1910-1918.

[51] Pollak, C.; Rosa, A.; Baerends, E. J., Cr-CO photodissociation in $Cr(CO)_6$: Reassessment of the role of ligand-field excited states in the photochemical dissociation of metal-ligand bonds. *J. Am. Chem Soc.* **1997,** 119, 7324-7329.

[52] Reiner, H.; Wittenzellner, C.; Schroder, H.; Kompa, K. L., Luminescence spectra after excimer laser photolysis of $Ni(CO)_4$. *Chem. Phys. Lett.* **1992,** 195, 169-173.

[53] Rosa, A.; Baerends, E. J.; van Gisbergen, S. J. A.; van Lenthe, E.; Groeneveld, J. A.; Snijders, J. G., Electronic spectra of $M(CO)_6$ (M = Cr, Mo, W) revisited by a relativistic TDDFT approach. *J. Am. Chem Soc.* **1999,** 121, 10356-10365.

[54] Frisch, M. J. Trucks., G. W.; Schlegel, H. B.; Scuseria, G. E.; Robb, M. A.; Cheeseman, J. R.; Montgomery, Jr., J. A.; Vreven, T.; Kudin, K. N.; Burant, J. C.; Millam, J. M.; Iyengar, S. S.; Tomasi, J.; Barone, V.; Mennucci, B.; Cossi, M.; Scalmani, G.; Rega, N.; Petersson, G. A.; Nakatsuji, H.; Hada, M.; Ehara, M.; Toyota, K.; Fukuda, R.; Hasegawa, J.; Ishida, M.; Nakajima, T.; Honda, Y.; Kitao, O.; Nakai, H.; Klene, M.; Li, X.; Knox, J. E.; Hratchian, H. P.; Cross, J. B.; Bakken, V.; Adamo, C.; Jaramillo, J.; Gomperts, R.; Stratmann, R. E.; Yazyev, O.; Austin, A. J.; Cammi, R.; Pomelli, C.; Ochterski, J. W.; Ayala, P. Y.; Morokuma, K.; Voth, G. A.; Salvador, P.; Dannenberg, J. J.; Zakrzewski, V. G.; Dapprich, S.; Daniels, A. D.; Strain, M. C.; Farkas, O.; Malick, D. K.; Rabuck, A. D.; Raghavachari, K.; Foresman, J. B.; Ortiz, J. V.; Cui, Q.; Baboul, A. G.; Clifford, S.; Cioslowski, J.; Stefanov, B. B.; Liu, G.; Liashenko, A.; Piskorz, P.; Komaromi, I.; Martin, R. L.; Fox, D. J.; Keith, T.; Al-Laham, M. A.; Peng, C. Y.; Nanayakkara, A.; Challacombe, M.; Gill, P. M. W.; Johnson, B.;

Chen, W.; Wong, M. W.; Gonzalez, C.; and Pople, J. A. Gaussian 09, Revision A.1, Gaussian, Inc., Wallingford CT, 2009.

[55] Frisch, M. J. Trucks., G. W.; Schlegel, H. B.; Scuseria, G. E.; Robb, M. A.; Cheeseman, J. R.; Montgomery, Jr., J. A.; Vreven, T.; Kudin, K. N.; Burant, J. C.; Millam, J. M.; Iyengar, S. S.; Tomasi, J.; Barone, V.; Mennucci, B.; Cossi, M.; Scalmani, G.; Rega, N.; Petersson, G. A.; Nakatsuji, H.; Hada, M.; Ehara, M.; Toyota, K.; Fukuda, R.; Hasegawa, J.; Ishida, M.; Nakajima, T.; Honda, Y.; Kitao, O.; Nakai, H.; Klene, M.; Li, X.; Knox, J. E.; Hratchian, H. P.; Cross, J. B.; Bakken, V.; Adamo, C.; Jaramillo, J.; Gomperts, R.; Stratmann, R. E.; Yazyev, O.; Austin, A. J.; Cammi, R.; Pomelli, C.; Ochterski, J. W.; Ayala, P. Y.; Morokuma, K.; Voth, G. A.; Salvador, P.; Dannenberg, J. J.; Zakrzewski, V. G.; Dapprich, S.; Daniels, A. D.; Strain, M. C.; Farkas, O.; Malick, D. K.; Rabuck, A. D.; Raghavachari, K.; Foresman, J. B.; Ortiz, J. V.; Cui, Q.; Baboul, A. G.; Clifford, S.; Cioslowski, J.; Stefanov, B. B.; Liu, G.; Liashenko, A.; Piskorz, P.; Komaromi, I.; Martin, R. L.; Fox, D. J.; Keith, T.; Al-Laham, M. A.; Peng, C. Y.; Nanayakkara, A.; Challacombe, M.; Gill, P. M. W.; Johnson, B.; Chen, W.; Wong, M. W.; Gonzalez, C.; and Pople, J. A.; Gaussian 03, Revision C.02, Gaussian, Inc., Wallingford CT, 2004.

[56] Trushin, S. A.; Kosma, K.; Fuss, W.; Schmid, W. E., Wavelength-independent ultrafast dynamics and coherent oscillation of a metal-carbon stretch vibration in photodissociation of $Cr(CO)_6$ in the region of 270-345 nm. *Chem. Phys.* **2008,** 347, 309-323.

[57] Trushin, S. A.; Fuss, W.; Schmid, W. E.; Kompa, K. L., Femtosecond dynamics and vibrational coherence in gas-phase ultraviolet photodecomposition of $Cr(CO)_6$. *J. Phys. Chem. A* **1998,** 102, 4129-4137.

[58] Christiansen, O., Coupled cluster theory with emphasis on selected new developments. *Theor. Chem. Acc.* **2006,** 116, 106-123.

[59] Gutmann, M.; Janello, J. M.; Dickebohm, M. S.; Grossekathofer, M.; Lindener-Roenneke, J., Ultrafast dynamics of transition metal carbonyls: Photodissociation of $Cr(CO)_6$ and $Cr(CO)_6$ $(CH_3OH)_n$ heteroclusters at 280 nm. *J. Phys. Chem. A* **1998,** 102, 4138-4147.

[60] Hada, M.; Imai, Y.; Hidaka, M.; Nakatsuji, H., Theoretical study on the excitation spectrum and the photofragmentation reaction of $Ni(CO)_4$. *J. Chem. Phys.* **1995,** 103, 6993-6998.

[61] Arnbjerg, J.; Paterson, M. J.; Nielsen, C. B.; Jorgensen, M.; Christiansen, O.; Ogilby, P. R., One- and two-photon photosensitized singlet oxygen production: Characterization of aromatic ketones as sensitizer standards. *J. Phys. Chem. A* **2007,** 111, 5756-5767.

[62] Badaeva, E.; Tretiak, S., Two photon absorption of extended substituted phenylenevinylene oligomers: A TDDFT study. *Chem. Phys. Lett.* **2008,** 450, 322-328.

[63] Pople, J. A.; Binkley, J. S.; Seeger, R., Theoretical models incorporating electron correlation. *Int. J. Quan. Chem.* **1976**, 1-19.

[64] Pople, J. A., Theoretical models for chemistry: Ab initio and empirical. *Abstr. Pap. Am. Chem. Soc.* **1998,** 215, U209-U209.

[65] Pople, J. A., Quantum chemical models (nobel lecture). *Angew. Chem.-Int. Edit.* **1999,** 38, 1894-1902.

[66] *Dalton, a molecular electronic structure program, release 2.0 (2005), see* http://www.Kjemi.Uio.No/software/dalton/dalton.Html, 2005.

Chapter 3

One- and two-photon electronic absorption spectroscopy of $Fe(CO)_5$

3.1 Introduction and literature review

One of the main subjects of this thesis is the electronic absorption spectroscopy of transition metal carbonyl complexes and in this chapter the electronic spectroscopy of iron pentacarbonyl ($Fe(CO)_5$) is discussed. As with all binary carbonyl complexes $Fe(CO)_5$ has been intensely investigated over the course of many years with regard to its structure, photoreactivity and spectroscopy. The power of new experimental and theoretical methods has improved the understanding of the spectroscopy and reactive photochemistry of this paradigm species [1, 2] and this will be shown here. Similar to the structure of the later chapters in this thesis this chapter will begin with a literature review of relevant studies relating to the aforementioned topics for $Fe(CO)_5$.

3.1.1 Experimental studies of electronic spectroscopy

The earliest work carried out investigating carbonyls of iron appeared one hundred and twenty years ago in 1891 by Mond and co-workers [3, 4]. Various techniques have been applied to $Fe(CO)_5$ such as X-ray or electron diffraction such as the study by Ewens and Lister [5] who used electron diffraction from a vapour. The structure was believed to be a trigonal bipyramid by analyzing diffraction photographs collected at -10^{o}C. An X-ray diffraction study that reported the crystal structure by Hanson [6] also suggested the structure was a trigonal bipyramid. The crystal structure was reported again by Donohue and Caron [7] where they reported the space group to be *C*2/*c* and confirmed that carbon bonded to the metal and not oxygen (though these types of 'isocarbonyl' structure are mentioned in the next chapter), and also concluded that the structure was indeed a trigonal bipyramid. Dahl and Rundle used X-ray diffraction to look at the structure of the unsaturated (i.e. with at least one coordination hole and less that 18 electrons) $Fe(CO)_4$ fragment. They reported a trimetric structure for $Fe(CO)_4$ with a *B*-centered unit cell and space group of $P2_1/n$. Discussions concerning the space group of $Fe(CO)_5$ is included for information purposes only, and can imply properties of the structure of the monomer such as potential molecular point groups. It is also included to

highlight that determining the crystal structure of a transition metal complex is not a trivial task, especially during the first half of the twenty first century.

Infrared spectroscopy has also been used many times to study $Fe(CO)_5$ such as the report of Sheline and Pitzer from 1950 in which the infrared spectrum of $Fe(CO)_5$ was produced and discussed [8]. It was shown that the IR bands in the spectrum supported the proposed trigonal bipyramid D_{3h} symmetry structure due to the structure and position of the carbonyl bands. The structure of the bicarbonyl $Fe_2(CO)_9$ was also studied in this paper and a triple carbonyl bridged structure was proposed based on the position and strengths of the carbonyl bands in the spectrum. The infrared spectrum was also reported by Swanson and co-workers but in matrices of xenon and argon at a temperature of 20K [9]. They found the spectra obtained had five carbonyl stretching peaks of which three decreased upon annealing. The two remaining peaks that persisted upon annealing were assigned to E′ and A_2' symmetry CO stretching modes that come from the D_{3h} symmetry of the molecule. The photoreactivity of $Fe(CO)_5$ has also been studied by infrared spectroscopy on the $Fe(CO)_4$, $Fe(CO)_3$ and $Fe(CO)_2$ fragments produced by excimer laser photolysis reported by Seder and co-workers [10]. The wavelength dependence of the production of each of the fragments was also looked at. It was found that $Fe(CO)_4$ and $Fe(CO)_3$ photofragments were produced after photolysis at 351nm and $Fe(CO)_2$ was produced by photolysis at 248nm. The results of this paper with respect to the reactive photochemistry of $Fe(CO)_5$ will be discussed in more detail in chapter 8.

The UV and electronic spectroscopy of $Fe(CO)_5$ has also been studied by a number of different groups with many similar themes present through all, namely the broad featureless nature of the spectrum and the number of electronic excited states of different chemical character that could contribute to each band. Kotzian and co-workers in 1989 reported the experimental gas phase electronic spectrum of $Fe(CO)_5$ along with those of $Cr(CO)_6$ and $Ni(CO)_4$ with analysis from INDO/S configuration interaction (CI) calculations [11]. From their results on $Fe(CO)_5$ they concluded that the observed spectrum was dominated by two bands at 5.0 and 6.2 eV and all visible bands were made up from MLCT transitions. All transitions originated from the metal 3d orbitals with d-d ligand field (LF) transitions constituting the lowest energy dark excited states. The spectrum produced from this study is reproduced in figure 3.1. Their conclusions

compare well with an earlier study from 1981 by Dick and co-workers that will be discussed later. Marquez and co-workers measured the gas phase UV spectrum in 1992 with additional theoretical analysis from CASSCF-CCI (contracted configuration interaction) calculations. The spectrum was dominated by a band at 6.39eV, followed by a series of overlapped bands. They paid particular attention to the presence of Rydberg states and found two Rydberg series at higher energy, one between 6.14eV and 7.66eV which was assigned to excitation from the 3d orbitals to the 4s,4p or 4d orbitals. The second series was between 7.94 and 8.90eV that was assigned to excitation form the $3d_{\pi}$ orbitals. Another earlier study by Hubbard and Lichtenberger from 1981 also studied the photo-electron spectrum of $Fe(CO)_5$ in the gas phase and found evidence of Jahn-Teller distortions in the $Fe(CO)_5^+$ cation photoelectron spectrum [12].

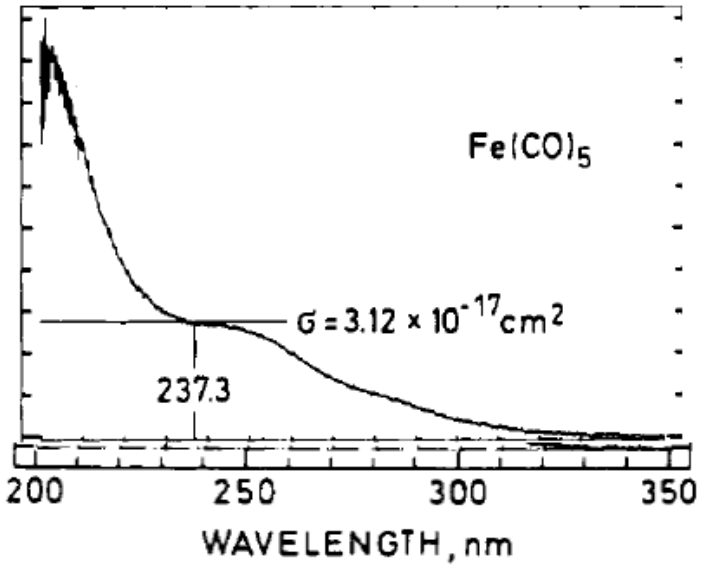

Figure 3.1 Gas phase near-UV electronic absorption spectrum of $Fe(CO)_5$ modified from the paper by Kotzian and co-workers [11]. The units of intensity on the vertical axis are in arbitrary units.

This was one of the first reports that discussed the possibility of highly symmetric metal complexes exhibiting Jahn-Teller activity in an ion and provided evidence to this point. They noticed that population of a doubly degenerate $^2E'$ positive ion state causes bands in the spectrum to broaden and their splitting to increase at high temperature, which they say, is indicative of a Jahn-Teller distortion where the molecule

has reduced its symmetry. They assigned the vibration that causes the distortion to an OC-Fe-CO bending vibration in the equatorial plane of D_{3h} symmetry $Fe(CO)_5$.

3.1.2 Theoretical studies of electronic spectroscopy

The experimental work reviewed above is only a highlight of the work that concern the spectroscopy of $Fe(CO)_5$ but what they do show is that the electronic absorption spectrum is challenging to study with many possible excited states making up the observed bands, many of which are degenerate due to the D_{3h} symmetry of $Fe(CO)_5$. Theoretical methods that can study excited states are needed here in order to resolve all these excited states that make up the spectrum; discussed below is a number of the most notable theoretical studies.

Multireference methods (already discussed in chapter 2) began to see use in the calculation of excited states of transition metal compounds in the 1980s, such as the work by Veillard and co-workers from 1984 who used truncated configuration interaction (CCI) calculations to look at the excited electronic states and photochemistry of $Fe(CO)_5$ [13]. They used two large CI spaces with 15 and 47 active orbitals, both containing the eight 3d electrons of iron and included all single and double excitations from the SCF reference state(s). The first excited state was calculated to be a $^3E''$ LF state with an excitation energy of 4.20eV, with many triplet and singlet excited states throughout the investigated range of both LF and MLCT character up to the highest energy calculated state at 6.33eV which was a $^1E''$ LF state. This study was revisited and improved in 1987 but using CCI calculations with a CASSCF reference [14]. Part of the reason for this study was to try and justify the study by Seder and co-workers using IR spectroscopy already discussed. For the $^1A_1$ ground state a CAS(8,9) active space was used and the CASSCF orbitals that were generated were then used for the CI calculations on the lowest excited states of the system. This study was not thought to be successful as this method overestimated excitation energies by 0.62eV according to the authors. The reason for this was believed to be that the use of the CASSCF orbitals optimized for the ground state was not accurate enough for states of different character, i.e. the method was not flexible enough to treat different excited states in a balanced manner. The experimental study of Marquez discussed earlier [15] also included CASSCF CCI studies of the excited states of $Fe(CO)_5$ but included a description of the

Rydberg states. A weakness of this method was highlighted in this report in that the authors could not calculate some states because of convergence problems in the CASSCF step of the calculations.

One more improved CASSCF study of the lowest electronic excited states (below 5.57eV) was reported in 1999 but this time the authors used multireference CI (MR-CI) and CASSCF calculations for each state of interest [2]. They found a large density of states between 3.09eV and 5.57eVand only three allowed transitions, two $^1E'$ and one $^1A_2''$. The CASSCF calculations used a CAS(8,16) active space that included all eight 3d electrons on iron, their antibonding equivalents and localized CO π orbitals. As in the previous study from 1987 using CASSCF, CASSCF wavefunctions were treated as references for the MR-CCI part of the calculation. The allowed transitions were found to have excitation energies of 3.34eV ($^1E'$), 4.58eV ($^1A_2''$) and 4.95eV ($^1E'$). The authors thought these states were responsible for the observed photochemistry from an earlier laser photodissociation study of the fragmentation and molecular dynamics of $Fe(CO)_5$ that will be discussed in chapter 8. The CASPT2 method was used by Persson, Roos and Peirloot [16] in which they separately computed the ligand field (LF) and charge transfer (CT) states of singlet and triplet E′ and E″ symmetry. They found that the lowest energy singlet LF state compared favorably to the shoulder at 4.3eV in the experimental spectrum produced by Kotzian and co-workers [11], the spectrum is shown in figure 3.1. They also found that the addition of dynamic electron correlation lowered excitation energies of the states studied by a few tenths of an eV compared to the same states calculated with CASSCF. There was a noticeable difference between CASSCF and CASPT2 for the allowed charge transfer state of 1.7eV showing a large dynamic correlation effect was present when describing a charge transfer state. What is apparent though from these studies is that only a few states of specific interest were studied, highlighting that multireference methods were so expensive for spectroscopic calculations of electronic excited states that only a few could be calculated with a reasonably high degree of accuracy.

These studies are a highlight of the work most relevant to this chapter and indeed more comprehensive reviews encompassing the photochemistry of $Fe(CO)_5$ have been published [17].

Up to this point no study can be found in the literature reporting a DFT study of the electronic excited states of $Fe(CO)_5$ which is surprising considering such studies are present for other binary carbonyls such as $Cr(CO)_6$, $Ni(CO)_4$ and $Mn_2(CO)_{10}$ [18, 19]. DFT has so far been used to study the vibrational spectrum of $Fe(CO)_5$ along with other binary metal carbonyls [20]. However as stated above there has only been a small number of studies reported using multireference methods. The purpose of this chapter is to build upon this body of work already reported concerning the study of the electronic spectroscopy of $Fe(CO)_5$. The reasons for this are numerous. Firstly the number of theoretical studies already reported are small and the youngest of these is now over ten years old. The assignment of the spectrum is still somewhat controversial especially regarding which states contribute to the experimental bands, as both CT and d-d LF states are allowed and there is a large density of states throughout the UV spectral range. An understanding of the lowest excited states could also provide valuable information on which states contribute to the ultrafast photochemistry $Fe(CO)_5$ exhibits in the singlet spin manifold involving ejection of a CO ligand and relaxation of the initial $Fe(CO)_4$ photoproduct through a Jahn-Teller induced conical intersection [21]. The initial state believed to be populated is an MLCT state followed by internal conversion to a dissociative ligand field state that causes the loss of the CO ligand. This photochemistry will be fully discussed in chapter 8.

Reinvestigating the electronic spectroscopy of $Fe(CO)_5$ using a more balanced method than CASSCF, CASPT2 or various forms of configuration interaction would address some of the issues that arose from previous studies such as convergence issues [15] and a limit on the number of states that can be computed (up to 5.57eV) due to limitations in computational power at the time [2]. It would also allow for a comparison between those methods and the methods used here. The methods used here are the hierarchy of coupled cluster response theory, CC2, CCSD and CCR(3). These methods have already been discussed in chapter 2 and are highly correlated methods that treat all states in a balanced manner, as excited states are free to mix at the correlated level. This means all states can be calculated from a single calculation rather than CASSCF, CASPT2 and CI calculations that require a separate calculation for each state of interest for systems of this size. The increase in computational power from the end of the last century to the present day also means that coupled cluster methods and reasonably large basis sets can be applied to a transition metal complex, and excited states can be probed

up to 10eV in excitation energy. Coupled cluster response methods have increased in prominence in recent years and have been successfully applied to the electronic spectroscopy of a range of organic species [22, 23, 24, 25] and now coupled cluster methods can be applied to the electronic spectroscopy of transition metal complexes such as the recent study on $Cr(CO)_6$ using the EOM-CCSD, similar to LR coupled cluster methods [26] discussed in chapter 2. Because no DFT study can be found in the literature regarding the electronic spectroscopy of $Fe(CO)_5$ the coupled cluster results will be additionally compared to time dependent DFT (CAM-B3LYP) results.

One other facet of the electronic spectroscopy of $Fe(CO)_5$ that will be investigated here is the two-photon absorption electronic spectrum of $Fe(CO)_5$. Experimental studies exciting $Fe(CO)_5$ with either one-photon or two-photons have already been published [21, 27] and while the response of nuclei to the added energy is the same, i.e. a breakdown of $Fe(CO)_5$ on a femtosecond timescale, the process by which this happens could be very different due to the large density of states. The selection rules indicating which states are allowed to be populated are different for either one-photon or two-photon absorption. As already shown in table 2.1 the symmetry of accessible electronic states differs, A_2'' and E′ symmetry states are allowed for one-photon absorption and A_1', E′ and E″ symmetry states are allowed for two-photon absorption. Note that E′ symmetry states are allowed for both indicating that spectral overlap may be observed. As will also be discussed in chapter 4 the difference between both types of absorption is a subtle one. The study by Trushin and co-workers [21] excited $Fe(CO)_5$ in the gas phase with one-photon at 267nm (4.64eV) and the study by Bañares and co-workers [27] excited $Fe(CO)_5$ in the gas phase with two-photons of 400nm (3.10eV) meaning a total excitation of 6.20eV. While both then studied the resulting photochemistry which was the break down of the $Fe(CO)_5$ molecule on an ultrafast timescale, subtle issues that arise from both studies could be which state is initially populated and was the process of dissociation concerted or sequential (concerted here means the dissociation of all carbonyl ligands within a few vibrational periods). Because different degenerate states also are available, then if they are populated different Jahn-Teller distortions may also occur via coupling to different non-totally symmetric vibrations. It is also possible for a non-degenerate state to be populated from which the dissociation proceeds directly or there could be ultrafast

internal conversion to a degenerate excited state that is close in energy. This photochemistry will be discussed in more detail in later chapters, but the point here is that such subtle potential differences in the early photochemistry between one- and two-photon absorption makes study of both spectra relevant.

More general points from the discussions above show that the electronic spectrum of $Fe(CO)_5$ is challenging to study and its assignment is still debatable. There are also only a small number of experimental and theoretical studies reported for $Fe(CO)_5$ compared to other carbonyls, like $Cr(CO)_6$, which themselves have been far from extensively studied, and that none of these studies is recent i.e. less than ten years old. It can be argued that a reinvestigation of the excited states of $Fe(CO)_5$ using highly correlated methods is therefore very pertinent.

3.2 Computational details

Two geometries of $Fe(CO)_5$ were used; the first was optimized in the $^1A_1'$ ground state with D_{3h} molecular symmetry at the CCSD level of theory with an SDD core ($1s^2 2s^2 2p^6$) on iron then cc-pVTZ on the iron valence orbitals, and carbon and oxygen. The other geometry used was based on the experimental gas phase structure. The calculated bond lengths for each geometry are shown in table 3.1.

Table 3.1 Bond lengths of the two geometries of $Fe(CO)_5$ used.

	Geometry	
Geometrical parameter	**CCSD**	**Experimental**
Fe-C bond (axial)	1.818Å	1.806Å
Fe-C bond (equatorial)	1.808Å	1.833Å
C-O bond (axial)	1.151Å	1.145Å
C-O bond (equatorial)	1.155Å	1.145Å

A number of different methods were used in this study. The hierarchy of coupled cluster methods were used that have already been discussed in chapter 2 for both one and two-photon absorption spectra, CC2, CCSD and the CCR(3) method which provides information on excitation energies only, therefore no transition moment data with the perturbative contribution of triples over the CCSD method.

The EOM-CCSD method was used for the one-photon absorption spectrum only for comparison with the linear response coupled cluster methods, as already stated in chapter 2, LR-CCSD and EOM-CCSD with exactly the same geometry and basis set will return the same excitation energies but the transition properties (i.e. oscillator strengths) will be different, LR-CCSD being slightly superior to EOM-CCSD but any differences should be very small. The CAM-B3LYP density functional has also been used to generate the one-photon spectrum. This functional, again already discussed in chapter 2, was designed to have the same ground state properties as the well-known B3LYP functional but improves upon the failure of B3LYP to accurately model charge transfer states. Because the spectrum of $Fe(CO)_5$ should contain many charge transfer states a comparison between the coupled cluster methods and CAM-B3LYP should be interesting. CASSCF was also used here to measure the excitation of the first ligand field (LF) state with a CAS(8,10) active space consisting of all eight 3d orbitals of iron with an equivalent set of d orbitals containing a node in M-L bonding regions of iron. CASSCF is used here because it is also used to study the potential energy surfaces concerned with the reactive photochemistry of $Fe(CO)_4$ in chapter 8 so this active space is introduced here to firstly test how well it can account for the first LF state. The difference in energy between the ground state and the doubly degenerate first excited state then corresponds to the first LF excitation energy. CASSCF should be a relatively accurate method for measuring LF state excitation energies so a comparison with the coupled cluster methods and CAM-B3LYP would also be interesting.

A number of basis sets were also used to investigate any differences in the spectra due to basis set effects. The hierarchy of coupled cluster response methods used three atomic natural orbital (ANO) basis sets [28] of various contraction size on iron and Dunning basis sets on carbon and oxygen, along with an SDD basis set on iron ($1s^2 2s^2 2p^6$ frozen core) with the Pople 6-31G* basis set on carbon and oxygen. Details of the number of primitive and contracted basis functions present in these basis sets are

presented in table 3.2. EOM-CCSD was used with a large Dunning style basis set with a polarized weighted core that treats the core electrons more accurately than a standard Dunning basis set. A cc-pWCTZ triple zeta basis set was used on iron and cc-pCVDZ basis set was used on carbon and oxygen with the d functions removed due to computational expense. This basis set consisted of 706 primitive GTOs and 232 contracted GTOs in total. CAM-B3LYP was used with a cc-pVTZ all electron basis set [29] on iron and cc-pVTZ basis sets on carbon and oxygen as implemented within the Gaussian 09 code [30]. This basis set consisted of 871 primitive GTOs and 368 contracted GTOs in total. CASSCF was used with a cc-pVDZ all electron basis set on iron [29] and cc-pVDZ on carbon and oxygen. This basis set consisted of 624 primitive GTOs and 183 contracted GTOs in total.

Table 3.2 Basis set contractions from all basis set combinations used in coupled cluster response methods.

Basis Set	Contraction (PGTO|CGTO) Fe C,O	Number of Basis Functions (PGTO|CGTO)			Total Functions (PGTO|CGTO)
		Fe	C	O	
ANO (small-S) cc-pVDZ	[21s15p10d6f|6s4p3d1f] [9s4p1d|3s2p1d]	158|40	26|14	26|14	418|180
ANO (medium-M) cc-pVDZ	[21s15p10d6f4g|6s4p3d2f1g] [9s4p1d|3s2p1d]	194|56	26|14	26|14	454|196
ANO (large-L) cc-pVDZ	[21s15p10d6f4g|7s6p4d2f1g] [9s4p1d|3s2p1d]	194|68	26|14	26|14	454|208
ecp-sdd-DZ 6-31G*	[7s6p5d|5s4p2d] [10s4p1d|3s2p1d]	50|27	27|14	27|14	320|167

The basis sets used with each method represents some of the largest and best quality possible with the computational resources and software available. Through the use of these basis sets it will be shown that differences in the spectra due to the size of basis set are minimal and that results generated while using a basis set of relatively modest size such as the smallest ANO/cc-pVDZ basis set could be analyzed with confidence. This will become more important in the next chapter where the spectroscopy of $Cr(CO)_6$ and $Ni(CO)_4$ is used with such modest sized basis sets.

3.3 One-photon absorption spectrum

A qualitative molecular orbital diagram for $Fe(CO)_5$ is presented in figure 3.2 [31].

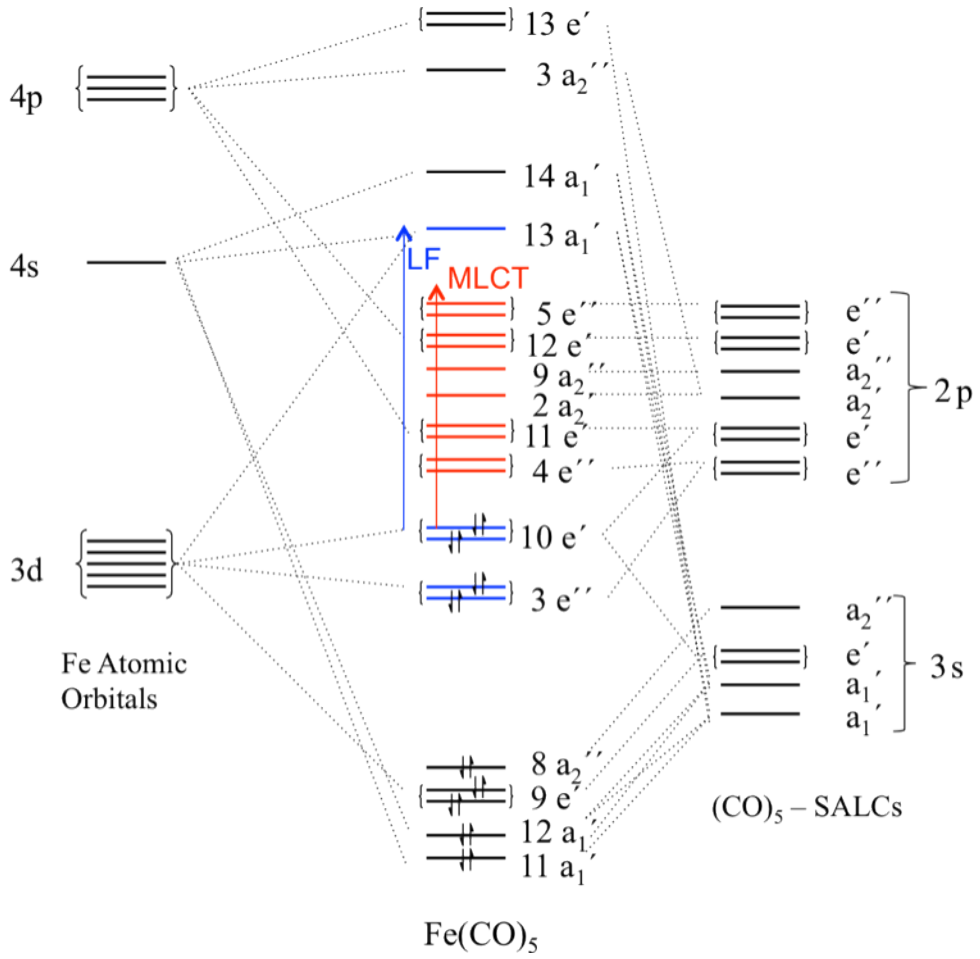

Figure 3.2 Qualitative molecular orbital diagram for $Fe(CO)_5$. Possible charge transfer states from the highest occupied MO are shown in red and the equivalent lowest energy ligand field transition is shown in blue. SALC stands for 'symmetry adapted linear combination' orbitals.

This diagram is included here to illustrate the number of orbitals available that can be populated and shows that from this classical inorganic picture the initial excitation should be into a manifold of metal to ligand charge transfer (MLCT) states, many of which are doubly degenerate indicating that the molecule may distort along some non-totally symmetric vibration from these degenerate states and possibly eject one or more carbonyl ligands. This qualitative diagram can be compared to a quantitative MO diagram centered around the highest occupied and lowest unoccupied molecular orbitals produced using the HF method and a cc-pVDZ all electron basis set on iron [29] and cc-pVDZ on carbon and oxygen with the CCSD optimized geometry. This diagram is shown in figure 3.3.

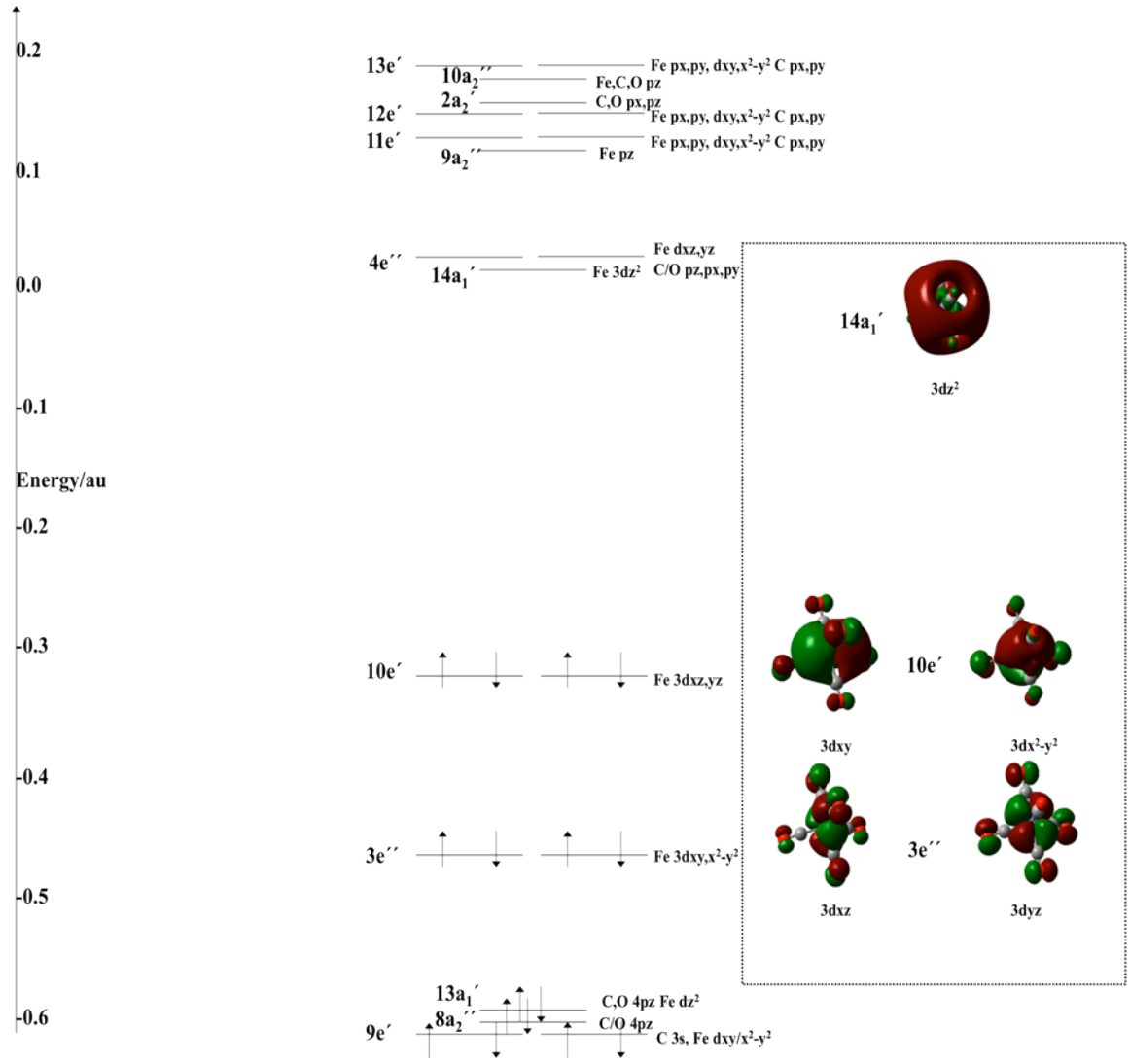

Figure 3.3 Quantitative MO diagram produced with the HF method using the CCSD optimized geometry and the cc-pVDZ all electron basis set on all atoms.

This diagram differs from the classic inorganic picture from figure 3.2 in that there is not a manifold of MLCT states between the highest energy metal d orbital and the lowest occupied d orbitals. Instead there is a large gap in energy between the highest occupied and lowest unoccupied MOs that are the 3d orbitals of iron followed by a number of degenerate orbitals that if populated would constitute MLCT states, though at this level the orbitals are heavily mixed. This is a prominent feature of the molecular orbitals and indeed the electronic transitions that will be presented in this and later chapters. It appears this is a common feature of metal carbonyls and could be a contributing factor to the difficulty of calculating and analyzing these spectra.

Aspects of the methods, basis sets and geometries will be discussed first before going on to discuss how closely they compare to the experimental spectrum and previous theoretical studies for $Fe(CO)_5$. The effect of geometry will be considered first. Tables 3.3 and 3.4 present selected excited states energies and oscillator strengths where applicable with experimental and CCSD optimized geometries respectively.

Table 3.3 Selected electronic excitation energies of $Fe(CO)_5$ for a range of linear response coupled cluster methods and EOM-CCSD with the experimental geometry. The basis sets used are the largest ANO basis set for the linear response coupled cluster methods (LR-CCSD) and the large basis set with EOM-CCSD. These energies are compared to previous CASSCF and MR-CCI results from [2]. Oscillator strengths where applicable are in brackets. This table is ordered by energy of the LR-CCSD method.

		Excitation Energy/eV – Experimental Geometry					
Excited State	**Character**	**CC2**	**MR-CCI [2]**	**CASSCF [2]**	**LR-CCSD**	**EOM-CCSD**	**CCR(3)**
1E′	LF dx^2-y^2,dxy - Fe 4p+	3.337 (0.000)	3.557 (0.003)	4.044	4.296 (0.000)	4.356 (0.000)	4.324
1E″	LF dxz,dyz – Fe 4p antibonding	3.235	4.561	4.384	4.747	4.623	4.925
$1A_1$″	MLCT dx^2-y^2,dxy - CO bonding SALC	4.258	4.126	4.336	4.565	4.451	4.718

$1A_2'$	MLCT dx^2-y^2,dxy - CO bonding SALC	3.542	4.717	4.699	4.962	4.906	4.983
2E′	MLCT dx^2-y^2,dxy - CO bonding SALC	3.445 (0.000)	4.873 (0.006)	4.748	5.057 (0.004)	4.987 (0.0007)	5.104
2E″	MLCT dx^2-y^2,dxy - CO bonding SALC/antibonding SALC 40%	4.071	4.405	4.384	5.085	5.088	5.056
$1A_2''$	MLCT dx^2-y^2,dxy - CO bonding SALC	3.839 (0.000)	4.591 (0.01)	4.865	5.119 (0.062)	5.025 (0.069)	5.040
3E″	MLCT dxz,dyz - CO antibonding SALC	4.101	5.289	5.194	5.293	5.179	5.367
$2A_2'$	MLCT dx^2-y^2,dxy - CO bonding SALC/antibonding SALC 40%	4.045			5.603	5.467	5.677
3E′	MLCT dx^2-y^2,dxy - CO bonding SALC 15%/antibonding SALC 48%	3.650 (0.000)			5.633 (0.087)	5.463 (0.016)	5.793
$1A_1'$	MLCT dx^2-y^2,dxy - CO antibonding SALC	3.537	5.583	5.442	5.637	5.517	5.686

4E′	LF dx^2-y^2,dxy – Fe 4s antibonding 53%/4p antibonding 10%	3.925 (0.000)			5.786 (0.040)	5.588 (0.159)	5.863
5E′	MLCT dx^2-y^2,dxy - CO bonding SALC 33%/antibonding SALC 33%	4.023 (0.000)			5.919 (0.050)	5.675 (0.055)	6.314
$2A_1$′	MLCT dx^2-y^2,dxy - CO bonding SALC 15%/antibonding SALC 48%	3.977			5.930	5.820	5.994
$3A_2$′	MLCT dxz,dyz - CO bonding 40%/antibonding 20% SALC	5.813			6.191	6.024	6.360
$2A_1$″	MLCT dxz,dyz - CO antibonding SALC	4.757			6.205	6.083	6.416
4E″	MLCT dxz,dyz - CO bonding 44%/antibonding 44% SALC	4.20515			6.313	6.165	6.529
6E′	MLCT dxz,dyz - CO bonding 39%/antibonding 44% SALC	4.76929 (0.000)			6.395 (0.050)	6.216 (0.048)	6.606

$2A_2''$	MLCT dxz,dyz - CO antibonding SALC	4.72021 (0.000)			6.675 (0.220)	6.572 (0.361)	6.819
$3A_1''$	MLCT dxz,dyz - CO bonding 12%/antibonding 37% SALC	-			6.757	6.600	6.917
$5E''$	MLCT dxz,dyz - CO antibonding SALC	4.52414			6.762	6.688	7.068

There is little difference between CCSD values using different geometries and the values of the oscillator strengths for allowed states are also very similar. It can be seen from tables 3.3 and 3.4 that the difference between the states with different geometries is minimal in most cases with all methods. The state characters included in tables 3.3 and 3.4 are included to analyze the nature of the excited states and to show their complexity.

Table 3.4 Selected electronic excitation energies of $Fe(CO)_5$ for a range of linear response coupled cluster methods and EOM-CCSD with the coupled cluster optimized geometry. The basis sets used are the largest ANO basis set for the linear response coupled cluster methods and the large basis set with EOM-CCSD. These energies are compared to previous CASSCF and MR-CCI results from [2]. Oscillator strengths where applicable are in brackets. This table is ordered by energy of the LR-CCSD method.

		Excitation Energy/eV – Coupled cluster Geometry					
Excited State	**Character**	**CC2**	**MR-CCI [2]**	**CASSCF [2]**	**LR-CCSD**	**EOM-CCSD**	**CCR(3)**
$1E'$	LF dx^2-y^2,dxy - Fe 4p+	3.515 (0.000)	3.557	4.044	4.332 (0.000)	4.386 (0.000)	4.368
$1E''$	LF dxz,dyz – Fe 4p antibonding	3.435	4.561	4.384	4.782	4.658	4.928

$1A_1''$	MLCT dx^2-y^2,dxy - CO bonding SALC	4.306	4.126	4.336	4.608	4.495	4.722
$1A_2'$	MLCT dx^2-y^2,dxy - CO bonding SALC	3.647	4.717	4.699	5.076	5.011	5.078
$2E'$	MLCT dx^2-y^2,dxy - CO bonding SALC	3.613 (0.000)	4.873	4.748	5.141 (0.001)	5.062 (0.000)	5.175
$2E''$	MLCT dx^2-y^2,dxy - CO bonding SALC/antibonding SALC 40%	4.248	4.405	4.384	5.116	5.119	5.076
$1A_2''$	MLCT dx^2-y^2,dxy - CO bonding SALC	3.889 (0.000)	4.591	4.865	5.172 (0.068)	5.077 (0.076)	5.048
$3E''$	MLCT dxz,dyz - CO antibonding SALC	4.258	5.289	5.194	5.330	5.215	5.372
$2A_2'$	MLCT dx^2-y^2,dxy - CO bonding SALC/antibonding SALC 40%	4.303			5.660	5.528	5.689
$3E'$	MLCT dx^2-y^2,dxy - CO bonding SALC 15%/antibonding SALC 48%	3.793 (0.000)			5.680 (0.083)	5.547 (0.056)	5.827
$1A_1'$	MLCT dx^2-y^2,dxy - CO antibonding	3.645	5.583	5.442	5.687	5.563	5.718

	SALC						
4E′	LF dx^2-y^2,dxy – Fe 4s antibonding 53%/4p antibonding 10%	4.280 (0.000)			5.864 (0.044)	5.691 (0.077)	5.882
5E′	MLCT dx^2-y^2,dxy - CO bonding SALC 33%/antibonding SALC 33%	4.884 (0.000)			6.047 (0.081)	5.758 (0.071)	6.418
$2A_1'$	MLCT dx^2-y^2,dxy - CO bonding SALC 15%/antibonding SALC 48%	4.240			5.983	5.871	6.029
$3A_2'$	MLCT dxz,dyz - CO bonding 40%/antibonding 20% SALC	5.879			6.206	6.038	6.347
$2A_1''$	MLCT dxz,dyz - CO antibonding SALC	5.191			6.271	6.134	6.470
4E″	MLCT dxz,dyz - CO bonding 44%/antibonding 44% SALC	4.299			6.347	6.190	6.553
6E′	MLCT dxz,dyz - CO bonding 39%/antibonding 44% SALC	5.167 (0.000)			6.408 (0.005)	6.226 (0.004)	6.594
$2A_2''$	MLCT dxz,dyz - CO antibonding	4.908			6.744 (0.265)	6.624 (0.361)	6.884

	SALC						
$3A_1''$	MLCT dxz,dyz - CO bonding 12%/antibonding 37% SALC	-			6.798	6.653	6.926
$5E''$	MLCT dxz,dyz - CO antibonding SALC	4.620			6.836	6.687	7.063

The majority of states in tables 3.3 and 3.4 have MLCT character with a few pure d-d LF states, including the first two excited states. The mixed nature of the orbitals, shown in figure 3.3, contribute to the mixed nature of the states where electron density from the metal 3d orbitals is transferred to a mixture of higher lying metal orbitals or a mixture of symmetry adapted linear combinations (SALCs) of carbonyl orbitals, either bonding orbitals or antibonding orbitals. It can be presumed from first principles that the arrangement of molecular orbitals in such non-octahedral transition metal complexes would be complicated and this is certainly the case for $Fe(CO)_5$ where the complex nature of the orbitals has contributed to the complex character of the excited states. It is this complex character that has contributed to the difficulty in the past to analyze features in the experimental spectrum and look at excited states high in energy, such as the intense experimental band at 6.20eV. The coupled cluster methods used here treat all states in a balanced manner and even though they are computationally expensive, especially with large ANO all electron basis sets, it has been shown that such higher energy states can be calculated and their characters investigated.

The influence the size of basis set has on the excitation energies and oscillator strengths of the spectrum can be seen in table 3.5. The difference in excitation energy for each state between each method with the different basis sets is quite small in almost all cases. For example the difference in excitation energy of the 1E′ state with the CCSD method using the smallest and biggest ANO basis sets was 0.052eV. There is more of a difference in oscillator strength with different basis set with each method but all are in reasonable agreement with one another.

Table 3.5 Selected one-photon excited states and oscillator strengths where applicable (in brackets) of $Fe(CO)_5$ with the three ANO basis sets and SDD basis set detailed in section 3.2. This table is ordered by state symmetries.

	Basis set and Excitation energy/eV									
State	**ANO-S**			**ANO-M**	**ANO-L**			**ECP-SDD**		
	CC2	CCSD	CCR(3)	CCR(3)	CC2	CCSD	CCR(3)	CC2	CCSD	CCR(3)
1E′	3.342 (0.118)	4.384 (0.000)	4.415	4.223	3.515	4.332 (0.000)	4.368	3.189	4.290 (0.000)	4.336
1E″	3.366	4.737	4.925	4.898	3.435	4.782	4.658	3.366	4.579	4.607
$1A_2''$	3.753 (0.460)	5.160 (0.064)	5.056	5.067	3.889	5.172 (0.068)	5.048	3.431 (0.486)	5.211 (0.028)	5.079
2E′	3.586 (0.130)	5.095	5.155	5.161	3.613	5.141 (0.001)	5.175	3.385 (0.075)	5.028 (0.004)	5.157
$2A_2''$	4.903 (0.019)	6.715 (0.315)	6.900	6.850	4.908	6.744 (0.265)	6.884	4.773 (0.018)	6.253 (0.487)	6.595
3E′	3.733 (0.005)	5.614 (0.086)	5.821	5.857	3.793	5.680 (0.083)	5.372	3.459 (0.021)	5.389 (0.046)	5.672
4E′	4.040 (0.063)	5.882 (0.031)	5.829	5.868	4.280	5.864 (0.077)	5.882	3.766 (0.055)	5.795 (0.002)	5.806
5E′	5.232 (0.062)	6.243 (0.069)	6.601	6.575	4.884	6.047 (0.071)	6.418	5.066 (0.037)	6.020 (0.017)	6.380
6E′	5.765 (0.164)	6.374 (0.057)	6.650	6.633	5.167	6.226 (0.048)	6.594	5.505 (0.173)	6.052 (0.015)	6.578

It can be concluded from the above results that geometrical effects of the one-photon absorption spectrum of $Fe(CO)_5$ are minimal as are the effects caused by increasing the size of the basis set. This means that results produced using a modestly sized basis set and a coupled cluster optimized geometry can be analyzed here with confidence.

The experimental spectrum of $Fe(CO)_5$ contains few clear spectral features as already discussed in section 3.1. From the results obtained here, the low energy part of the spectrum contains three main states with reasonable oscillator strength, namely 1E′, $1A_2''$ and 2E′. The 1E′ state was assigned by a previous study from 1999 [2] as a LF state while the other two were thought to be MLCT states. The authors of this study reported that states higher in energy than 5.58eV could not be calculated due to convergence problems with the MR-CCI method. It can be seen from tables 3.3, 3.4 and 3.5 that using a more balanced method such as the coupled cluster response methods used here allows states higher in energy to be calculated with little extra difficulty. It can also be seen from these tables that there is a large density of states within the investigated spectral range. To illustrate these points table 3.6 presents all excited states calculated with the coupled cluster response methods with the ANO-S, ANO-M and ECP basis (with the CCSD optimized geometry) sets along with the previously reported CASSCF, MR-CCI and CASPT2 results [2, 16].

The low energy part of the spectrum is reproduced quite well by coupled cluster methods with the $1A_2''$ and 2E′ states present and both have reasonably large oscillator strengths. These MLCT states were thought to correspond to a shoulder at 4.43eV, and a band at 5.16eV in the experimental spectrum respectively from the 1999 MR-CCI study, and in this study the former state is of lower excitation energy than the latter. Here it is found that it is the other way round with the experimental band at 5.16eV corresponding to the $1A_2''$ state and the shoulder at 4.43eV corresponding to 2E′. The CCSD methods, both linear response and equation of motion, very accurately match this experimental band to this state. The value of excitation energy of the 2E′ state is slightly higher than it should be but can still correspond to this shoulder in the spectrum. The lowest energy shoulder in the experimental spectrum at 3.72eV that is of weak intensity is thought to correspond to the LF 1E′ state. This state is indeed calculated to be a LF state but at all levels of coupled cluster theory shows little or zero oscillator strength. This would be expected as the state would be formally forbidden but could show some oscillator strength through vibronic coupling, or an intensity borrowing mechanism if the state is nearly degenerate to an allowed state. The excitation energy of this state with both coupled cluster methods and the CCR(3) method is also slightly higher than reported for the experimental spectrum. The CC2 method produces better values for this

state but not for the previous two states discussed that could comprise features of the experimental spectrum. These two states are approximately 1eV lower than observed in the experimental spectrum or the other coupled cluster methods. To calculate the value of this first LF state CASSCF has been used with a CAS(8,10) active space already detailed in section 3.1 and used in chapter 8 to measure the excitation energy.

Table 3.6 All excited states calculated using the coupled cluster response methods using the ANO-S, ANO-M and ECP basis sets with the CCSD optimized geometry. The table is ordered by state symmetry and oscillator strengths where available are included in brackets. Previous CASSCF, MR-CCI and CASPT2 results from [2, 16] are included for comparison.

State	CC2 (ANO-S)	CC2 (ECP)	CCSD (ANO-S)	CCSD (ECP)	CCR(3) (ANO-S)	CCR(3) (ECP)	CCR(3) (ANO-M)	CASSCF [2]	MR-CCI [2]	CASPT2 [16]
1E´	3.342 (0.118)	3.189 (0.155)	4.384 (0.000)	4.290 (0.000)	4.415	4.336	4.223	4.04	3.55	4.42
1E´´	3.366	3.241	4.737	4.579	4.925	4.607	4.898	4.41	4.55	5.27
$1A_1$´	3.441	3.286	5.608	5.490	5.664	5.627	5.675	5.44	5.58	
$1A_1$´´	4.144	3.868	4.574	4.598	4.724	4.768	4.740	4.33	4.12	
$1A_2$´	3.447	3.324	5.051	5.013	5.093	5.105	5.079	4.69	4.71	
$1A_2$´´	3.753 (0.460)	3.431 (0.486)	5.160 (0.064)	5.211 (0.028)	5.056	5.079	5.067	4.86 (0.01)	4.59 (0.01)	
2E´	3.586 (0.130)	3.385 (0.075)	5.095 (0.000)	5.028 (0.004)	5.155	5.157	5.161	4.74 (0.006)	4.87 (0.006)	4.94
2E´´	4.090	3.809	5.142	4.674	5.104	4.937	4.922	4.53	4.40	
$2A_1$´	5.515	5.245	6.009	5.848	6.074	6.068	6.069			
$2A_1$´´	5.012	4.897	6.200	5.704	6.423	6.071	6.413			
$2A_2$´	5.791	6.881	5.669	5.848	5.679	5.706	5.720			
$2A_2$´´	4.903 (0.019)	4.773 (0.018)	6.715 (0.351)	6.253 (0.487)	6.900	6.595	6.850			
3E´	3.733 (0.005)	3.459 (0.021)	5.614 (0.086)	5.389 (0.046)	5.821	5.672	5.857			
3E´´	4.400	3.926	5.287	5.226	5.328	5.266	5.356	5.19	5.28	
$3A_1$´	5.824	6.046	8.426	7.861	8.344	7.912	8.275			
$3A_1$´´	7.186	6.631	6.790	6.378	6.890	6.626	6.926			
$3A_2$´	6.924	7.668	6.167	5.873	6.342	5.954	6.313			

$3A_2''$	6.726 (0.162)	5.521 (0.001)	7.155 (0.068)	6.717 (0.054)	7.173	6.855	7.194			
4E′	4.04 (0.063)	3.766 (0.055)	5.882 (0.031)	5.795 (0.002)	5.829	5.806	5.868			
4E′′	4.454	4.137	6.259	5.731	6.469	6.064	6.474			
$4A_1'$	7.166	8.014	8.494	8.571	10.462	8.385	8.388			
$4A_1''$	7.740	7.812	6.875	6.685	6.935	6.761	6.937			
$4A_2'$	7.208	8.557	8.436	7.862	8.385	7.932	8.400			
$4A_2''$	7.415 (0.134)	6.562 (0.219)	7.281 (0.115)	7.172 (0.087)	7.216	7.113	7.228			
5E′	5.232 (0.062)	5.066 (0.037)	6.243 (0.069)	6.020 (0.017)	6.601	6.380	6.575			
5E′′	4.999	4.874	6.759	6.163	6.987	6.515	7.009			
$5A_1'$	8.213	8.673	10.327	10.338	-	10.170	10.468			
$5A_1''$	9.055	8.498	10.098	10.027	9.990	9.913	10.102			
$5A_2'$	8.125	-	9.790	10.248	10.137	9.916	10.106			
$5A_2''$	7.730	6.631	10.100	9.934 (0.249)	10.001	10.050	10.267			
6E′	5.765 (0.164)	5.505 (0.173)	6.374 (0.057)	6.052 (0.015)	6.650	6.578	6.633			
6E′′	6.835	6.826	7.068	6.930	6.995	7.246	7.026			
$6A_1'$	-	-	-	-	-	-	-			
$6A_1''$	-	9.095	-	-	-	9.916	-			
$6A_2'$	-	-	-	-	-	10.111	-			
$6A_2''$	-	7.864	-	-	-	10.347 (0.247)	-			
7E′	7.056 (0.060)	6.984 (0.034)	6.950 (0.344)	6.557 (0.485)	7.060	6.659	7.064			
7E′′	6.975	8.025	7.428	6.945	7.494	7.484	7.446			
$7A_1'$	-	-	-	-	-	-	-			
$7A_1''$	-	9.138	-	-	-	10.050	-			
$7A_2'$	-	-	-	-	-	-	-			
$7A_2''$	-	8.490 (0.246)	-	-	-	-	-			
8E′	7.291	7.777	8.397	7.831	8.365	7.910	8.383			

	(0.072)	(0.001)	(0.133)	(0.181)						
8E′′	7.152	8.649	7.608	7.157	8.025	-	7.997			
$8A_1'$	-	-	-	-	-	-	-			
$8A_1''$	-	-	-	-	-	-	-			
$8A_2'$	-	-	-	-	-	-	-			
$8A_2''$	-	8.971 (0.721)	-	-	-	-	-			
9E′	7.498 (0.0001)	8.103 (0.300)	10.025 (0.0004)	10.166 (0.016)	10.064	10.243	10.163			
9E′′	7.385	-	9.456	10.022	9.720	-	9.635			
$9A_2''$	-	-	-	-	-	-	-			
10E′	8.068 (0.019)	8.494 (0.002)	10.207 (0.003)	10.340 (0.135)	10.293	10.434	10.260			
10E′′	7.791	-	10.062	10.160	9.979	-	10.001			

Because only the first d-d excitation energy is being calculated then a CASSCF active space of CAS(8,10) is suitable and should be reasonably accurate, but bigger active spaces would be required to study MLCT states thus highlighting the fact that multireference methods can be unbalanced when dealing with excited states of transition metal complexes. With the experimental geometry the excitation energy to the first LF state was 3.86eV and 3.94eV with the coupled cluster optimized geometry. Both of these values are in good agreement with the experimental shoulder at 3.72eV. This shows that the coupled cluster methods are still reasonable for this first LF state, but CASSCF in this example provides a better description. The last experimental feature from the experimental spectrum was an intense MLCT band at 6.20eV. According to the results presented here this band is assigned to the $2A_2''$ state. This band could not be characterized for $Fe(CO)_5$ in previous CASSCF studies already discussed due to the limitations in the number of states that could be calculated and convergence problems. The 3E′, 4E′, 5E′, and 6E′ states all have reasonably sized oscillator strengths with the CCSD methods, of the same magnitude as the $1A_2''$ transition that is thought to correspond to a band lower in energy already discussed. However, the $2A_2''$ MLCT state dominates the higher energy part of the spectrum with an oscillator strength one order of magnitude higher than these earlier transitions. The

number of degenerate allowed states throughout the investigated energy range shows potential opportunities to look at different photochemical pathways in $Fe(CO)_5$. These different degenerate states could couple to non-totally symmetric vibrations and distort $Fe(CO)_5$ leading to multiple concerted CO ligand loss. Indeed the density of states around these allowed states also shows the possibility for mechanisms such as internal conversion to states near in energy to occur. One such photochemical pathway will be discussed in chapter 8.

Concentrating on the allowed states that appear in the experimental spectrum also allows for a comparison between the coupled cluster methods themselves as to how well they can predict the one-photon spectrum and the other forbidden electronic states of $Fe(CO)_5$. It can be seen from the previous tables 3.3-3.6 that the excitation energies calculated with the CC2 method are generally red-shifted compared to the CCSD methods and the CCR(3) method blue-shifts excitation energies compared to the CCSD methods, but much less so than CC2 red-shifts excitation energies. Although both CCSD methods fail to very accurately model the lowest LF state of the spectrum other allowed states are in reasonable agreement with the other experimental features. Both LR-CCSD and EOM-CCSD methods return similar excitation energies for each state, which is expected, and while the oscillator strengths of these two methods should be different, and they are, the relative magnitudes of the allowed states are in reasonable agreement. From these results it can be concluded that the CCSD methods are the best of the coupled cluster methods to be used for this system out of the coupled cluster methods used here. For the CC2 method, even though it produced a good description for the first LF state of the system, the degree of red-shifting compared to the CCSD methods and even CCR(3) makes this method unsuitable for spectroscopic studies for this complex. It will be shown in the next chapter that the CC2 method does an even worse job in predicting the electronic spectra of $Cr(CO)_6$ and $Ni(CO)_4$. Although CCR(3) is theoretically more accurate, the oscillating convergence of this method is often observed. Thus, CCSD returns the best estimate for the experimental findings and also provides here the best computational cost/accuracy balance.

Perhaps the most popular range of methods that have been used to study the electronic structure of molecules are the density functional theory (DFT) methods. Their success in theoretical chemistry is well known, including the time-dependent (TD-DFT)

version for the study of electronic excited states. But a key weakness of TD-DFT methods is their failure to predict charge transfer states accurately. Charge transfer states are prevalent in transition metal complexes. Attempts have been made in recent years to develop TD-DFT functionals to describe charge transfer states accurately, and here one such method is used to see if DFT methods can accurately predict the electronic excited states of $Fe(CO)_5$. The DFT functional used here is the CAM-B3LYP functional of Handy and co-workers [32]. This method uses variable ratios of either Becke (B88) exchange or HF exchange depending on the interelectronic distance. These two types of exchange are respectively better for short- and long-range exchange. By comparison the TD-B3LYP functional does not change the ratio of B88 and HF exchange keeping a larger amount of B88 exchange so not enough long-range HF exchange is included to account for charge transfer states. Table 3.7 presents selected excited states and oscillator strengths where applicable calculated using the CAM-B3LYP functional compared with LR-CCSD results.

It can be seen from table 3.7 that differences between the CAM-B3LYP results with different geometries are very small just as with the coupled cluster methods. This reinforces the conclusion from earlier that geometrical effects are minimal. The CAM-B3LYP method also returns accurate values for the first 1E′ state that is in good agreement with experiment, indeed closer to experiment than LR-CCSD. The other allowed states are also in good agreement with the experimental values. The ordering of the allowed states is slightly different to the coupled cluster results, and agrees with the CASSCF/MR-CCI results of Rubner and co-workers [2].

Table 3.7 Selected electronic excited states of $Fe(CO)_5$ with oscillator strengths in brackets where applicable with the CAM-B3LYP density functional with both CCSD optimized and experimental geometries. LR-CCSD results with the CCSD optimized geometry and large ANO basis set are included for comparison.

State	CAM-B3LYP (CCSD geometry)	CAM-B3LYP (Exp geometry)	LR-CCSD (CCSD geometry)
1E′	3.876 (0.0001)	3.818 (0.000)	4.332 (0.000)
1E″	4.121	4.094	4.782
$1A_2''$	4.320 (0.055)	4.276 (0.051)	5.172 (0.068)

2E′	4.601 (0.023)	4.496 (0.030)	5.141 (0.001)
$2A_2''$	6.122 (0.045)	6.023 (0.046)	6.744 (0.265)
3E′	5.317 (0.025)	5.279 (0.024)	5.680 (0.083)
4E′	5.524 (0.074)	5.492 (0.078)	5.864 (0.044)
5E′	5.899 (0.050)	5.885 (0.048)	6.047 (0.081)
6E′	6.562 (0.022)	6.447 (0.026)	6.408 (0.005)

Here the $1A_2''$ state calculated with CAM-B3LYP is very close in energy to the shoulder at 4.43eV in the experimental spectrum and the intense shoulder at 5.17eV should relate to the 3E′ transition as the 2E′ transition with CAM-B3LYP is too low in energy. The intense band at 6.20eV assigned to the $2A_2''$ is however present and is also in good agreement with the experimental spectrum. The other allowed MLCT states, which are all states in table 3.7 apart from the LF 1E′, 1E″ and 4E′ states, compare well with LR-CCSD showing that in this case the CAM-B3LYP is successful in calculating the one-photon absorption electronic spectrum of a transition metal carbonyl complex.

What can be said from the application of both DFT and coupled cluster methods is that effects of basis set and geometry on the spectrum are minimal and that there is a large density of states within the investigated spectral range of which MLCT states dominate. The coupled cluster method which gave best results in this case is the CCSD method, either LR-CCSD or EOM-CCSD. CAM-B3LYP has also been shown to predict the spectrum with a good agreement with experiment and with CCSD methods. Care must be taken when using the CC2 method or the CCR(3) method that respectively red and blue shift the excitation energies of most states compared to the CCSD methods, though the CC2 method red shifts the excitation energies to a greater extent than the CCR(3) method blue shifts. This is the first time coupled cluster methods and the CAM-B3LYP density functional method have been applied to the one-photon electronic absorption spectrum of $Fe(CO)_5$ and while the spectrum has a great number of different states in a small spectral range, all the main spectral features can be accounted for with each method, albeit with a slight discrepancy between the CAM-B3LYP and CCSD methods for the first MLCT band shoulder of the experimental

spectrum. In this instance the assignments of the coupled cluster method are preferred over DFT and the CASSCF/MR-CCI study due to the problems with convergence reported for CASSCF/MR-CCI and the need to specify a different active space to describe each state of interest, making the method unbalanced.

3.4 Two-photon absorption spectrum

The two-photon electronic absorption spectrum, as already discussed above, has not been fully investigated so far. Two-photon excitation of $Fe(CO)_5$ could be interesting as higher excited states could be probed by using two-photons of quite low energy instead of one-photon of high energy. Populating these states could cause different photochemistry to occur. Two-photon absorption has already been used to trigger the photodissociation of $Fe(CO)_5$ by exciting a state at 6.20eV using two photons of 3.10eV in energy [27]. The selection rules are different from a one-photon excitation to a two-photon excitation as states of A_1', E′ and E″ symmetry are allowed, so there may be more spectral detail than the one-photon spectrum and there could also be some spectral overlap due to E′ symmetry states being allowed for both spectra. As will also be discussed in the next chapter the difference between the two methods is a subtle one due to the spectral overlap and ultrafast photodissociation occurring from both one- and two- photon absorption. The two-photon spectrum of $Fe(CO)_5$ using the quadratic response CCSD (QR-CCSD) method with the large ANO basis set and both CCSD optimized and experimental geometries are presented in table 3.8.

What is immediately apparent from the results in table 3.8 is that there are many allowed states that exhibit a significant δ^{TPA} value. This means that the two-photon spectrum may be rich in detail, and be as complex as the one-photon absorption spectrum. The values for the excitation energies are unchanged from LR-CCSD, but the allowed states are different and on the whole do not change by a large degree with the different geometries, showing that geometrical effects for the two-photon spectrum are minimal just like the one-photon spectrum. There is also a great degree of spectral overlap between one- and two-photon spectra as the E′ symmetry states 2E′-6E′ both

have an significant oscillator strength and δ^{TPA} value. The number of allowed degenerate states available with two-photon excitation means it could be possible to directly excite into a manifold of MLCT states which could cause Jahn-Teller distortions by coupling to non-totally symmetric vibrations or internal conversion to other states close in energy to occur. From these results the state populated by Bañares and co-workers is the $2A_1'$ MLCT state although with the QR-CCSD method the excitation energy value is slightly lower than that energy by 0.2eV. Other allowed states close to 6.20eV are the 4E″ and 6E′ MLCT states. These both have lower δ^{TPA} values but could have an influence on the excitation or the initial process after excitation.

Table 3.8 Selected two-photon absorption electronic excited states of $Fe(CO)_5$ calculated using the QR-CCSD method with the large ANO basis sets and both CCSD optimized and experimental geometries.

		CCSD optimized geometry		**Experimental geometry**	
State	**Character**	**Excitation Energy/eV**	**δ^{TPA}/au**	**Excitation Energy/eV**	**δ^{TPA}/au**
1E′	LF dx^2-y^2,dxy - 4p	4.332	0.048	4.296	0.038
1E″	LF dxz,dyz – Fe 4p antibonding	4.782	1.615	4.747	0.920
$1A_2'$	MLCT dx^2-y^2,dxy - CO bonding SALC	5.076	0.000	4.962	0.000
2E″	MLCT dx^2-y^2,dxy - CO bonding SALC/antibonding SALC 40%	5.116	1.438	5.085	1.806
2E′	MLCT dx^2-y^2,dxy - CO bonding SALC	5.141	1.707	5.057	0.850
$1A_2''$	MLCT dx^2-y^2,dxy - CO bonding SALC	5.172	0.000	5.119	0.000
3E″	MLCT dxz,dyz - CO antibonding SALC	5.330	24.479	5.293	27.675
3E′	MLCT dx^2-y^2,dxy - CO bonding SALC 15%/antibonding SALC 48%	5.680	41.665	5.633	65.991

$1A_1'$	MLCT dx^2-y^2,dxy - CO antibonding SALC	5.687	195.312	5.637	177.683
4E′	LF dx^2-y^2,dxy - Fe 4s antibonding 53%/4p antibonding 10%	5.864	29.345	5.786	25.212
5E′	MLCT dx^2-y^2,dxy - CO bonding SALC 33%/antibonding SALC 33%	6.047	9.526	5.919	9.108
$2A_1'$	MLCT dxz,dyz - CO antibonding SALC	5.983	67.869	5.930	89.698
4E″	MLCT dxz,dyz - CO bonding 44%/antibonding 44% SALC	6.347	1.581	6.313	1.561
6E′	MLCT dxz,dyz - CO bonding 39%/antibonding 44% SALC	6.408	11.940	6.395	11.596
$3A_2''$	MLCT dx^2-y^2,dxy - CO bonding SALC	7.163	1.005	7.121	0.530
5E″	MLCT dxz,dyz - CO antibonding SALC	6.836	0.049	6.762	110.727
6E″	MLCT dx^2-y^2 – CO SALC 71%, LF dxz,dyz – Fe 4s antibonding 29%	6.878	11.940	6.840	6.342

The spectrum is dominated by the $1A_1'$ MLCT transition that has a large δ^{TPA} value. This is the first time the two-photon absorption spectrum has been studied theoretically. As already mentioned the character of the states are very mixed making total analysis of the spectrum a difficult task, especially when states have both MLCT and LF character (e.g. 6E″). However there is enough detail here to establish that the two-photon absorption spectrum looks promising for future study due to the rich detail in the number of allowed states and the large amount of overlap with the one-photon

spectrum and the possibility of a two-photon experiment to probe excited states higher up in energy. The one- and two-photon spectra are shown graphically in figure 3.4.

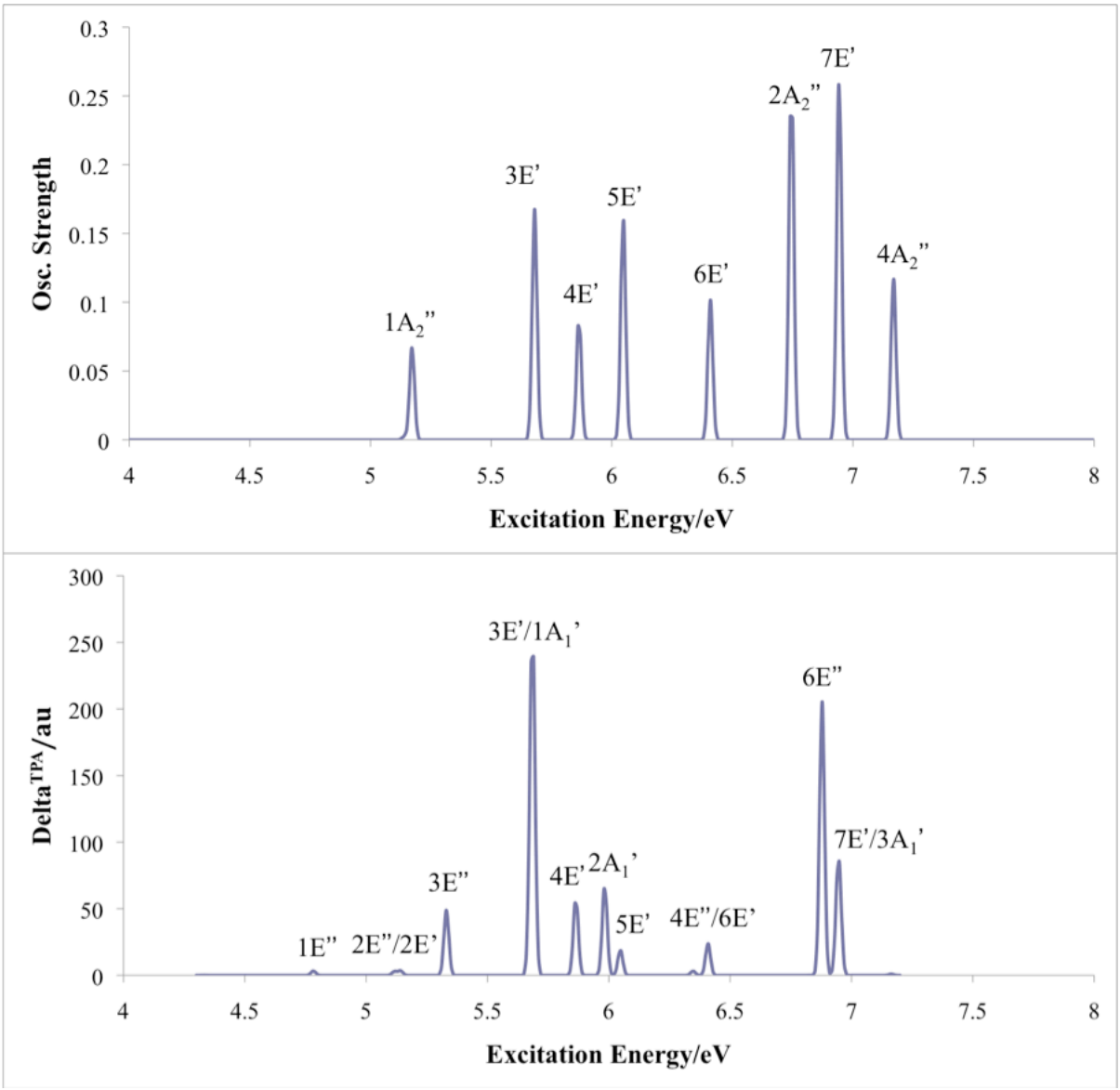

Figure 3.4 The one-photon (top) and two-photon (bottom) electronic absorption spectra of $Fe(CO)_5$ using the LR-CCSD and QR-CCSD methods respectively and the large ANO basis set and CCSD optmised geometry. Where a (/) is used this means one spectral peak is made up of more than one state. Note the scale on the y-axis is for illustrative purposes only, but the size of the peaks relative to each other are correct.

3.5 Conclusions

The one-photon and two-photon electronic absorption spectra of $Fe(CO)_5$ have been reported and analyzed using both coupled cluster and DFT methods along with two different geometries of $Fe(CO)_5$ and a range of basis sets of increasing size. $Fe(CO)_5$ is a challenging system to study with research groups in the past reporting failures in their methods to produce accurate excitation energies [2, 15] and a large density of excited states of different chemical character within a small energy range. This is the first time that highly correlated methods such as coupled cluster response and equation of motion coupled cluster response methods have been used to study the electronic spectroscopy of $Fe(CO)_5$. This is also the first time the two-photon electronic absorption spectrum has been studied at all theoretically for $Fe(CO)_5$. There have been few theoretical studies reported studying the electronic spectroscopy of $Fe(CO)_5$ compared to other metal carbonyls such $Cr(CO)_6$ (this system will be discussed in the next chapter and even then there are not many theoretical spectroscopic studies reported for this system). This is indicative of the difficulty involved in studying the excited states of transition metal complexes. The mixed character of the excited states further justifies the level of complexity with some showing complex MLCT and LF character showing that state mixing is essential in any theoretical treatment, indeed the reduced symmetry compared to octahedral $Cr(CO)_6$ allows for mixing at the orbital level, and so mixing at the configurational level and therefore mixing at the state level. For the one-photon spectrum the excited states have been matched with features in the experimental spectrum and the results of previous studies, showing good agreement between these new results and the experimental spectrum.

The differences in the results using different geometries or basis sets are minimal and it was found that the best of the coupled cluster methods used here were either of the CCSD methods. This was because the CC2 method red shifts the position of the excited states compared to the CCSD methods, in most cases by over 1eV, making this method unsuitable for spectroscopic study for this complex. The effect of perturbative triples corrections to the CCSD method was investigated using the CCR(3) method and this was found to slightly blue shift the excitation energies compared to the CCSD methods. This effect is quite small and this method can be used to study triply

excited configurations with caution. The CAM-B3LYP density functional was used to see if this method could accurately describe charge transfer states in this system and in general it was shown to be successful.

The two-photon electronic absorption spectrum was produced theoretically for the first time using the quadratic response CCSD (QR-CCSD) method. This spectrum was shown to be rich in spectral detail and had some overlap with the one-photon spectrum evident because states of E′ symmetry are allowed in both spectra. According to the literature this is the first time in over ten years that the electronic spectroscopy of $Fe(CO)_5$ has been studied theoretically, and highly correlated methods and large basis sets can be successfully applied shedding new light on the nature of the excited states and features in the experimental spectrum. Also that DFT methods can be successful in describing the electronic spectrum of such a transition metal complex due to improvements in functionals for the treatment of charge transfer states.

3.6 References

[1] Trushin, S. A.; Fuss, W.; Schmid, W. E., Conical intersections, pseudorotation and coherent oscillations in ultrafast photodissociation of group-6 metal hexacarbonyls. *Chem. Phys.* **2000,** 259, 313-330.

[2] Rubner, O.; Engel, V.; Hachey, M. R.; Daniel, C., A CASSCF/MR-CCI study of the excited states of $Fe(CO)_5$. *Chem. Phys. Lett.* **1999,** 302, 489-494.

[3] Mond, L.; Quincke, F., Note on a volatile compound of iron with carbonic acid. *J. Che. Soc., Trans.* **1891,** 59, 604-607.

[4] Mond, L.; Langer, C., On iron carbonyls. *J. Chem. Soc., Trans.* **1881,** 59, 1090-1093.

[5] Ewens, R. V. G.; Lister, M. W., The structure of iron pentacarbonyl, and of iron and cobalt carbonyl hydrides. *Trans. Faraday. Soc.* **1939,** 35, 681-691.

[6] Hanson, A. W., The crystal structure of iron pentacarbonyl. *Acta Crystallographica* **1962,** 15, 930-933.

[7] Donohue, J.; Caron, A., The crystal structure of iron pentacarbonyl: Space group and refinement of the structure *Acta Crystallographica* **1964,** 17, 6.

[8] Sheline, R. K.; Pitzer, K. S., The infrared spectra and structures of the iron carbonyls. *J. Am. Chem Soc.* **1950,** 72, 1107-1112.

[9] Swanson, B. I.; Jones, L. H.; Ryan, R. R., Infrared-spectrum of $Fe(CO)_5$ in rare-gas matrices. *J. Mol. Spectrosc.* **1973,** 45, 324-325.

[10] Seder, T. A.; Ouderkirk, A. J.; Weitz, E., The wavelength dependence of excimer laser photolysis of $Fe(CO)_5$ in the gas-phase - transient infrared-spectroscopy and kinetics of the $Fe(CO)_4$, $Fe(CO)_3$, $Fe(CO)_2$ photofragments. *J. Chem. Phys.* **1986,** 85, 1977-1986.

[11] Kotzian, M.; Rosch, N.; Schroder, H.; Zerner, M. C., Optical spectra of transition-metal carbonyls - $Cr(CO)_6$, $Fe(CO)_5$ and $Ni(CO)_4$. *J. Am. Chem Soc.* **1989,** 111, 7687-7696.

[12] Hubbard, J. L.; Lichtenberger, D. L., The Jahn-Teller effect in the photoelectron-spectrum of iron pentacarbonyl. *J. Chem. Phys.* **1981,** 75, 2560-2568.

[13] Daniel, C.; Benard, M.; Dedieu, A.; Wiest, R.; Veillard, A., Theoretical aspects of the photochemistry of organometallics 3. Potential-energy curves for the photodissociation of $Fe(CO)_5$. *J. Phys. Chem.* **1984,** 88, 4805-4811.

[14] Veillard, A.; Strich, A.; Daniel, C.; Siegbahn, P. E. M., A CASSCF study of the lowest excited states of $HMn(CO)_5$ and $Fe(CO)_5$. *Chem. Phys. Lett.* **1987,** 141, 329-333.

[15] Marquez, A.; Daniel, C.; Sanz, J. F., The vacuum-ultraviolet spectrum of $Fe(CO)_5$ - an experimental analysis supported by a CASSCF-CCI study of the Rydberg states. *J. Phys. Chem.* **1992,** 96, 121-123.

[16] Persson, B. J.; Roos, B. O.; Pierloot, K., A theoretical-study of the chemical bonding in M(CO)(X) (M=Cr, Fe, and Ni). *J. Chem. Phys.* **1994,** 101, 6810-6821.

[17] Leadbeater, N., Enlightening organometallic chemistry: The photochemistry of $Fe(CO)_5$ and the reaction chemistry of unsaturated iron carbonyl fragments. *Coord. Chem. Rev.* **1999,** 188, 35-70.

[18] Ben Arnor, N.; Villaume, S.; Maynau, D.; Daniel, C., The electronic spectroscopy of transition metal carbonyls: The tough case of $Cr(CO)_6$. *Chem. Phys. Lett.* **2006,** 421, 378-382.

[19] van Gisbergen, S. J. A.; Groeneveld, J. A.; Rosa, A.; Snijders, J. G.; Baerends, E. J., Excitation energies for transition metal compounds from time-dependent density functional theory. Applications to MnO_4^-, $Ni(CO)_4$, and $Mn_2(CO)_{10}$. *J. Phys. Chem. A* **1999,** 103, 6835-6844.

[20] Jonas, V.; Thiel, W., Theoretical study of the vibrational spectra of the transition metal carbonyls $M(CO)_6$ [M=Cr, Mo, W], $M(CO)_5$ [M=Fe, Ru, Os] and $M(CO)_4$ [M=Ni, Pd, Pt]. *J. Chem. Phys.* **1995,** 102, 8474-8485.

[21] Trushin, S. A.; Fuss, W.; Kompa, K. L.; Schmid, W. E., Femtosecond dynamics of $Fe(CO)_5$ photodissociation at 267 nm studied by transient ionization. *J. Phys. Chem. A* **2000,** 104, 1997-2006.

[22] de Meras, A.; Cuesta, I. G.; Koch, H., A coupled cluster calculation of the spectrum of urea. *Chem. Phys. Lett.* **2001,** 348, 469-476.

[23] Christiansen, O.; Koch, H.; Halkier, A.; Jorgensen, P.; Helgaker, T.; deMeras, A. S., Large-scale calculations of excitation energies in coupled cluster theory: The singlet excited states of benzene. *J. Chem. Phys.* **1996,** 105, 6921-6939.

[24] Christiansen, O.; Jorgensen, P., The electronic spectrum of furan. *J. Am. Chem Soc.* **1998,** 120, 3423-3430.

[25] Christiansen, O.; Gauss, J.; Stanton, J. F.; Jorgensen, P., The electronic spectrum of pyrrole. *J. Chem. Phys.* **1999,** 111, 525-537.

[26] Villaume, S.; Strich, A.; Daniel, C.; Perera, S. A.; Bartlett, R. J., A coupled cluster study of the electronic spectroscopy and photochemistry of $Cr(CO)_6$. *Phys. Chem. Chem. Phys.* **2007,** 9, 6115-6122.

[27] Banares, L.; Baumert, T.; Bergt, M.; Kiefer, B.; Gerber, G., Femtosecond photodissociation dynamics of $Fe(CO)_5$ in the gas phase. *Chem. Phys. Lett.* **1997,** 267, 141-148.

[28] Pouamerigo, R.; Merchan, M.; Nebotgil, I.; Widmark, P. O.; Roos, B. O., Density-matrix averaged atomic natural orbital (ANO) basis-sets for correlated molecular wave-functions .3. First row transition-metal atoms. *Theor. Chim. Acta* **1995,** 92, 149-181.

[29] Balabanov, N. B.; Peterson, K. A., Systematically convergent basis sets for transition metals. I. All-electron correlation consistent basis sets for the 3d elements Sc–Zn. *J. Chem. Phys.* **2005,** 123, 064107.

[30] Frisch, M. J. Trucks, G. W.; Schlegel, H. B.; Scuseria, G. E.; Robb, M. A.; Cheeseman, J. R.; Montgomery, Jr., J. A.; Vreven, T.; Kudin, K. N.; Burant, J. C.; Millam, J. M.; Iyengar, S. S.; Tomasi, J.; Barone, V.; Mennucci, B.; Cossi, M.; Scalmani, G.; Rega, N.; Petersson, G. A.; Nakatsuji, H.; Hada, M.; Ehara, M.; Toyota, K.; Fukuda, R.; Hasegawa, J.; Ishida, M.; Nakajima, T.; Honda, Y.; Kitao, O.; Nakai, H.; Klene, M.; Li, X.; Knox, J. E.; Hratchian, H. P.; Cross, J. B.; Bakken, V.; Adamo, C.; Jaramillo, J.; Gomperts, R.; Stratmann, R. E.; Yazyev, O.; Austin, A. J.; Cammi, R.; Pomelli, C.; Ochterski, J. W.; Ayala, P. Y.; Morokuma, K.; Voth, G. A.; Salvador, P.; Dannenberg, J. J.; Zakrzewski, V. G.; Dapprich, S.; Daniels, A. D.; Strain, M. C.; Farkas, O.; Malick, D. K.; Rabuck, A. D.; Raghavachari, K.; Foresman, J. B.; Ortiz, J. V.; Cui, Q.; Baboul, A. G.; Clifford, S.; Cioslowski, J.; Stefanov, B. B.; Liu, G.; Liashenko, A.; Piskorz, P.; Komaromi, I.; Martin, R. L.; Fox, D. J.; Keith, T.; Al-Laham, M. A.; Peng, C. Y.; Nanayakkara, A.; Challacombe, M.; Gill, P. M. W.; Johnson, B.; Chen, W.; Wong, M. W.; Gonzalez, C.; and Pople, J. A. Gaussian 09, Revision A.1, Gaussian, Inc., Wallingford CT, 2009.

[31] Jean, Y., *Molecular orbtials of transition metal complexes*. Oxford University Press: Oxford, 2005.

[32] Yanai, T.; Tew, D. P.; Handy, N. C., A new hybrid exchange-correlation functional using the Coulomb-attenuating method (CAM-B3LYP). *Chem. Phys. Lett.* **2004,** 393, 51-57.

Chapter 4

One- and Two-Photon Electronic Absorption Spectroscopy of $Cr(CO)_6$ and $Ni(CO)_4$

4.1 Introduction and literature review

It has been demonstrated in chapter 3 that coupled cluster response theory can be successfully applied to study both the one-photon and two-photon absorption electron spectroscopy of $Fe(CO)_5$. It is the purpose of this chapter to demonstrate that coupled cluster response theory can be applied to other, more studied, binary carbonyls to gain more information about the excited states of such carbonyls as $Cr(CO)_6$ and $Ni(CO)_4$. These two carbonyl complexes are perhaps the most intensely studied of all the binary carbonyls in terms of the number of reports in the literature relating to them. A large number of such reports concentrate on structure, spectroscopy and reactive photochemistry.

4.1.1 Early experimental structure, spectroscopy and reactive photochemistry studies

Some of the earliest work on these carbonyls was carried out in the 1930s trying to establish their structure, such as the report from 1935 by Rüdalt and Hofmann [1] who used X-ray diffraction to investigate the structures of the hexacarbonyls of chromium, molybdenum and tungsten. This study failed to produce an accurate structure so the structure of these complexes were studied again in 1938 by Brockoway, Ewans and Lister [2] but this time using electron diffraction from a vapour. Both methods produce diffraction patterns and the main difference is that either X-rays or electrons are fired at the system under study to produce the diffraction patterns that can be used for analysis. They concluded that the structure of all three hexacarbonyls was a rectangular octahedron. In 1952 the crystal structure of $Ni(CO)_4$ was reported by Ladell, Post and Frankuchen [3] and a tetrahedral structure was determined with Ni-C bond lengths of 1.84±0.03Å. The crystal structure of $Cr(CO)_6$ was reported in 1967 by Whitaker and Jeffery [4] who found that the structure was indeed an octahedron and that the mean Cr-C bond length was 1.916Å.

Later experimental works concentrated on the photoreactivity of these complexes. It had earlier in 1934 been suggested that the first stage in the photochemistry of these carbonyls was the ejection of a single carbonyl ligand. This

was suggested by Garrat and Thomson [5] when studying the rate of photodecomposition of $Ni(CO)_4$ in the gas and solution phases. As discussed in later chapters, this initial process is accepted today but when first proposed was considered controversial. Further studies looking at the reactive photochemistry of $Ni(CO)_4$ and $Cr(CO)_6$ used methods such as infrared spectroscopy to look at reactive intermediates. Examples of such studies include the paper by Church and co-workers [6] who used flash photolysis of $Cr(CO)_6$ in cyclohexane solution and reported proof of a $Cr(CO)_5$ photoproduct believed to be of C_{4v} symmetry and another similar study but looking at $Cr(CO)_6$ in cyclohexane and saturated with H_2 [7]. IR spectroscopy was also used to try to discount the possibility of the existence of a D_{3h} symmetry $Cr(CO)_5$ reactive intermediate, such as the studies by Graham and co-workers [8], and Black and Braterman [9].

Turner and co-workers produced a series of papers in the mid-1970s [8, 10, 11, 12] looking at the nature of the initial photoproducts of the group 6 hexacarbonyls chromium, molybdenum and tungsten spectroscopically in low temperature matrices. They were one of the first groups to try and study the structures of these pentacarbonyl photoproducts and reasoned that a study in low temperature matrices should produce very sharp bands in the IR spectra making it easier to identify any fine structure. They concluded that these pentacarbonyl species were very matrix sensitive whereby the observed band in the spectrum would change position depending on the type of matrix used, due to the matrix interacting with the coordination hole created by the loss of the CO ligand. They further concluded that the structure of this pentacarbonyl intermediate had C_{4v} symmetry but the authors mentioned that there could also be another stable structure of this pentacarbonyl intermediate of D_{3h} symmetry formed from the C_{4v} photoproduct. Other types of early spectroscopic studies on either $Cr(CO)_6$ or $Ni(CO)_4$ used ultraviolet (UV) or electronic spectroscopy. These investigations were important because they tried to establish the nature of the excited states and therefore the types of electronic transitions that dictate the reactive photochemistry. Perhaps the best-known work in this area was carried out by Gray and co-workers in the 1960s which includes a paper from 1963 in which Beach and Gray [13] investigated the electronic structure and bonding of octahedral metal hexacarbonyls and hexacyanides. They used qualitative molecular orbital theory to try and rationalise the spectroscopic results for these hexacarbonyls. This was the first time such as study had been attempted, and they also

tried to generalise the molecular orbital structure for such species. They proposed a molecular orbital energy scheme for these carbonyls, and discussed the different types of states present in the spectra of these carbonyls such as metal centred or ligand field (LF) states, metal-to-ligand charge transfer (MLCT), states and assigned these types of states to different bands in the spectrum. Most significantly for the reactive photochemistry and the discussions in chapters 6, 7 and 8 they believed that the observed dissociation of a carbonyl ligand took place on a LF state. This was because the $6e_g$ orbital between metal and ligand was thought to be antibonding from qualitative MO theory. To confirm this the authors irradiated at a wavelength on the spectrum corresponding to a shoulder on an MLCT band, which they assigned to this dissociative LF state, and CO loss was indeed observed. The LF was thus thought to be observed on the spectrum as a weak intensity shoulder, and whilst formally Laporte forbidden effects such as vibronic interactions can cause this selection rule to break down, destroying the inversion centre at short timescales with respect to non-totally symmetric vibrations thereby making LF states accessible but with weak intensity. Further papers also supported the conclusions of the authors for these carbonyls [14, 15].

4.1.2 Early theoretical structure, spectroscopy and reactive photochemistry studies

Some of the earliest theoretical studies on these carbonyl complexes investigated the molecular orbital ordering and character. Methods used included semi-empirical theory such as the paper by Schreiner and Brown [16] looking at molecular orbitals of $Cr(CO)_6$, $Fe(CO)_5$ and $Ni(CO)_4$. They discussed the importance of 3d and 4s orbitals in bonding of these carbonyls and constructed a partial molecular orbital diagram for each carbonyl. However their spectroscopic assignments were not in agreement with the experimental work of Beach and Gray mentioned earlier in that they assigned a low energy low intensity shoulder of an MLCT transition as another MLCT transition and not a $t_{2g} \rightarrow e_g$ LF one.

Many theoretical studies from the early part of this century and final decade of the last that looked at the structure of these two carbonyls used single reference methods such as density functional theory, MP2 or CCSD(T) methods which were found to be quite accurate for bond lengths [17] with relativistic effects becoming more important

for the M-L bond lengths of second and third row transition metals. As well as structure other energetic features were also investigated such as the first dissociation energies by Ehlers and Frenking [18] calculated in 1993. MP2 was used to optimise the ground state geometries with the CCSD(T) method then used to calculate the energetics, which were in agreement with an experimental investigation carried out by Lewis and co-workers [19] using laser pyrolysis. A similar treatment was performed in $Ni(CO)_4$ by Rosch and co-workers [20] who performed both an experimental and theoretical study. Investigations like these showed that to achieve accurate geometry optimisation and quantitative energetics for these carbonyls quite highly correlated methods must be used.

Time dependent DFT (TD-DFT) methods have also been used to study the electronic excited states of these complexes such as the studies by van Gisbergen and co-workers [21, 22] but no solid conclusions could be established because of the sensitivity of the results to the type of functional used. The efficiency of TD-DFT methods compared to ab initio methods was described as an advantage, but the method sometimes supported one ab initio method, or another, or none at all. This showed that TD-DFT methods might be computationally cheaper to use but care must be taken when selecting a suitable functional and analysing the results. This is the reason why no new TD-DFT results will be presented here, and also links to the TD-DFT results in chapter 3 where one functional might give a good answer like the CAM-B3LYP results with $Fe(CO)_5$, while another functional might give a different answer like those results discussed above by van Gisbergen.

$Cr(CO)_6$ and $Ni(CO)_4$ are two of the most studied binary carbonyls, and indeed transition metal complexes, so the work highlighted above gives a snapshot of some of the work that has been performed over the last eighty years on these two carbonyls in terms of structure, spectroscopy and photoreactivity. The more modern experimental and theoretical photoreactivity studies performed on these carbonyls that were briefly mentioned in section 1.2, and which have fuelled the on-going interest in these carbonyls will be discussed in chapters 6-8 in relation to the ultrafast relaxation of other metal carbonyls. For the topic of discussion in this chapter will focus on modern electronic spectroscopy studies of both $Ni(CO)_4$ and $Cr(CO)_6$.

4.1.3 Modern theoretical studies of electronic spectroscopy

The one-photon electronic absorption spectra of $Cr(CO)_6$ and $Ni(CO)_4$ share some properties with that of $Fe(CO)_5$ in that they are broad with few clear features, and a large density of states of different chemical character within the investigated spectral range. This is a challenge for computational chemists because there could be many electronic transitions in a given band. The number of theoretical studies using a wide range of methodologies is testament to the scale of the challenge.

The experimental near-UV gas-phase spectra of both $Cr(CO)_6$ and $Ni(CO)_4$ [23] are reported by Kotzian and co-workers and reproduced in figure 4.1.

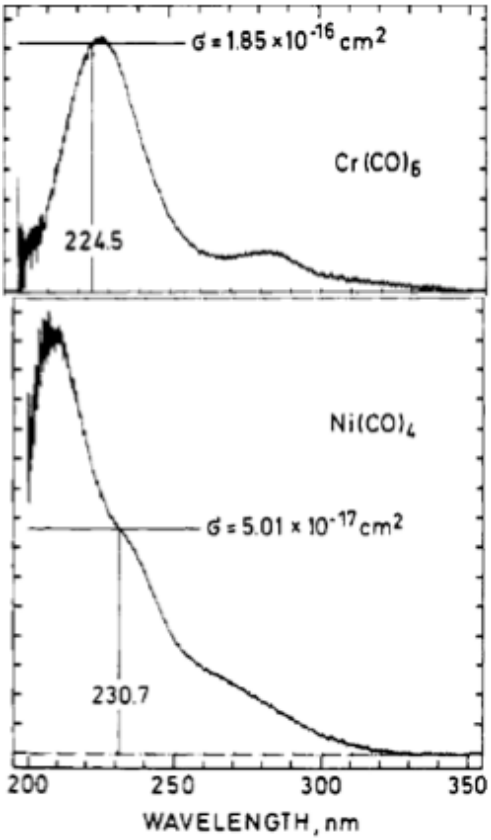

Figure 4.1 Gas phase near-UV electronic absorption spectra of $Cr(CO)_6$ and $Ni(CO)_4$ modified from the paper by Kotzian and co-workers [23]. The units of intensity are arbitrary.

Over the years many different theoretical methods have been applied to these complexes to try and resolve their electronic spectra and determine the character of their excited states. Methods that have been attempted include the INDO/S method [23],

symmetry adapted cluster configuration interaction (SAC-CI) [24], CASSCF/CASPT2 [25], TD-DFT [22, 26] and most recently EOM-CCSD/STEOM-CCSD [27] with some methods giving conflicting results. The most recent theoretical study of $Cr(CO)_6$ [27] showing that there is a shoulder in the lowest part of the spectrum at 3.92eV which was assigned the $^1A_{1g} \rightarrow {}^1T_{2u}$ MLCT transition which was of weak intensity, with two other absorption bands of stronger intensity at 4.37 and 5.20eV, which were assigned to $^1A_{1g} \rightarrow {}^1T_{1u}$ MLCT transitions. These two strong intensity bands dominate the experimental spectrum with little other clear detail. The experimental spectrum of $Ni(CO)_4$ [16, 23] is equally lacking in detail with few absorption bands visible though this can be better explained with respect to $Cr(CO)_6$ because only $^1A_1 \rightarrow {}^1T_2$ MLCT transitions are allowed because nickel has a filled 3d orbital shell. Both gas and solution phase spectra contain one broad intense band at 6.0eV with shoulders slightly lower in energy at 5.5 and 5.2eV in solution and 5.4 and 4.6eV in the gas phase. All of these transitions are thought to be $^1A_1 \rightarrow {}^1T_2$ MLCT transitions.

One area that has not been investigated is the two-photon absorption spectra of $Cr(CO)_6$ and $Ni(CO)_4$, which is one subject of this chapter. In a one- photon absorption spectrum for $Cr(CO)_6$ a change of parity is required from the Laporte rule for a state to be allowed but in a two-photon experiment parity is conserved. It is important to stress that the difference between one-photon and two-photon absorption is a subtle one with different higher order effects like vibronic coupling affecting the spectra. Indeed the influence of the g-u parity in multiphoton spectroscopy has been discussed before for other systems where the spectra can look the same regardless of the need for a change in parity due to density of states effects where the large density of states overrules any symmetry constraints on transitions so spectra for two different species with different symmetry can look the same when they should be different a priori [28]. Similarly to the case of $Fe(CO)_5$ different states are allowed from the absorption of two-photons than the absorption of one so different initial photochemistry could result. Further to this from simple analysis of the high symmetry of these complexes it can be argued that degenerate states (E or T symmetry) can be populated upon excitation and these degenerate states couple to non-totally symmetric vibrations via Jahn-Teller distortions. Table 2.1 details the different state symmetries that are available after the absorption of one or two photons. There is no possibility of spectral overlap in $Cr(CO)_6$ due to its

inversion centre but there is for $Ni(CO)_4$ as states of T_2 symmetry are allowed for both one- and two-photon absorptions. In the same way that two-photon spectroscopy can be applied to $Fe(CO)_5$, it can be shown that highly correlated theoretical methods can be used to generate the two-photon spectra of $Cr(CO)_6$ and $Ni(CO)_4$. These ideas are promising from the point of view of experimental studies [29].

4.2 Computational details

$Cr(CO)_6$ and $Ni(CO)_4$ were initially optimised for their electronic ground states with O_h and T_d molecular symmetry respectively at the CCSD level of theory with an SDD core ($1s^2 2s^2 2p^6$) basis set on the metal and cc-pVDZ basis set on carbon and oxygen. Figure 5.2 shows the geometries used and the bond lengths, which are in reasonable agreement with experimental measurements [3, 4]. A CCSD optimised geometry was used because these have been used in previous coupled cluster benchmark calculations and as shown in chapter 3, geometrical effects are largely negligible when compared to choice of method or basis set. The methods used to generate the spectra are the hierarchy of coupled cluster response methods CC2, CCSD and CCR(3) as discussed previously for the one- and two-photon spectroscopy of $Fe(CO)_5$ in chapter 3. CCR(3) could not be successfully applied to the one-photon spectrum of $Cr(CO)_6$ due to convergence problems when including the one-photon absorption allowed states. EOM-CCSD (which are equivalent to LR-CCSD methods for excitation energies) methods have already been applied successfully to the one-photon absorption spectrum of $Cr(CO)_6$ by Villaume and co-workers [27] and the one-photon absorption results produced here using CCSD response theory will be compared to these. The one-photon absorption spectrum of $Ni(CO)_4$ will also be studied, including CIS/CIS(D) results with an SDD/cc-pVDZ basis set, before moving onto two-photon absorption results. EOM-CCSD results will also be given for the one-photon absorption spectrum of $Ni(CO)_4$.

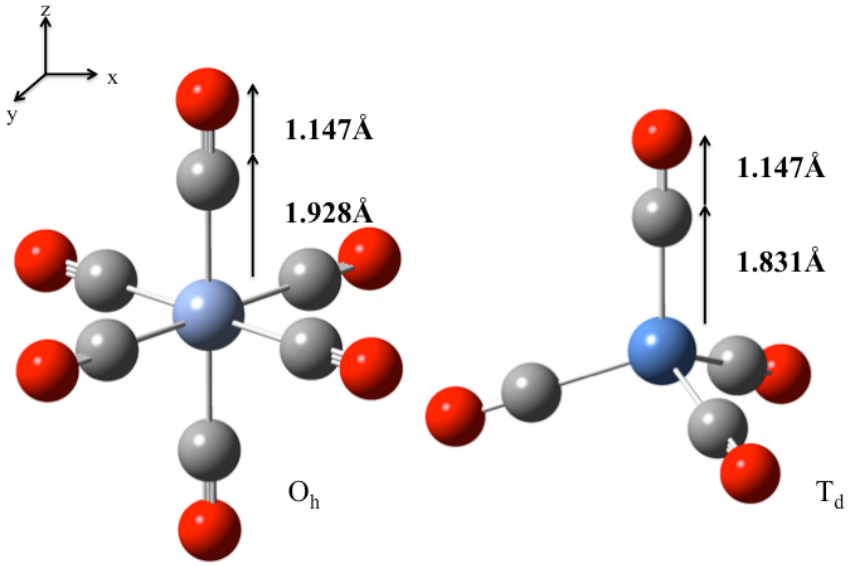

Figure 4.2 Optimised geometries of $Cr(CO)_6$ and $Ni(CO)_4$ with calculated bond lengths.

Two basis sets were used for the spectroscopy calculations on these carbonyls. The first was a generally contracted ANO-3 basis set that was discussed in chapter 2 by Pouamerigo and co-workers [30] and a cc-pVDZ basis set on carbon and oxygen. The second basis set was an SDD core ($1s^2 2s^2 2p^6$) basis set on the metal, and a 6-31G* basis set on carbon and oxygen. Table 4.1 summarises the number of primitive and contracted GTOs in each basis set, the number of total functions in the larger basis set is the same as the basis set used by Pierloot and co-workers [25] who have previously studied the electronic spectroscopy of $Cr(CO)_6$ and $Ni(CO)_4$ using large scale CASSCF and CASPT2. This allows a more direct comparison with these results. The size of the basis sets used here are also comparable with the basis sets used in the EOM-CCSD study of $Cr(CO)_6$ [27].

Table 4.1 Summary of primitive and contracted Gaussian type orbitals (GTOs) for both basis set combinations used for $Cr(CO)_6$ and $Ni(CO)_4$.

Basis Set	**Contraction (PGTO|CGTO)**	**Number of Basis Functions (PGTO|CGTO)**				**Total Functions (PGTO|CGTO)**
		Cr	**Ni**	**C**	**O**	
ANO-3	[21s15p10d6f|6s4p3d1f]	158|40	158|40	26|14	26|14	470|208 $Cr(CO)_6$
cc-pVDZ	[21s15p10d6f|6s4p3d1f]					366|152 $Ni(CO)_4$

	[9s4p1d|3s2p1d]					
ecp-sdd-DZ 6-31G*	[7s7p5d|5s5p2d] [7s7p5d|5s5p2d] [10s4p1d|3s2p1d]	53|30	53|30	27|14	27|14	377|198 $Cr(CO)_6$ 269|142 $Ni(CO)_4$

4.3 The one-photon absorption spectrum of $Cr(CO)_6$

In order to establish the accuracy of the methods used here with respect to $Cr(CO)_6$, presented first is a comparison of selected one-photon transitions of $Cr(CO)_6$ against various methods that have previously been reported including the most recent EOM-CCSD [27], CASPT2 [25] and TD-B3LYP [22] results along with experimental results from Beach and Gray [13]. These results are shown in table 4.2.

Table 4.2 Comparison of selected excitation energies and oscillator strengths for $Cr(CO)_6$. Oscillator strengths where applicable are given in brackets.

Excited State	Character	CASPT2	EOM-CCSD	LR-CCSD	TD-B3LYP	Experiment
1^1T_{2u}	MLCT	3.70-3.56	4.39	4.43	4.21	3.90
1^1T_{1u}	MLCT	4.54-4.11 (1.33-0.20)	4.95 (0.14)	4.99 (0.11)	4.50 (0.02)	4.46 (0.25)
1^1T_{1g}	MC	4.85	4.87	4.94	4.98	
1^1T_{2g}	MC	5.08	5.31	5.38	5.69	4.87
2^1T_{2u}	MLCT	4.32-4.43	5.46	5.47	4.79	
2^1T_{1u}	MLCT	5.07-5.20 (1.63-2.58)	6.10 (0.70)	6.12 (0.65)	6.01 (0.59)	5.53 (2.3)

The EOM-CCSD values shown here were also calculated using a CCSD optimised geometry but a slightly larger basis set was used on chromium (Watchers plus *f* functions, with 8*s*6*p*4*d*1*f* contracted GTOs on chromium). It can be seen that the difference between LR-CCSD excitation energies and oscillator strengths from the EOM-CCSD results differ by only a few tenths of an eV, with a similar difference in oscillator strength, thus the effect of a larger chromium basis set is negligible. For example the two allowed $^1T_{1u}$ transitions shown here have excitation energies of 4.95 and 6.10eV respectively, oscillator strengths of 0.14 and 0.70 for EOM-CCSD,

compared with 4.99 and 6.12eV and oscillator strengths of 0.11 and 0.65 respectively for LR-CCSD. The first calculated $^1T_{1u}$ state is believed to relate to a shoulder at 3.90eV in the experimental spectrum. This state is very close in energy to the next forbidden metal centred $^1T_{1g}$ state. This metal centred ligand field state is believed to be dissociative with respect to the ejection of a CO ligand. The closeness in energy between the lowest absorbing state and this dissociative ligand field state lends weight to the belief the mechanism for ultrafast dissociation of a CO ligand in $Cr(CO)_6$, further discussed in chapter 7, involves initial population of the lowest absorbing state followed by internal conversion to the dissociative ligand field state. Figure 4.3 shows a modern gas phase UV spectrum of $Cr(CO)_6$ with theoretical assignments from previous studies included. To expand on these results of the coupled cluster response methods further the two allowed states from table 4.2 are presented again in table 4.3 along with the results calculated using the CC2 method.

Table 4.3 Selected allowed states compared against CC2 and LR-CCSD methods.

Excited State	CC2	LR-CCSD	EOM-CCSD	CASPT2	TD-B3LYP	Experiment
1^1T_{1u}	4.15 (0.38)	4.99 (0.11)	4.95 (0.14)	4.54-4.11 (1.33-0.20)	4.50 (0.02)	4.46 (0.25)
2^1T_{1u}	4.82 (0.31)	6.12 (0.65)	6.10 (0.70)	5.07-5.20 (1.63-2.58)	6.01 (0.59)	5.53 (2.30)

The CC2 method in chapter 3 was shown to give poor results when applied to the excited states of $Fe(CO)_5$ and here the ordering of the states is markedly different compared to LR-CCSD but the identifiable allowed transitions that correspond to the experimental bands detailed above are red-shifted compared all other methods in table 4.3. Electron correlation effects clearly have a large effect on this and other carbonyls, so marking cheaper methods like CC2 unsuitable for spectroscopy in transition metal carbonyls. This conclusion will be reinforced later in this chapter.

This comparison is included because coupled cluster response methods have been gaining popularity recently for organic systems [31] and this is one of the first studies on an inorganic system, and to benchmark coupled cluster response methods against previously used well known methods for the prediction of electronic spectra. It

can be seen that CCSD response theory compares favourably to EOM-CCSD and other methods for the one-photon absorption spectrum of $Cr(CO)_6$ so the two-photon absorption results presented here can be looked upon with some degree of confidence.

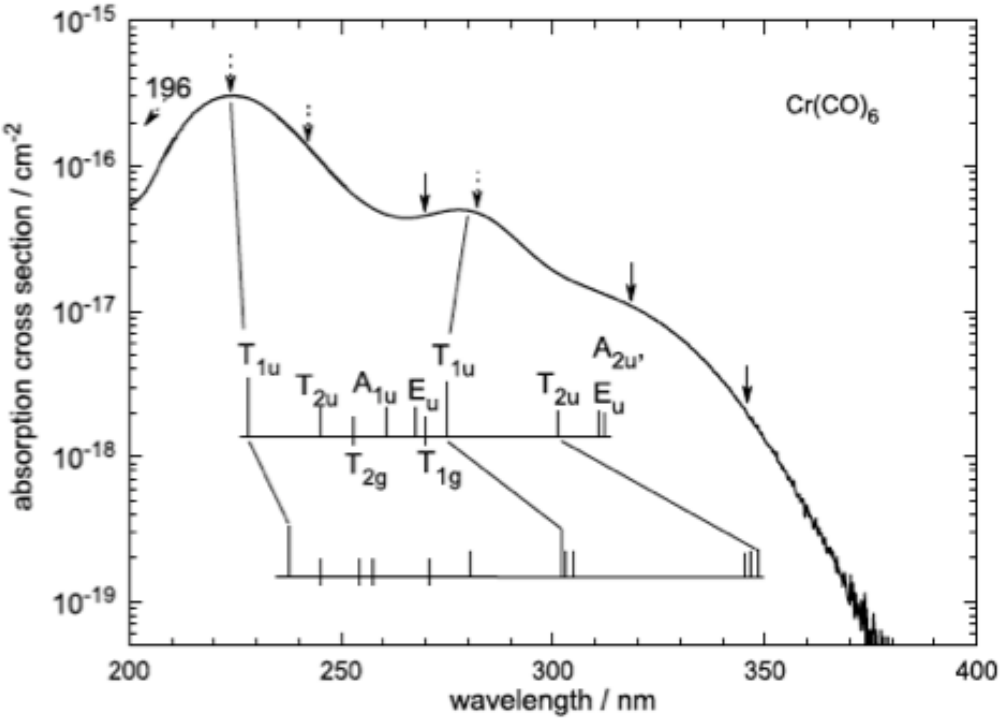

Figure 4.3 Experimental gas phase UV spectrum of $Cr(CO)_6$ from [32]. The theoretical postions of the excited states are inside the cross section on two ladders with the lower ladder from [25] and the upper ladder from [26].

4.4 The two-photon absorption spectrum of $Cr(CO)_6$

The theoretical two-photon absorption spectrum of $Cr(CO)_6$ has never been reported before. As previously discussed in chapter 4 it is possible to use two-photon absorption spectroscopy to trigger photochemistry in a transition metal complex [33] and the different selection rules than one-photon spectroscopy may give rise to different spectroscopy and initial photochemistry. The allowed two-photon absorption excited states using the hierarchy of coupled cluster response methods for $Cr(CO)_6$ are presented in table 4.4.

Table 4.4 Allowed two-photon transition energies of $Cr(CO)_6$ calculated with the hierarchy of coupled cluster response methods with both basis sets. Respective TPA δ in au are given in brackets.

Excited State	CC2 (ANO)	CC2 (ECP)	CCSD (ANO)	CCSD (ECP)	CCR(3) (ANO)	CCR(3) (ECP)
1^1T_{2g}	5.0198 (284.70)	4.8447 (537.76)	4.9455 (0.000)	4.5182 (0.000)	5.0897	4.6950
4^1T_{2g}	6.2314 (72.64)	6.1758 (0.000)	6.0566 (94.30)	5.7889 (126.30)	6.0459	5.9530
5^1T_{2g}	6.4868 (0.000)	6.3081 (0.000)	6.2339 (3.1714)	6.2704 (2.79)	6.1113	5.9611
1^1E_g	6.1149 (0.000)	7.9928 (0.000)	5.8644 (119.83)	5.8877 (47.61)	5.6143	5.4871
2^1E_g	6.6321 (521.70)		7.4611 (2395.57)	7.0948 (2685.45)		6.7051
1^1A_{1g}	6.6125 (0.000)	6.0593 (0.000)	7.8680 (0.002)	6.4936 (0.000)	7.036	6.3585

The CCR(3) method here shows the effect of perturbative triples on the values of the CCSD excitation energies only because the CCR(3) method only produces excited state energies. The broad effect here of the perturbative effect of triples is that the excitation energies are increased or decreased compared to CCSD by a few tenths of an eV or less. For one-photon absorption spectroscopy the only allowed state for $Cr(CO)_6$ is of T_{1u} symmetry but for two-photon spectroscopy T_{2g}, E_g and A_{1g} symmetry states are accessible. It can indeed be seen that multiple states could theoretically absorb, showing this spectrum may be different to the one-photon absorption spectrum. The full calculated spectra of both $Cr(CO)_6$ and $Ni(CO)_4$ are included in appendix 4. Basis set effects can be observed in table 4.3 in that the excitation energies are slightly red-shifted going from ANO to ECP basis sets. Also more evident is that when comparing each level of theory with the different basis sets the ordering of the states is quite different; the 2^1E_g state was not within the calculated first 40 excited states of the CC2 method with the ECP basis set and the CCR(3) method with the ANO basis set. At all levels of theory no states absorb below 4.84eV with strongly absorbing states throughout the energy range up to the limit of the calculations at ~8.0eV or the first 40 excited states. At the CC2 level of theory the spectrum is dominated by two medium intensity transitions of $^1T_{2g}$ symmetry, which are at 5.01 and 6.45eV (not shown in table 4.4, δ of 327 au) with the ANO basis set and are slightly red shifted to 4.84 and 6.13eV (not shown in table 4.4 with respective δ of 537 and 858 au) with the ECP basis set

respectively. The CC2 results with different basis sets also give different results for the 2^1E_g transition whereby it has a large δ value with the ANO basis set but was not within the investigated first 40 excited states with the ECP basis set. CC2 also gives the highest excitation energy for the 1^1E_g of all levels of theory for an allowed state at 7.99eV state with the ECP basis set.

The CCSD results follow in a similar way the results of CC2 whereby there are absorbing states all through the spectra with both basis sets, actually more so than with CC2. With either basis set only two transitions do not have a δ value. Generally the transitions between CC2 and CCSD with the same basis set are red-shifted from CC2 to CCSD but there are exceptions, for example the 2^1E_g transition is over 0.5eV higher in energy at the CCSD level than the same transition with CC2 with the ANO basis set. The ANO basis set also gives higher excitation energies in general than the ECP basis set with CCSD as with CC2, by at least a few tenths of an eV. The CCSD spectra with the ANO and ECP basis sets are generally very similar to each other in terms of the absorbing states with the CCSD spectra absolutely dominated by a very intense 2^1E_g transition with δ values of over 2000 au. When compared to the one-photon spectrum results with CCSD and the previous results from other methods in table 4.2 it can be concluded here that the CCSD results with either basis set should be considerably more accurate than the CC2 results. The use of the full CC3 model for excitation energies and transition moments would be a useful comparison and would be a priority in future work in this area.

What can be said from these results is that the two-photon spectrum would theoretically have more detail than the equivalent one-photon spectrum but differences occur when considering which level of theory should be applied to the problem. In this case general trends can be seen but exceptions are evident and the ordering of the states does differ when connected triples contributions are included. Calculated δ values from the CC3 model would be advantageous here but the results presented here illustrate the limit of the calculations on this complex at the present time. Overall CCSD is believed to be the best method to use in this case as the results gathered are quite sensitive to the method and basis set used. As with $Fe(CO)_5$ in chapter 3 CCR(3) should be the most accurate but some feature of the perturbative triples corrections is having an adverse

effect on the results presented here. The CC3 method should be used here to definitively answer this question. The differences between the spectra are pictorially represented in figure 4.4.

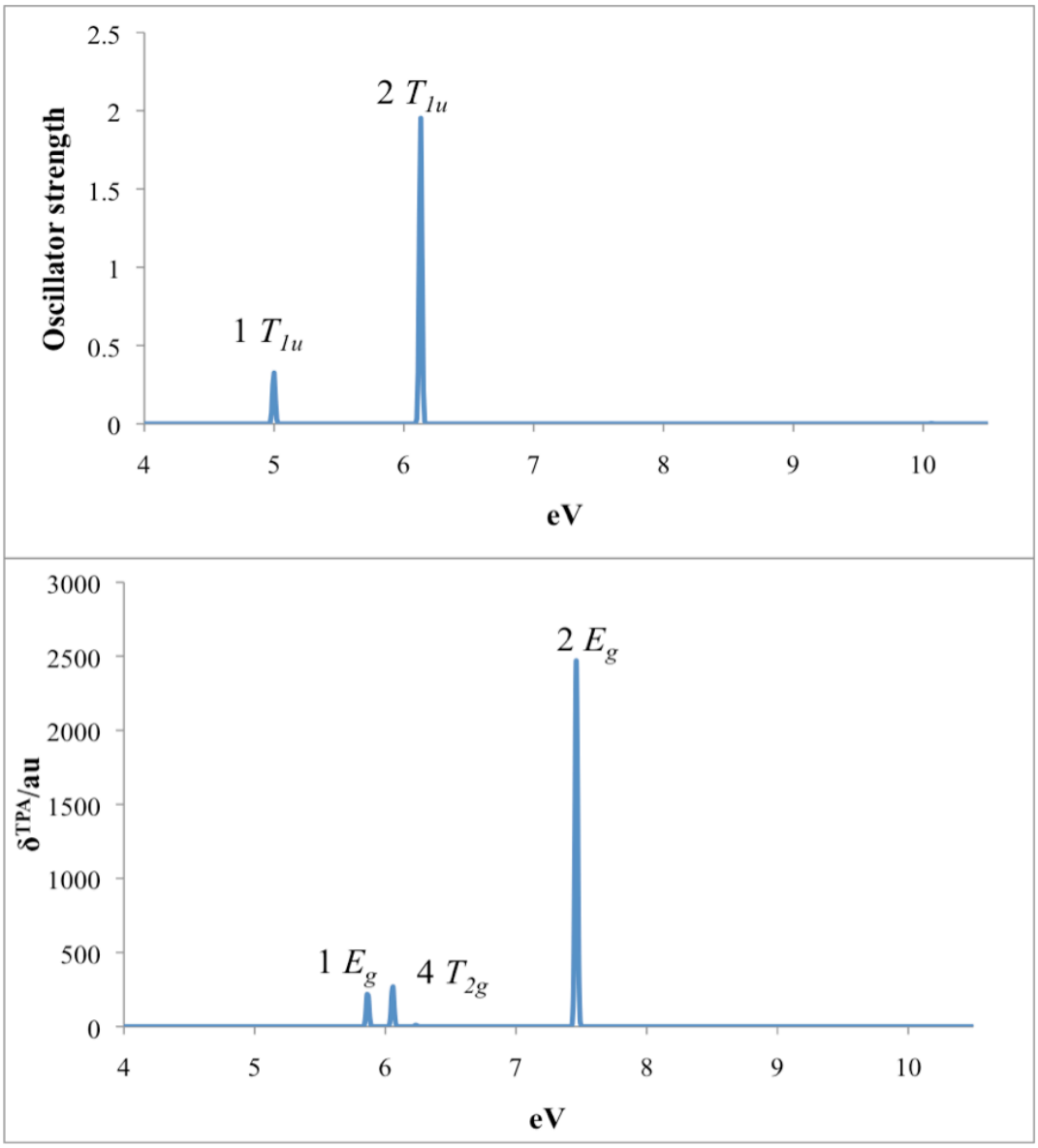

Figure 4.4 One-photon and two-photon absorption spectra of $Cr(CO)_6$ produced using the LR-CCSD method with the ANO basis set. Note the scale on the y-axis is for illustrative purposes only, but the size of the peaks relative to each other are correct.

One other question that can be asked is can two-photon excitation of $Cr(CO)_6$ initiate the same ultrafast photochemistry already mentioned in chapter 1 and will be further discussed in chapters 6,7 and 8. According to the latest work of Trushin and co-workers [32] who performed ultrafast pump-probe laser experiments on $Cr(CO)_6$ they found that ultrafast photodissociation of the molecule is independent with respect to the excitation pulse wavelength between 270 and 345nm (3.59 to 4.59eV). Included in this

is the first absorbing state of $^1T_{1u}$ symmetry that is visible in figure 4.4 that can be directly populated prior to population transfer to the dissociative LF state. The results shown here for the two-photon spectrum show that the lowest absorbing state falls outside this range at 5.86eV for a ^1E_g state which is a classed here as a MLCT state. Population of this lowest absorbing state should not present a great challenge to achieve as two-photon spectroscopy is possible for transition metal complexes and two photons of each of half the excitation energy of the ^1E_g state would be needed. Population of this state or the $^1T_{2g}$ state that is close in energy is entirely possible and furthermore as already mentioned population of these degenerate states could trigger Jahn-Teller distortions if these states couple to some non-totally symmetric vibrations. This in turn could cause the loss of one CO ligand as occurs from one-photon absorption, or possibly multiple CO loss which would be new photochemistry. Experimental investigation of this would be interesting given these possibilities.

4.5 The one-photon absorption spectrum of $Ni(CO)_4$

The results for $Ni(CO)_4$ are presented in a similar way to those for $Cr(CO)_6$. Firstly predictions for one-photon spectroscopy for $Ni(CO)_4$ by coupled cluster response methods are discussed in table 4.5. The theoretical spectroscopy of $Ni(CO)_4$ has not been investigated as much as for $Cr(CO)_6$ but nevertheless results have been reported using CASSCF/CASPT2 [25], TD-DFT [22], SAC-CI [24] and an experimental gas-phase study with theoretical INDO/S predictions [23] also exists. A coupled cluster study of both the one-photon and two-photon absorption spectrum has never been reported and both are presented here with the one-photon results compared to CASSCF and CASPT2 results produced by Pierloot and co-workers [25] in table 4.5. The spectrum of $Ni(CO)_4$ is different to those of $Cr(CO)_6$ or $Fe(CO)_5$ as the filled 3d shell of electrons on nickel means no 3d $\rightarrow$ 3d ligand field transitions are possible. In the experimental gas phase spectrum it was found that similar to other binary carbonyls the UV spectrum was broad and contained few features, being dominated by a main band at 6.0eV with shoulders at 5.4 and 4.6eV in the gas phase. The general understanding was that the spectrum is built up from MLCT transitions from the 3d shell of nickel to the π^* orbitals of the carbonyl ligands. These allowed transitions are of T_2 symmetry, which is the only allowed one-photon transition at T_d symmetry.

With the coupled cluster response also included are some results produced using the EOM-CCSD method using an SDD basis set on nickel and a cc-pVDZ basis set on carbon and oxygen as implemented in the Gaussian code [34]. As already discussed in this chapter EOM-CCSD and LR-CCSD should give the same excitation energies but may give different transition properties. For EOM-CCSD the first fifteen electronic excited state energies were calculated with oscillator strengths. The first twenty excited electronic states were calculated with all coupled cluster response methods. What can immediately be seen from the results presented in table 4.5 is that at the CC2 level, excitation energies and oscillator strengths are extremely poorly described, with disasterous results obtained using the ECP basis set (these returned negative excitation energies so are not included in these results) and transitions red-shifted by a few eV with the ANO basis set when compared to any other method presented in table 4.5. Comparison with CIS and CIS(D) results for the two allowed states show that these methods also give a relatively poor description of the states showing that a CIS reference state is not a good reference state. The failure of CC2 to predict the electronic spectra of transition metal complexes has recently been discussed by Taylor and Paterson who reported unfeasible CC2 data for the lowest excited states of TiO_2 and $(TiO_2)_n$ nanoclusters [35]. This is believed to be due to the greater importance of electron correlation in metal complexes than organic molecules, already mentioned above. Further investigations on the poor performance of the CC2 method with regards to transition metal complexes are in progress.

Table 4.5 Comparison of selected excitation energies and oscillator strengths for the one-photon absorption spectrum of $Ni(CO)_4$. CASSCF and CASPT2 results are from reference [25] and experimental results are from reference [23]. Oscillator strengths where applicable are given in brackets.

Excited State	CC2 (ANO)	CCSD (ANO)	CCSD (ECP)	EOM-CCSD (SDD)	CCR(3) (ANO)	CCR(3) (ECP)	CASSCF	CASPT2	CIS/CIS(D)	Experiment
1^1E	1.932	4.881	4.209	4.695	6.106	6.840	7.31	3.58		-
1^1A_1	1.955	6.063	4.448	-	6.815	6.418	-	-		-
1^1T_1	1.899	4.853	3.681	4.670	-	6.711	7.15	4.04		-
1^1T_2	1.361 (0.490)	5.198 (0.038)	4.415 (0.059)	4.998 (0.044)	6.387	7.406	7.49 (0.29)	4.34 (0.29)	5.160/2.820 (0.097)	4.5
2^1E	2.012	6.321	-	5.299	6.751	-	8.57	5.20		-
2^1A_1	-	-	4.633		-	7.173	9.12	3.72		-
2^1T_1	2.047	5.185	4.602	5.016	6.333	7.433	7.06	4.88		-
2^1T_2	1.979 (0.015)	5.640 (0.098)	4.718 (0.000)	5.461 (0.087)	6.658	7.619	7.57 (0.38)	5.22 (0.38)	6.149/2.023 (0.120)	5.2-5.4
3^1T_1	2.086	5.543	5.111	-	6.758	7.881	6.76	5.14		-

This shows that the minimum level of coupled cluster theory needed to describe this problem with any confidence is CCSD. Within the investigated range of excitations there are two absorbing states, 1^1T_2 and 2^1T_2 and in general both CCSD response and EOM-CCSD compare favourably with CASPT2 results, although the reported oscillator strengths are much lower than those reported in the CASSCF/CASPT2 results. The lowest absorbing state is believed to relate to the band in the gas-phase spectrum relating to a $9t_2 \rightarrow 10t_2$ transition, which the CCSD method replicates quite well, especially for LR-CCSD with the ECP basis set. The same can also be said for the next absorbing state (2^1T_2). This state is believed to relate in part to a shoulder at 5.4eV in the gas-phase spectrum, or completely to a shoulder at 5.3eV in the solution phase spectrum [16]. Again the results in table 4.5 show that CCSD gives the closest value for this transition, either CCSD response with the ANO basis set or EOM-CCSD. The effect of perturbative triples with the CCR(3) method this time overestimates the values of the transition energies, mostly by over 1eV compared to CCSD and CASPT2, more closely mirroring the results of CASSCF of which Peirloot and co-workers also found overestimated transition energies. It may be that the perturbative nature of the triples correction in CCR(3) is not suited to these states. Again, in theory the CCR(3) method should be better than the CCSD method but some feature of this method makes it less accurate compared to CCSD for the values of the excitation energies. To confirm this assessment using CC3 results will be needed.

4.6 The two-photon absorption spectrum of $Ni(CO)_4$

The coupled cluster response results for the two-photon absorption spectrum of $Ni(CO)_4$ are presented in table 4.6. As with $Cr(CO)_6$ the theoretical two-photon absorption spectrum of $Ni(CO)_4$ shows the added spectral detail that is possible by the fact that there are a larger number of allowed states in the two-photon spectrum than for the one-photon spectrum: $^1A_1$, ^1E and $^1T_2$ symmetry states are allowed compared to just $^1T_2$ for the one-photon spectrum. Spectral overlap is possible because states of symmetry $^1T_2$ are allowed in both spectra since there is no g-u selection rule with T_d symmetry.

Table 4.6 Allowed two-photon transition energies of $Ni(CO)_4$ calculated with the hierarchy of coupled cluster response methods with both combinations of basis sets. Respective TPA δ values in au where applicable are given in brackets.

Excited State	CC2 (ANO)	CCSD (ANO)	CCSD (ECP)	CCR(3) (ANO)	CCR(3) (ECP)
1^1E	1.932 (0.000	4.881 (1.020)	4.209 (2.200)	6.106	6.840
1^1A_1	1.955 (0.000)	6.063 (0.000)	4.448 (0.000)	6.815	6.418
1^1T_1	1.899	4.853	3.681	-	6.711
1^1T_2	1.361 (39.290)	5.198 (0.180)	4.415 (11.870)	6.387	7.406
2^1E	2.012 (0.000)	6.321 (76.330)	-	6.751	-
2^1A_1	-	-	4.633 (0.000)	-	7.173
2^1T_1	2.047	5.185	4.602	6.333	7.433
2^1T_2	1.979 (0.000)	5.640 (27.160)	4.718 (0.000)	6.658	7.619
3^1T_1	2.086	5.543	5.111	6.758	7.881

As with $Cr(CO)_6$ only the number and type of absorbing states changes when going from a one-photon to a two-photon absorption spectrum, so EOM-CCSD and CCSD linear response are believed to give the best approximation to both spectra for $Ni(CO)_4$ as with $Cr(CO)_6$. Figure 4.5 graphically shows the pure electronic one-photon and two-photon absorption spectra produced using the LR-CCSD and QR-CCSD methods.

Similar photochemistry could be produced by two-photon excitation if the overlapped MLCT state was populated but different photochemistry could result from populating the lower energy, weaker intensity ^1E state or the higher intensity, higher energy ^1E state. Experimentally $Ni(CO)_4$ undergoes an ultrafast ejection of one CO ligand followed by luminescence in a long lived excited state of the $Ni(CO)_3$ photoproduct. Two-photon excitation could produce similar results but as with $Cr(CO)_6$,

two-photon absorption allows different degenerate states to be populated that can couple to non-totally symmetric vibrations so Jahn-Teller distortions, multiple CO loss and luminescence from a different long lived excited state are all feasible. An experimental investigation would also be interesting here.

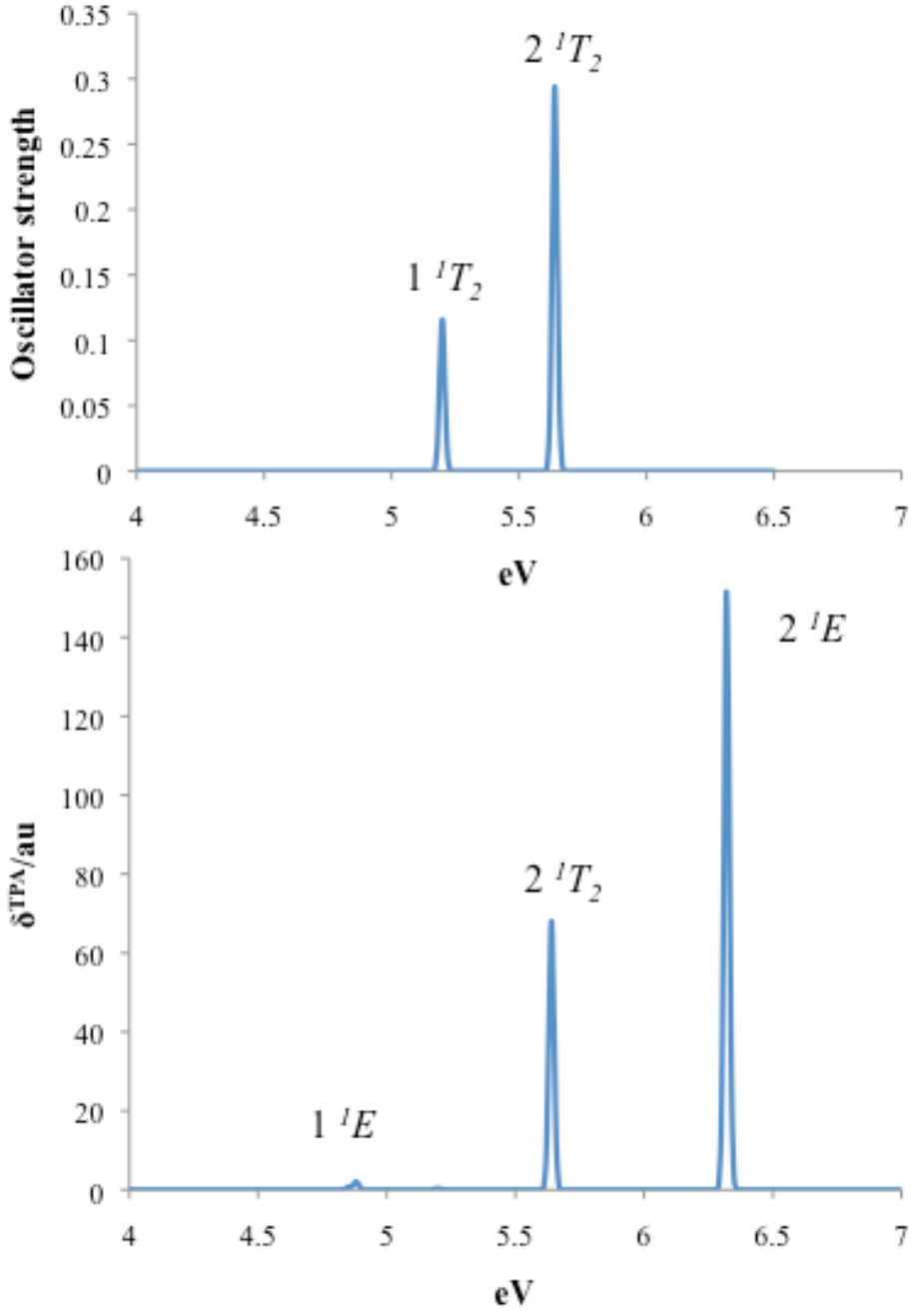

Figure 4.5 The one-photon and two-photon absorption spectra of $Ni(CO)_4$ produced using the LR-CCSD and QR-CCSD methods respectively with the ANO basis set. Note the scale on the y-axis is for illustrative purposes only, but the size of the peaks relative to each other are correct.

4.7 Conclusions

The hierarchy of coupled cluster response methods CC2, CCSD and CCR(3) have been applied to the one- and two-photon absorption spectra of $Cr(CO)_6$ and $Ni(CO)_4$, with EOM-CCSD also applied to the one-photon absorption spectra of $Ni(CO)_4$. The results of these methods have been compared to each other and to other previous theoretical and experimental results. The CCSD method with an ANO basis set was found to agree well with previous EOM-CCSD results for the one-photon absorption spectrum of $Cr(CO)_6$ creating a solid basis for these methods to be used to calculate the two-photon absorption spectrum of $Cr(CO)_6$. Again, CCSD was found to be the most accurate and cost effective method of the three for the prediction of the spectrum for this system. The spectrum is obviously quite different to the one-photon absorption spectrum with the lowest absorbing state almost 1eV higher meaning different photochemistry could result if these states are populated experimentally.

This is the first known report of the use of coupled cluster methods for the prediction of the one- and two-photon absorption spectra of $Ni(CO)_4$. The results for the one-photon spectrum were compared to previous theoretical results. This showed that the CC2 method gave an extremely poor description of the spectrum, with EOM-CCSD and LR-CCSD giving more realistic values for the most important states such as the first absorbing $^1T_2$ states which should relate to bands in the experimental spectrum. Again it was found that the CCSD methods give the most accurate and cost effective description of the states in this case with the CCR(3) method overestimating the excitation energies like CASSCF. These results mostly agreed with the findings of the previous CASSCF/CASPT2 study. The results for the two-photon spectrum showed some spectral overlap with the one-photon spectrum around a shoulder in the experimental one-photon absorption spectrum with other absorbing states lower and higher in energy than this overlapped transition.

Both of these carbonyl complexes are regarded as very difficult systems to study with respect to their electronic spectroscopy. One previous study is even entitled “The tough case of $Cr(CO)_6$” [26] so it can be understood that this type of study is a challenge both in selecting methods to look at their excited states and analysing the results. With regards to methods this study highlights the degree of care needed when

applying these highly correlated methods to transition metal complexes especially the CC2 method. It is apparent here that low-cost methods such as CC2 can have severe problems when applied to metal complexes. Further work will be needed to develop low cost methods for inorganic photochemistry and transition metal complex photochemistry in comparison to organic photochemistry due to the failure of the CC2 method here and in chapter 3. The high levels of electron correlation in transition metal complexes marks the CC2 method as insufficient for these systems, indeed when compared to CIS and CIS(D) results these methods also provide relatively poor results showing that a CIS reference state is a poor choice of reference state. The effect of perturbative triples in the CCR(3) method over CCSD should mark the CCR(3) method out as the most accurate but some feature of this method be it an unusual cancellation of errors or something else makes it less accurate than the CCSD method in this case.

4.8 References

[1] Rudalt, W.; Hofmann, U., *Z. Physik. Chem.* **1935,** 28, 351.

[2] Brockway, L. O.; Ewens, R. V. G.; Lister, M. W., An electron diffraction investigation of the hexacarbonyls of chromium, molybdenum and tungsten. *Trans. Faraday. Soc.* **1938,** 34, 1350-1357.

[3] Ladell, J.; Post, B.; Frankuchen, I., The crystal structure of nickel carbonyl, $Ni(CO)_4$. *Acta Crystallographica* **1952,** 5.

[4] Whitaker, A.; Jeffery, J. W., The crystal structure of chromium hexacarbonyl. *Acta Crystallographica* **1967,** 23, 977.

[5] Garrat, A. P.; Thompson, H. W., The spectra and photochemical decomposition of metallic carbonyls. Part II. Photochemical data. *J. Chem. Soc.* **1934**, 1817-1822.

[6] Church, S. P.; Grevels, F. W.; Hermann, H.; Schaffner, K., Structures and kinetics of $Cr(CO)_5$ and $Cr(CO)_5 \bullet H_2O$ in cyclohexane solution - flash-photolysis study of $Cr(CO)_6$ with infrared and visible detection. *Inorg. Chem.* **1985,** 24, 418-422.

[7] Church, S. P.; Grevels, F. W.; Hermann, H.; Schaffner, K., Flash-photolysis of $Cr(CO)_6$ in H_2-saturated cylcohexane solution - IR spectroscopic evidence for a $Cr(CO)_5(H_2)$ complex at room temperature. *J. Chem. Soc.-Chem. Commun.* **1985**, 30-32.

[8] Graham, M. A.; Poliakoff, M.; Turner, J. J., Photochemistry of the group-VI hexacarbonyls in low-temperature matrices 1. Pentacarbonyls of chromium, molybdenum, and tungsten. *J. Chem. Soc. A., Inorg. Chem.* **1971**, 2939.

[9] Black, J. D.; Braterman, P. S., Purported trigonal bipyramidal $Cr(CO)_5$ *J. Am. Chem Soc.* **1975,** 97, 2908-2909.

[10] Burdett, J. K.; Graham, M. A.; Perutz, R. N.; Poliakoff, M.; Rest, A. J.; Turner, J. J.; Turner, R. F., Photochemistry of group-6 hexacarbonyl in low-temperature matrices 5. Routes to square pyramidal matrix-isolated chromium pentacarbonyl. *J. Am. Chem Soc.* **1975,** 97, 4805-4808.

[11] Perutz, R. N.; Turner, J. J., Photochemistry of group vi hexacabonyls in low-temperature matrices 2. Infrared spectra and structures of CO^{13} enriched hexacarbonyls and pentacarbonyls of chromium, molybdenum and tungsten. *Inorg. Chem.* **1975,** 14, 262-270.

[12] Perutz, R. N.; Turner, J. J., Photochemistry of the group 6 hexacarbonyls in low-temperature matrices. III. Interaction of the pentacarbonyls wth noble gases and other matrices. *J. Am. Chem Soc.* **1975,** 97, 4791-4800.

[13] Gray, H. B.; Beach, N. A., The electronic structure of octahedral metal complexes. I. Metal hexacarbonyls and hexacynanides. *J. Am. Chem Soc.* **1963,** 85, 2922-2927.

[14] Beach, N. A.; Gray, H. B., Electronic structure of metal hexacarbonyls. *J. Am. Chem Soc.* **1968,** 90, 5713-5721.

[15] Graham, M. A.; Rest, A. J.; Turner, J. J., Ultraviolet/visible absoprtion spectrum and photochromism of pentacarbonyl tungsten, ($W(CO)_5$). *J. Organomet. Chem.* **1970,** 24, C54-C56.

[16] Schreiner, A. F.; Brown, T. L., A semiempirical molecular orbital model for $Cr(CO)_6$, $Fe(CO)_5$, and $Ni(CO)_4$. *J. Am. Chem Soc.* **1968,** 90, 3366-3374.

[17] Ziegler, T.; Autschbach, J., Theoretical methods of potential use for studies of inorganic reaction mechanisms. *Chem. Rev.* **2005,** 105, 2695-2722.

[18] Ehlers, A. W.; Frenking, G., Theoretical studies of M-CO bond lengths and first dissociation energies of hte transition metal hexacarbonyls $Cr(CO)_6$, $Mo(CO)_6$ and $W(CO)_6$. *J. Chem Soc. Chem. Commun.* **1993**, 1709.

[19] Lewis, K. E.; Golden, D. M.; Smith, G. P., Organometallic bond-dissociation energies - laser pyrolysis of $Fe(CO)_5$, $Cr(CO)_6$, $Mo(CO)_6$ and $W(CO)_6$. *J. Am. Chem Soc.* **1984,** 106, 3905-3912.

[20] Rosch, N.; Kotzian, M.; Jorg, H.; Schroder, H.; Rager, B.; Metev, S., On visible transients in gas-phase UV photolysis of transition-metal compuonds - experimental and theoretical results for $Ni(CO)_4$. *J. Am. Chem Soc.* **1986,** 108, 4238-4239.

[21] Rosa, A.; Baerends, E. J.; van Gisbergen, S. J. A.; van Lenthe, E.; Groeneveld, J. A.; Snijders, J. G., Electronic spectra of $M(CO)_6$ (M = Cr, Mo, W) revisited by a relativistic TD-DFT approach. *J. Am. Chem Soc.* **1999,** 121, 10356-10365.

[22] van Gisbergen, S. J. A.; Groeneveld, J. A.; Rosa, A.; Snijders, J. G.; Baerends, E. J., Excitation energies for transition metal compounds from time-dependent density functional theory. Applications to MnO_4^-, $Ni(CO)_4$, and $Mn_2(CO)_{10}$. *J. Phys. Chem. A* **1999,** 103, 6835-6844.

[23] Kotzian, M.; Rosch, N.; Schroder, H.; Zerner, M. C., Optical spectra of transition-metal carbonyls - $Cr(CO)_6$, $Fe(CO)_5$ and $Ni(CO)_4$. *J. Am. Chem Soc.* **1989,** 111, 7687-7696.

[24] Hada, M.; Imai, Y.; Hidaka, M.; Nakatsuji, H., Theoretical study on the excitation spectrum and the photofragmentation reaction of $Ni(CO)_4$. *J. Chem. Phys.* **1995,** 103, 6993-6998.

[25] Pierloot, K.; Tsokos, E.; Vanquickenborne, L. G., Optical spectra of $Ni(CO)_4$ and $Cr(CO)_6$ revisited. *J. Phys. Chem.* **1996,** 100, 16545-16550.

[26] Ben Arnor, N.; Villaume, S.; Maynau, D.; Daniel, C., The electronic spectroscopy of transition metal carbonyls: The tough case of $Cr(CO)_6$. *Chem. Phys. Lett.* **2006,** 421, 378-382.

[27] Villaume, S.; Strich, A.; Daniel, C.; Perera, S. A.; Bartlett, R. J., A coupled cluster study of the electronic spectroscopy and photochemistry of $Cr(CO)_6$. *Phys. Chem. Chem. Phys.* **2007,** 9, 6115-6122.

[28] Arnbjerg, J.; Jimenez-Banzo, A.; Paterson, M. J.; Nonell, S.; Borrell, J. I.; Christiansen, O.; Ogilby, P. R., Two-photon absorption in tetraphenylporphycenes: Are porphycenes better candidates than porphyrins for providing optimal optical properties for two-photon photodynamic therapy? *J. Am. Chem Soc.* **2007,** 129, 5188-5199.

[29] Trushin, S. A.; Fuss, W.; Schmid, W. E.; Kompa, K. L., Femtosecond dynamics and vibrational coherence in gas-phase ultraviolet photodecomposition of $Cr(CO)_6$. *J. Phys. Chem. A* **1998,** 102, 4129-4137.

[30] Pouamerigo, R.; Merchan, M.; Nebotgil, I.; Widmark, P. O.; Roos, B. O., Density-matrix averaged atomic natural orbital (ANO) basis-sets for correlated molecular wave-functions .3. First row transition-metal atoms. *Theor. Chim. Acta* **1995,** 92, 149-181.

[31] de Meras, A.; Cuesta, I. G.; Koch, H., A coupled cluster calculation of the spectrum of urea. *Chem. Phys. Lett.* **2001,** 348, 469-476.

[32] Trushin, S. A.; Kosma, K.; Fuss, W.; Schmid, W. E., Wavelength-independent ultrafast dynamics and coherent oscillation of a metal-carbon stretch vibration in photodissociation of $Cr(CO)_6$ in the region of 270-345 nm. *Chem. Phys.* **2008,** 347, 309-323.

[33] Banares, L.; Baumert, T.; Bergt, M.; Kiefer, B.; Gerber, G., Femtosecond photodissociation dynamics of $Fe(CO)_5$ in the gas phase. *Chem. Phys. Lett.* **1997,** 267, 141-148.

[34] Frisch, M. J. Trucks, G. W.; Schlegel, H. B.; Scuseria, G. E.; Robb, M. A.; Cheeseman, J. R.; Montgomery, Jr., J. A.; Vreven, T.; Kudin, K. N.; Burant, J. C.; Millam, J. M.; Iyengar, S. S.; Tomasi, J.; Barone, V.; Mennucci, B.; Cossi, M.; Scalmani, G.; Rega, N.; Petersson, G. A.; Nakatsuji, H.; Hada, M.; Ehara, M.; Toyota, K.; Fukuda, R.; Hasegawa, J.; Ishida, M.; Nakajima, T.; Honda, Y.; Kitao, O.; Nakai, H.; Klene, M.; Li, X.; Knox, J. E.; Hratchian, H. P.; Cross, J. B.; Bakken, V.; Adamo, C.; Jaramillo, J.; Gomperts, R.; Stratmann, R. E.; Yazyev, O.; Austin, A. J.; Cammi, R.; Pomelli, C.; Ochterski, J. W.; Ayala, P. Y.; Morokuma, K.; Voth, G. A.; Salvador, P.; Dannenberg, J. J.; Zakrzewski, V. G.; Dapprich, S.; Daniels, A. D.; Strain, M. C.; Farkas, O.; Malick, D. K.; Rabuck, A. D.; Raghavachari, K.; Foresman, J. B.; Ortiz, J. V.; Cui, Q.; Baboul, A. G.; Clifford, S.; Cioslowski, J.; Stefanov, B. B.; Liu, G.; Liashenko, A.; Piskorz, P.; Komaromi, I.; Martin, R. L.; Fox, D. J.; Keith, T.; Al-Laham, M. A.; Peng, C. Y.; Nanayakkara, A.; Challacombe, M.; Gill, P. M. W.; Johnson, B.; Chen, W.; Wong, M. W.; Gonzalez, C.; and Pople, J. A. Gaussian 09, Revision A.1, Gaussian, Inc., Wallingford CT, 2009.

[35] Taylor, D. J.; Paterson, M. J., Calculations of the low-lying excited states of the TiO_2 molecule. *J. Chem. Phys.* **2010,** 133.

Chapter 5

Structure and Electronic Spectroscopy of the Group 7 Mixed Metal Bimetallic Carbonyls

5.1 Introduction and literature review

A further aim of this thesis is to illustrate the depth and variety of binary carbonyls that exist and can be studied using methods already discussed. A group of such carbonyls are the group 7 mixed bimetallics $MnTc(CO)_{10}$, $MnRe(CO)_{10}$ and $TcRe(CO)_{10}$. The equivalent group 7 bimetallics $Mn_2(CO)_{10}$, $Tc_2(CO)_{10}$ and $Re_2(CO)_{10}$ have already been extensively investigated both experimentally and theoretically for structure and spectroscopy with examples of such studies in references [1, 2, 3, 4, 5, 6]. However the mixed metal bimetallics have received much less attention. This is surprising, as the ground state structures of these carbonyls have no bridging ligands and a bond between two different transition metal atoms. Reports relating to them in the literature are comparatively rare, with $MnRe(CO)_{10}$ the most studied of the three carbonyls with synthesis, spectroscopy and reactivity all investigated, with a review by Coville and Leins [7]. Two recent papers have been published on the subject of the structure of $MnRe(CO)_{10}$, the first by Tanjaroon *et al* [8] reported the experimental rotational spectrum using a high-resolution pulsed beam microwave spectrometer with density functional and *ab initio* calculations used to determine the nuclear quadrupole coupling constants and electric field gradients. The second paper by Palmer and co-workers [9] reported in detail the possible equilibrium structures of $MnRe(CO)_{10}$ using density functional theory, using both the B3LYP and BP86 density functionals. Two different conformers of C_{4v} symmetry were found in either staggered or eclipsed geometries with respect to rotation around the metal-metal bond. The staggered conformation was found to be lower in energy by no more than 4.07 kcal mol^{-1}, with interconversion between the two conformers thought to be readily accessible via one imaginary harmonic frequency in the eclipsed conformation which relates to internal rotation around the metal-metal bond. Reports on $MnTc(CO)_{10}$ and $TcRe(CO)_{10}$ are much less common with the only real study reported in the literature by Michels and Svec from 1981 [10] where their synthesis and characterisation by infrared spectroscopy and mass spectrometry was discussed. At the present time no report has been found in the literature relating to a theoretical study of the structure of $MnTc(CO)_{10}$ or $TcRe(CO)_{10}$ and the theoretical electronic spectra of any of these three complexes. This is surprising as one could hypothesise that the structural and spectral properties of all three should be largely similar. In this chapter such a study will be presented and discussed. Here TD-DFT with

three different hybrid density functionals will be used as coupled cluster response and EOM-CCSD methods that have been used in previous chapters on monometallic carbonyls have been found to be too expensive for these larger bimetallic complexes. This also presents an opportunity to compare how the three different functionals can predict the electronic spectra of these carbonyls, especially with respect to MLCT transitions, and whether the low barrier to interconversion between staggered and eclipsed conformers holds for all three complexes.

5.2 Computational details

The Gaussian 09 [11] code was used to perform all calculations in which both the staggered and eclipsed conformers of all three complexes were investigated using three different DFT functionals. The first is the three parameter B3LYP hybrid functional of Becke, Lee, Yang and Parr [12] which is one of the most highly used DFT methods in modern electronic structure theory and is included here for this reason. The second is the M062X functional developed by Zhao and Truhlar [13] that is a hybrid functional where the '2X' notation means it uses twenty percent Hartree-Fock exchange as opposed to its 'M06L' and 'M06HF' sister functionals which respectively include zero percent and one hundred percent Hartree-Fock exchange. This functional is used as it is a recently developed functional that is similar to B3LYP in its make up and is seeing increasing use in problems where functionals such as B3LYP are normally used so a comparison is interesting to perform. Neither of these two functionals is designed with electronic spectroscopy or treatment of charge transfer states in mind as the ratio of short and long-range exchange does not change depending on the interelectronic distance. These functionals should not be able to describe the charge transfer states present in the spectrum of these carbonyls as accurately as the third functional used in this chapter which is the Coulomb attenuated B3LYP (CAM-B3LYP) functional developed by Yanai, Tew and Handy [14] which has already been discussed in chapter 3 and purports to include all the benefits of the B3LYP functional in terms of low computational cost and ground state energy and structure predictions while also including a better treatment of quantum mechanical exchange at short and long range so improving the description of charge transfer states. Because these states are predicted to dominate the spectra of all three carbonyls studied, and CAM-B3LYP has already

been successfully applied to problems of charge transfer states such as an investigation on the charge transfer band in a zincbacteriochlorin-bacteriochlorin complex by Kobayashi and Amos [15], and a study of temporary anion states in a range of first – row transition metal (Cr, Mn, Fe, Co) cyclopentadienyl carbonyl complexes by Cheng, Chang and Shih [16], it is included here.

Both staggered and eclipsed conformers were optimised using all three functionals including analytical frequency calculations to establish the presence of any imaginary vibrational frequencies. Two basis sets were used in all calculations, the Los Alamos effective core potential double zeta (LanL2DZ) basis set on all atoms already discussed in chapter 2 which has 224 basis functions and the second larger basis set a mix of the SDD core ($1s^2 2s^2 2p^6$) basis set on the metal atoms and the Pople 6-311G* basis set on carbon and oxygen which were also discussed in chapter 2 which has 439 basis functions in total. These optimised geometries were then used to generate the electronic spectrum of each carbonyl using both basis sets and all three functionals for each, encompassing the first 60 vertical excited states.

5.3 Structure

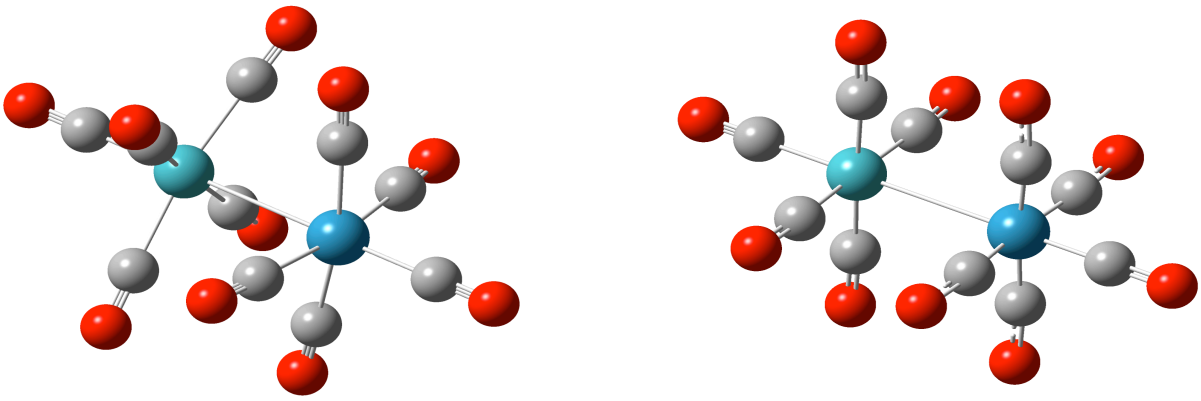

C$_{4v}$ staggered *C*$_{4v}$ eclipsed

Figure 5.1 Optimised geometries of the staggered and eclipsed C_{4v} transition states for all carbonyls studied.

The main results of all geometry optimisations for both staggered and eclipsed conformations of all three carbonyls are shown in tables 5.1, 5.2 and 5.3. Both energetic and geometrical parameter results are presented, table 5.1 for energetics and tables 5.2 and 5.3 for staggered and eclipsed geometrical parameters. All results are compared to previously reported experimental and theoretical results where applicable. The structures of each conformer are pictorially presented in figure 5.1.

It was found that the staggered conformation was lower in energy than the eclipsed conformation. Analytical frequency calculations showed that the staggered conformation was a valid minimum and that the eclipsed conformation was a first order saddle point with one imaginary vibrational frequency. This frequency relates to rotation around the metal-metal bond for interconversion to the staggered conformation. These results agree with the findings of Palmer and co-workers who reported this only for $MnRe(CO)_{10}$.

Table 5.1 Energetics of all optimised geometries. Energies are quoted in Atomic units and barrier to rotation values are in kcal mol^{-1}.

Complex	**Functional**	**Basis set**	**Energy of Conformer/au**		**Barrier to rotation/kcal mol^{-1}**
			Staggered	**Eclipsed**	
$MnTc(CO)_{10}$	B3LYP	LanL2DZ	-1317.2763	-1317.2690	4.6
		SDD/6-311G*	-1319.0281	-1319.0217	4.0
	M062X	LanL2DZ	-1316.5661	-1316.5557	6.5
		SDD/6-311G*	-1318.3405	-1318.3314	5.7
	CAM-B3LYP	LanL2DZ	-1316.6562	-1316.6475	5.4
		SDD/6-311G*	-1318.4360	-1318.4286	4.6
	B3LYP	LanL2DZ	-1316.3252	-1316.3173	4.9
		SDD/6-	-1316.5258	-1316.5193	4.0

		311G*			
$MnRe(CO)_{10}$	M062X	LanL2DZ	-1315.6058	-1315.5945	7.0
		SDD/6-311G*	-1315.8417	-1315.8323	5.9
	CAM-B3LYP	LanL2DZ	-1316.6562	-1316.6475	5.4
		SDD/6-311G*	-1318.4360	-1318.4286	4.6
$TcRe(CO)_{10}$	B3LYP	LanL2DZ	-1292.5308	-1292.5244	4.0
		SDD/6-311G*	-1293.0759	-1293.0705	3.3
	M062X	LanL2DZ	-1291.7824	-1291.7732	5.7
		SDD/6-311G*	-1292.3558	-1292.3483	4.7
	CAM-B3LYP	LanL2DZ	-1291.9036	-1291.8964	4.5
		SDD/6-311G*	-1292.4715	-1292.4656	3.7

The difference in energy between staggered and eclipsed conformations is very small in all cases and similar in magnitude to the results of Palmer and co-workers. The barrier to rotation is also very small and never more than 7.1 kcal mol^{-1} in all cases although it is smaller in the other two carbonyls than in $MnRe(CO)_{10}$ in the order of $MnRe(CO)_{10}$ > $MnTc(CO)_{10}$ > $TcRe(CO)_{10}$. The larger basis set gives a slightly lower barrier to rotation in all cases. CAM-B3LYP claims to have similar properties and predict similar results for ground state structures and energetics as B3LYP and here the energy values predicted by CAM-B3LYP and B3LYP are closer to one another than those values predicted by M062X but there is still a difference between them. The barriers to rotation reported by Palmer and co-workers of 3.82 and 4.07 kcal mol^{-1} for B3LYP and BP86 respectively for $MnRe(CO)_{10}$ are comparable to the results presented here.

The crystal structure of $MnRe(CO)_{10}$ was determined by Rheingold and co-workers [17] who measured an Mn-Re bond length of 2.96Å with a space group of $I_{2/a}$. Each individual molecule in the complex was found to have C_{4v} symmetry in the staggered conformation, which is in accordance with the results presented here. The value of the Mn-Re bond length measured in the crystal structure is also in reasonable agreement with the presented results and from this the calculated bond lengths of the other two carbonyls studied should be in reasonable agreement with the real values.

Table 5.2 Selected geometrical parameters of all carbonyls studied in the staggered conformation. All numbers are given in angstrom. The subscript numbers 1 and 2 for each M-CO bond correspond to the metals in the order they are written in the table.

Complex	Functional	Basis set	Geometrical Parameter/Å				
			M-M	M_1-CO_{ax}	M_2-CO_{ax}	M_1-CO_{eq}	M_2-CO_{eq}
$MnTc(CO)_{10}$	B3LYP	LanL2DZ	3.0448	1.843	2.000	1.796	1.939
		SDD/6-311G*	3.06436	1.862	2.009	1.814	1.944
	M062X	LanL2DZ	2.98098	1.871	1.995	1.811	1.928
		SDD/6-311G*	2.99391	1.899	2.001	1.831	1.929
	CAM-B3LYP	LanL2DZ	2.97612	1.831	1.993	1.788	1.937
		SDD/6-311G*	3.00086	1.853	2.001	1.806	1.941
$MnRe(CO)_{10}$	B3LYP	LanL2DZ	3.04372	1.844	1.996	1.798	1.934
		SDD/6-311G*	3.07887	1.863	2.023	1.816	1.959
	M062X	LanL2DZ	2.97806	1.874	1.987	1.816	1.924
		SDD/6-311G*	3.00488	1.900	2.012	1.834	1.947
	CAM-B3LYP	LanL2DZ	2.97722	1.833	1.989	1.790	1.932
		SDD/6-311G*	3.01600	1.853	2.016	1.808	1.956

$TcRe(CO)_{10}$	B3LYP	LanL2DZ	3.12659	1.997	1.994	1.944	1.936
		SDD/6-311G*	3.15230	2.006	2.021	1.949	1.960
	M062X	LanL2DZ	3.03208	1.995	1.986	1.933	1.926
		SDD/6-311G*	3.05294	2.002	2.013	1.931	1.948
	CAM-B3LYP	LanL2DZ	3.06808	1.990	1.986	1.941	1.934
		SDD/6-311G*	3.09708	1.999	2.014	1.945	1.957

Table 5.3 Selected geometrical parameters of all carbonyls studied in the eclipsed conformation. All numbers are given in angstrom. The subscript numbers 1 and 2 for each M-CO bond correspond to the metals in the order they are written in the table.

Complex	**Functional**	**Basis set**	**Geometrical Parameter/Å**				
			M-M	**M_1-CO_{ax}**	**M_2-CO_{ax}**	**M_1-CO_{eq}**	**M_2-CO_{eq}**
$MnTc(CO)_{10}$	B3LYP	LanL2DZ	3.168	1.843	2.000	1.792	1.933
		SDD/6-311G*	3.188	1.863	2.008	1.810	1.937
	M062X	LanL2DZ	3.117	1.870	1.997	1.802	1.916
		SDD/6-311G*	3.123	1.899	2.002	1.821	1.916
	CAM-B3LYP	LanL2DZ	3.093	1.832	1.992	1.784	1.930
		SDD/6-311G*	3.118	1.854	2.001	1.801	1.934
$MnRe(CO)_{10}$	B3LYP	LanL2DZ	3.166	1.843	1.996	1.794	1.929
		SDD/6-311G*	3.198	1.863	2.022	1.811	1.952
	M062X	LanL2DZ	3.110	1.873	1.988	1.808	1.915
		SDD/6-	3.131	1.900	2.013	1.824	1.936

		311G*					
	CAM-B3LYP	LanL2DZ	3.093	1.833	1.989	1.786	1.926
		SDD/6-311G*	3.128	1.854	2.016	1.803	1.949
$TcRe(CO)_{10}$	B3LYP	LanL2DZ	3.232	1.997	1.994	1.937	1.931
		SDD/6-311G*	3.254	2.007	2.021	1.942	1.954
	M062X	LanL2DZ	3.157	1.996	1.987	1.920	1.917
		SDD/6-311G*	3.168	2.003	1.919	2.014	1.937
	CAM-B3LYP	LanL2DZ	3.167	1.990	1.986	1.934	1.928
		SDD/6-311G*	3.193	1.999	2.014	1.938	1.951

Here the smaller LanL2DZ basis set gives shorter bond lengths than the SDD/6-311G* basis set and the Mn-Re bond lengths match well with the crystal structure. From this it can be seen that the Mn-Tc bonds are generally shorter and Tc-Re bond generally longer than Mn-Re bonds, but this can be understood due to the relative size of the two metal atoms in the complexes. If the lengths of equivalent M-M bonds are compared between both staggered and eclipsed conformations the bonds in the eclipsed conformation are slightly longer but the difference is negligible.

5.4 Electronic spectroscopy

Andrea and co-workers [18] have reported the experimental ultraviolet photoelectron spectrum of $MnRe(CO)_{10}$ where the metal-metal σ and π interactions were specifically studied. Levenson and Gray [19] have also studied the electronic spectrum of $MnRe(CO)_{10}$ in detail along with its bimetallic analogues of manganese, rhenium and technetium. The spectral data from this study are given in table 5.4.

Table 5.4 Experimental spectral data for the main bands $MnRe(CO)_{10}$ at 77K in a 6:1 mixture of isopentane and 3-methylpentane from [19]. Excitation energies have been converted from cm^{-1} to eV. Numbers in brackets relate to measurements taken at 300K.

Excitation Energy/eV	Molar Absorptivity/ $cm^2\ mol^{-1}$	Assignment
3.961 (3.84)	20100 (14900)	$\sigma\rightarrow\sigma^*$
4.463	11400	$\sigma\rightarrow\pi^*$
4.674	8900	$d\pi\rightarrow\pi^*$
6.410	86600	$M\rightarrow\pi^*$

Although the theoretical results presented here are in the gas phase at room temperature and the results in table 5.3 are in solvent at low temperatures some common features are still present between the two sets of results. Moreover it is hoped to calibrate the presented results with the four experimental bands reported above. All spectra presented in this chapter contain a large density of states within a relatively small spectral range between 3 and 6eV and most show little or no oscillator strength, even though A_1 and E symmetry transitions are allowed for one-photon absorption spectra and all spectra contain a large number of transitions with such symmetry. All transitions with oscillator strength greater than 0.01 are presented in tables 5.5-5.10 for the purposes of assigning these states to the experimental bands. Full data tables of all spectra are given in appendix 5.2.

Table 5.5 Selected allowed transitions for $MnTc(CO)_{10}$ with the LanL2DZ basis set. Oscillator strength, *f*, is given next to each transition and the assignment of each state given in brackets below the excitation energy.

$MnTc(CO)_{10}$/LanL2DZ					
B3LYP		M062X		CAM-B3LYP	
Excitation Energy/eV	*f*	Excitation Energy/eV	*f*	Excitation Energy/eV	*f*
3.6534 ($\sigma\rightarrow\sigma^*$)	0.3910	3.7492 ($\sigma\rightarrow\sigma^*$)	0.4667	3.7386 ($\sigma\rightarrow\sigma^*$)	0.4967
4.2027 ($\sigma\rightarrow\pi^*$)	0.0142	4.1294 ($\sigma\rightarrow\pi^*$)	0.0225	4.5157 ($\sigma\rightarrow\pi^*$)	0.0266

4.4065 (π→π*)	0.0261	4.2226 (σ→π*)	0.0127	4.9395 (π→π*)	0.0509
4.6212 (σ→σ*)	0.0512	4.6616 (σ→σ*)	0.0131	4.9694 (σ→σ*)	0.0232
4.8308 (π→π*)	0.0301	4.8536 (σ→σ*)	0.0280	5.2943 (π→π*)	0.0149
4.9924 (σ→σ*)	0.0335	5.2546 (σ→σ*)	0.0401	5.3702 (σ→σ*)	0.0355

Table 5.6 Selected allowed transitions for $MnTc(CO)_{10}$ with the SDD/6-311G* basis set. Oscillator strength, *f*, is given next to each transition and the assignment of each state given in brackets below the excitation energy.

$MnTc(CO)_{10}$/SDD 6-311G*					
B3LYP		**M062X**		**CAM-B3LYP**	
Excitation Energy/eV	***f***	**Excitation Energy/eV**	***f***	**Excitation Energy/eV**	***f***
3.8028 (σ→σ*)	0.4208	3.9137 (σ→σ*)	0.4695	3.8758 (σ→σ*)	0.5155
4.4089 (σ→π*)	0.0143	4.3371 (σ→π*)	0.0232	4.7356 (σ→π*)	0.0217
4.6254 (π→π*)	0.0321	4.4339 (σ→π*)	0.0126	5.1097 (σ→σ*)	0.0363
4.7584 (σ→σ*)	0.0307	4.7861 (σ→σ*)	0.0251	5.1687 (π→π*)	0.0210
5.0042 (π→π*)	0.0354	5.5043 (π→π*)	0.0398	5.4415 (π→π*)	0.0218
5.1462 (σ→σ*)	0.0143	5.8072 (π→π*)	0.0582	5.5638 (σ→σ*)	0.0188

Table 5.7 Selected allowed transitions for $MnRe(CO)_{10}$ with the LanL2DZ basis set. Oscillator strength, *f*, is given next to each transition and the assignment of each state given in brackets below the excitation energy.

$MnRe(CO)_{10}$/LanL2DZ					
B3LYP		**M062X**		**CAM-B3LYP**	
Excitation Energy/eV	***f***	**Excitation Energy/eV**	***f***	**Excitation Energy/eV**	***f***
3.7197 (σ→σ*)	0.3720	3.8958 (σ→σ*)	0.4336	3.8304 (σ→σ*)	0.4624
4.3099 (π→π*)	0.0394	4.3763 (σ→π*)	0.0181	4.6597 (σ→π*)	0.0134
4.8019 (π→π*)	0.0180	5.0486 (σ→σ*)	0.0526	4.7892 (π→π*)	0.0403
4.8367	0.0102	5.1283	0.0209	5.1642	0.0100

(π→π*)		(π→π*)		(σ→σ*)	
4.9977 (σ→σ*)	0.0104	5.608 (π→π*)	0.0316	5.2913 (π→π*)	0.0238
5.4648 (σ→π*)	0.0108	5.8376 (σ→π*)	0.0307	5.8829 (σ→π*)	0.0335

Table 5.8 Selected allowed transitions for $MnRe(CO)_{10}$ with the SDD/6-311G* basis set. Oscillator strength, *f*, is given next to each transition and the assignment of each state given in brackets below the excitation energy.

$MnRe(CO)_{10}$/SDD 6-311G*					
B3LYP		**M062X**		**CAM-B3LYP**	
Excitation Energy/eV	***f***	**Excitation Energy/eV**	***f***	**Excitation Energy/eV**	***f***
3.802 (σ→σ*)	0.3824	3.9882 (σ→σ*)	0.4257	3.9091 (σ→σ*)	0.4705
4.4767 (π→π*)	0.0405	4.4314 (σ→π*)	0.0126	4.8188 (π→π*)	0.0146
4.8467 (σ→π*)	0.0144	4.5381 (σ→π*)	0.0165	4.9745 (π→π*)	0.0419
4.9615 (π→π*)	0.0280	4.8328 (π→π*)	0.0115	5.2271 (σ→σ*)	0.0202
		5.0403 (σ→σ*)	0.0204	5.434 (π→π*)	0.0238
		5.2943 (π→π*)	0.0569	6.0107 (σ→σ*)	0.0243

Table 5.9 Selected allowed transitions for $TcRe(CO)_{10}$ with the LanL2DZ basis set. Oscillator strength, *f*, is given next to each transition and the assignment of each state given in brackets below the excitation energy.

$TcRe(CO)_{10}$/LanL2DZ					
B3LYP		**M062X**		**CAM-B3LYP**	
Excitation Energy/eV	***f***	**Excitation Energy/eV**	***f***	**Excitation Energy/eV**	***f***
3.8387 (σ→σ*)	0.3813	4.1022 (σ→σ*)	0.4064	4.0098 (σ→σ*)	0.4686
4.4383 (π→π*)	0.0617	5.1107 (σ→σ*)	0.0140	4.738 (π→π*)	0.0180
5.2551 (π→σ*)	0.0151	5.1612 (π→π*)	0.0970	4.8998 (π→π*)	0.0570
		6.1893 (σ→π*)	0.0102	5.786 (π→σ*)	0.0267
				5.9521 (π→π*)	0.0176
				5.9582	0.0107

				(σ→π*)	

Table 5.10 Selected allowed transitions for $TcRe(CO)_{10}$ with the SDD 6-311G* basis set. Oscillator strength, *f*, is given next to each transition and the assignment of each state given in brackets below the excitation energy.

$TcRe(CO)_{10}$/SDD 6-311G*					
B3LYP		**M062X**		**CAM-B3LYP**	
Excitation Energy/eV	***f***	**Excitation Energy/eV**	***f***	**Excitation Energy/eV**	***f***
4.0058 (σ→σ*)	0.3999	4.2835 (σ→σ*)	0.4283	4.1807 (σ→σ*)	0.4887
4.4763 (π→π*)	0.0203	5.1981 (π→π*)	0.0310	4.5312 (π→σ*)	0.0107
4.657 (π→π*)	0.0605	5.4247 (π→π*)	0.0902	4.9267 (π→π*)	0.0333
5.6097 (π→σ*)	0.0129	6.3281 (σ→π*)	0.0157	5.1323 (π→π*)	0.0523
				6.0008 (σ→π*)	0.0359
				6.303 (σ→π*)	0.0113

The first band in the spectrum was assigned as a metal-metal transition due to its lower energy position in the spectrum counting it out as a MLCT state. This is because the effort required to excite metal electrons away to a ligand orbital increases relative to the effective nuclear charge of the metal [19]. An A_1 symmetry band transition with large oscillator strength of ~0.3 or higher dominates the lower part of the theoretical spectra in all cases. The excitation energies of this transition for $MnRe(CO)_{10}$ are ~3.70 and ~4.0eV for the LanL2DZ and SDD/6-311G* basis set respectively which is in good accordance the σ→σ* band of the experimental spectrum. Figure 5.2 pictorially represents the orbitals that are involved in this transition.

The following bands present more of a challenge to assign. In the experimental spectrum the next two bands were assigned as MLCT bands however both were poorly resolved which as already discussed in previous chapters is a common feature of such complexes. The remaining allowed transitions reported here are mainly classified as MLCT states. Keeping $MnRe(CO)_{10}$ in mind, the experimental spectrum splits the third band into two parts called A and B.

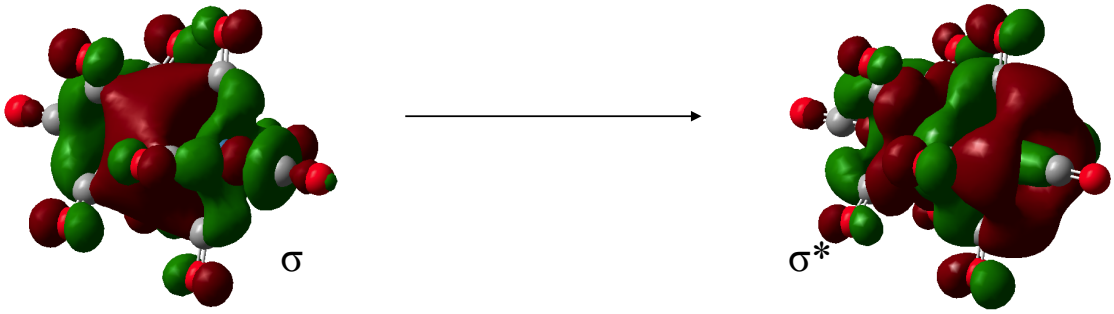

Figure 5.2 Orbital transition for the early σ→σ* metal-metal band in the spectra for all carbonyls studied. C_i, the dominant component of the time-dependant response eigenvector, in all cases is around 0.600. Orbitals shown here were produced using the CAM-B3LYP functional with SDD/6-311g* basis set for $MnRe(CO)_{10}$.

This band lies between 4.463 and 4.675eV in energy and part A of the third band was assigned as a σ→π* character MLCT state and such transitions are present in our results in the correct energy region, especially with the M062X functional and LanL2DZ basis set which has a σ→π* character allowed state with an excitation energy of 4.376eV. However CAM-B3LYP and B3LYP both fail to reproduce this state with the LanL2DZ basis set, CAM-B3LYP not showing any σ→π* transition with oscillator strength greater than 0.01 and no such transition with B3LYP with an excitation energy lower than 4.846eV. With the SDD/6-311G* basis set generally blue-shifts (higher energy, lower wavelength shift) the excitation energies of the equivalent states than calculated using the LanL2DZ basis set. The excitation energies of the first σ→σ* band is a good example of this. The general features of the spectrum are the same using all three functionals with MLCT states dominating the higher energy part of the spectrum, although the ordering of the states is slightly different in each case. Though one would expect differences such as this in principle due to their differing abilities to treat charge transfer states.

Part B of the third band is assigned in the experimental spectrum as a π→π* character transition at 4.674eV. All functionals with either basis set predicts such a transition with the CAM-B3LYP and M062X functionals most closely matching the experimental band with respective calculated excitation energies of 4.818 and 4.832eV. Figure 5.3 pictorially represents the orbitals which are involved in this transition.

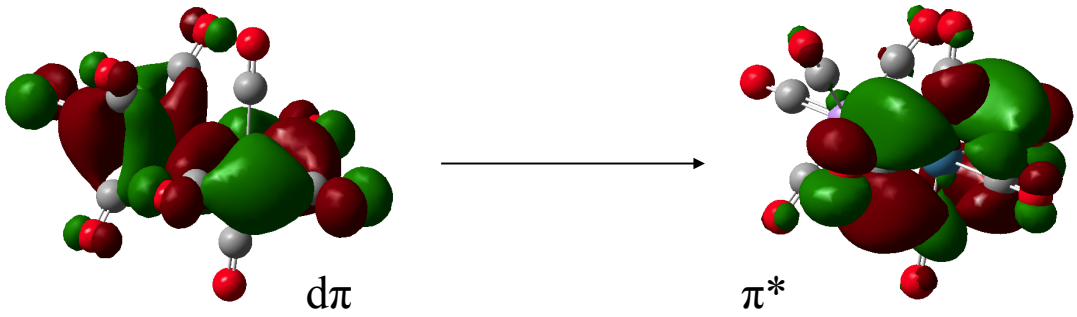

Figure 5.3 Orbital transition for the third dπ→π* MLCT part B band in the spectra for all carbonyls studied. C_i is around 0.460 in most cases. Orbitals shown here were produced using the CAM-B3LYP functional with SDD/6-311G* basis set for $MnRe(CO)_{10}$.

B3LYP at higher energies provides a poor description of the spectrum with very few transitions with oscillator strength over 0.01. Higher up in energy from the third band there is a mixture of allowed states of different character. Surrounding these allowed states there is a large number of forbidden excited states including states with oscillator strengths below 0.01 throughout the investigated spectral range.

The calculated spectra of $MnTc(CO)_{10}$ are quite similar to the spectra of $MnRe(CO)_{10}$ with the main features broadly the same. The lower part of the spectra in all cases is dominated with a $\sigma\rightarrow\sigma^*A_1$ symmetry transition with large oscillator strength. The next transition higher in energy from this state in all cases is calculated to be a $\sigma\rightarrow\pi^*$ MLCT state. Higher in energy from this state, MLCT states continue to dominate the spectra with $\sigma\rightarrow\sigma^*$ metal centred states also present that involve a transition from the HOMO orbital to a higher lying metal σ^* orbital than the σ^* orbital populated in the first intense band. When compared with $MnRe(CO)_{10}$ the excitation energies of the allowed states are lower for $MnTc(CO)_{10}$ which is most notably seen in the excitation energy values for the initial $\sigma\rightarrow\sigma^*$ intense band.

The low energy part of the calculated spectrum of $TcRe(CO)_{10}$ is very similar to those of the other two carbonyls studied here including the intense $\sigma\rightarrow\sigma^*$ metal centred state which is present with all functionals and basis sets, and the excitation energy value for this state higher than the equivalent state in $MnRe(CO)_{10}$. However at higher energies both B3LYP and M062X functionals fail to show many MLCT states with oscillator strength greater than 0.01. There is still a large density of forbidden states and

states with weak oscillator strengths but this highlights the inability in this example of hybrid functionals that are not corrected for long-range exchange to accurately predict the presence of charge transfer states of any type in experimental spectra. Indeed only CAM-B3LYP which is designed to better describe charge transfer states than B3LYP, does predict a range of charge transfer states throughout the spectral range investigated here of $\pi\rightarrow\sigma^*$, $\pi\rightarrow\pi^*$ and $\sigma\rightarrow\pi^*$ character. Such a pattern favourably compares with the other two complexes studied in this chapter and so with the experimental spectrum of $MnRe(CO)_{10}$. No evidence is seen of $\sigma\rightarrow\pi^*$ allowed transition from the CAM-B3LYP results for $TcRe(CO)_{10}$ which is predicted to be band 3A in the experimental spectrum of $MnRe(CO)_{10}$ and is present in the theoretical spectra of both $MnRe(CO)_{10}$ and $MnTc(CO)_{10}$. However $\pi\rightarrow\pi^*$ states are present at higher energies which is in accordance with the experimental 3B band of $MnRe(CO)_{10}$ and the theoretical spectra of $MnTc(CO)_{10}$. As no experimental electronic spectrum of either $MnTc(CO)_{10}$ or $TcRe(CO)_{10}$ has ever been reported in the literature these assignments are tentative at the moment but due to the close structural similarities between all three complexes studied here it can be argued that the theoretical spectra presented here should be close to what the experimental electronic absorption spectra of $MnTc(CO)_{10}$ and $TcRe(CO)_{10}$ would look like.

5.5 Conclusions

Density functional theory has been used to study the structural features and electronic absorption spectra of the group 7 mixed metal bimetallic carbonyl complexes $MnTc(CO)_{10}$, $MnRe(CO)_{10}$ and $TcRe(CO)_{10}$ using the B3LYP, M062X and CAM-B3LYP functionals and two basis sets. In all cases the favoured ground state structure of all three carbonyls was found to be a C_{4v} symmetry staggered conformation with respect to rotation along the metal-metal bond. Another conformer that is close in energy to the staggered conformation was also found which was also of C_{4v} symmetry but eclipsed with respect to rotation around the metal-metal bond. This eclipsed conformation was calculated to be a first order saddle point using analytical frequency calculations with one imaginary frequency that corresponded to rotation around the metal-metal bond. The barrier to rotation and therefore interconversion to the staggered conformation was found to be low, and in all cases no more than 7.10 kcal mol^{-1}.

The electronic absorption spectra were calculated for each complex and compared to an experimental spectrum for $MnRe(CO)_{10}$. The theoretical spectra for $MnRe(CO)_{10}$ were found to be in good agreement with the experimental spectrum with many spectral features the same. The spectra of the other two complexes were predicted to be similar to that of $MnRe(CO)_{10}$ with CAM-B3LYP giving the best overall description of the spectra of all three carbonyls.

From a perspective of the reactive photochemistry of these complexes the most intense $\sigma \rightarrow \sigma^*$ transition would be similar to that present in the spectroscopy of $Mn_2(CO)_{10}$, [5] population of which causes homolytic bond cleavage and ultrafast photochemistry of the type to be discussed in chapter 7. Though for these species the photochemistry should be more complex as there will be two different monometallic fragments involved in the subsequent reactive photochemistry.

5.6 References

[1] Xie, Y. M.; Jang, J. H.; King, R. B.; Schaefer, H. F., Binuclear homoleptic manganese carbonyls: $Mn_2(CO)_x$ (x = 10, 9, 8, 7). *Inorg. Chem.* **2003,** 42, 5219-5230.

[2] Seder, T. A.; Church, S. P.; Weitz, E., Photodissociation pathways and recombination kinetics for gas-phase $Mn_2(CO)_{10}$. *J. Am. Chem. Soc.* **1986,** 108, 7518-7524.

[3] Rosa, A.; Ricciardi, G.; Baerends, E. J.; Stufkens, D. J., Density functional study of the photodissociation of $Mn_2(CO)_{10}$. *Inorg. Chem.* **1996,** 35, 2886-2897.

[4] Rosa, A.; Ricciardi, G.; Baerends, E. J.; Stufkens, D. J., Density-functional study of ground and excited-states of $Mn_2(CO)_{10}$. *Inorg. Chem.* **1995,** 34, 3425-3432.

[5] Kuhn, O.; Hachey, M. R. D.; Rohmer, M. M.; Daniel, C., A CASSCF/CASPT2 study of the low-lying excited states of $Mn_2(CO)_{10}$. *Chem. Phys. Lett.* **2000,** 322, 199-206.

[6] Kim, S. K.; Pedersen, S.; Zewail, A. H., Femtochemistry of organometallics - dynamics of metal-metal and metal-ligand bond-cleavage in $M_2(CO)_{10}$. *Chem. Phys. Lett.* **1995,** 233, 500-508.

[7] Coville, N. J.; Leins, A. L., $MnRe(CO)_{10}$: A review of the chemical and physical properites of a simple heterobimetallic non-bridged dimer. *J. Clust. Sci.* **1993,** 4, 185-230.

[8] Tanjaroon, C.; Keck, K. S.; Kukolich, S. G.; Palmer, M. H.; Guest, M. F., The rotational spectrum and theoretical study of a dinuclear complex, $MnRe(CO)_{10}$. *J. Chem. Phys.* **2004,** 120, 4715-4725.

[9] Palmer, M. H.; Camp, P. J.; Tanjaroon, C.; Keck, K. S.; Kukolich, S. G., A theoretical study of the staggered and eclipsed forms of the dinuclear complex $MnRe(CO)_{10}$. *J. Chem. Phys.* **2004,** 121, 7187-7194.

[10] Michels, G. D.; Svec, H. J., Characterization of $MnTc(CO)_{10}$ and $TcRe(CO)_{10}$. *Inorg. Chem.* **1981,** 20, 3445-3447.

[11] Frisch, M. J. Trucks, G. W.; Schlegel, H. B.; Scuseria, G. E.; Robb, M. A.; Cheeseman, J. R.; Montgomery, Jr., J. A.; Vreven, T.; Kudin, K. N.; Burant, J. C.; Millam, J. M.; Iyengar, S. S.; Tomasi, J.; Barone, V.; Mennucci, B.; Cossi, M.; Scalmani, G.; Rega, N.; Petersson, G. A.; Nakatsuji, H.; Hada, M.; Ehara, M.; Toyota, K.; Fukuda, R.; Hasegawa, J.; Ishida, M.; Nakajima, T.; Honda, Y.; Kitao, O.; Nakai, H.; Klene, M.; Li, X.; Knox, J. E.; Hratchian, H. P.; Cross, J. B.; Bakken, V.; Adamo, C.; Jaramillo, J.; Gomperts, R.; Stratmann, R. E.; Yazyev, O.; Austin, A. J.; Cammi, R.; Pomelli, C.; Ochterski, J. W.; Ayala, P. Y.; Morokuma, K.; Voth, G. A.; Salvador, P.; Dannenberg, J. J.; Zakrzewski, V. G.; Dapprich, S.; Daniels, A. D.; Strain, M. C.; Farkas, O.; Malick, D. K.; Rabuck, A. D.; Raghavachari, K.; Foresman, J. B.; Ortiz, J. V.; Cui, Q.; Baboul, A. G.; Clifford, S.; Cioslowski, J.; Stefanov, B. B.; Liu, G.; Liashenko, A.; Piskorz, P.; Komaromi, I.; Martin, R. L.; Fox, D. J.; Keith, T.; Al-Laham, M. A.; Peng, C. Y.; Nanayakkara, A.; Challacombe, M.; Gill, P. M. W.; Johnson, B.; Chen, W.; Wong, M. W.; Gonzalez, C.; and Pople, J. A. Gaussian 09, Revision A.1, Gaussian, Inc., Wallingford CT, 2009.

[12] Becke, A. D., Density-functional thermochemistry .3. The role of exact exchange. *J. Chem. Phys.* **1993,** 98, 5648-5652.

[13] Zhao, Y.; Truhlar, D. G., The M06 suite of density functionals for main group thermochemistry, thermochemical kinetics, noncovalent interactions, excited states, and transition elements: Two new functionals and systematic testing of four M06-class functionals and 12 other functionals. *Theor. Chem. Acc.* **2008,** 120, 215-241.

[14] Yanai, T.; Tew, D. P.; Handy, N. C., A new hybrid exchange-correlation functional using the coulomb-attenuating method (CAM-B3LYP). *Chem. Phys. Lett.* **2004,** 393, 51-57.

[15] Kobayashi, R.; Amos, R. D., The application of CAM-B3LYP to the charge-transfer band problem of the zincbacteriochlorin-bacteriochlorin complex. *Chem. Phys. Lett.* **2006,** 420, 106-109.

[16] Cheng, H. Y.; Chang, J. T.; Shih, C. C., Application of the stabilization method to temporary anion states of pi-ligand transition-metal carbonyls in density functional theory. *J. Phys. Chem. A* **2010,** 114, 2920-2929.

[17] Rheingold, A. L.; Meckstroth, W. K.; Ridge, D. P., Crystal and molecular-structure of rhenium manganese decacarbonyl, $ReMn(CO)_{10}$, containing an unexpectedly short Re-Mn bond. *Inorg. Chem.* **1986,** 25, 3706-3707.

[18] Andrea, R. R.; Terpstra, A.; Stufkens, D. J.; Oskam, A., A complete assignment of the ultraviolet photoelectron spectrum of MnRe(co)10. *Inorg. Chimi. Acta.* **1985,** 96, L57-L58.

[19] Levenson, R. A.; Gray, H. B., Electronic-structure of compounds containing metal-metal bonds - decacarbonyldimetal and related complexes. *J. Am. Chem. Soc.* **1975,** 97, 6042-6047.

Chapter 6

Analysis of the potential energy surface of the $^{1}Cr(CO)_5$ Jahn-Teller conical intersection

6.1 Introduction and literature review

A main subject of this thesis is the study of photochemistry that happens immediately after excitation of these binary carbonyls. Although the general response of the nuclei is known, i.e. the complete dissociation of the complex on a sub-picosecond timescale into the metal atom and carbonyl ligands, it will be shown in this and the remaining chapters that this process is very complex and presents a challenge to model theoretically with a high degree of accuracy. The subject of this chapter is the photodissociation process of $Cr(CO)_6$ induced by laser excitation, specifically the topology of the potential energy surface around a point of conical intersection of the singlet spin $Cr(CO)_5$ photoproduct at a Jahn-Teller active geometry which sits at the apex of the cone of intersection. This species is perhaps the most intensely studied of the binary carbonyls in this regard. Therefore the purpose of this chapter is to serve as an introduction into the photochemistry of such unsaturated carbonyls using $Cr(CO)_6$ photodissociation as an example. Two diagnostic tools will also be applied to study the potential energy surface of $Cr(CO)_5$ relaxation, before going on to discuss the dissociation of other carbonyls that have not been paid the same level of attention as $Cr(CO)_6$ in the next two chapters. The diagnostic tools are the epikernel principle and a test for the presence of the pseudo-Jahn-Teller effect using the CASSCF method. These two tools will be discussed fully in sections 6.2 and 6.3. We begin with a review of the most pertinent literature, both experimental and theoretical, of investigations into the photodissociation mechanism of $Cr(CO)_6$.

6.1.1 Experimental studies of the photochemistry of $Cr(CO)_6$

Some of the earliest work that looked at the photochemistry of $Cr(CO)_6$ used infrared spectroscopy and techniques such as flash photolysis to investigate the unsaturated intermediates in the photodissociation process. Such papers include the studies of Church and co-workers [1] who studied $Cr(CO)_6$ in a solution of cyclohexane using flash photolysis. They presented results which indicated the presence of a $Cr(CO)_5$ photoproduct with C_{4v} symmetry, already mentioned in chapter 4. Another paper [2] showed production of $Cr(CO)_5(H_2)$ following flash photolysis of $Cr(CO)_6$ in a solution of cyclohexane saturated with H_2. Stolz, Dobson and Sheline looked at the infrared

spectra of the then suspected group 6 pentacarbonyl intermediates of chromium, molybdenum and tungsten in 1962 and 1963 [3, 4]. These papers are important because they supported the idea that the initial step in the photodissociation process is the loss of one CO ligand as opposed to multiple CO loss. Analysis of the infrared spectra CO stretching vibrations managed to rule out the presence of other possible intermediates of the dissociation process such as the $W(CO)_5$ anion and the $W_2(CO)_{10}$ anion dimer with analogous results obtained for the other group 6 pentacarbonyls. Other groups also provided early studies of the structure of the pentcarbonyl intermediates of chromium and the other group 6 metals using infrared spectroscopy. These include the study by Kundig and Ozin from 1974 [5] in which they used matrix isolation infrared spectroscopy with CO/Ar matrices. They concluded that the structure of the $Cr(CO)_5$ intermediate was a D_{3h} symmetry trigonal bipyramid in the CO/Ar matrix but when a pure CO matrix is used then the structure believed to be present was '$Cr(CO)_5S$' where 'S' denotes either an oxygen bonded 'isocarbonyl' ligand (discussed in chapter 1) or a carbonyl ligand that binds sideways through its multiple bond in an *x*2 manner (again, this bonding mode was discussed in chapter 1). Graham and co-workers in 1971 also used infrared spectroscopy to study the photochemistry of the group 6 pentacarbonyl intermediates [6] in low temperature matrices. They looked to disprove the possibility that $Cr(CO)_5$ could form a D_{3h} symmetry structure that is more stable than a C_{4v} symmetry structure. Their proposed reaction scheme agreed with the results of Black and Braterman [7] in that there could not be a stable D_{3h} symmetry structure of $Cr(CO)_5$ but Graham and co-workers did mention that there could be a rapid equilibrium lying between C_{4v} and D_{3h} symmetry structures lying towards the C_{4v} symmetry structure.

Turner and co-workers performed a number of spectroscopic studies in low temperature matrices on the group 6 metal carbonyls chromium, molybdenum and tungsten [6, 8, 9, 10, 11]. These studies are important here because they were some of the first to investigate the nature of the initial photoproducts of the group 6 metal carbonyls. One paper looked at both hexa- and pentacarbonyls of these three metals and found that the preferred structure of the pentacarbonyl intermediates was of C_{4v} symmetry and not a D_{3h} symmetry trigonal bipyramid. These species were also shown in another paper to be very matrix-sensitive in a variety of matrices. They concluded in this study that interaction between the matrix and the coordination 'hole' of the pentcarbonyl caused changes in the visible band of the spectrum. They also went on to

discuss how care should be taken when using these low temperature matrix methods when looking at the photochemistry of unstable reaction intermediates. However they also note that further, more in-depth, studies of these species should reveal new properties of these, at the time, mysterious carbonyls and that other stable structures of the carbonyls could exist. The other study performed by this group considered the possible mechanism to reach $Cr(CO)_5$ from $Cr(CO)_6$ in a variety of matrices. Evidence from UV, and IR spectra in a CO/Ar matrix, showed the formation of $Cr(CO)_5$•CO and $Cr(CO)_5$•Ar adducts. The authors looked at reacting Cr and CO in the argon matrix and also changing the concentration of the matrix in order to get more information, but found that broad bands in the spectra and CO affecting the high frequency region of the spectra made them very difficult to interpret. The high concentrations of CO in all matrices also diluted any clear features and contributed to the difficulty in interpreting the spectra. These studies showed how hard it was to predict the structure of these initial pentacarbonyl intermediates using the best methods available at the time. They also show that debate had begun as to what structure the pentacarbonyl intermediates actually adopted, and it will be shown that it was not until recently that major advances in experimental and theoretical methods allowed these questions to be definitively answered for the group 6 metal carbonyls and other binary carbonyls.

Early matrix-based experimental studies like the ones discussed above, when absorption data are well defined, can provide valuable information on the structure of the unsaturated fragments formed in the photodissociation of these carbonyls. They can resolve structural features of these intermediates if the spectroscopic methods used are highly sensitive. However much effort in the last thirty years or so has gone into studying the excited states of $Cr(CO)_6$ and the photochemistry of the unsaturated fragments formed during the photodissociation process without matrix or solvent effects. It should be noted here that these fragments are extremely reactive even in a relatively inert matrix such as an argon matrix. Therefore, in order to investigate this many studies looking at the photodissociation of $Cr(CO)_6$ in the gas phase have been reported (similar studies for other binary carbonyls are discussed in chapters 7 and 8). Early gas phase studies include the report of Seder, Church and Weitz [12] from 1986 that studied the excimer laser photolysis of gas phase $Cr(CO)_6$. Transient infrared spectra of the unsaturated fragments $Cr(CO)_x$ (x=5,4,3,2) were studied and the

structures of these studies were predicted. It was found here that the initial product of photodissociation was $Cr(CO)_5$, produced on a short (picosecond) timescale with a structure of C_{4v} symmetry, probably a square pyramid structure. The authors then compared and contrasted their results with that of condensed phase studies, as they believed that the initial $Cr(CO)_5$ photoproduct, with large amounts internal vibrational internal energy, could be rapidly relaxed (on a picosecond timescale) in the condensed phase due to collisions with the solvent molecules. This same fragment in the gas phase could not be relaxed on such a fast timescale by collisions and instead further dissociation occurs to produce the other fragments observed. Weitz later reviewed the study of metal carbonyl fragments in the gas phase using transient infrared spectroscopy [13].

The recent development of ultrafast, laser-based experiments and their use in the study of the photodissociation process of $Cr(CO)_6$ and other binary carbonyls has shed new information on the initial photodissociation dynamics and states which are involved in the photodissociation process. These femtosecond lasers are used to 'pump' the system with laser pulses that are ultrafast in duration so are broad in the frequency domain. The 'pumping' of the system creates non-stationary excited state vibrational wavepackets, as the broad frequency domain laser pulses coherently and simultaneously (at the same time) excite several vibrational levels in an excited electronic state of the system. As the nuclei respond to the excitation further laser pulses at fixed time delays from the initial 'pump' pulse can probe the complex and retrieve information about the excited state dynamics of the photodissociation such as time constants for each sequential step in the process, and the intermediates formed in the process. This type of experiment is very important because the results they produce give an unprecedented insight into the complex dissociation pathway. The group of Fuβ have performed perhaps the most experimental work on $Cr(CO)_6$, and indeed other binary carbonyls as discussed in chapter 1 and in chapters 7 and 8 [14, 15, 16, 17]. Also the work of Gutmann *et al* in [18]. Through these studies a general reaction scheme was proposed. The initial state populated after excitation is a charge transfer state, not a ligand field state as was previously believed [19, 20, 21] and vibronic interactions on a ultrafast timescale then take place that causes the system to relax down to a dissociative state. From here a CO ligand is lost from this state in a timescale of a few hundred femtoseconds. The resulting initial photoproduct can then adopt a structure that is Jahn-

Teller degenerate in the singlet spin manifold, a D_{3h} symmetry trigonal bipyramid structure that has already been mentioned above, which can then relax to the lowest electronic singlet state on a timescale of less than a hundred femtoseconds. The process from initial excitation to the $Cr(CO)_5$ singlet photoproduct relaxing to the lowest singlet state takes less than one picosecond in total. This photochemical process has also been reported for other binary carbonyls such as the other group 6 carbonyls $Mo(CO)_6$ and $W(CO)_6$, $Mn_2(CO)_{10}$ and $Fe(CO)_5$. A schematic of this process was presented in chapter 1. The case of $Mn_2(CO)_{10}$ and $Fe(CO)_5$ are slightly more complicated and these species are the subjects of chapters 7 and 8 respectively, and so will not be discussed further here. $Ni(CO)_4$ is thought to undergo a different dissociation after initial excitation and ejection of a single CO ligand that involves a long-lived electronic excited state that instead undergoes radiative (fluorescence) decay. This is due to the fact that $Ni(CO)_3$ will not be able to form a Jahn-Teller active geometry with its full $3d^{10}$ shell. The other carbonyls here do not have a full d^{10} shell so will have an electron 'hole' in the degenerate orbitals of the Jahn-Teller geometry that will facilitate coupling between the electronic states.

An examination of the geometries that singlet $Cr(CO)_5$ can adopt leads to the conclusion that if it should adopt a D_{3h} symmetry trigonal bipyramid structure then the Fuβ experiments indicate that the system passes through a conical intersection to the lowest singlet state because the timescale of the process is much faster than other relaxation pathways such as fluorescence, intersystem crossing to some long-lived intermediate, and phosphorescence. The other clue comes in the observation of coherent oscillations in the transient ion spectra produced by the probe laser pulses. Such spectra are shown in figure 6.1 and include both the oscillatory part in the middle and the Fourier transform of this spectrum, the frequency part, on the right. The feature of these spectra that is important here is that the frequency spectra are all dominated by one peak that relates to a single molecular vibration. What this indicates is that the ground state unsaturated species are focussing almost all their energy into one molecular vibration, by measurement of the ion signals. This is indicative of a highly efficient relaxation pathway such as a conical intersection where the $Cr(CO)_5$ fragment was believed to 'pseudo-rotate' around the lower half of the cone of intersection, and the active

vibration in the spectra relates to an OC-Cr-CO bending vibration that causes this pseudo-rotation.

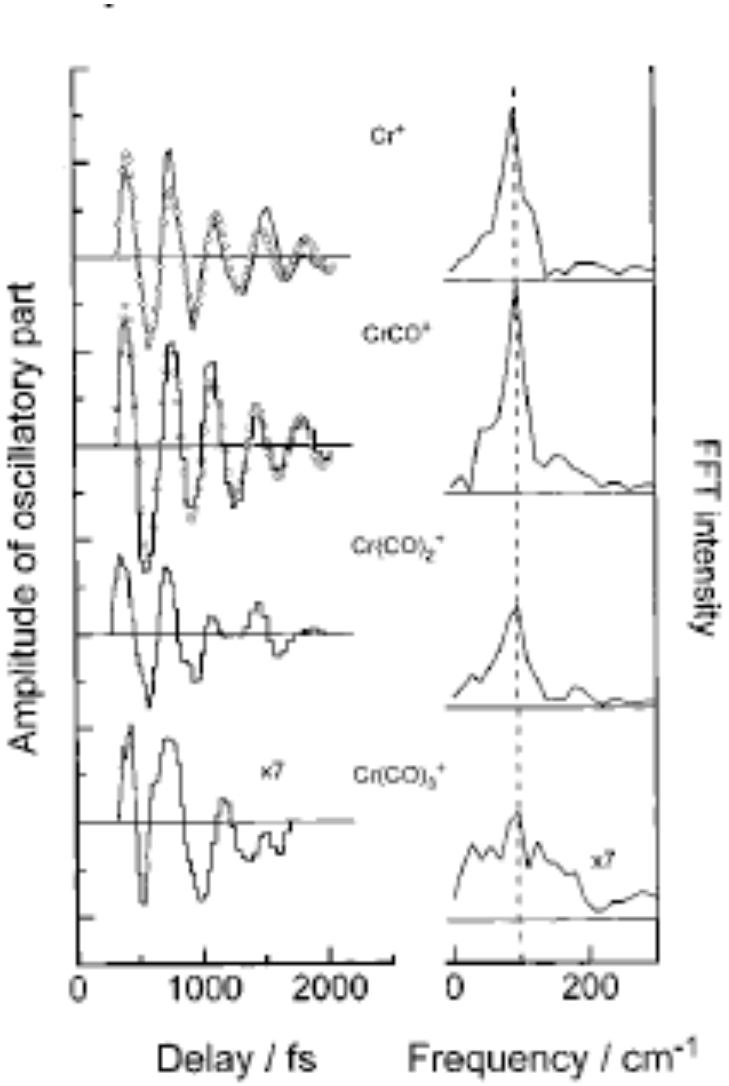

Figure 6.1 Coherent oscillations observed by Fuβ and co-workers in the transient ion spectra in the photodissociation of $Cr(CO)_6$ [16].

Though whilst experiment can imply the presence of a conical intersection in this system only a theoretical investigation can accurately probe the relevant coupled potential energy surfaces. Such investigations have already been carried out and are reviewed in section 6.1.2 along with other theoretical studies of the photochemistry of $Cr(CO)_6$.

6.1.2 Theoretical studies of the photochemistry of $Cr(CO)_6$

Recent (within the last twenty years or so) theoretical studies which looked at the reactive photochemistry of $Cr(CO)_6$ looked at the bonding properties such as bond lengths and dissociation energies using highly correlated methods such as CCSD(T), CASSCF and CASPT2 [22, 23]. Following on from the results and photodissociation mechanism for $Cr(CO)_6$ proposed by the group of Fuβ theoretical studies have been reported that tried to explain the ultrafast relaxation behaviour and dynamics of the processes inferred by experiment [24, 25]. They focussed on the steps involving ultrafast relaxation of the $Cr(CO)_5$ fragment to the lowest singlet state through a conical intersection. It is this process along with ejection of the first CO ligand that are the fundamental steps in the photochemistry of $Cr(CO)_6$ and other binary carbonyls discussed above and in chapters 7 and 8.

In the works reported by Paterson and co-workers they focused on the relaxation of the singlet $Cr(CO)_5$ through a point of conical intersection, looking at the surface topology around the point of intersection, and ran dynamics simulations of this process. The CASSCF method was used as multi-configurational methods are needed to give a balanced description of the potential energy surfaces in the region of a conical intersection with a range of geometries including a Jahn-Teller geometry, and seam of degeneracy, as discussed in chapter 2. An active space consisting of all six d electrons of chromium and the four lowest energy 3d orbitals together with higher lying equivalents of each orbital with a node in the internuclear Cr-CO region was used. Figure 6.2 shows a picture of a pair of such orbitals. A basic active space to describe the ground and LF states would be CAS(6,5) but it was found that inaccurate bond lengths and symmetry breaking problems occurred with this active space. This can be explained when considering the intra-orbital dynamic correlation effects on the Cr-CO bonds due to the nature of dative bonding. This process has been used before for improving CASSCF active spaces [26] and was found to give a reliable and accurate description of the Cr-CO bonds. The extra d orbitals are effectively the 4d atomic orbitals of chromium and are the out of phase combinations of the smaller and larger exponents basis functions, while the 3d orbitals are the in phase combinations in at least a double zeta sized basis set. The extra dynamic correlation contributions in the Cr-CO bonds were evident in the ground state occupation numbers of the optimised active space

orbitals that are obtained from the diagonal elements of the one electron density matrix. The occupation number of each 4d orbital is non zero, around 0.2. It was argued that this method of constructing active spaces in this way was effective in describing a range of different geometries around the point of intersection, as well as ground state barrier heights and geometrical parameters [24].

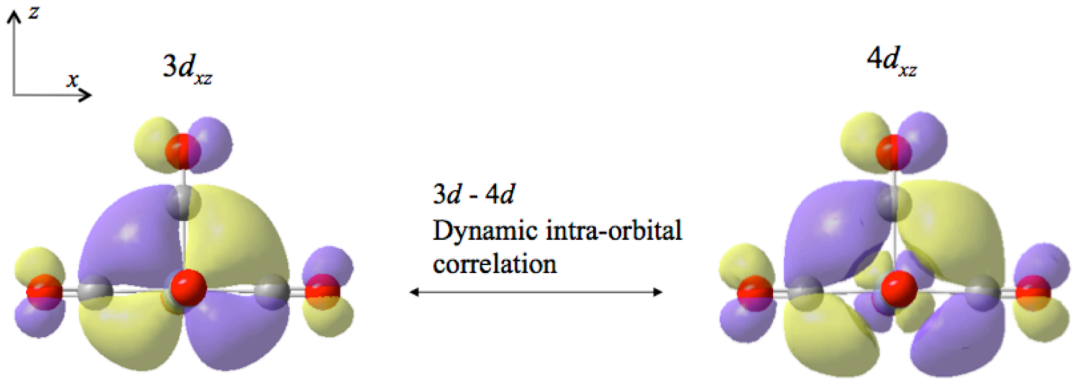

Figure 6.2 Schematic of both types of d orbtial used in the 'orbital doubling' procedure implemented by Paterson and co-workers [24]. Here the d_{xz} in phase and out of phase combinations of the smaller and larger exponent metal centred basis functions give the '3d' and '4d' orbitals.

As already mentioned a Jahn-Teller distortion may occur in the singlet $Cr(CO)_5$ initial photoproduct at a D_{3h} symmetry trigonal bipyramid geometry. Therefore the symmetry of the vibrational modes that will couple the component states can be established from Jahn-Teller theory. The following electronic states are possible by placing two electrons in the e′ orbitals of $Cr(CO)_5$ at this geometry: $e' \otimes e' = {}^1E' \oplus {}^1A_1' \oplus {}^3A_2'$.

The $^3A_2'$ state would be predicted to be stable at this geometry but because the photochemistry being studied here occurs in the singlet spin manifold this state is no longer considered. It was found by the authors that the lowest energy states was the $^1E'$ state (i.e. the Jahn-Teller active state) and not the open-shell non-degenerate $^1A_1'$ state.

The lowest singlet state potential energy surface around the point of intersection was investigated with the CASSCF method. The size of the CASSCF active space was reduced from CAS(6,10) to CAS(6,8) where one 3d and one 4d orbital was removed

from the CAS(6,10) active space because according to the schematic orbital correlation diagram one orbital remains unoccupied at the three geometries relevant to the surface topology around the intersection (d_z^2 and d_x^2-$_y^2$ in the D_{3h} and C_{4v} symmetry geometries respectively), and that these two orbitals can mix at intermediate geometries between these. Reducing the size of the active space therefore had no adverse effect on the accuracy on the results obtained; while this smaller active space also allowed analytical gradients and Hessian matrices to be calculated. They determined that from the Jahn-Teller D_{3h} symmetry geometry the system distorts along either of a pair of e′ symmetry vibrational modes down to a C_{4v} symmetry square pyramidal minimum. An orbital correlation diagram between these geometries is shown in figure 6.3.

Semi-classical surface hopping dynamics simulations were carried out to give a mechanistic insight of the relaxation process of singlet $Cr(CO)_5$ and determine whether the system can dynamically reach this Jahn-Teller induced conical intersection and relax to the lowest singlet state in less than one picosecond. It was found that a CO ligand was ejected approximately 90fs after running the trajectory on the lowest energy singlet ligand field state. This state was thought to be populated after initial excitation to a charge transfer state as discussed above. The ejected CO ligand left in a rotationally excited state, and the remaining ligands began to bend inwards to fill the coordination hole on the newly formed $Cr(CO)_5$ fragment. The positions and momenta of the remaining $Cr(CO)_5$ fragments after 100fs were then used alone for further study, including the non-adiabatic event.

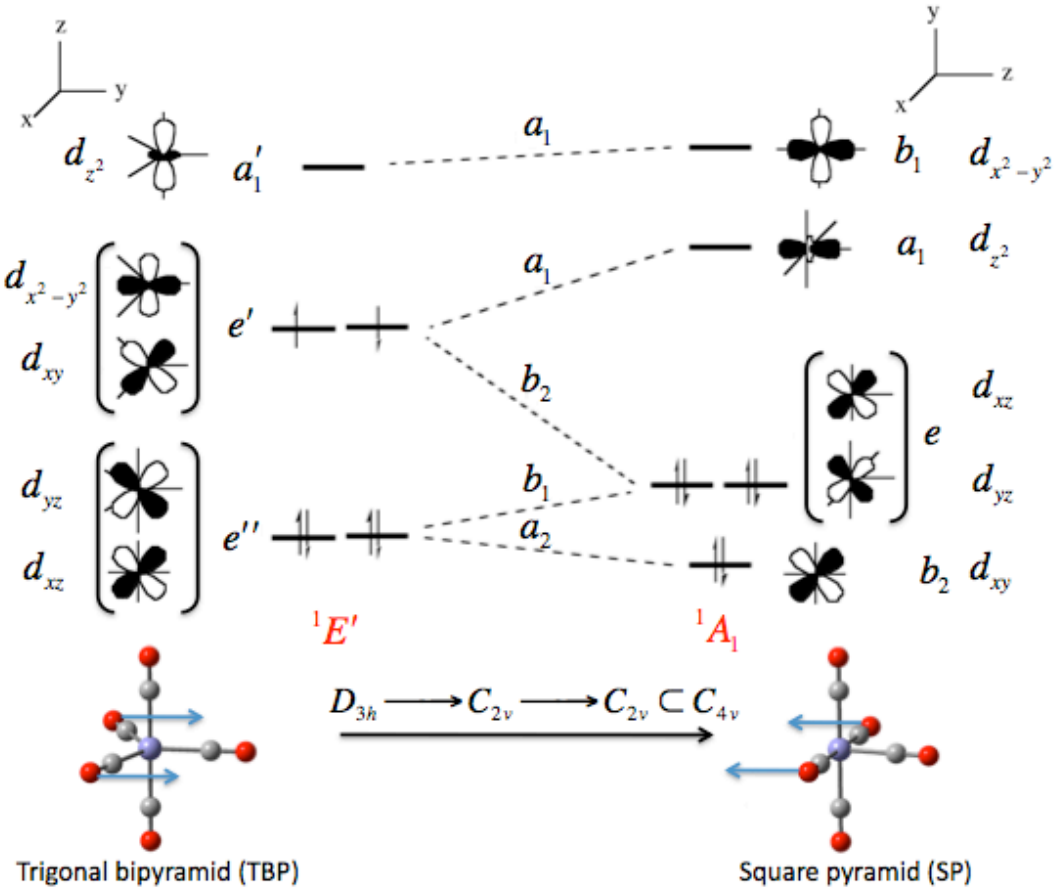

Figure 6.3 Orbital correlation diagram between the D_{3h} trigonal bipyramid and C_{4v} square pyramidal geometries of $Cr(CO)_5$ taken from [27]. Here in the singlet spin manifold the trigonal bipyramidal structure is unstable and is the Jahn-Teller geometry of this fragment.

After ejection of a CO ligand the remaining CO ligands bend inwards to fill in the coordination hole and form a D_{3h} trigonal bipyramid symmetry structure within a further 80fs with angles between equatorial CO ligands all equal to 120^0. From this point the system ultimately decays to the lowest singlet state through a Jahn-Teller conical intersection. As the system passes to the lower surface the motion in the branching space changes from symmetric to antisymmetric bending, and the system starts to vibrate along a pseudo-rotational coordinate shown in figure 6.3. It was found that the system becomes trapped in the well of a square pyramidal minimum. The OC-Cr-CO bending vibration was found to have a vibrational frequency of $98cm^{-1}$ that compared favourably to the frequency of the coherent oscillation found by Fuβ and co-workers in their experimental investigations of this system. It should be stressed that this study was conducted to give mechanistic detail of the photodissociation process but was also of use in constructuing fully quantum mechanical dynamics as it was able to

point out the important vibrational modes that are needed to construct model Hamiltonians for wavepacket dynamics studies as discussed below.

Thus, following on from the CASSCF/surface hopping study a quantum wavepacket dynamics study was then performed [25]. This dynamics method accurately simulates the non-stationary excited state wavepackets evolving on the coupled potential energy surfaces, but requires a model vibronic coupling Hamiltonian to provide the potential energy surfaces. Adiabatic potentials were generated using the same electronic structure methods as in the previous surface hopping study. These potentials were then used to fit the parameters of the linear vibronic coupling model Hamiltonian. The authors reported that an important issue arose when trying to fit the vibronic coupling model to the adiabatic surfaces in that the $E \otimes e$ Jahn-Teller model assumed to be present was not accurate enough to fit the adiabatic surfaces. An accurate fit was only obtained when a non-degenerate state was included, that was pseudo-Jahn-Teller coupled to the degenerate E state. The inclusion of this state to make the Jahn-Teller model at the point of conical intersection $(E \oplus A) \otimes e$ through the presence of pseudo-Jahn-Teller coupling is justified in section 6.4. This dynamics method, if given correct potentials using a scale model Hamiltonian will give very accurate information about the different coupling effects that occur as the system passes through the intersection and it was indeed found that a pseudo-Jahn-Teller effect was responsible for the warping of the 'trough' between C_{4v} minima and C_{2v} transition states and not second order Jahn-Teller effects (discussed in chapter 2). Subsequent dynamics simulations were found to get the essential features of the Jahn-Teller surfaces the same as the previous surface hopping studies but motion on the surface after passing through the intersection was found to be radial rather than circular as was found with surface hopping study. This is an interesting difference between the two dynamics methods and future improved dynamics studies are needed to resolve this difference.

The most recent theoretical study of the photochemistry of $Cr(CO)_6$ can from Crespo-Otero and Barbatti [28] who looked at the one-photon absorption cross sections of $Cr(CO)_6$ in relation to how well TD-DFT methods can predict the oscillator strengths of allowed electronic states (i.e. the two main bands in the electronic spectrum already discussed in chapter 4) and also performed dynamics simulations on the

photodissocition of $Cr(CO)_6$ into $Cr(CO)_5$ using potential energy curves for Cr-C bond dissociation in the ground and first five excited states with TD-DFT (B3LYP functional and basis sets triple zeta in size). Nonadiabatic coupling terms were accounted for numerically, based on overlap between TD-DFT excited states at distorted geometries, as TD-DFT on its own is unable to simulate a system passing through a conical intersection or compute a degenerate ground state. From the dynamics simulations it was found that the dissociation process from initial excitation until the system passes through the conical intersection followed three regimes, the first being initial relaxation of $Cr(CO)_6$ to the dissociative ligand field state in 19fs, dissociation of one carbonyl ligand a further 22fs later (with the ejected CO ligand highly rotationally excited) and relaxation of the $Cr(CO)_5$ fragment through the conical intersection after 148fs. As already stated this nonadiabatic motion through the intersection was not investigated because the TD-DFT methods used were not able to compute this. The dynamics calculations were stopped when the difference in energy between the S_1 and S_0 state of $Cr(CO)_5$ at a D_{3h} trigonal bipyramid geometry became less than 0.2eV. These results showed the same general features of the dissociation process as the previous two studies discussed but observed differences in the time constants for each step between their study and the previous two theoretical studies and experiment. They believed their results to be the most accurate and that experimental studies slightly underestimated the time for the system to pass through the intersection.

The work already performed on this system as regards its photodissociation in the singlet spin manifold is already quite extensive, and in this chapter two diagnostic tools are applied to this system to further resolve the potential energy surface on the lowest singlet state of $Cr(CO)_5$ around the point of conical intersection. These tools deal with the presence of the pseudo-Jahn-Teller coupling between the upper and lower surfaces, and the number of equivalent minima and transition states around the point of intersection based on the symmetry of the Jahn-Teller geometry.

6.2 Computational details

The application of the epikernel principle required no new computation; instead it is applied by analysing the symmetry properties of the Jahn-Teller geometry. The CASSCF pseudo-Jahn-Teller diagnostic required computation of the C_{2v} symmetry transition state of $Cr(CO)_5$ and this was performed using a CAS(6,8) active space discussed above with a cc-pVDZ basis set (all electron basis set on chromium from [29]).

6.3 Application of the epikernel principle

The tool used to study the Jahn-Teller surface here, which is also applied to $Mn(CO)_5$ and $Fe(CO)_4$ in the next two chapters, is the epikernel principle of Ceulemans and Vanquickenborne [30]. To apply this tool one evaluates the kernels (K_i) and epikernels (E_i) for a given irreducible representation in a molecular point group. Standard nomenclature was proposed in the form $K_i(G, \Lambda)$ and $E_i(G, \Lambda)$ where this means the *i*-th kernel/epikernel of the irreducible representation Λ in the group *G*. Kernels are groups of symmetry elements preserved by distortion along a vector spanning the irreducible representation Λ, and epikernels are selected preserved groups of higher symmetry that are only preserved in part of the (degenerate) distortion space. The epikernel principle states that in a given linear Jahn-Teller distortion the highest-ranking epikernels will correspond to point groups of minima, and lower ranking epikernels and kernels will correspond to saddle points of various orders.

When this tool is applied to the D_{3h} symmetry $Cr(CO)_5$ Jahn-Teller geometry, in a doubly degenerate state, the largest epikernel of e' is $E(D_{3h}, e')=C_{2v}$. The quotient between the orders of the non-abelian Jahn-Teller point group with the epikernel subgroup determines the number of equivalent epikernel distortion directions. So this would be $n_{E(D_{3h},e')} = \frac{|n_{D_{3h}}|}{|n_{C_{2v}}|} = \frac{12}{4} = 3$. The ground state S_0 potential energy surface around the point of conical intersection is shown in figure 6.4. The three equivalent C_{2v} distortion directions (orange arrows) in figure 6.4 are labeled $E^1(D_{3h},e'), E^2(D_{3h},e')$ and

$E^3(D_{3h}, e')$. The sign of these terms indicates the distortion direction where a positive case as shown above is for the forward direction and when each label is preceded by a minus (-) sign this is for the reverse direction. The epikernels are the same with these labels only the distortion direction changes. The Jahn-Teller distortion shown in figure 6.4 is the $E \otimes e$ Jahn-Teller model and it can be seen that forward distortion leads to minima and reverse distortion leads to the saddle point (C_{2v} transition state) of the same symmetry. These distortion directions relate to the bending of the OC-Cr-CO equatorial bond angles away from the value of 120^0 at the D_{3h} geometry, with the total with the other two angles still summing up to 360^0. A forward distortion from figure 6.4 relates to two equatorial angles closing while the third opens up, and vice versa for reverse distortion.

One other point to note here is that while the Jahn-Teller trough in figure 6.4 maintains C_{2v} symmetry in line with the prediction from the epikernel principle, there are points of (accidental) higher symmetry. If two equatorial OC-Cr-CO angles are equal and close to 90^0, with the remaining one close to 180^0 then this will result in the C_{4v} square pyramidal minimum structure mentioned earlier. C_{4v} is a super group of C_{2v} so care must be taken when using the epikernel principle, as it cannot predict the presence of these higher symmetry points. As there are three equivalent C_{2v} structures there must also be three equivalent C_{4v} minima, one coming from each C_{2v} and this is shown in figure 6.4.

This is an interesting case where the reverse epikernel is the transition structure and the forward epikernel the minimum due to the accidental supergroup symmetry, although the entire surface contains C_{2v} symmetry. For further details see [27].

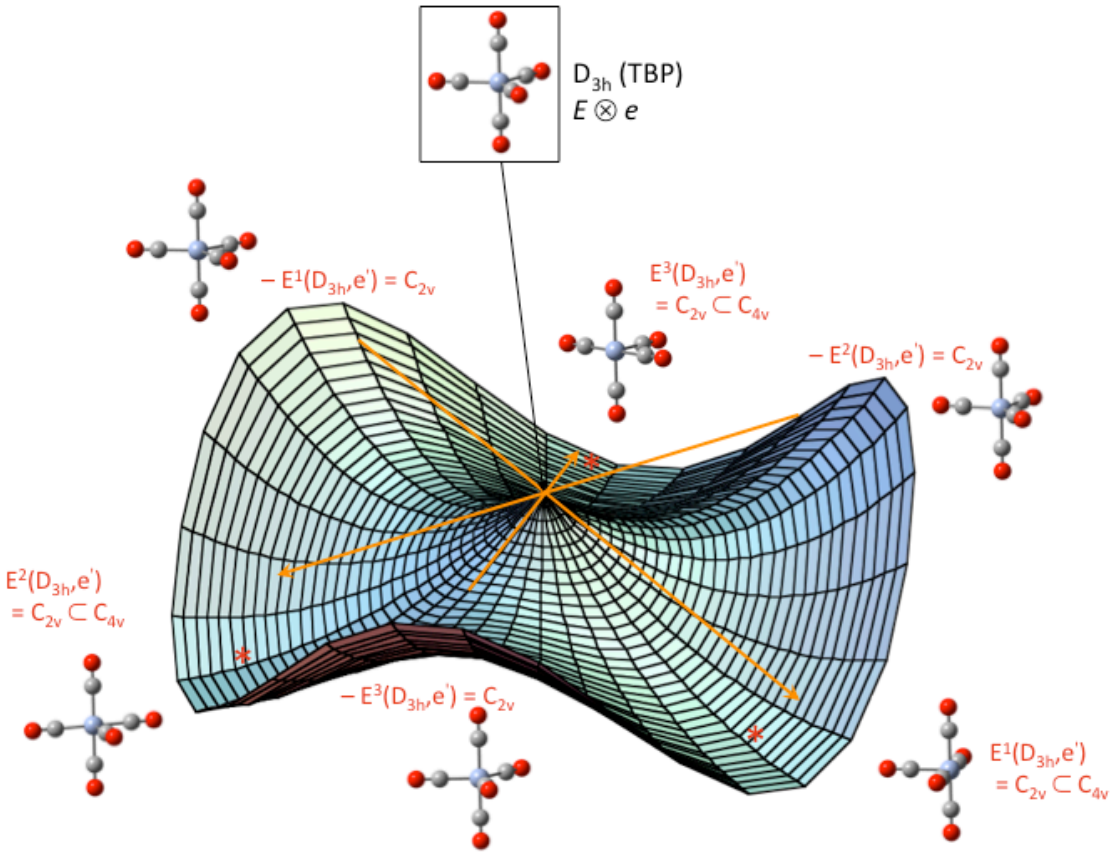

Figure 6.4 $Cr(CO)_5$ lowest adiabatic potential around $E \otimes e$ Jahn-Teller conical intersection at trigonal bipyramid (TBP) D_{3h} geometry (From [27]). There are three equivalent epikernel distortion directions (orange arrows) for a vibrational coordinate pair spanning e', $E^i(D_{3h},e')$. Motion in the forward direction leads to one of three equivalent square planar (SP) C_{4v} minima, indicated by red (*) symbols; while motion in the reverse direction leads to C_{2v} saddle-points (transition states for the interconversion of SP structures). The barrier is between minima and the transition states is around 12 kcal mol^{-1}.

6.4 Application of the pseudo-Jahn-Teller CASSCF diagnostic tool

Another tool that will be applied to this system is the pseudo-Jahn-Teller CASSCF diagnostic test developed by Bearpark and co-workers [31]. This follows on from the previously discussed dynamics study by Worth and co-workers [25] that suggested pseudo-Jahn-Teller coupling between a component of the degenerate E′ state and a higher lying non-degenerate A state. This tool is based on symmetry restrictions to CASSCF Hessian matrices, and recognises that while in a state-specific CASSCF calculation the gradient vector is totally-symmetric, and non-totally-symmetric

contributions are important for the Hessian matrix. Solutions of the so-called coupled-perturbed MCSCF (CP-MCSCF) equations can obtain these contributions and if one uses only those configuration state functions (CSFs) of a given symmetry in the Hessian evaluation, then one can exclude certain symmetry classes. This will 'switch off' the contribution of non-totally symmetric (derivative) couplings. A pseudo-Jahn-Teller interaction will be detected if one obtains a different Hessian matrix when these couplings are included to when they are not. To get a clearer understanding of what this test means it has been applied to the C_{2v} saddle point of $Cr(CO)_5$. This point was computed using only totally symmetric (A_1) CSFs and it was found that all vibrational frequencies were real, the lowest frequency mode was of b_2 symmetry with υ=51.1cm^{-1}. This point was computed again, this time including all CSFs of all symmetry classes, and it was observed that the lowest frequency mode was again of b_2 symmetry but this time υ=95.6*i*cm^{-1}. So what has occurred here at this point is that pseudo-Jahn-Teller coupling has caused a mixing of the closed shell non-degenerate ground state with an excited state, and this caused the adiabatic potential energy surface to have a negative curvature along this vibrational mode, confirming the presence of pseudo-Jahn-Teller coupling. The coupling was between the $...\left(d_{xy}\right)^2\left(d_{yz}\right)^2\left(d_{xy}\right)^2 - {}^1A_1$, and the $...\left(d_{xy}\right)^2\left(d_{yz}\right)^2\left(d_{xy}\right)^1\left(d_{x^2-y^2}\right)^1 - {}^1B_2$ adiabatic states. From a symmetry perspective this b_2 vibrational mode may couple these two states because $A_1 \otimes B_2 \otimes B_2 = A_1$. This $^1B_2$ state correlates with the open-shell non-degenerate $^1A_1'$ state at D_{3h} symmetry discussed above. Thus, this work confirms the result obtained in the wavepacket dynamics study showing the transition state arises from pseudo-Jahn-Teller coupling and not second-order coupling between components of the ^1E state as previously believed. This tool is very useful and gives information on the presence and natures of pseudo-Jahn-Teller couplings and how they can affect the topology of potential energy surfaces and the structure of transition metal complexes, an example of which is the ground state structure of an edge-sharing $Mo_2(DXylF)_2(O_2CCH_3)_2(\mu_2\text{-}O)_2$ (DXyIF=N,N'-di(2,6-xylyformamidine) complex that was believed to have a square central moiety but some surprising experimental findings found instead the central moiety was a rhomboid, application of this diagnostic test confirmed the presence of a pseudo-Jahn-Teller effect that caused the central moiety to 'skew' into a rhomboid from a square [32]. For further details see [33]. However this method does have limitations, mainly that the CP-

MCSCF equations need to be solved which is only practicable for CASSCF active spaces up to around CAS(8,8) in size. Given this it can still be applied to other systems such as $^{2}Mn(CO)_5$ in the next chapter, but could not be applied to $^{1}Fe(CO)_4$ (discussed in chapter 8) due the size of the CASSCF active space needed to accurately describe the potential energy surfaces (CAS(8,10)).

6.5 Conclusions

The photochemistry and photodissociation mechanism of singlet $Cr(CO)_6$ has been given much attention in the past. Adding to the established body of work two theoretical tools have been applied to gain more information about the potential energy surface of the lowest singlet state of $Cr(CO)_5$ after it has passed through a conical intersection and also on the presence and natures of pseudo-Jahn-Tellers couplings, and how they affect the surface topology around the point of conical intersection. This system is used here as an introduction to the ultrafast photochemical mechanism than many binary carbonyls exhibit, and how theoretical methods can be used to gain information that experiment is not able to, especially around a point of conical intersection. Further theoretical work on the Jahn-Teller effect, conical intersections and metal carbonyl photochemistry can be seen in the following works [34, 35, 36, 37]. With this chromium carbonyl, and its mechanism for photodissociation in mind, the next two chapters focus on two other binary carbonyls whose photodissociation mechanisms are potentially more complicated than that of $Cr(CO)_6$ and much less well researched theoretically, namely $Mn_2(CO)_{10}$ and $Fe(CO)_5$.

6.6 References

[1] Church, S. P.; Grevels, F. W.; Hermann, H.; Schaffner, K., Structures and kinetics of $Cr(CO)_5$ and $Cr(CO)_5 \bullet H_2O$ in cyclohexane solution - flash-photolysis study of $Cr(CO)_6$ with infrared and visible detection. *Inorg. Chem.* **1985,** 24, 418-422.

[2] Church, S. P.; Grevels, F. W.; Hermann, H.; Schaffner, K., Flash-photolysis of $Cr(CO)_6$ in H_2-saturated cylcohexane solution - IR spectroscopic evidence for a $Cr(CO)_5(H_2)$ complex at room temperature. *J. Chem. Soc.-Chem. Commun.* **1985**, 30-32.

[3] Stolz, I. W.; Dobson, G. R.; Sheline, R. K., The infrared spectrum and evidence for the structure of a new metal carbonyl. *J. Am. Chem Soc.* **1962,** 84, 3589.

[4] Stolz, I. W.; Dobson, G. R.; Sheline, R. K., IR spectra and structures of metal carbonyl deravites III. *Inorg. Chem.* **1963,** 2, 1264.

[5] Kundig, E. P.; Ozin, G. A., Trigonal bipyramid chromium pentacarbonyl and its implications to structure and bonding considerations of pentacarbonyls and pentacarbonyl anions. *J. Am. Chem Soc.* **1974,** 96, 3820-3823.

[6] Graham, M. A.; Poliakof.M; Turner, J. J., Photochemistry of the group-VI hexacarbonyls in low-temperature matrices 1. Pentacarbonyls of chromium, molybdenum, and tungsten. *J. Chem. Soc. A., Inorg. Chem.* **1971**, 2939-&.

[7] Black, J. D.; Braterman, P. S., Purported trigonal bipyramidal $Cr(CO)_5$ *J. Am. Chem Soc.* **1975,** 97, 2908-2909.

[8] Burdett, J. K.; Graham, M. A.; Perutz, R. N.; Poliakoff, M.; Rest, A. J.; Turner, J. J.; Turner, R. F., Photochemistry of group-6 hexacarbonyl in low-temperature matrices 5. Routes to square pyramidal matrix-isolated chromium pentacarbonyl. *J. Am. Chem Soc.* **1975,** 97, 4805-4808.

[9] Burdett, J. K.; Perutz, R. N.; Poliakoff, M.; Turner, J. J., Polarized photochemistry and photoorientation of pentacarbonylchromium in low-temperature matrices. *J. Chem. Soc.-Chem. Commun.* **1975**, 157-159.

[10] Perutz, R. N.; Turner, J. J., Photochemistry of group vi hexacabonyls in low-temperature matrices 2. Infrared spectra and structures of ^{13}CO enriched hexacarbonyls and pentacarbonyls of chromium, molybdenum and tungsten. *Inorg. Chem.* **1975,** 14, 262-270.

[11] Perutz, R. N.; Turner, J. J., Photochemistry of the group 6 hexacarbonyls in low-temperature matrices. III. Interaction of the pentacarbonyls wth noble gases and other matrices. *J. Am. Chem Soc.* **1975,** 97, 4791-4800.

[12] Seder, T. A.; Church, S. P.; Weitz, E., Wavelength dependence of excimer laser photolysis of $Cr(CO)_6$ in the gas-phase - a study of the infrared-spectroscopy and reactions of the $Cr(CO)_5$, $Cr(CO)_4$, $Cr(CO)_3$, $Cr(CO)_2$ fragments. *J. Am. Chem Soc.* **1986,** 108, 4721-4728.

[13] Weitz, E., Studies on coordinatively unstaurated metal carbonyls in the gas phase. *J. Phys. Chem.* **1987,** 91, 3945-3953.

[14] Fuss, W.; Trushin, S. A.; Schmid, W. E., Ultrafast photochemistry of metal carbonyls. *Res. Chem. Intermed.* **2001,** 27, 447-457.

[15] Trushin, S. A.; Fuss, W.; Schmid, W. E., Conical intersections, pseudorotation and coherent oscillations in ultrafast photodissociation of group-6 metal hexacarbonyls. *Chem. Phys.* **2000,** 259, 313-330.

[16] Trushin, S. A.; Fuss, W.; Schmid, W. E.; Kompa, K. L., Femtosecond dynamics and vibrational coherence in gas-phase ultraviolet photodecomposition of $Cr(CO)_6$. *J. Phys. Chem. A* **1998,** 102, 4129-4137.

[17] Trushin, S. A.; Kosma, K.; Fuss, W.; Schmid, W. E., Wavelength-independent ultrafast dynamics and coherent oscillation of a metal-carbon stretch vibration in photodissociation of $Cr(CO)_6$ in the region of 270-345 nm. *Chem. Phys.* **2008,** 347, 309-323.

[18] Gutmann, M.; Janello, J. M.; Dickebohm, M. S.; Grossekathofer, M.; Lindener-Roenneke, J., Ultrafast dynamics of transition metal carbonyls: Photodissociation of $Cr(CO)_6$ and $Cr(CO)_6(CH_3OH)(n)$ heteroclusters at 280 nm. *J. Phys. Chem. A* **1998,** 102, 4138-4147.

[19] Beach, N. A.; Gray, H. B., Electronic structure of metal hexacarbonyls. *J. Am. Chem Soc.* **1968,** 90, 5713-5721.

[20] Ben Arnor, N.; Villaume, S.; Maynau, D.; Daniel, C., The electronic spectroscopy of transition metal carbonyls: The tough case of $Cr(CO)_6$. *Chem. Phys. Lett.* **2006,** 421, 378-382.

[21] Rosa, A.; Baerends, E. J.; van Gisbergen, S. J. A.; van Lenthe, E.; Groeneveld, J. A.; Snijders, J. G., Electronic spectra of $M(CO)_6$ (M = Cr, Mo, W) revisited by a relativistic TD-DFT approach. *J. Am. Chem Soc.* **1999,** 121, 10356-10365.

[22] Ehlers, A. W.; Frenking, G., Theoretical studies of M-CO bond lengths and first dissociation energies of hte transition metal hexacarbonyls $Cr(CO)_6$, $Mo(CO)_6$ and $W(CO)_6$. *J. Chem Soc. Chem. Commun.* **1993**, 1709.

[23] Persson, B. J.; Roos, B. O.; Pierloot, K., A theoretical-study of the chemical bonding in $M(CO)_6$ (M=Cr, Fe, and Ni). *J. Chem. Phys.* **1994,** 101, 6810-6821.

[24] Paterson, M. J.; Hunt, P. A.; Robb, M. A.; Takahashi, O., Non-adiabatic direct dynamics study of chromium hexacarbonyl photodissociation. *J. Phys. Chem. A* **2002,** 106, 10494-10504.

[25] Worth, G. A.; Welch, G.; Paterson, M. J., Wavepacket dynamics study of $Cr(CO)_5$ after formation by photodissociation: Relaxation through an $(e \oplus a) \otimes e$ Jahn-Teller conical intersection. *Mol. Phys.* **2006,** 104, 1095-1105.

[26] Pierloot, K.; Tsokos, E.; Vanquickenborne, L. G., Optical spectra of $Ni(CO)_4$ and $Cr(CO)_6$ revisited. *J. Phys. Chem.* **1996,** 100, 16545-16550.

[27] Mckinlay, R. G.; Paterson, M. J., The jahn-teller effect in binary transition metal carbonyl complexes. In *The Jahn Teller effect: Fundamentals and implications for physics and chemistry*, Koppel, H.; Barentzen, H.; Yarkony, D. R., Eds. Springer-Verlag: Heidelberg, 2009.

[28] Crespo-Otero, R.; Barbatti, M., $Cr(CO)_6$ photochemistry: Semi-classical study of uv absorption spectral intensities and dynamics of photodissociation. *J. Chem. Phys.* **2011,** 134, 164305.

[29] Balabanov, N. B.; Peterson, K. A., Systematically convergent basis sets for transition metals. I. All-electron correlation consistent basis sets for the 3d elements Sc–Zn. *J. Chem. Phys.* **2005,** 123, 064107.

[30] Ceulemans, A.; Vanquickenborne, L. G., The epikernel principle. *Struct. Bond.* **1989,** 71, 125-159.

[31] Bearpark, M. J.; Blancafort, L.; Robb, M. A., The pseudo-Jahn-Teller effect: A CASSCF diagnostic. *Mol. Phys.* **2002,** 100, 1735-1739.

[32] Zurek, J. M.; Paterson, M. J., Theoretical study of the pseudo-Jahn-Teller effect in the edge-sharing bioctahedral complex $Mo_2(DXyIF)_2(O_2CCH_3)_2(\mu_2O_2)$. *Inorg. Chem.* **2009,** 48, 10652-10657.

[33] McKinlay, R. G.; Zurek, J. M.; Paterson, M. J., Vibronic coupling in inorganic systems: Photochemistry, conical intersections, and the Jahn-Teller and pseudo-Jahn-Teller effects. *Adv. Inorg. Chem.* **2010,** 62, 351-390.

[34] Wrighton, M., Photochemistry of metal carbonyls. *Chem. Rev.* **1974,** 74, 401-430.

[35] Paterson, M. J.; Bearpark, M. J.; Robb, M. A.; Blancafort, L.; Worth, G. A., Conical intersections: A perspective on the computation of spectroscopic Jahn-Teller parameters and the degenerate 'intersection space'. *Phys. Chem. Chem. Phys.* **2005,** 7, 2100-2115.

[36] Ceulemans, A.; Beyens, D.; Vanquickenborne, L. G., Symmetry aspects of Jahn-Teller activity: Structure and reactivity. *J. Am. Chem. Soc.* **1984,** 106, 5824-5837.

[37] Bersuker, I. B., Modern aspects of the Jahn-Teller effect theory and applications to molecular problems. *Chem. Rev.* **2001,** 101, 1067-1114.

Chapter 7

Analysis of the photodissociation mechanism of $Mn_2(CO)_{10}$ and relaxation mechanism of the $^2Mn(CO)_5$ initial photoproduct through a Jahn-Teller induced conical intersection

7.1 Introduction and literature review

With the previous chapter discussing the mechanism of ultrafast photodissociation that such binary carbonyls can undergo, the attention in this chapter moves to the binary carbonyl of a transition metal that sits immediately to the right of chromium in the periodic table: manganese. It has already been shown in chapter 1 that manganese forms a metal-metal bonded dimer when forming a binary carbonyl, $Mn_2(CO)_{10}$, with no bridging ligands. What is immediately apparent when thinking about the photodissociation mechanism for this species, while believed to be broadly similar to that of $Cr(CO)_6$ in terms of timescale and Jahn-Teller activity in the resulting photoproducts [1], is (that it may be) potentially more complicated than $Cr(CO)_6$ as two initial dissociation channels are possible. In $Cr(CO)_6$ all carbonyl ligands are equivalent through symmetry but with $Mn_2(CO)_{10}$ both the Mn-Mn bond or an Mn-C bond could be cleaved, and not all carbonyl ligands are equivalent. These points will be detailed, and the relaxation pathway for the $^2Mn(CO)_5$ photoproduct formed from the homolytic cleavage of the Mn-Mn bond will be analysed here. We begin, as with previous chapters, with a review of pertinent literature relating to experimental and theoretical studies of the photochemistry of $Mn_2(CO)_{10}$.

7.1.1 Experimental studies of the photochemistry of $Mn_2(CO)_{10}$

Similarly to the carbonyls discussed in previous chapters, the earliest studies of $Mn_2(CO)_{10}$ date back into the earlier and middle parts of the 20th century, establishing the structure of this bimetallic carbonyl that included establishing the structure through characterisation of the crystal structure [2, 3] which concluded that $Mn_2(CO)_{10}$ has D_{4d} symmetry, an Mn-Mn bond and no bridging carbonyl ligands.

However the focus of this chapter is the photoinduced decomposition of $Mn_2(CO)_{10}$ in the gas phase, of which there have been numerous experimental studies. Such studies, in the same fashion as those discussed in the previous chapter for $Cr(CO)_6$, but with the added complexity of two distinct reaction pathways being identified rather than one have been performed. These two channels are a heterolytic cleavage of a single Mn-CO bond or homolytic cleavage of the Mn-Mn bond. An example of an early photolysis study that looked at these two pathways is the 1986

paper by Seder, Church and Weitz [4]. They excited gas-phase $Mn_2(CO)_{10}$ with nanosecond laser pulses of various energies and monitored the dissociation process via transient infrared spectroscopy. They found that these two pathways are evident by detection of both $Mn(CO)_5$ and $Mn_2(CO)_9$ fragments in their transient spectra, but also found, as discussed before, that photoexcitation of metal carbonyls has many subtle effects in that the ratio of the dissociation pathway can be shifted to favour the Mn-CO dissociation channel by increasing the photolysis energy from 351 to 248 to 193nm, and also that by increasing the photolysis energy that further reaction pathways become available such as multiple CO loss. This was indicated by the detection of different $Mn_2(CO)_x$ fragments where $x<9$.

The seminal experimental work on $Mn_2(CO)_{10}$ that showcased its ability to photodissociate on an ultrafast timescale came in 1995 when Zewail and co-workers [5] applied femtosecond laser pulses to 'pump' $Mn_2(CO)_{10}$ and the subsequent photodissociation dynamics were probed by time-of-flight (TOF) mass spectrometry. Both of the main dissociation channels were detected with ejection of a single CO ligand believed to occur twice as fast as the cleavage of the Mn-Mn bond, which according to the authors, was due to the reduced mass in the Mn-CO cleavage being four times smaller than the Mn-Mn bond. Fuβ and co-workers have also studied the dissociation dynamics of $Mn_2(CO)_{10}$ in a similar way to that of $Cr(CO)_6$ mentioned in the previous chapter with one photon pumping at 267nm followed by multiphoton ionization at 800nm to probe the response of the nuclei. Only the Mn-CO dissociation channel was observed because the time constants for detection of ions with one metal were the same as ions with two, (so the experimental setup was concluded to be insensitive to the Mn-Mn dissociation channel). The dissociation time was found to be 42fs and two different coherent oscillations were observed that were thought to relate to the loss of an axial or equatorial CO ligand. The resulting fragments then relax and persist for up to 1.7ps.

Near ultrafast photodissociation of $Mn_2(CO)_{10}$ was also detected in the solution phase. A study by Zhang and Harris in 1991 [6] used pico-second time resolved laser pulses. Both dissociation channels were observed with initial photodissociation found to occur in less than 2-3 picoseconds with vibrationally hot $Mn_2(CO)_9$ reaching an

equilibrium with the cyclohexane solvent between 15 and 170ps through two decay channels. This $Mn_2(CO)_9$ fragment then persists for longer time periods (many ns) once vibrationally cooled. The $Mn(CO)_5$ fragment was found to vibrationally cool in less than 10ps then also persists for many ns, and this showed that the $Mn(CO)_5$ fragment transfers its excess vibrational energy to the solvent much faster than the $Mn_2(CO)_9$ fragment. Vibrational coherence effects were also observed in the dissociation process in a later cyclohexane solution study using near ultrafast (ps) infrared spectroscopy by Owrutsky and Baronavski [7], and as well as relaxation through a conical intersection, another relaxation pathway that includes bridging of two carbonyl ligands to produce a long lived intermediate has also been suggested here. These solution phase studies have shown that the initial photoproducts display substantial solvent effects in their decay pathways, and as already discussed for $Cr(CO)_6$, gas phase studies remove these effects. It can be seen that the number of studies related to the ultrafast dissociation mechanism of $Mn_2(CO)_{10}$ is less than those related to $Cr(CO)_6$, and as will be seen in chapter 8, $Fe(CO)_5$. This could be due to the size and complexity of the system, but nevertheless this carbonyl is a very important inorganic system, especially as a model complex for its structure and bonding, so further experimental work in this dissociation process would be interesting. To support, and provide a greater insight into this process from the comparatively few gas-phase experimental studies of the photodissociation, a small number of theoretical studies have been reported and are discussed in the next section.

7.1.2 Theoretical studies of the photochemistry of $Mn_2(CO)_{10}$

The number of theoretical studies that have been reported relating to the excited states and photodissociation mechanism of $Mn_2(CO)_{10}$ is quite small, both compared to the other binary carbonyls that also exhibit ultrafast photodissociation in the gas phase, and in general. This is mainly due to the size of the system.

The one-photon electronic absorption spectrum has been theoretically studied both with DFT and with CASSCF/CASPT2 [8, 9, 10] methods, with the spectrum being dominated by two main bands relating to $^1E_1$ $3d_\pi \rightarrow \sigma^*_{Mn\text{-}Mn}$ and $^1B_2$ $\sigma_{Mn\text{-}Mn} \rightarrow \sigma^*_{Mn\text{-}Mn}$ transitions of which the latter high intensity transition is believed to be the state responsible for dissociation of the Mn-Mn bond, a similar transition was discussed in chapter 5. The excitation energies of these states with the CASPT2 method were found

to be 3.31eV and 3.69eV respectively. TD-DFT predicted these bands to appear at 3.22eV and 3.76eV with respective weak and strong intensities. These values compare well to experimental values [11] by Levenson and co-workers that are 3.31eV and 3.69eV. For the CASPT2 study, it was reported by the authors that this pushed the limits of the CASPT2 method at the time as two CAS(14,14) active spaces were used that included varying numbers of 3d orbitals of manganese, π^* CO orbitals and the σ and σ^* orbitals for the Mn-Mn bond. In between these bands there are a number of other excited states of various chemical character and degeneracy, again highlighting that the electronic spectra of these carbonyl complexes is a subtle subject where the excitation wavelength defines the reactive photochemistry, but will not be further discussed here.

One theoretical study has been reported looking at the photodissociation mechanism of $Mn_2(CO)_{10}$ using DFT (LSDA) by Rosa and co-workers [12] who calculated potential energy curves for selected excited states along Mn-Mn and Mn-CO (axial and equatorial) dissociation coordinates. This study was performed to find the states that correspond to the main dissociation channels of $Mn_2(CO)_{10}$. It was concluded that the curve for the $^1B_2$ $\sigma_{Mn\text{-}Mn} \rightarrow \sigma^*_{Mn\text{-}Mn}$ state causes homolysis of the Mn-Mn bond, and near E states cause the dissociation of either axial or equatorial CO ligands.

DFT was also used to used in 2003 by Xie and co-workers [13] to characterise the fragments $Mn_2(CO)_x$ (x=7,8,9) in terms of their geometries, vibrational frequencies and thermochemistry. It was found that the most stable conformer of the $Mn_2(CO)_9$ fragment was a semi-bridged structure with an unbridged staggered structure close in energy, both were found to be valid minima with no imaginary vibrational frequencies. These structures are shown in figure 7.1. There have been comparatively few theoretical studies looking at the photochemistry of $Mn_2(CO)_{10}$, even though this complex has been shown through experiment to have relaxation mechanisms in the initial photoproducts that should be rich in detail including the possible involvement of vibronically coupled states. In this chapter the relaxation pathways of the two main photoproducts will be investigated using both DFT and CASSCF methods.

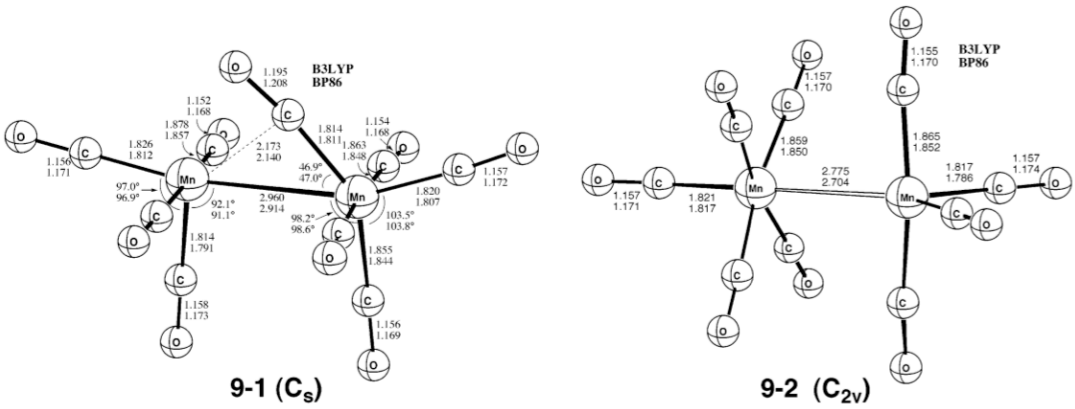

Figure 7.1 Two most stable conformers of the $Mn_2(CO)_9$ fragment determined by DFT study from [13].

7.2 Computational details

The CASSCF method was used for both the $Mn(CO)_5$ fragment in the doublet spin manifold and the singlet $Mn_2(CO)_9$, along with analysis of the ground state geometries with the B3LYP density functional. Three different basis sets were used, the LanL2DZ basis set on all atoms, and two basis sets with an all electron cc-pVDZ basis set on manganese from [14] and the 6-31G* basis set on carbon and oxygen. Another slightly smaller version of this basis set was used with the most diffuse set of d and f functions removed from manganese. The CASSCF orbital active space used for the $Mn(CO)_5$ doublet spin fragment was the same in principle as that used for $Cr(CO)_5$, with seven metal d electrons in eight orbitals, two sets of four metal d orbitals, such as those detailed in chapter 6.

7.3 Relaxation of initial photoproducts of ultrafast $Mn_2(CO)_{10}$ photodissociation in the gas phase

7.3.1 Initial Relaxation of $^2Mn(CO)_5$ photoproduct

The formation of the $Mn(CO)_5$ fragment in the doublet spin manifold occurs through homolytic cleavage of the Mn-Mn by the excitation of the intense $\sigma_{Mn\text{-}Mn} \rightarrow \sigma^*_{Mn\text{-}Mn}$ transition. The initial geometry of this fragment is a C_{4v} square pyramid in an excited doublet state. From symmetry considerations the process of how this fragment can relax

down to the ground state should be very similar to the $Cr(CO)_5$ singlet photoproduct discussed in detail in chapter 6. The main difference here between these two photoproducts is the extra electron in the manganese fragment. Therefore if this fragment behaves in the same way at short timescales as $Cr(CO)_5$ a pair of ligands will begin to bend inwards to 'fill-in' the coordination hole formed by Mn-Mn bond cleavage. This could then form a D_{3h} symmetry trigonal bipryamid geometry that in the doublet spin state will be Jahn-Teller active (with the main difference of three electrons in the degenerate d_{xy} and $d_{x^2-y^2}$ as opposed to two in $Cr(CO)_5$) .

CASSCF investigations on this geometry did find a conical intersection connecting the D_1/D_0 states. Again similarly to the relaxation of $Cr(CO)_5$ through a Jahn-Teller induced conical intersection, C_{4v} symmetry square pyramidal minima and C_{2v} symmetry saddle points were also found. Details of the energetics of these points with CASSCF and DFT where applicable, and all three basis sets are reported in table 7.1. The Jahn-Teller model is $E \otimes e$ with the vibrational modes that make up the branching space being a pair of degenerate *e* symmetry vibrational modes. Figure 7.2 shows the geometrical parameters of the three optimised geometries.

The biggest difference between this system and $Cr(CO)_5$ around the point of conical intersection is the difference in barrier heights, the barrier height between C_{4v} minima, and C_{2v} saddle points, and the difference in energy between C_{4v} minima and the D_{3h} conical intersection geometry are much smaller than the in the case of $Cr(CO)_5$. Application of the epikernel principle [15] results in the same surface topology as that for $Cr(CO)_5$ with the same number of equivalent stationary points and distortion directions. This surface is shown in figure 7.3 and a pictorial representation of the branching space vibrational modes is shown in figure 7.4.

Table 7.1 Energetics of stationary points of $Mn(CO)_5$ on (the potential energy surface) and around the point of conical intersection.

	CAS(7,8)/LanL2DZ		CAS(7,8)/cc-pVDZ* 6-31g*		CAS(7,8)/cc-pVDZ 6-31g*		B3LYP/cc-pVDZ 6-31G*	
Optimised Point	Energy (au)	Energy relative to C_s, minimum (kcal mol^{-1})	Energy (au)	Energy relative to C_s, minimum (kcal mol^{-1})	Energy (au)	Energy relative to C_s, minimum (kcal mol^{-1})	Energy (au)	Energy relative to C_s, minimum (kcal mol^{-1})
C_s, Minimum	-666.6892	0	-1713.5384	0	-1713.5463	0	-1717.7469	0
C_2, Transition State	-666.6871	1.31	-1713.5353	1.94	-1713.5422	2.57	-1717.7405	4.01
D_{3h} Conical Intersection	-666.6804	5.52	-1713.5293	5.71	-1713.5361	6.40	NA	NA

* Denoted outermost d functions and f functions on Mn removed

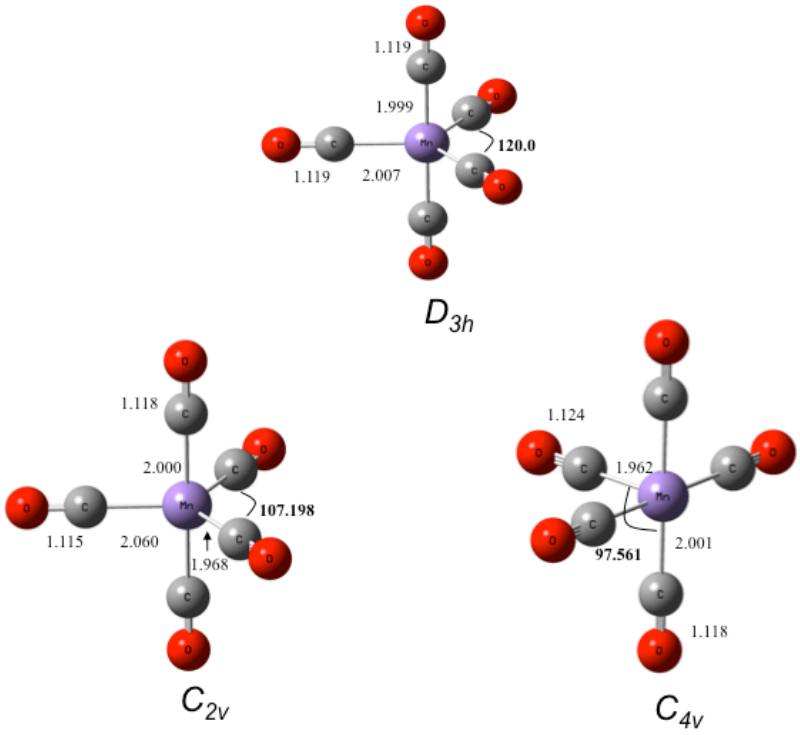

Figure 7.2 Selected geometrical parameters of the stationary point on and around the point of conical intersection in Angstrom.

The possible presence of pseudo-Jahn-Teller coupling between the degenerate *E* state and a close lying higher exited state that affects the ground state surface topology around the point of conical intersection, has been investigated using the pseudo-Jahn-Teller diagnostic test discussed in the previous chapter. This has been applied to the C_{2v} saddle point found that if only configuration state functions (CSFs) of A_1 symmetry are included then all vibrational frequencies are real, with lowest frequency vibrational mode having b_1 symmetry with υ=43.91cm^{-1}. When all CSFs of all irreducible

representations of C_{2v} symmetry are included then the lowest frequency vibrational mode still has b_1 symmetry but now υ=153.05*i*cm^{-1}. This confirms the presence of pseudo-Jahn-Teller coupling causing a mixing of the non-degenerate open-shell ground state. Although this coupling is much smaller which is evident by the lower barrier between minima and saddle points compared to $Cr(CO)_5$, and as we shall discuss below is quite different due to the extra electron in $Mn(CO)_5$.

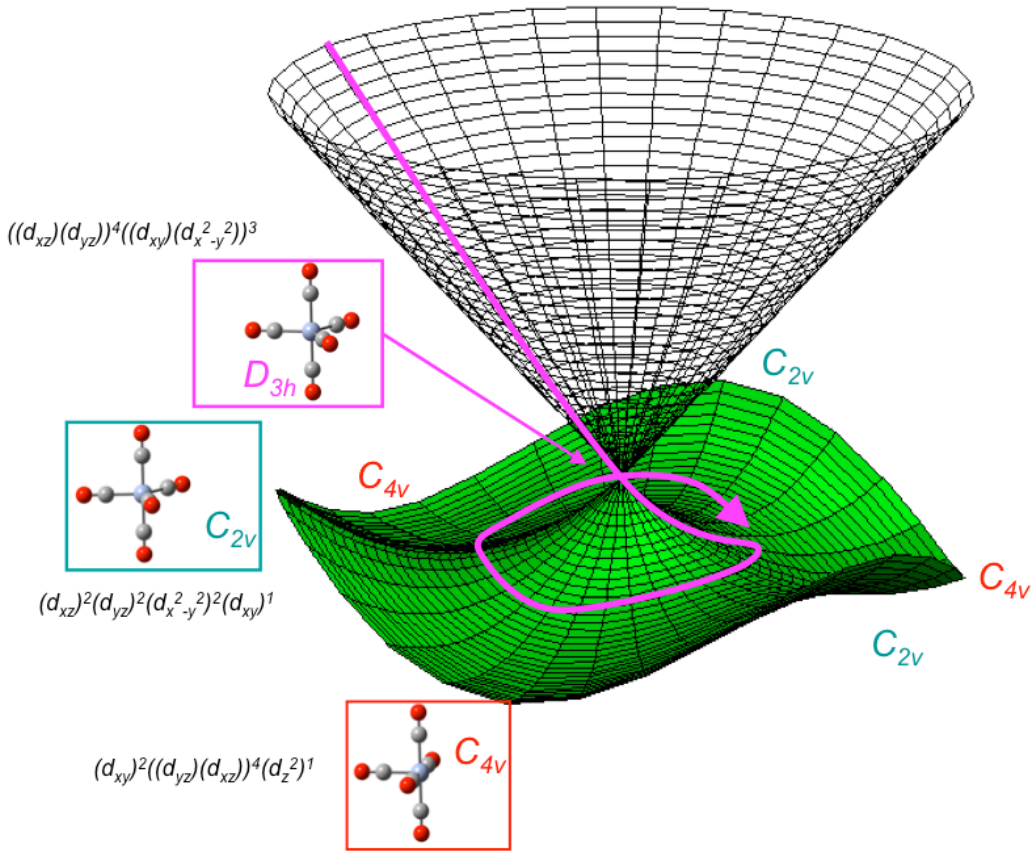

Figure 7.3 $Mn(CO)_5$ D_0/D_1 adiabatic potential energy surface around the $E \otimes e$ Jahn-Teller conical intersection at a trigonal bipyramid D_{3h} geometry. Manganese d electron configurations are in brackets beside each stationary point of the surface. Motion of the system through the point of intersection is shown with the pink arrow and placements of equivalent points are indicated by the use of colour.

In $Cr(CO)_5$ the d^6 electron configuration gives $^1E'$ and $^1A_1'$ states which pseudo-Jahn-Teller couple to give the barrier on the lower surface. In $Mn(CO)_5$ the d^7 electron configuration only gives the $^2E'$ state, with the next state a higher lying $^2E'$ state (15.67 kcal mol^{-1} higher in energy). The pseudo-Jahn-Teller coupling in $Mn(CO)_5$ is actually between the components of the $^2E'$ state, and is therefore a true second-order Jahn-Teller effect. Note that using our terminology this is second-order Jahn-Teller at D_{3h}

geometries, but pseudo-Jahn-Teller at non-degenerate C_{2v} geometries. This is a much smaller effect than the $(E \oplus A) \otimes e$ coupling present in $Cr(CO)_5$, and is absent in $Mn(CO)_5$ due to the extra d electron.

Figure 7.4 Pictorial representation of the branching space *e* symmetry vibrational modes for the $Mn(CO)_5$ double spin fragment at D_{3h} symmetry. Arrows indicate the direction of distortion to lift the degeneracy and reduce the symmetry.

Motion of the system around the lower part of the conical intersection point is the same as that of $Cr(CO)_5$ and is caused by the motion of the equatorial ligand pairs with the OC-Mn-CO bond angles opening and closing to reach the C_{4v} and C_{2v} stationary points. This is shown in figure 7.4 where only the equatorial ligands distort. While this relaxation pathway has been investigated, a dynamics study of this process will be needed to see if this pathway is followed following direct excitation following Mn-Mn bond homolysis via the $\sigma_{Mn\text{-}Mn} \rightarrow \sigma^*_{Mn\text{-}Mn}$ transition. We finish this section by noting that the very small barriers should allow complete pseudorotation and further interesting dynamical effects.

7.3.2 Initial Relaxation of $Mn_2(CO)_9$ photoproduct

The other possible dissociation channel comes from dissociation of a CO ligand, either axial or equatorial. This fragment was found to be much more challenging to study due to the computational cost of actually modelling this fragment with CASSCF and the size of the active space needed to accurately model this system. A CAS(14,10) active space was initially used which included the same 3d orbitals as used for the $Cr(CO)_5$ and $Mn(CO)_5$ fragments, and all d electrons of both manganese atoms. However this active space was found to be poor representation of the system at the geometries initially investigated shown in figure 7.5 suggested by Fuβ [1], and when considering

the active spaces needed by Kuhn and co-workers to study the lowest excited states of $Mn_2(CO)_{10}$ were CAS(14,14), and these pushed the limits of the method, further work is needed here. Initial $Mn_2(CO)_9$ geometries were investigated with the B3LYP density functional to assess the difference in energy between ground state and lowest excited state together with their vibrational frequencies to look for clues to a possible conical intersection geometry.

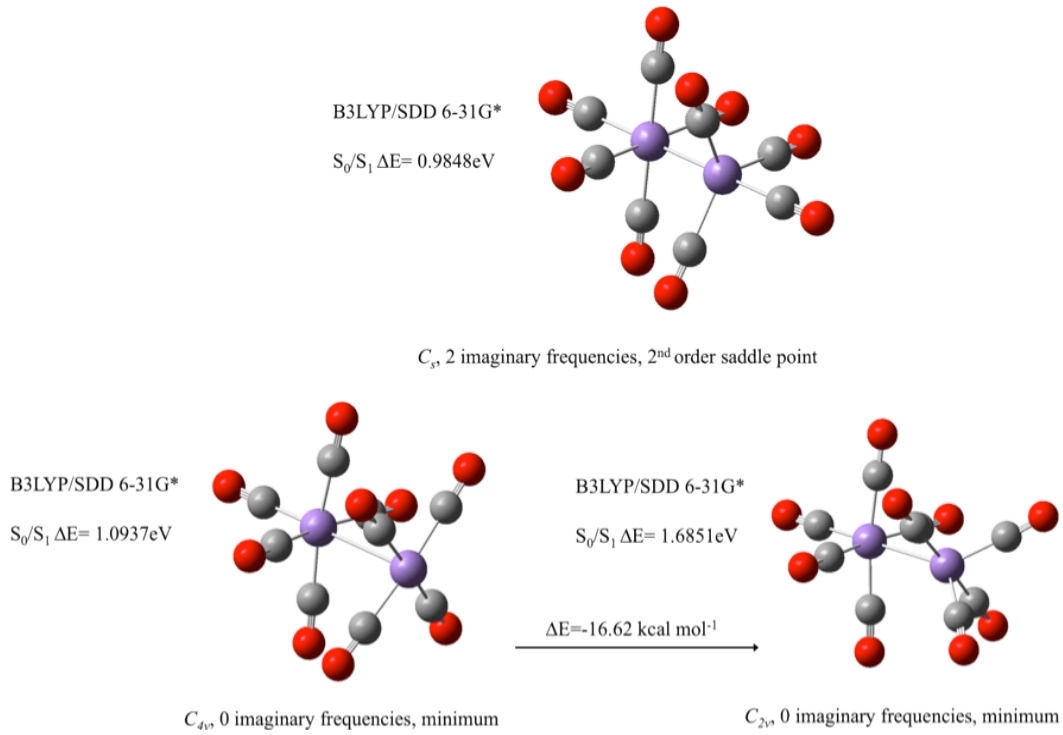

Figure 7.5 Selected $Mn_2(CO)_9$ geometries investigated for their suitability as a conical intersection geometry. All points were investigated with the B3LYP density functional with a cc-pVDZ/6-31G* basis set discussed above. The symmetry and number of imaginary vibrational frequencies is shown below each geometry along with their character as a minimum or saddle point. The difference in energy between ground and lowest excited states and between the two lower geometries is shown also as calculated with TD-DFT.

From simple symmetry considerations it can be seen that the $Mn_2(CO)_9$ fragment would be unable to form a Jahn-Teller active geometry in the singlet spin manifold and points to the possibility that this fragment instead relaxes through a general non-Jahn-Teller induced conical intersection of the types that are prevalent in organic photochemistry. The vibrational coherences and timescale of this dissociation channel observed by Fuβ strongly indicates some sort of avoided crossing or conical intersection so further study on this channel is ongoing.

7.4 Conclusions

The two possible initial dissociation channels of $Mn_2(CO)_{10}$ in the gas phase have been investigated using CASSCF and DFT. The relaxation pathway of the $Mn(CO)_5$ doublet spin photoproduct from Mn-Mn bond homolysis has been investigated and it was found it relaxes to the ground state via a Jahn-Teller induced conical intersection in the same manner as the $Cr(CO)_5$ photoproduct discussed in chapter 6. The main difference being the different origins of pseudo-Jahn-Teller coupling resulting in lower barrier heights between C_{4v} and C_{2v} stationary points compared to $Cr(CO)_5$. The Mn-CO dissociation channel is an ongoing work of which only initial DFT investigations of the $Mn_2(CO)_9$ fragment have been carried out, and we have found that a large CASSCF active space will be needed to accurately model the system and its relaxation. From experimental observations and symmetry considerations it is thought that this fragment relaxes through a general non-Jahn-Teller conical intersection or a pseudo-Jahn-Teller type avoided crossing. Further spectroscopic work on bimetallic systems was discussed in chapter 5.

7.5 References

[1] Fuss, W.; Trushin, S. A.; Schmid, W. E., Ultrafast photochemistry of metal carbonyls. *Res. Chem. Intermed.* **2001,** 27, 447-457.

[2] Dahl, L. F.; Rundle, R. E., The crystal structure of dimanganese decacarbonyl $Mn_2(CO)_{10}$. *Acta Crystallographica* **1963,** 16, 419-426.

[3] Dahl, L. F.; Ishishi, E.; Rundle, R. E., Polynuclear metal carbonyls. I. Structures of $Mn_2(CO)_{10}$ and $Re_2(CO)_{10}$. *J. Chem. Phys.* **1957,** 26, 1750-1751.

[4] Seder, T. A.; Church, S. P.; Weitz, E., Photodissociation pathways and recombination kinetics for gas-phase $Mn_2(CO)_{10}$. *J. Am. Chem Soc.* **1986,** 108, 7518-7524.

[5] Kim, S. K.; Pedersen, S.; Zewail, A. H., Femtochemistry of organometallics - dynamics of metal-metal and metal-ligand bond-cleavage in $Mn_2(CO)_{10}$. *Chem. Phys. Lett.* **1995,** 233, 500-508.

[6] Zhang, Z.; Harris, C. B., Photodissociation dynamics of $Mn_2(CO)_{10}$ in solution on ultrafast timescales. *J. Chem. Phys.* **1991,** 95, 4024-4032.

[7] Owrutsky, J. C.; Baronavski, A. P., Ultrafast infrared study of the ultraviolet photodissociation of $Mn_2(CO)_{10}$. *J. Chem. Phys.* **1996,** 105, 9864-9873.

[8] Rosa, A.; Ricciardi, G.; Baerends, E. J.; Stufkens, D. J., Density functional study of ground and excited states of $Mn_2(CO)_{10}$. *Inorg. Chem.* **1995,** 34, 3425-3432.

[9] van Gisbergen, S. J. A.; Groeneveld, J. A.; Rosa, A.; Snijders, J. G.; Baerends, E. J., Excitation energies for transition metal compounds from time-dependent density functional theory. Applications to MnO_4^-, $Ni(CO)_4$, and $Mn_2(CO)_{10}$. *J. Phys. Chem. A* **1999,** 103, 6835-6844.

[10] Kuhn, O.; Hachey, M. R. D.; Rohmer, M. M.; Daniel, C., A CASSCF/CASPT2 study of the low-lying excited states of $Mn_2(CO)_{10}$. *Chem. Phys. Lett.* **2000,** 322, 199-206.

[11] Levenson, R. A.; Gray, H. B., Electronic structure of compounds containing metal-metal bonds - decarbonyldimetal and related complexes. *J. Am. Chem Soc.* **1975,** 97, 6042-6047.

[12] Rosa, A.; Ricciardi, G.; Baerends, E. J.; Stufkens, D. J., Density functional study of the photodissociation of $Mn_2(CO)_{10}$. *Inorg. Chem.* **1996,** 35, 2886-2897.

[13] Xie, Y. M.; Jang, J. H.; King, R. B.; Schaefer, H. F., Binuclear homoleptic manganese carbonyls: $Mn_2(CO)_x$ (x = 10, 9, 8, 7). *Inorg. Chem.* **2003,** 42, 5219-5230.

[14] Balabanov, N. B.; Peterson, K. A., Systematically convergent basis sets for transition metals. I. All-electron correlation consistent basis sets for the 3d elements Sc–Zn. *J. Chem. Phys.* **2005,** 123, 064107.

[15] Ceulemans, A.; Vanquickenborne, L. G., The epikernel principle. *Struct. Bond.* **1989,** 71, 125-159.

Chapter 8

Photodissociation mechanism of $Fe(CO)_5$ and relaxation mechanism of the $^1Fe(CO)_4$ initial photoproduct through a Jahn-Teller induced conical intersection

8.1 Introduction and literature review

The last system to be discussed in terms of the relaxation mechanism of the initial photoproduct on an ultrafast timescale is perhaps the most complex, $Fe(CO)_5$. Iron forms a stable 18 electron monometallic structure with a D_{3h} symmetry trigonal bipyramid structure, as already discussed in chapter 3. While the photodissociation mechanism of $Mn_2(CO)_{10}$ is more complex to study theoretically in terms of the different possible dissociation channels, and the computational cost of accurately modelling the larger bimetallic systems with multi-configurational methods, it will be shown that $Fe(CO)_5$ is perhaps even more complex due to different dissociation channels (either axial or equatorial CO loss) and the nature of the Jahn-Teller conical intersection that the $Fe(CO)_4$ initial photoproduct forms in the singlet spin manifold. We begin, as with previous chapters, with a review of pertinent literature relating to experimental and theoretical study of the photochemistry of $Fe(CO)_5$.

8.1.1 Experimental studies of the photochemistry of $Fe(CO)_5$

Some of the earliest work looking at the reactive photochemistry of $Fe(CO)_5$, as with $Cr(CO)_6$, looked at the photolysis of $Fe(CO)_5$ in a rare gas matrix such as the study by Poliakoff and Turner from 1974 [1] in which they performed such a study to look at the structure of the initial $Fe(CO)_4$ photoproduct. It was concluded that at 20K in an argon matrix $Fe(CO)_4$ had C_{2v} symmetry. The same authors revisited this system in 1977 [2] this time studying the intramolecular ligand exchange process of the C_{2v} $Fe(CO)_4$ photoproduct in an argon matrix where the ligand exchange process was induced using infrared laser pulses. They concentrated on the mechanism of the laser induced ligand exchange process after the system was enriched with ^{13}CO. They reported the first experimental observation of a non-Berry pseudo-rotation as the mechanism for ligand exchange. These results were compared to the ligand exchange process in the C_{2v} symmetry structure of SF_4 whose ligands can exchange thermally via a Berry pseudo-rotation. The difference between a Berry and non-Berry pseudo-rotation is closely related to the nature of the point of maximum symmetry (central point) around which the pseudo-rotation takes place, whether it is a maximum or a point of conical intersection. Other studies from the late 1970s and early 1980s looked at the fragmentation dynamics of $Fe(CO)_5$ using laser pulses set at various wavelengths

including the study by Yardley and co-workers [3] who excited $Fe(CO)_5$ with one photon absorption and observed a high degree of fragmentation where sequential CO ligand loss was suggested where intermediate fragments have a high degree of internal excitation, and a similar study by Whetten and co-workers [4] in which they estimated the excited state lifetimes, which they found to be between 0.6 and 1.0ps in the region between 290 and 310nm. Already discussed in chapter 3 another early paper by Hubbard and Lichtenberger [5] from 1981 that examined the photoelectron spectrum of $Fe(CO)_5$ in the gas phase and touched upon for the first time the type of degenerate Jahn-Teller induced photochemistry discussed later in this chapter. They suggested there was evidence in their results of Jahn-Teller distortions in the $Fe(CO)_5^+$ cation. It was shown in this study for the first time that highly symmetrical transition metal carbonyls in general can potentially have observable Jahn-Teller activity in their photochemistry during ionization of the dissociation process. It was concluded that ionization to the $^2E'$ state displayed Jahn-Teller activity that related to a non-Berry pseudo-rotation. State-resolved photofragmentation dynamics of $Fe(CO)_5$ were reported by Waller and Hepburn in 1988 [6] at a range of wavelengths (193, 248, 266 and 351nm). $Fe(CO)_5$ was used in a supersonic molecular beam, and the photofragments were detected using vacuum ultraviolet laser-induced fluorescence. By using this method information on properties of the photoproducts such as rotational and vibrational distributions can be found. A photodissociation mechanism was proposed that involved sequential loss of all carbonyl ligands, and noted that after irradiation at a wavelength of 193nm a minor channel opens which produces $Fe(CO)_4$ on a very fast timescale. This connected with an earlier paper by Seder and co-workers [7] from 1986 that suggested the role of $Fe(CO)_4$ in the photodissociation process, and relates to ultrafast laser induced studies that will be discussed later in this section. Other experiments such as infrared monitored flash photolysis in a solution of benzene have also been reported where highly reactive intermediates were involved in the photoreaction that resulted in the formation of a binuclear carbonyl complex [8].

The work of Poliakoff and co-workers, mentioned above, was perhaps the most comprehensive in looking at the formation, structure and properties of the $Fe(CO)_4$ fragment, that by the mid 1980s was believed to be the initial photoproduct when $Fe(CO)_5$ was photoexcited by the application of laser pulses at various wavelengths.

One paper from 1984 [9] looked to further explain the believed non-Berry pseudo-rotation that they observed in the $Fe(CO)_4$ molecule. They believed this was unusual because the SF_4 molecule that also has C_{2v} symmetry undergoes a Berry pseudo-rotation. They used infrared laser induced isomerisation techniques and proposed a 'distorted octahedron' topological model to account for this isomerisation based on distortions of a T_d symmetry $Fe(CO)_4$ molecule with a number of equivalent lowest energy pathways to equivalent C_{2v} symmetry distorted geometries via equivalent C_s symmetry transition states. They described this by a qualitative application of the Jahn-Teller theorem where distortion occurs via axial-axial and equatorial-equatorial ligand exchange to axial-equatorial or equatorial-axial, but not direct exchange between axial-axial and equatorial-equatorial ligands. A picture of this model is shown in figure 8.1. This model will be shown later in this chapter to be quite accurate when describing the relaxation pathway of $Fe(CO)_4$ in the singlet spin manifold induced by the Jahn-Teller effect. The $Fe(CO)_4$ molecule was the first system where this effect could be observed spectroscopically via time-resolved infrared studies. Other systems thought to undergo this process either underwent rapid ligand interconversion to other distorted structures, or the process was frozen out due to the low temperatures used in the experimental setups used. The reactivity of this highly reactive fragment was studied again in 1987, [10] and the apparatus used to study highly reactive photoinduced intermediates of metal carbonyl complexes was reported by the same group in 1986 [11].

These older studies of the reactive photochemistry of $Fe(CO)_5$ showed that the photodissociation process of this important inorganic complex could be quite complicated and could involve contributions from degenerate, vibronically coupled states. This system was investigated almost as intensely as $Cr(CO)_6$ and the other group 6 binary carbonyls. In the same way to the experimental studies carried out on $Cr(CO)_6$, and discussed in chapter 6, more recent studies started to look at the reactive photochemistry in the gas-phase because while matrix isolation experiments at low temperature can provide valuable information on the reactive intermediates, a picture of the dissociation process and (very) reactive intermediates was desired without matrix or solvent effects.

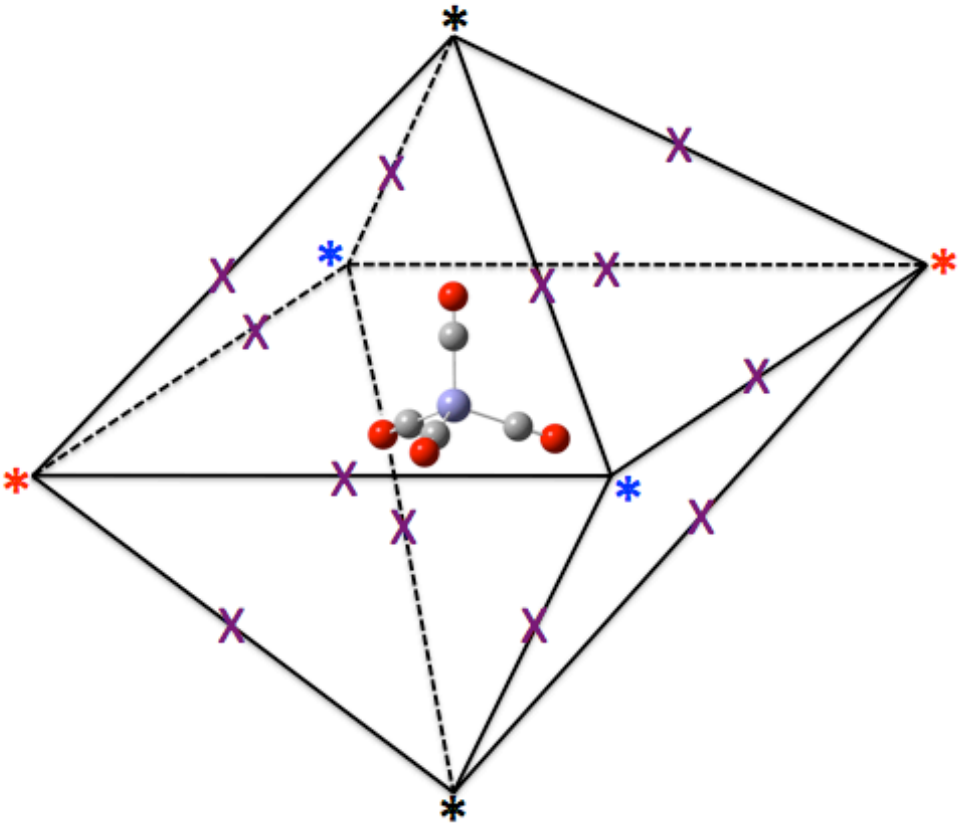

Figure 8.1 Pictorial representation of the distorted octahedron model proposed by Poliakoff and co-workers [9] from [12]. $Fe(CO)_4$ in the singlet spin manifold at a tetrahedral geometry (the centre of the octahedron) will distort to a number of equivalent C_{2v} symmetry minima (*) via equivalent C_s symmetry transition states (X).

Early works in the gas-phase included the studies by Waller and Hepburn discussed above [6] and by Seder and co-workers, also discussed above [7] who both studied the state-resolved photodissociation process. More recent studies in the gas-phase looked at the ultrafast (sub-picosecond) photodissociation dynamics such as the study by Bañares and co-workers [13], already discussed in chapter 3, who looked at the photodissociation dynamics of $Fe(CO)_5$ in a molecular beam using femtosecond laser pulses with two-photon absorption at 400nm, with probing of the resulting dynamics via non-resonant ionisation at 800nm, and time-of-flight (TOF) mass spectrometry. The timescales for the dissociation of each carbonyl ligand was measured in the sequential dissociation process, and it was concluded that $Fe(CO)_4$ was formed after 20±5 fs, Fe(CO) was formed after 100fs and complete dissociation of all ligands occurred at a time after 230fs.

Rubnerq and co-workers produced two papers that also reported the fragmentation dynamics of $Fe(CO)_5$. The first paper [14] proposed a simple time-dependent statistical model for the ejection of a CO ligand after excitation from femtosecond laser pulses. Through this they tried to establish whether the dissociation process was concerted or sequential. The difference defined here as whether each CO ligand is ejected from an electronically excited state or whether initial CO loss occurs from an electronically excited state, and all further CO loss is from the electronic ground state. They applied their model to the results presented by Zewail [15] that are discussed separately below, and concluded that a sequential CO loss mechanism was correct. Their second paper was experimental, and used a setup similar to Bañares and co-workers discussed above, coupled with a more detailed theoretical model [16]. They concluded here that both concerted and sequential CO loss mechanisms are valid, and further to that they are able to compete with each other.

Zewail and co-workers used ultrafast electron diffraction methods to look in detail at the very reactive $Fe(CO)_4$ photodissociation intermediate [15, 17]. It was found from these studies that the timescale for complete dissociation of the CO ligands was less than 10ps. The most important conclusion from these studies from the point of view of this thesis was that after UV irradiation of $Fe(CO)_5$, $Fe(CO)_4$ in its lowest singlet state was the major product formed within 200fs. Justification for this (an unusual conclusion at the time given that $Fe(CO)_4$ has a triplet ground state, and this was the state expected to be detected) was based upon structural information in their diffraction data that indicated more open pair-wise OC-Fe-CO angles. This transient species with C_{2v} symmetry had to be in the singlet state to be consistent with high level quantum chemical calculations, with the most obtuse angle being 169 ± 2^{o}, with the other being 125 ± 3^{o}. This type of experiment and the results it could produce were important in the field of ultrafast electron diffraction and for those who study the photochemistry of transition metal complexes because the resolution of the structural information was great enough to distinguish between two different states of the same molecule for the first time, each with very similar geometries and the same molecular symmetry (C_{2v}). From these results it can be argued that after ejection of a single CO ligand the resulting $Fe(CO)_4$ fragment is able to relax from an upper exited state manifold on an ultrafast timescale, and does not undergo intersystem crossing to the more stable triplet state. This kind of result, and similarly to the experimental and theoretical results for other

carbonyls, such as those studied in chapters 5 and 6, along with examples from organic photochemistry, for example see [18], strongly indicates the presence of a conical intersection connecting the excited state products with the lowest energy singlet state. The experimental structure of $Fe(CO)_4$ in its $^1A_1$ state predicted by Zewail is reproduced in figure 8.2.

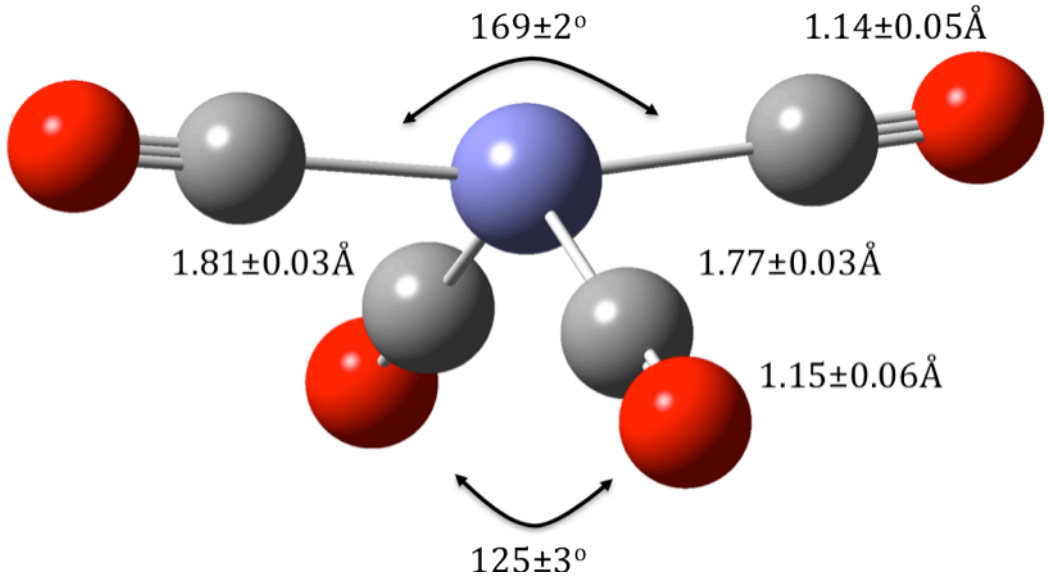

Figure 8.2 Refined molecular structure of C_{2v} symmetry $Fe(CO)_4$ in the $^1A_1$ lowest singlet state determined by ultrafast electron diffraction by Zewail and co-workers [17].

Further experiments looking at the dynamics of the $Fe(CO)_4$ photoproduct and Jahn-Teller distortion in the singlet state were carried out by Fuβ and co-workers in the same vane as the studies they have reported for other binary carbonyls, as already discussed in chapters 6 and 7 [19, 20, 21, 22]. Their paper from 2000 [23] utilised their time-resolved ultrafast methods to look at the gas-phase photolysis of $Fe(CO)_5$ at 267nm using femtosecond UV laser excitation. A TOF mass spectrometer was used to monitor the resulting ion signals generated. They concluded that near the Franck-Condon region the dissociation proceeds via a series of Jahn-Teller induced conical intersections due to the very small time-constants for several sequential processes, and rationalized that the initial state populated was probably a metal-ligand charge-transfer (MLCT) state and must somehow reach a ligand field (LF) state before full dissociation occurs. It was shown in chapter 3 that there is a manifold of doubly degenerate states that can be populated so Jahn-Teller induced conical intersections in this region could be almost guaranteed. They proposed a Jahn-Teller induced conical intersection in $Fe(CO)_5$ in the

Franck-Condon (vertically excited) region of $E \otimes e$ nature from population of an E′ electronic state which couples to the e' symmetry vibrational coordinates, corresponding to stretching of the equatorial Fe-C and C-O bonds reached within 21fs. This is followed by relaxation to the $1A_2''$ state, then again proceeding back to the path of the same E′ state components by distorting along an e'' mode. A further conical intersection was also predicted in the next lowest 1E′ state, and passage through this intersection leading to a LF state followed by ejection of a single CO ligand. This points towards very complex initial photodynamics. They referenced the work of Poliakoff and co-workers discussed earlier [2, 9] to explain a measured time constant of 47fs that was thought to relate to internal conversion from the $^1B_2$ first excited state to the $^1A_1$ lowest singlet state of C_{2v} symmetry $Fe(CO)_4$ via a Jahn-Teller induced conical intersection at a tetrahedral geometry. The authors assumed a tetrahedral geometry, and therefore a possible $T \otimes (t \oplus e)$ intersection based upon qualitative MO arguments.

As already mentioned there has been a large number of studies looking at the photochemistry of this paradigm transition metal complex, Leadbeater has provided a comprehensive review of this subject [24], as well as the recent highlight by Poliakoff and Turner [25]. What these latest time-resolved ultrafast studies have shown is that for $Fe(CO)_5$, as well as the other binary carbonyls, the photochemistry is far from simple and display a variety of phenomena, including strong vibronic coupling effects.

8.1.2 Theoretical studies of the photochemistry of $Fe(CO)_5$

Theoretical works that studied the photoreactivity of $Fe(CO)_4$ looked at the bond dissociation energies of $Fe(CO)_5$ using a range of electronic structure methods. For example the study by Barnes and co-workers [26] who used ab initio methods and basis sets larger than double zeta in size to optimise the ground state structure of $Fe(CO)_5$ and calculated dissociation energies for the sequential loss of the five carbonyl ligands. The first dissociation energy was calculated to be 39 kcal mol^{-1}, decreasing to 5 kcal mol^{-1} for the final CO dissociation. A plethora of other methods have been applied to study the same parameters including density functional theory and the coupled cluster (CCSD(T)) method [27, 28, 29, 30]. Density functional theory has also been used to

study the unsaturated carbonyl fragments of $Fe(CO)_5$ and the reaction of $Fe(CO)_4$ with a hydrogen molecule [31, 32].

The group of Harvey have also carried our some interesting works in recent years studying the spin forbidden reactions of the $Fe(CO)_4$ product including oxidative addition to H_2 and spin cross-over between the singlet and triplet spin states of $Fe(CO)_4$ through 'minimum energy crossing points' using ab initio methods and density functional theory [33, 34, 35].

Theoretical works looking at the relaxation pathway of the $Fe(CO)_4$ photoproduct are limited to one study by Apostolova [36] from 2006 who used HF and MCSCF methods with relatively large basis sets to study an avoided crossing relaxation pathway via a D_{4h} square pyramidal $Fe(CO)_4$ geometry in the singlet spin manifold with triplet spin structures also investigated. The author also claimed that this showed the stereochemical flexibility of the $Fe(CO)_4$ molecule. However there has been no theoretical studies looking at the surface topology around the point of conical intersection in $Fe(CO)_4$ at a tetrahedral geometry induced by the Jahn-Teller effect. Such studies have already been successfully carried out for $Cr(CO)_5$, already discussed in chapter 6, and for $Mn(CO)_5$ in the doublet spin manifold, discussed in chapter 7. These studies provided new information on the relaxation mechanisms of these highly reactive intermediates. The experimental works discussed above clearly indicate that the photodissociation mechanism of $Fe(CO)_5$ includes generation and relaxation of an initial $Fe(CO)_4$ photoproduct, probably through a Jahn-Teller induced conical intersection at a tetrahedral geometry. A detailed study of the surface topology around this point will provide new information on this complex mechanism and complement the studies already carried out on other binary carbonyl intermediates.

8.2 Computational details

The CASSCF method was again used to study the important points on the potential energy surface of singlet spin $Fe(CO)_4$. Two basis sets were used, the LanL2DZ basis set and a combination of an SDD ($1s^2 2s^2 2p^6$ core) basis set on iron and 6-31G* on carbon and oxygen with polarization functions added to all atoms. The active space was

the same in general as the ones successfully applied to $Cr(CO)_5$ and $Mn(CO)_5$ in that all eight iron d orbitals were correlated with two sets of d orbitals, effectively '3d' and '4d' sets to account for extra dynamic correlation effects, making a CAS(8,10) active space. A CAS(8,5) active space was initially tried but this gave poor results and produced spurious symmetry breaking in $Fe(CO)_4$, in a similar way as reported with $Cr(CO)_5$, so the larger CAS(8,10) active space was needed with all d orbitals needed from each set as there were no higher lying d orbitals that remained unoccupied and therefore could be removed from the space, as was the case with $Cr(CO)_5$ and $Mn(CO)_5$. This was found to give a very good description of the stationary points on the potential energy surfaces investigated for example by comparison with experiment where appropriate. On the other hand this active space was too large for analytical frequency calculations to be performed so the pseudo-Jahn-Teller effect diagnostic test [37] applied to $Cr(CO)_5$ and $Mn(CO)_5$ cannot be used here, but the epikernel principle was applied here, as will be discussed later. Although we are principally interested in the singlet spin manifold, the Jahn-Teller topology for the lowest triplet state was also investigated at the same level of theory.

8.3 Relaxation mechanism of the initial $Fe(CO)_4$ photoproduct in the singlet spin manifold

When considering the mechanism of relaxation of $Fe(CO)_4$ in the singlet spin state some issues arise that immediately suggest this mechanism is more complicated than the other carbonyl systems discussed previously. Firstly two dissociation channels are possible, with ejection of either an axial or equatorial CO ligand possible depending on the nature of the dissociative LF state. An orbital correlation diagram is shown in figure 8.3 that shows the effect of CO loss in either channel has on the d orbitals of $Fe(CO)_5$. Though it has still not been established which CO ligand is initially lost, as either $Fe(CO)_4$ structure immediately resulting from CO loss could form a tetrahedral geometry in the singlet state.

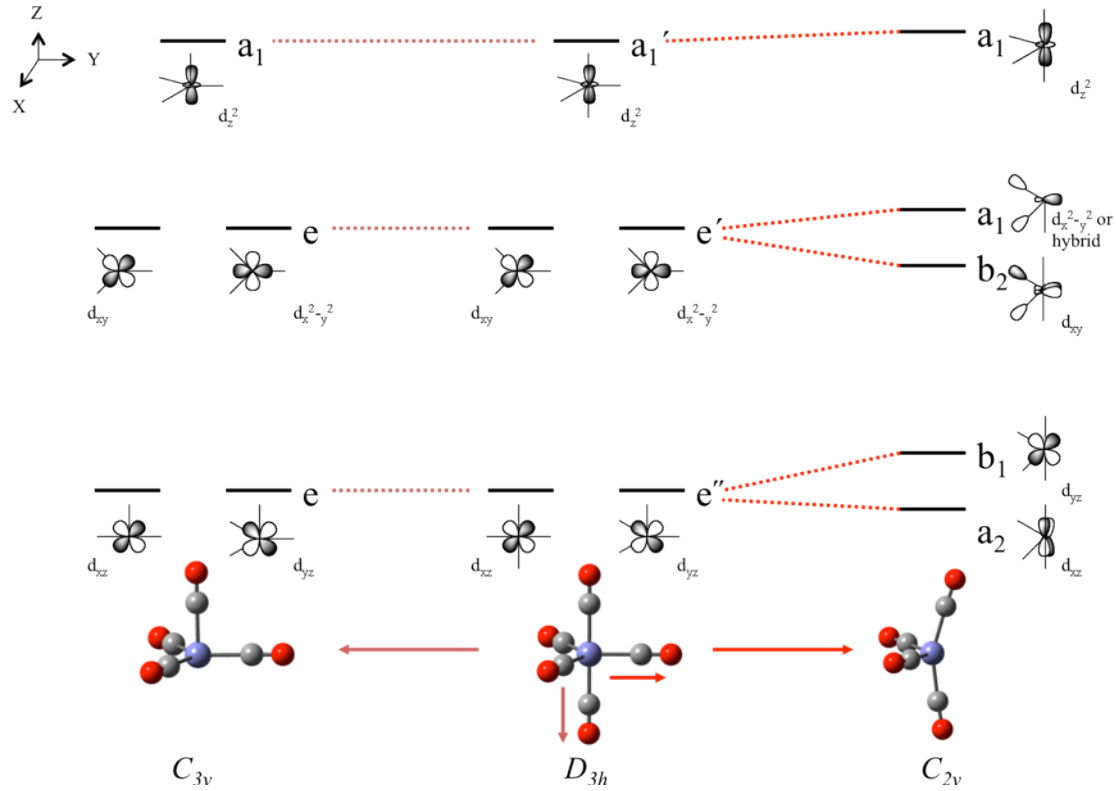

Figure 8.3 Orbital correlation diagram between the d orbitals of $Fe(CO)_5$ and $Fe(CO)_4$ resulting from axial or equatorial CO loss.

Several possible degenerate states can arise at a tetrahedral geometry with a d^8 configuration ($e^4t_2^4$), i.e. $t_2 \otimes t_2 = {}^1A_1 \oplus {}^1E \oplus {}^1T_2 \oplus {}^3T_1$. Degenerate Jahn-Teller active states exist in both triplet and singlet spin manifolds, and the correct ordering of these states can only be determined by computation, with classic inorganic chemistry models like that of Tanabe-Sugano [38] unable to predict the lowest energy state in this case. In a Tanabe-Sugano diagram the energies of various metal atomic terms are correlated with molecular terms in the correct ligand-field splitting molecular point group. This is across the domain of LF d orbital splitting energies. These energies are set relative to the lowest energy state that is set to the horizontal axis. This lowest energy term can change at different ligand-field strengths. In this case a Tanabe-Sugano diagram for $Fe(CO)_4$ predicts that the first singlet state above the triply degenerate triplet ground state is a triply degenerate singlet state. These empirically derived methods can sometimes fail in low-spin manifolds so this result is not surprising here, it should also be noted that Tanabe-Sugano diagrams for non-octahedral diagrams are not easy to find.

In their analysis Fuβ assumed a tetrahedral geometry with a triply degenerate state for the reactive photochemistry. In the results presented here the lowest energy degenerate state was found to be ^1E, lower in energy to $^1T_2$ by 5 kcal mol^{-1}. Analysis of the different canonical vibrational modes of $Fe(CO)_4$, $Fe(CO)_4$ (T_d): $Q_{3N-6} \in 2A_1 \oplus 2E \oplus T_1 \oplus 4T_2$ show that many Jahn-Teller models are possible such as $E \otimes e$, $T \otimes t$, $(T \oplus E) \otimes t$, $(T \oplus E) \otimes (t \oplus e)$. To investigate the energy difference between E and T_2 states, the tetrahedral $Fe(CO)_4$ molecule was displaced along a totally-symmetric 'breathing' mode and the difference in energy between the states checked at set points along the breathing mode of +0.1Å of the Fe-C bond from the optimised geometry, these results are presented in figure 8.4.

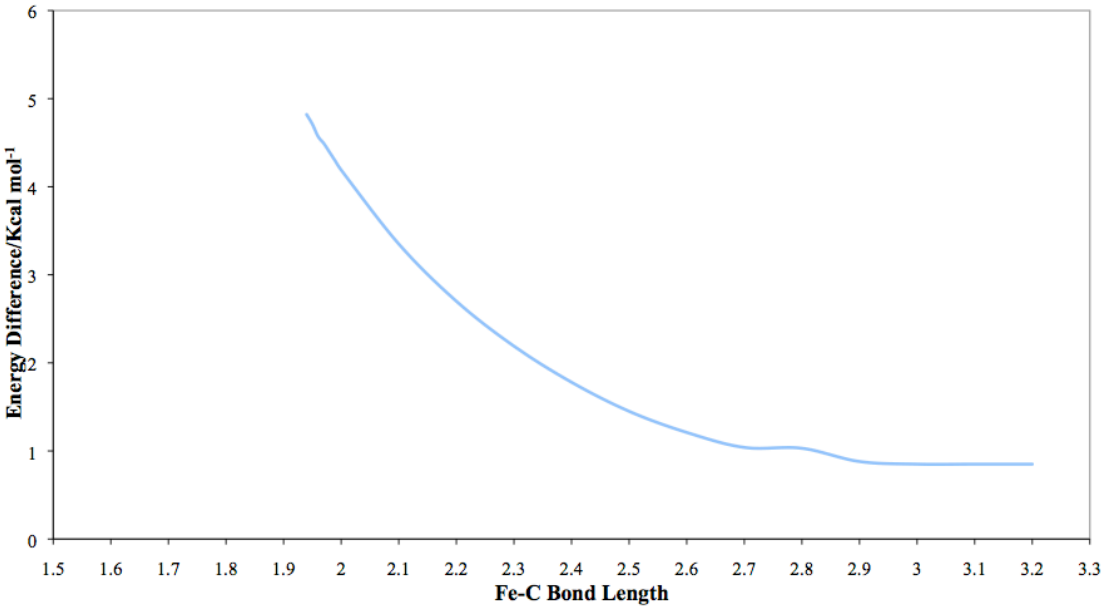

Figure 8.4 Energy difference between ^1E and $^1T_2$ states of T_d symmetry $Fe(CO)_4$ along a totally-symmetric Fe-C 'breathing' vibrational mode.

What can be seen from figure 8.4 is that the difference in energy between these two states gets smaller then plateaus at long Fe-C bond distances at around 1 kcal mol^{-1}. This indicates that it is very probable that both of these states can pseudo-Jahn-Teller couple via an appropriate vibrational mode or indeed 'switch over' so that the T_2 state is lower in energy. This would result in a full five-state five-mode Jahn-Teller model of the type mentioned above, as is already known for the P_4^+ cation [39]. A pictorial

representation of the derivative coupling and gradient difference vectors for the ^1E conical intersection and T_d geometry is shown in figure 8.5.

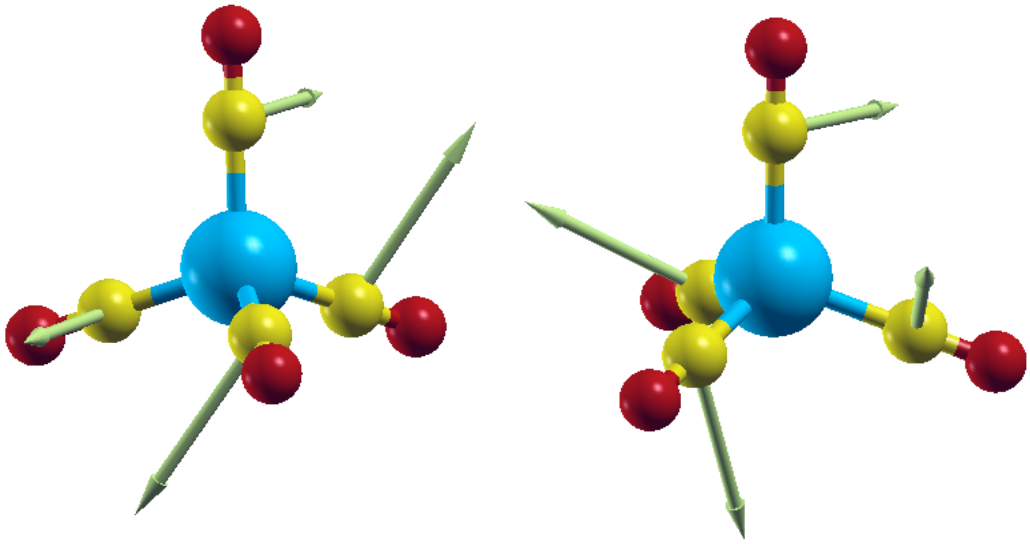

Figure 8.5 Pictorial representation of the gradient difference and derivative coupling vectors for the ^1E conical intersection.

The rest of the analysis discussed here is for the triply degenerate case because as there has been a substantial amount of experimental work dedicated to this (as discussed above). Distortion of the system around the point of conical intersection, similarly to $Cr(CO)_5$ and $Mn(CO)_5$, involves changes in the OC-Fe-CO bond angles that differentiate the geometrical structures. In the case of tetrahedral $Fe(CO)_4$ the main geometrical distinguishing feature is choosing two pairs of ligands so that each OC-Fe-CO angle changes from 109.5^o. This is alluded to in figure 8.6. So there will be three distinct ligand pair choices, the Jahn-Teller distortion corresponding primarily to one ligand pair bend. Analysis of this triply degenerate T_d symmetry case using the epikernel principle shows multiple possible epikernels $E_i(T_d, t_2) = C_{3v}, C_{2v}, C_s$ and here both positive and negative epikernel distortion leads to equivalent geometrical critical points, which is different to the cases of $Cr(CO)_5$ and $Mn(CO)_5$, and marks a difference between doubly- and triply degenerate cases. Our analysis using CASSCF finds C_{2v} symmetry minima separated by C_s symmetry saddle points. Table 8.1 summarises the energetics of these critical points.

Table 8.1 Energetics of stationary point around the point of conical intersection.

Optimised Point	M06L/ SDD(cc-pVDZ)	CAS(8,10)/ LanL2DZ	CAS(8,10)/ SDD+POL
T_d Conical Intersection	-	-573.4087	-
C_{2v} Minimum	-1717.19229897	-573.4238	-574.1783
C_{2v} Minimum (triplet)	-1717.20590886	-573.4631	-574.2169
C_s Transition state	-1717.18512411	-	-

The C_s symmetry saddle points could only be optimised using density functional theory as CASSCF optimisation required analytical Hessians that were not available for the CAS(8,10) active spaced used here, the smallest possible active space. The barrier height was found to be 4.5 kcal mol^{-1}. The number of equivalent epikernels is calculated in the same way as was done for $Cr(CO)_5$ and $Mn(CO)_5$; $n_{E_1(T_d,t_2)} = \frac{|n_{T_d}|}{|n_{C_{2v}}|} = \frac{24}{4} = 6$ for C_{2v}, and $n_{E_2(T_d,t_2)} = \frac{|n_{T_d}|}{|n_{C_s}|} = \frac{24}{2} = 12$ for C_s. So there are six equivalent C_{2v} minima separated by twelve C_s symmetry saddle points. A two dimensional representation of this surface around the point of intersection is shown schematically in figure 8.6.

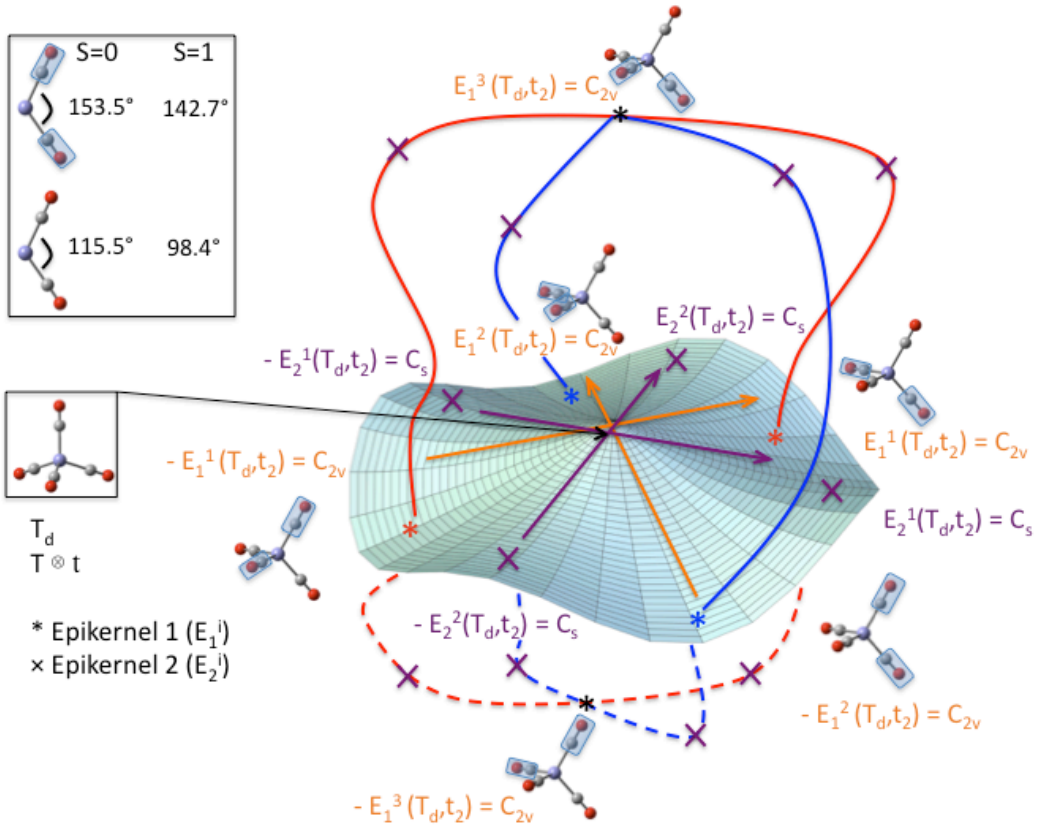

Figure 8.6 Representation of lowest adiabatic potential of singlet (S=0) and triplet (S=1) $Fe(CO)_4$ around $T \otimes t$ Jahn-Teller conical intersection at tetrahedral (T_d) geometry. There are three equivalent two-dimensional 'troughs' in the space spanned by each pair-wise selection of equal L-M-L angles (boxed vs unboxed). The topological connectivity where the 'troughs' intersect is indicated. There are two non-equivalent epikernel distortion directions $E^i_{1,2}(T_d,t_2)$ leading to 6 equivalent C_{2v} minima (*), and 12 equivalent C_s (×) saddle-points respectively. The non-Berry pseudo-rotation barrier is very small (~5 kcal mol^1). CASSCF optimised geometrical parameters for singlet and triplet states are shown at the top left.

Figure 8.7 shows the geometrical parameters of the Cs symmetry transition state structure. In figure 8.6 the 2D distortion space for four equivalent type 1 C_{2v} epikernels is shown $E_1^1(T_d,t_2) = C_{2v}$, $-E_1^1(T_d,t_2) = C_{2v}$, $E_2^1(T_d,t_2) = C_{2v}$, $-E_2^1(T_d,t_2) = C_{2v}$. Forward and reverse epikernels are distinguished by opening of the OC-Fe-CO ligand pair angles. Forward opens one pair and reverse opens the other. Orthogonal to this space is another equivalent epikernel distortion, forward and reverse as the others to match the prediction of the epikernel principle regarding the number of equivalent critical points. The higher dimensionality of this problem compared to that of chromium

and manganese is reflected in the colours used for each distortion path in figures 8.1 and 8.6. The vibrationally hot intermediates formed after the system has passed through the point of intersection can non-Berry pseudorotate around the 2D part of the surface coloured orange and purple and can equivalently distort around the blue line and the red line that are shown schematically to be 'above' and 'below' the 2D part of the surface because these higher dimensional pathways cannot be properly drawn as they are higher in dimension than 2D. The system can follow any of these paths but cannot switch between them i.e. follow half of the blue path then half of the red. This is also true in figure 8.1 where the system can pseudorotate around the octahedron as long as it does not pass through vertices of three different colours. For example it can move around the equatorial plane of the octahedron passing past minima or red and blue colours, or red and black or blue and black but not red, blue and black. The barrier to rotation is quite small, around 5 kcal mol^{-1}, so we believe the system will be free to pseudorotate many times on this surface before going onto further dissociate. This picture compares very well with the work of Poliakoff and Turner discussed above and their distorted octahedron model shown in figure 8.1.

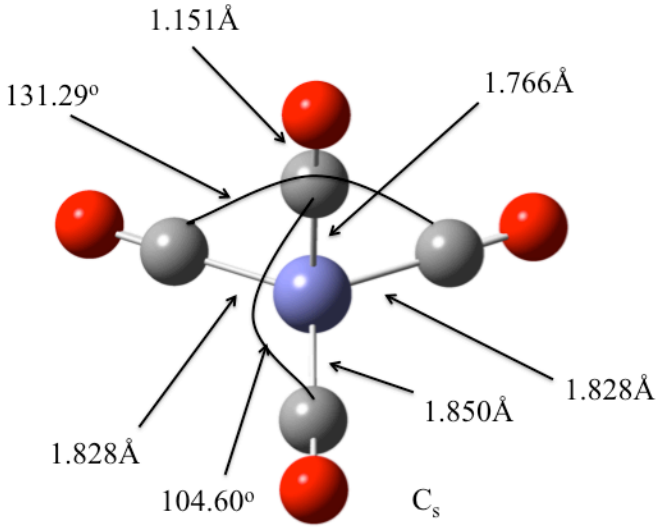

Figure 8.7 Structure and geometrical parameters of the $Fe(CO)_4$ C_s symmetry transition state.

8.4 Conclusions

The relaxation pathway of singlet $Fe(CO)_4$ through a Jahn-Teller induced conical intersection at a tetrahedral geometry has been investigated using multiconfigurational methods. The surface topology was resolved and found to closely match experimental prediction. The complexity of the surface and nature of the conical intersection degeneracy shows the increased complexity over the chromium and manganese cases discussed in previous chapters and the ultrafast photochemistry of transition metal carbonyls in general. Although high level CASSCF modelling of the $^1T_2$ state compares well to experiment the fact that the ^1E state lies lower in energy has not been fully resolved. Further work here will include construction of the full 5D $(T \oplus E) \otimes (t \oplus e)$ potential energy surface for quantum wavepacket simulation. It is expected that the model potentials will help to "unpick" the different couplings involved [40].

8.5 References

[1] Poliakoff, M.; Turner, J. J., Structure and reactions of matrix-isolated tetracarbonyl(0). *J. Chem. Soc., Dalton. Trans.* **1974,** 20, 2276-2285.

[2] Davies, B.; McNeish, A.; Poliakoff, M.; Turner, J. J., Infrared-laser induced isomerization of $Fe(CO)_4$ - 1st non-Berry pseudorotation. *J. Am. Chem Soc.* **1977,** 99, 7573-7579.

[3] Yardley, J. T.; Gitlin, B.; Nathanson, G.; Rosan, A. M., Fragmentation and molecular dynamics in the laser photodissociation of iron pentacarbonyl. *J. Chem. Phys.* **1981,** 74, 370-378.

[4] Whetten, R. L.; Fu, K. J.; Grant, E. R., Photodissociation dynamics of $Fe(CO)_5$ - excited state lifetimes and energy disposal. *J. Chem. Phys.* **1983,** 79, 4899-4911.

[5] Hubbard, J. L.; Lichtenberger, D. L., The Jahn-Teller effect in the photoelectron-spectrum of iron pentacarbonyl. *J. Chem. Phys.* **1981,** 75, 2560-2568.

[6] Waller, I. M.; Hepburn, J. W., State-resolved photofragmentation dynamics of $Fe(CO)_5$ at 193, 248, 266 and 351nm. *J. Chem. Phys.* **1988,** 88, 6658-6669.

[7] Seder, T. A.; Ouderkirk, A. J.; Weitz, E., The wavelength dependence of excimer laser photolysis of $Fe(CO)_5$ in the gas-phase - transient infrared-spectroscopy and kinetics of the $Fe(CO)_4$, $Fe(CO)_3$, $Fe(CO)_2$ photofragments. *J. Chem. Phys.* **1986,** 85, 1977-1986.

[8] Church, S. P.; Grevels, F. W.; Hermann, H.; Kelly, J. M.; Klotzbucher, W. E.; Schaffner, K., IR-monitored flash-photolysis of $Fe(CO)_5$ in benzene solution. *J. Chem. Soc.-Chem. Commun.* **1985**, 594-596.

[9] Poliakoff, M.; Ceulemans, A., Ir laser induced isomerization of iron tetracarbonyl ($Fe(CO)_4$): A unique example of the Jahn-Teller effect. *J. Am. Chem. Soc.* **1984,** 106, 50-54.

[10] Poliakoff, M.; Weitz, E., Shedding light on organometallic reactions - the characterization of $Fe(CO)_4$, a prototypical reaction intermediate. *Accounts Chem. Res.* **1987,** 20, 408-414.
[11] Dixon, A. J.; Healy, M. A.; Hodges, P. M.; Moore, B. D.; Poliakoff, M.; Simpson, M. B.; Turner, J. J.; West, M. A., Apparatus for fast time-resolved infrared detection of reaction intermediates in the solution photochemistry of transition-metal carbonyls. *J. Chem. Soc., Faraday Trans.* **1986,** 82, 2083-2092.
[12] Mckinlay, R. G.; Paterson, M. J., The Jahn-Teller effect in binary transition metal carbonyl complexes. In *The Jahn Teller effect: Fundamentals and implications for physics and chemistry*, Koppel, H.; Barentzen, H.; Yarkony, D. R., Eds. Springer-Verlag: Heidelberg, 2009.
[13] Banares, L.; Baumert, T.; Bergt, M.; Kiefer, B.; Gerber, G., Femtosecond photodissociation dynamics of $Fe(CO)_5$ in the gas phase. *Chem. Phys. Lett.* **1997,** 267, 141-148.
[14] Rubner, O.; Engel, V., Fragmentation dynamics of $Fe(CO)_5$ upon femtosecond excitation: A time-dependent statistical description. *Chem. Phys. Lett.* **1998,** 293, 485-490.
[15] Ihee, H.; Cao, J.; Zewail, A. H., Ultrafast electron diffraction: Structures in dissociation dynamics of $Fe(CO)_5$. *Chem. Phys. Lett.* **1997,** 281, 10-19.
[16] Rubner, O.; Baumert, T.; Bergt, M.; Kiefer, B.; Gerber, G.; Engel, V., Theoretical analysis of femtosecond excitation and fragmentation dynamics of $Fe(CO)_5$. *Chem. Phys. Lett.* **2000,** 316, 585-592.
[17] Ihee, H.; Cao, J. M.; Zewail, A. H., Ultrafast electron diffraction of transient $[Fe(CO)_4]$: Determination of molecular structure and reaction pathway. *Angew. Chem.-Int. Edit.* **2001,** 40, 1532.
[18] Klessinger, M., Conical intersections and the mechanism of singlet photoreactions. *Angew. Chem.-Int. Edit. Engl.* **1995,** 34, 549-551.
[19] Fuss, W.; Trushin, S. A.; Schmid, W. E., Ultrafast photochemistry of metal carbonyls. *Res. Chem. Intermed.* **2001,** 27, 447-457.
[20] Trushin, S. A.; Fuss, W.; Schmid, W. E., Conical intersections, pseudorotation and coherent oscillations in ultrafast photodissociation of group-6 metal hexacarbonyls. *Chem. Phys.* **2000,** 259, 313-330.
[21] Trushin, S. A.; Fuss, W.; Schmid, W. E.; Kompa, K. L., Femtosecond dynamics and vibrational coherence in gas-phase ultraviolet photodecomposition of $Cr(CO)_6$. *J. Phys. Chem. A* **1998,** 102, 4129-4137.
[22] Trushin, S. A.; Kosma, K.; Fuss, W.; Schmid, W. E., Wavelength-independent ultrafast dynamics and coherent oscillation of a metal-carbon stretch vibration in photodissociation of $Cr(CO)_6$ in the region of 270-345 nm. *Chem. Phys.* **2008,** 347, 309-323.
[23] Trushin, S. A.; Fuss, W.; Kompa, K. L.; Schmid, W. E., Femtosecond dynamics of $Fe(CO)_5$ photodissociation at 267 nm studied by transient ionization. *J. Phys. Chem. A* **2000,** 104, 1997-2006.
[24] Leadbeater, N., Enlightening organometallic chemistry: The photochemistry of $Fe(CO)_5$ and the reaction chemistry of unsaturated iron carbonyl fragments. *Coord. Chem. Rev.* **1999,** 188, 35-70.
[25] Poliakoff, M.; Turner, J. J., The structure of $[Fe(CO)_4]$ - an important new chapter in a long-running story. *Angew. Chem.-Int. Edit.* **2001,** 40, 2809-2812.
[26] Barnes, L. A.; Rosi, M.; Bauschlicher, C. W., An ab initio study of $Fe(CO)_1$, $Fe(CO)_5$ and $Cr(CO)_6$. *J. Chem. Phys.* **1991,** 94, 2031-2039.

[27] Radius, U.; Bickelhaupt, F. M.; Ehlers, A. W.; Goldberg, N.; Hoffmann, R., Is CO a special ligand in organometallic chemistry? Theoretical investigation of ab, $Fe(CO)_4(ab)$, and $Fe(ab)_5$ (ab = N_2, CO, BF, SiO). *Inorg. Chem.* **1998,** 37, 1080-1090.

[28] Li, J.; Schreckenbach, G.; Ziegler, T., A reassessment of the first metal-carbonyl dissociation-energy in $M(CO)_4$ (M=Ni,Pd,Pt), $M(CO)_5$ (M=Fe,Ru,Os), and $M(CO)_6$ (M=Cr,Mo,W) by a quasi-relativistic density-functional method. *J. Am. Chem Soc.* **1995,** 117, 486-494.

[29] Gonzalez-Blanco, O.; Branchadell, V., Density functional study of the Fe-CO bond dissociation energies of $Fe(CO)_5$. *J. Chem. Phys* **1999,** 110, 778-783.

[30] Ehlers, A. W.; Frenking, G., Structures and bond energies of the transition-metal carbonyls $M(CO)_5$ (M=Fe,Ru,Os) and $M(CO)_4$ (M=Ni,Pd,Pt). *Organometallics* **1995,** 14, 423-426.

[31] Wang, W. H.; Weitz, E., A theoretical study of the reaction $H_2Fe(CO)_4$ reversible arrow $H_2Fe(CO)_4$. *J. Phys. Chem. A* **1997,** 101, 2358-2363.

[32] Lyne, P. D.; Mingos, D. M. P.; Ziegler, T.; Downs, A. J., Molecular-orbital analysis of the intermediates and products generated by the photooxidation of iron pentacarbonyl. *Inorg. Chem.* **1993,** 32, 4785-4796.

[33] Harvey, J. N.; Aschi, M., Modelling spin-forbidden reactions: Recombination of carbon monoxide with iron tetracarbonyl. *Faraday. Disc.* **2003,** 124, 129-143.

[34] Harvey, J. N.; Poli, R., Computational study of the spin-forbidden H_2 oxidative addition to 16-electron complexes. *Dalton. Trans.* **2003**, 4100-4106.

[35] Besora, M.; Carrero-Macedo, J. L.; Cowan, A. J.; George, M. W.; Harvey, J. N.; Portius, P.; Ronayne, K. L.; Sun, X.; Towrie, M., A combined theoretical and experimental study on the role of spin states in the chemistry of Fe(CO) photoproducts. *J. Am. Chem Soc.* **2009,** 131, 3583-3592.

[36] Apostolova, E. S., $Fe(CO)_4$ flexible as a two-level system avoided conical intersection. *Int. J. Quan. Chem.* **2006,** 106, 1225-1236.

[37] Bearpark, M. J.; Blancafort, L.; Robb, M. A., The pseudo-Jahn-Teller effect: A CASSCF diagnostic. *Mol. Phys.* **2002,** 100, 1735-1739.

[38] Tananbe, Y.; Sugano, S., On the absorption spectra of complex ions I. *J. Phys. Soc. Jap.* **1954,** 9, 753-766.

[39] Meiswinkel, R.; Koppel, H., Combined Jahn-Teller and pseudo-Jahn-Teller effects in the P_4^+ cation. *Chem. Phys. Lett.* **1993,** 201, 449-457.

[40] Bersuker, I. B., Modern aspects of the Jahn-Teller effect theory and applications to molecular problems. *Chem. Rev.* **2001,** 101, 1067-1114.

Chapter 9

Conclusions

The work described in this thesis looked at important aspects of the photochemistry of binary transition metal carbonyl complexes. These important inorganic complexes have been studied intensely for many years in terms of their structure and reactivity but it has only been in recent years with the development of modern laser based experimental techniques and theoretical methodologies that can account for vibronic coupling related behaviour that the complex spectroscopy and reactive photochemistry exhibited by these carbonyl complexes can be accurately probed.

The first section of this thesis concentrated on the electronic spectra of a number of binary carbonyls. It had been noted throughout the thesis that the electronic spectra of these carbonyls are challenging to accurately study due to the complexity of the spectra. They are poorly resolved experimentally with few experimental features, and a large density of electronic states within a relatively narrow energy range. Some previous theoretical investigations of a few carbonyls had been reported in the literature, but none had been performed using highly correlated methodologies such as coupled cluster response theory.

In chapter 3 the one- and two-photon electronic absorption spectra of $Fe(CO)_5$ were studied using a range of state-of-the-art theoretical methods, including a hierarchy of coupled cluster response methods. It was concluded from this work that these coupled cluster response methods along with the CAM-B3LYP density functional, can be successfully applied to this system. It was found that the spectra were indeed dominated by MLCT states and there was a large density of electronic states within the investigated energy range. It was concluded that the best method for this molecule was the LR-CCSD method that agreed reasonably with experiment. The CAM-B3LYP method was also found to compare favourably to this method however further study would be needed to fully confirm this. It was also found that the CC2 method would be unsuitable in this case giving excitation energies that were much lower in energy than experiment or the related CCSD method. The two-photon absorption spectrum was produced using the QR-CCSD method for the first time and it was shown that the spectrum is different to the one-photon spectrum with some spectral overlap between the two. This show promise as a two-photon absorption experiment could trigger new photochemistry by exciting the system to a state not available in one-photon absorption.

In chapter 4 a similar study was performed, this time looking at the binary carbonyls of chromium and nickel, $Cr(CO)_6$ and $Ni(CO)_4$ respectively. The electronic spectrum of these two carbonyls were thought to be just as challenging to study as the $Fe(CO)_5$, with a spectra dominated by charge transfer states. Again it was found from this study that the CCSD method was the best method for these systems for the study of electronic excited states, with the CC2 method giving disastrous results for both systems. Again, the one-photon and two-photon spectra of each carbonyl were found to be very different showing promise for new photochemistry with a two-photon absorption experiment. The spectrum of $Ni(CO)_4$ was found to contain only MLCT states but this was expected due to the full 3d orbital shell of nickel stopping the possibility of metal centred transitions.

In chapter 5 some the structure and one-photon absorption spectra of the group 7 mixed-metal bimetallic carbonyls, $MnTc(CO)_{10}$, $MnRe(CO)_{10}$ and $TcRe(CO)_{10}$ were presented. These species showed that a wide range of carbonyls can be studied theoretically, in this case a group of carbonyls that have not been studied to such an extent as their monometallic group 7 analogues, for example $Mn_2(CO)_{10}$. DFT methods were used to test their performance in terms of characterising charge transfer states in their electronic spectra. Coupled cluster methods could not be used due to system size. In agreement with previous theoretical studies on the structure of one carbonyl, $MnRe(CO)_{10}$, all carbonyls were found to adopt the same ground state structure, a staggered C_{4v} symmetry structure close in energy to a eclipsed C_{4v} symmetry transition state structure, which can connect equivalent staggered minima through one imaginary vibrational frequency that relates to rotation around the metal-metal bond. The electronic spectra were also found to be largely the same for all carbonyls with the early part of the spectrum dominated by one high intensity state responsible for homolytic cleavage of the metal-metal bond. TD-DFT methods in this case were found to preform reasonably well in comparison with experiment.

The general conclusions from the results presented in the first part of the thesis centre around how the electronic spectra of a range of different transition metal carbonyls have been studied, some for the first time, theoretically using a range of modern state-of-the-art theoretical methods. The spectra are dominated by charge transfer states and there is a large density of states within the investigated energy range,

confirming past theoretical reports that these systems are very difficult to study accurately in this respect. Both DFT and coupled cluster methods were found to give reasonable results with respect to previous theoretical and experimental methods where applicable with the CCSD methods giving the best cost/accuracy balance. However the CC2 method was found to give extremely poor results, especially in for $Cr(CO)_6$ and $Ni(CO)_4$. Possible reasons the poor performance of the CC2 for these and related systems could be: CIS reference states are very poor reference states as shown in chapter 4, the excited states studied here have multiconfigurational character which requires a treatment of the level of at least EOM-CCSD, the convergence of excitation energies is extremely oscillatory and this explains why CCSD predicts results that are closer to experiment than CC2 and CCR(3) by cancellation of errors. Finally it can be argues that given the importance of electron correlation in these transition metal complexes (i.e. via dative bonding pairs) then any approximations to the doubles amplitudes in methods like CC2 is inappropriate here.

The second part of the thesis looked at the reactive photochemistry of three binary carbonyls, $Cr(CO)_6$, $Mn_2(CO)_{10}$ and $Fe(CO)_5$. The light-induced ultrafast photodissociation mechanism of these species was the focal point here. It had been shown by the group of Fuβ that these systems, after excitation with a femtosecond laser pulse, undergo dissociation of one carbonyl ligand, or the metal-metal bond in the case of $Mn_2(CO)_{10}$, before the new unsaturated photoproduct relaxed to its ground state. The mechanism for relaxation of the initial photoproduct was thought to proceed through a Jahn-Teller induced conical intersection, and coherent oscillations in the transient ion spectra of this process provided some evidence to support this conclusion. A theoretical study was performed on these carbonyls to accurately probe the coupled potential energy surfaces around the points of conical intersection.

In chapters 6 and 7 the photodissociation mechanism of the singlet $Cr(CO)_5$ and doublet $Mn(CO)_5$ products from the respective dissociations of $Cr(CO)_6$ and $Mn_2(CO)_{10}$ were investigated using the CASSCF method and two other analytical tools, namely: The conical intersections for both these species were found to be at a D_{3h} symmetry trigonal bipyramidal structures, with three equivalent C_{4v} minima around the bottom cone of the intersection, separated by three equivalent C_{2v} symmetry transition state structures. The small energy gaps on the lower surface between transition states and

minima suggest pseudorotation around the lower half of the surface by these very vibrationally hot photoproducts would be possible, more so in $Cr(CO)_5$ that $Mn(CO)_5$ due to the large energy gap, possibly leading to trapping at low temperatures. A conical intersection was also found in the relaxation process of the $Fe(CO)_4$ photoproduct of the $Fe(CO)_5$ photodissociation studied in chapter 8. This conical intersection was found to occur at a T_d symmetry geometry with a much more complex surface topology than those reported in chapters 6 and 7, though pseudorotation was again believed to be possible once the system had passed down to the lower state, due to low barriers connecting C_{2v} minima. All three intersections were induced by the Jahn-Teller effect at the point of intersection.

Other transition metal systems have been shown to possess conical intersections and other vibronic coupling related phenomena in their photodissociation and photoisomerisation mechanisms, and even though such systems are not as symmetrical as the carbonyls presented here, some common features regarding the orientation of ligands around the central metal atom(s) endures. What this means is the carbonyl systems presented in this thesis can act as model complexes once more, as they have already done for structure and bonding over the last century. As more and more theoretical studies on transition metal photochemistry appear it becomes apparaent that conical intersections and avoided crossings are becoming ubiquitous in this field so a set of model systems and mechanisms such as the ones presented here are very useful.

The work presented in this thesis looks at two very different parts of the photochemistry of transition metal carbonyls in their electronic spectroscopy and reactive photochemistry, and therefore the contrast in methods used to study these two properties is evident. While both highly correlated, coupled cluster response methods and multireference methods like CASSCF are very different in both in their input and in their deployment. However one thing these methods do have in common is that great care must be taken when using either of them, especially when applying them to the challenging photochemistry presented in this thesis, although it is only through the application of these methods that insight will be gained on this difficult and important topic.

Appendices

Appendix 2.1 Derivation of non-adiabatic coupling term

$$\widehat{H}_e|i\rangle = V^i|i\rangle$$

$$\nabla_n \widehat{H}_e|i\rangle = \nabla_n V^i|i\rangle$$

$$\nabla_n \widehat{H}_e|i\rangle + \widehat{H}_e \nabla_n|i\rangle = V^i \nabla_n|i\rangle + |i\rangle V^i$$

$$\langle j|\nabla_n \widehat{H}_e|i\rangle + \langle j|\widehat{H}_e \nabla_n|i\rangle = V^i \langle j|\nabla_n|i\rangle + \langle j||i\rangle$$

$$\langle j|\nabla_n \widehat{H}_e|i\rangle + V^j \langle j|\nabla_n|i\rangle = V^i \langle j|\nabla_n|i\rangle$$

$$\langle j|\nabla_n \widehat{H}_e|i\rangle = (V^i - V^j)(\langle j|\nabla_n|i\rangle)$$

$$\langle j|\nabla_n|i\rangle = \frac{\langle j|\nabla_n \widehat{H}_e|i\rangle}{V^i - V^j}$$

Appendix 3.1 Table 3.4 unformatted

		Excitation Energy/eV – Coupled cluster Geometry					
Excited State	**Character**	**CC2**	**MR-CCI [2]**	**CASSCF [2]**	**LR-CCSD**	**EOM-CCSD**	**CCR(3)**
1E′	LF dx^2-y^2,dxy - Fe 4p+	3.515 (0.000)	3.557	4.044	4.332 (0.000)	4.386 (0.000)	4.368
1E″	LF dxz,dyz – Fe 4p antibonding	3.435	4.561	4.384	4.782	4.658	4.928
$1A_1$″	MLCT dx^2-y^2,dxy - CO bonding SALC	4.306	4.126	4.336	4.608	4.495	4.722
$1A_2$′	MLCT dx^2-y^2,dxy - CO bonding SALC	3.647	4.717	4.699	5.076	5.011	5.078
2E′	MLCT dx^2-y^2,dxy - CO bonding SALC	3.613 (0.000)	4.873	4.748	5.141 (0.001)	5.062 (0.000)	5.175
2E″	MLCT dx^2-y^2,dxy - CO bonding SALC/antibonding SALC 40%	4.248	4.405	4.384	5.116	5.119	5.076
$1A_2$″	MLCT dx^2-y^2,dxy - CO bonding SALC	3.889 (0.000)	4.591	4.865	5.172 (0.068)	5.077 (0.076)	5.048
3E″	MLCT dxz,dyz - CO	4.258	5.289	5.194	5.330	5.215	5.372

3E″	MLCT dxz,dyz - CO antibonding SALC	4.258	5.289	5.194	5.330	5.215	5.372
$2A_2'$	MLCT dx^2-y^2,dxy - CO bonding SALC/antibonding SALC 40%	4.303			5.660	5.528	5.689
3E′	MLCT dx^2-y^2,dxy - CO bonding SALC 15%/antibonding SALC 48%	3.793 (0.000)			5.680 (0.083)	5.547 (0.056)	5.827
$1A_1'$	MLCT dx^2-y^2,dxy - CO antibonding SALC	3.645	5.583	5.442	5.687	5.563	5.718
4E′	LF dx^2-y^2,dxy – Fe 4s antibonding 53%/4p antibonding 10%	4.280 (0.000)			5.864 (0.044)	5.691 (0.077)	5.882
5E′	MLCT dx^2-y^2,dxy - CO bonding SALC 33%/antibonding SALC 33%	4.884 (0.000)			6.047 (0.081)	5.758 (0.071)	6.418
$2A_1'$	MLCT dx^2-y^2,dxy - CO bonding SALC 15%/antibonding SALC 48%	4.240			5.983	5.871	6.029
$3A_2'$	MLCT dxz,dyz - CO bonding 40%/antibonding 20% SALC	5.879			6.206	6.038	6.347
$2A_1''$	MLCT dxz,dyz - CO antibonding SALC	5.191			6.271	6.134	6.470
4E″	MLCT dxz,dyz - CO bonding 44%/antibonding 44% SALC	4.299			6.347	6.190	6.553
6E′	MLCT dxz,dyz - CO bonding 39%/antibondin	5.167 (0.000)			6.408 (0.005)	6.226 (0.004)	6.594

$2A_2''$	MLCT dxz,dyz - CO antibonding SALC	4.908			6.744 (0.265)	6.624 (0.361)	6.884
$3A_1''$	MLCT dxz,dyz - CO bonding 12%/antibonding 37% SALC	-			6.798	6.653	6.926
$5E''$	MLCT dxz,dyz - CO antibonding SALC	4.620			6.836	6.687	7.063

Appendix 3.2 Cartesian coordinates from chapter 3

CCSD optimised geometry

Fe	0.000000	0.000000	0.000000
C	0.000000	1.808782	0.000000
C	-1.566452	-0.904391	0.000000
C	0.000000	0.000000	1.818668
C	1.566452	-0.904391	0.000000
C	0.000000	0.000000	-1.818668
O	0.000000	0.000000	2.970306
O	2.567368	-1.482271	0.000000
O	0.000000	0.000000	-2.970306
O	0.000000	2.964542	0.000000
O	-2.567368	-1.482271	0.000000

Experimental geometry

Fe	-0.00000000	0.00000000	-0.00000000
C	-0.00000000	0.00000000	1.80600000
C	-1.58742457	-0.91650000	-0.00000000
C	1.58742457	-0.91650000	-0.00000000
C	-0.00000000	0.00000000	-1.80600000
C	-0.00000000	1.83300000	-0.00000000
O	-0.00000000	0.00000000	2.95100000
O	-2.57902365	-1.48900000	-0.00000000
O	2.57902365	-1.48900000	-0.00000000
O	-0.00000000	0.00000000	-2.95100000
O	-0.00000000	2.97800000	-0.00000000

Appendix 3.2 Full spectra of $Fe(CO)_5$ – One-photon absorption

Experimental geometry with ANO-L basis set – CC2

Excitation Energy	Symmetry	Assignment
3.23545	B1	1E"
3.23545	A2	1E"
3.33775	A1	1E'
3.33775	B2	1E'
3.44509	A1	2E'
3.44509	B2	2E'
3.53762	A1	1A1'
3.54273	B2	1A2'
3.65061	A1	3E'
3.65061	B2	3E'
3.839	B1	1A2"
3.92544	A1	4E'
3.92544	B2	4E'
3.9771	A1	2A1'
4.02337	A1	5E'
4.02337	B2	5E'
4.04545	B2	2A2'
4.07196	B1	2E"
4.07196	A2	2E"
4.1014	B1	3E"
4.1014	A2	3E"
4.20515	B1	4E"
4.20515	A2	4E"
4.25813	A2	1A1"
4.52414	B1	5E"
4.52414	A2	5E"
4.72021	B1	2A2"
4.74219	B1	6E"
4.74219	A2	6E"
4.7573	A2	2A1"
4.76929	A1	6E'
4.76929	B2	6E'
4.94592	B1	3A2"
5.04183	B1	7E"
5.04183	A2	7E"
5.05243	A2	2A1"
5.24773	A1	7E'
5.24773	B2	7E'
5.42664	A1	3A1'

5.81366	B2	3A2'

Experimental geometry with ANO-L basis set – LR-CCSD

Symmetry	Excitation Energy/eV	Osc. Strength	Assignment
A1	4.2966	0	1E'
B2	4.2966	0	1E'
A2	4.56544	0	1A1"
B1	4.74793	0	1E"
A2	4.74793	0	1E"
B2	4.96284	0	1A2'
A1	5.05745	0.00453307	2E'
B2	5.05745	0.00453307	2E'
B1	5.08533	0	2E"
A2	5.08533	0	2E"
B1	5.1197	0.06263735	1A2"
B1	5.29314	0	3E"
A2	5.29314	0	3E"
B2	5.60369	0	2A2'
A1	5.63387	0.08771272	3E'
B2	5.63387	0.08771271	3E'
A1	5.6378	0	1A1'
A1	5.78695	0.04098369	4E'
B2	5.78695	0.04098373	4E'
A1	5.91932	0.10409783	5E'
B2	5.91932	0.10409786	5E'
A1	5.93004	0	2A1'
B2	6.1913	0	3A2'
A2	6.20599	0	2A1"
B1	6.3131	0	4E"
A2	6.3131	0	4E"
A1	6.39552	0.05045611	6E'
B2	6.39552	0.05045628	6E'
B1	6.67507	0.22030669	2A2"
A2	6.75727	0	3A1"
B1	6.7621	0	5E"
A2	6.7621	0	5E"
A1	6.80763	0	3A1'
B2	6.81256	0	4A2'
A1	6.83729	0.03124485	3A1'
B1	6.84007	0	6E"
A2	6.84007	0	6E"
A2	6.92736	0	4A1"
B1	7.12112	0	3A2"

B1	7.1492	0.14082936	4A2"

Experimental geometry with ANO-L basis set – CCR(3)

Excitation Energy	Symmetry	Assignment
4.32473	A1	1E'
4.32473	B2	1E'
4.71802	A2	1A1"
4.92575	B1	1E"
4.92575	A2	1E"
4.98375	B2	1A2'
5.04091	B1	1A2"
5.05604	B1	2E"
5.05604	A2	2E"
5.10414	A1	2E'
5.10414	B2	2E'
5.36731	B1	3E"
5.36731	A2	3E"
5.67784	B2	2A2'
5.68607	A1	1A1'
5.79333	A1	3E'
5.79333	B2	3E'
5.86314	A1	4E'
5.86314	B2	4E'
5.99468	A1	2A1'
6.31485	A1	5E'
6.31485	B2	5E'
6.36053	B2	3A2'
6.41621	A2	2A1"
6.52906	B1	4E"
6.52906	A2	4E"
6.60685	A1	6E'
6.60685	B2	6E'
6.81951	B1	2A2"
6.91745	A2	3A1"
6.98235	A2	4A1"
7.06819	B1	5E"
7.06819	A2	5E"
7.09321	B1	3A2"
7.13183	B1	6E"
7.13183	A2	6E"
7.1831	A1	3A1'
7.22213	A1	4A1'
7.24985	B2	4A2'

7.27991	B1	4A2"

CCSD optimised geometry with ANO-L basis set – CC2

Excitation Energy	Symmetry	Assignment
3.43507	B1	1E"
3.43508	A2	1E"
3.51575	A1	1E'
3.51575	B2	1E'
3.61303	A1	2E'
3.61303	B2	2E'
3.64533	A1	1A1'
3.64727	B2	1A2'
3.79334	A1	3E'
3.79334	B2	3E'
3.88982	B1	1A2"
4.07023	A1	4E'
4.07023	B2	4E'
4.24056	A1	2A1'
4.24843	A2	2E"
4.24844	B1	2E"
4.25874	B1	3E"
4.25874	A2	3E"
4.28018	A1	4E'
4.28018	B2	4E'
4.29912	B1	4E"
4.29913	A2	4E"
4.30377	B2	2A2'
4.30637	A2	1A1"
4.62092	B1	5E"
4.62093	A2	5E"
4.88484	A1	5E'
4.88484	B2	5E'
4.90827	B1	2A2"
4.93543	B1	6E"
4.93543	A2	6E"
4.95128	A2	2A1"
5.08177	B1	3A2"
5.16741	A1	6E'
5.16741	B2	6E'
5.1791	B1	7E"
5.1791	A2	7E"
5.1915	A2	2A1"
5.66071	A1	3A1'

5.87926	B2	3A2'

CCSD optimised geometry with ANO-L basis set – LR-CCSD

Symmetry	Excitation Energy/eV	Osc. Strength	Assignment
A1	4.33262	0	1E'
B2	4.33262	0	1E'
A2	4.6086	0	1A1"
A2	4.78249	0	1E"
B1	4.7825	0	1E"
B2	5.07684	0	1A2'
B1	5.11666	0	2E"
A2	5.11666	0	2E"
A1	5.14145	0.00135658	2E'
B2	5.14145	0.00135654	2E'
B1	5.17223	0.0680522	1A2"
B1	5.33067	0	3E"
A2	5.33068	0	3E"
B2	5.66098	0	2A2'
A1	5.68028	0.08380878	3E'
B2	5.68028	0.08380572	3E'
A1	5.68707	0	1A1'
A1	5.86409	0.04480281	4E'
B2	5.86409	0.04480761	4E'
A1	5.98313	0	2A1'
A1	6.04744	0.08177299	5E'
B2	6.04745	0.08177175	5E'
B2	6.2062	0	3A2'
A2	6.27135	0	2A1"
B1	6.34708	0	4E"
A2	6.34708	0	4E"
A1	6.40871	0.05108259	6E'
B2	6.40871	0.05108143	6E'
B1	6.74494	0.26552304	2A2"
A2	6.79837	0	3A1"
A2	6.83644	0	5E"
B1	6.83645	0	5E"
B1	6.87865	0	6E"
A2	6.87866	0	6E"
A2	6.92964	0	4A1"
A1	6.94288	0.13346932	7E'
B2	6.94288	0.13346912	7E'
A1	6.95048	0	3A1'
B1	7.16351	0	3A2"

B1	7.16817	0.11810923	7E"

Experimental geometry – EOM-CCSD

Excitation Energy/eV	Oscillator Strength	Assignment
4.3566	0	1E'
4.3566	0	1E'
4.4517	0	1A1"
4.6236	0	1E"
4.6236	0	1E"
4.9068	0	1A2'
4.9878	0.0007	2E'
4.9878	0.0007	2E'
5.0258	0.0698	1A2"
5.0883	0	2E"
5.0883	0	2E"
5.1792	0	3E"
5.1792	0	3E"
5.4632	0.0163	3E'
5.4632	0.0163	3E'
5.4676	0	2A2'
5.5174	0	1A1'
5.5888	0.1592	4E'
5.5888	0.1591	4E'
5.6755	0.0556	5E'
5.6755	0.0556	5E'
5.8203	0	2A1'
6.0248	0	3A2'
6.0833	0	2A1"
6.1656	0	4E"
6.1656	0	4E"
6.2169	0.0486	6E'
6.2169	0.0486	6E'
6.5728	0.2944	2A2"
6.6008	0	3A1"
6.6889	0	5E"
6.6889	0	5E"
6.7462	0	4A1"
6.7534	0.2181	7E'
6.7534	0.2181	7E'
6.7831	0	6E"
6.7832	0	6E"
6.7967	0	3A1'
6.9526	0	3A2"

6.9545	0.1647	4A2"

CCSD optimised geometry – EOM-CCSD

Excitation Energy/eV	Oscillator Strength	Assignment
4.3866	0.0001	1E'
4.3866	0.0001	1E'
4.4951	0	1A1"
4.6587	0	1E"
4.6587	0	1E"
5.0119	0	1A2'
5.0625	0	2E'
5.0625	0	2E'
5.0773	0.0765	1A2"
5.1192	0	2E"
5.1192	0	2E"
5.2154	0	3E"
5.2154	0	3E"
5.5282	0	2A2'
5.5473	0.0561	3E'
5.5473	0.056	3E'
5.5633	0	1A1'
5.6918	0.0778	4E'
5.6918	0.0778	4E'
5.7587	0.0711	5E'
5.7587	0.0711	5E'
5.8714	0	2A1'
6.0385	0	3A2'
6.1343	0	2A1"
6.1908	0	4E"
6.1908	0	4E"
6.2264	0.0485	6E'
6.2264	0.0485	6E'
6.6244	0.3617	2A2"
6.6532	0	3A1"
6.6876	0	5E"
6.6877	0	5E"
6.7484	0	4A1"
6.8171	0.2908	7E'
6.8171	0.2907	7E'
6.8793	0	6E"
6.8793	0	6E"
6.944	0	3A1'
6.9816	0.1072	3A2"

7.0248	0	4A2"

CCSD optimised geometry with ANO-M basis set – CCR(3)

Excitation Energy/eV
4.23315
4.23315
4.74038
4.89816
4.89816
4.92219
4.92219
5.06708
5.07955
5.16182
5.16182
5.35628
5.35629
5.67541
5.72089
5.85798
5.85798
5.8689
5.8689
6.06996
6.31346
6.41384
6.47469
6.47469
6.57569
6.57569
6.63325
6.63325
6.85022
6.92695
6.93791
7.00932
7.00932
7.02662
7.02662
7.06425
7.06425
7.19471
7.22841

7.44648
7.44648
7.99785
7.99785
8.27541
8.3835
8.3835
8.38863
8.40065
9.63537
9.63538
10.00138
10.00138
10.10219
10.10644
10.16398
10.16398
10.26019
10.26019
10.26772
10.46861

CCSD optimised geometry with ANO-S basis set – CC2

Excitation Energies/eV	**Osc Strength**
3.34259	0.11881159
3.34259	0.11881178
3.36608	0
3.36609	0
3.44108	0
3.44758	0
3.58663	0.13049232
3.58663	0.13049035
3.73361	0.00552581
3.73362	0.00552739
3.75354	0.46053416
4.0432	0.06387922
4.04321	0.06387926
4.09068	0
4.09068	0
4.14494	0
4.40033	0
4.40033	0

4.45428	0
4.45428	0
4.90354	0.01952607
4.99945	0
4.99945	0
5.01242	0
5.23278	0.0628417
5.23278	0.06284046
5.51525	0
5.76537	0.16499715
5.76537	0.16499764
5.79156	0
5.82459	0
6.72604	0.16220461
6.83526	0
6.83526	0
6.924	0
6.97535	0
6.97536	0
7.0562	0.06080974
7.0562	0.06080746
7.15281	0
7.15281	0
7.16649	0
7.18643	0
7.20821	0
7.29182	0.07274152
7.29183	0.07273825
7.38587	0
7.38587	0
7.4153	0.13463541
7.49821	0.00010349
7.49821	0.00010352
7.7306	0
7.74022	0
7.79149	0
7.79149	0
8.06825	0.01980094
8.06825	0.01980073
8.12518	0
8.21382	0
9.05295	0

CCSD optimised geometry with ANO-S basis set – LR-CCSD

Excitation Energy/eV	Osc Strengths
4.38488	0
4.38488	0
4.57454	0
4.73769	0
4.7377	0
5.05177	0
5.09576	0
5.09576	0
5.14281	0
5.14281	0
5.16049	0.0641203
5.28772	0
5.28772	0
5.60883	0
5.61482	0.08695428
5.61482	0.08695207
5.66983	0
5.88252	0.03137852
5.88252	0.0313816
6.00942	0
6.16793	0
6.20059	0
6.24386	0.06938161
6.24386	0.06938163
6.2592	0
6.2592	0
6.37474	0.05706494
6.37474	0.05706344
6.71563	0.35133029
6.75942	0
6.75943	0
6.79096	0
6.87542	0
6.95009	0.34450965
6.95009	0.34450866
7.06873	0
7.06873	0
7.15572	0.06836129
7.28193	0.11543316
7.42834	0
7.42834	0
7.60861	0

7.60861	0
8.39702	0.13311479
8.39702	0.13311492
8.42601	0
8.43655	0
8.4945	0
9.45647	0
9.45648	0
9.7901	0
10.02529	0.00045375
10.02529	0.00045379
10.0627	0
10.0627	0
10.09844	0
10.10025	0
10.20795	0.00325147
10.20796	0.00325099
10.32765	0

CCSD optimised geometry with ANO-S basis set – CCR(3)

Excitation Energy/eV
4.41541
4.41541
4.72448
4.92574
4.92574
5.05678
5.09345
5.10493
5.10494
5.15524
5.15524
5.32851
5.32851
5.66417
5.67947
5.82132
5.82133
5.8293
5.8293
6.07495
6.34264
6.42389

6.46929
6.46929
6.60198
6.60198
6.65056
6.65057
6.89093
6.90062
6.93595
6.98714
6.98715
6.99503
6.99504
7.06037
7.06037
7.17311
7.21609
7.49432
7.49433
8.02592
8.02592
8.3444
8.35269
8.36565
8.36565
8.38527
9.72058
9.72059
9.97942
9.97942
9.99055
10.00187
10.06482
10.06482
10.13703
10.29328
10.29328
10.46238

CCSD optimised geometry with SDD basis set – CC2

Excitation Energies/eV	Osc Strength
3.18901	0.1556793
3.18901	0.1556801

3.24149	0
3.2415	0
3.28681	0
3.32492	0
3.38547	0.07533209
3.38548	0.07533794
3.43162	0.48654718
3.45939	0.02166925
3.45939	0.02166222
3.7661	0.05543726
3.7661	0.05543759
3.80979	0
3.80979	0
3.86844	0
3.92604	0
3.92604	0
4.13784	0
4.13784	0
4.773	0.01836864
4.87451	0
4.87451	0
4.89727	0
5.06648	0.03759337
5.06648	0.03759254
5.24567	0
5.50585	0.17329751
5.50586	0.1732975
5.52119	0.00000001
6.0465	0
6.56229	0.21945643
6.63149	0.00000001
6.6315	0
6.8263	0
6.8263	0
6.88102	0
6.98443	0.03431084
6.98444	0.03431006
7.66827	0
7.77725	0.00192447
7.77725	0.00192458
7.81232	0
7.86425	0
8.01417	0
8.025	0

8.025	0
8.10374	0.30083853
8.10375	0.30083993
8.49062	0.24617476
8.49453	0.0027336
8.49453	0.00273388
8.49809	0
8.55793	0
8.64906	0
8.64906	0
8.67393	0
8.97152	0.7210077
9.09582	0
9.13873	0

CCSD optimised geometry with SDD basis set – LR-CCSD

Excitation Energy/eV	**Osc Strength**
4.29039	0
4.29039	0
4.57963	0
4.57963	0
4.59851	0
4.67487	0
4.67487	0
5.01372	0
5.02805	0.00415774
5.02805	0.00415778
5.21186	0.0283709
5.22652	0
5.22652	0
5.3899	0.04696001
5.3899	0.04696017
5.45822	0
5.4906	0
5.70402	0
5.73159	0
5.73159	0
5.79535	0.00213319
5.79535	0.00213268
5.84858	0
5.87313	0
6.02025	0.01751283
6.02025	0.01751389

6.05283	0.01556619
6.05284	0.01556474
6.16333	0
6.16333	0
6.25374	0.4874372
6.37877	0
6.55745	0.48531251
6.55745	0.48531168
6.68552	0
6.71774	0.05457376
6.93056	0
6.93056	0
6.94584	0
6.94584	0
7.15731	0
7.15732	0
7.17211	0.08743862
7.83111	0.18124135
7.83111	0.18124137
7.86199	0
7.86211	0
8.57155	0
9.93403	0.24966939
10.02214	0
10.02215	0
10.02727	0
10.16004	0
10.16004	0
10.16663	0.01696426
10.16663	0.01696713
10.24899	0
10.3389	0.00000675
10.34013	0.1355026
10.34014	0.13550668

CCSD optimised geometry with SDD basis set – CCR(3)

Excitation Energy/eV
4.33616
4.33617
4.60738
4.60738
4.76856
4.93788

4.93789
5.07938
5.10539
5.15789
5.15789
5.26618
5.26618
5.62712
5.67241
5.67241
5.70692
5.80622
5.80622
5.95464
6.06469
6.06469
6.06855
6.07128
6.38001
6.38002
6.51572
6.51572
6.57845
6.57845
6.59567
6.62652
6.65914
6.65914
6.76161
6.85518
6.99745
6.99747
7.11313
7.24673
7.24674
7.48481
7.48482
7.91006
7.91006
7.91244
7.93296
8.38534
9.9134
9.9167

9.91672
10.05088
10.05089
10.11182
10.17094
10.24377
10.24379
10.34727
10.43481
10.43482

CCSD optimised geometry – CAM-B3LYP

Excitation Energy/eV	Oscillator Strength
3.8153	0
3.8767	0.0001
3.8767	0.0001
4.1217	0
4.1217	0
4.3208	0.0554
4.4587	0
4.6012	0.0236
4.6012	0.0236
4.7377	0
4.7377	0
5.0089	0
5.0089	0
5.1398	0
5.266	0
5.3176	0.0258
5.3176	0.0258
5.4758	0
5.5242	0.0745
5.5242	0.0745
5.5773	0
5.745	0
5.8998	0.0501
5.8998	0.0501
6.1221	0.0455
6.123	0
6.123	0
6.2523	0
6.5409	0
6.5409	0

6.5623	0.0228
6.5625	0.0228
6.5956	0
6.6406	0
6.6406	0
6.7533	0.0038
6.8826	0
6.8826	0
7.0207	0.2136
7.0207	0.2136
7.4413	0.46
7.7155	0
7.7307	0
7.7308	0
7.818	0
7.8275	0.0038
7.8276	0.0038
8.0987	0
8.2243	0
8.2244	0
8.2244	0
8.2634	0.1688
8.2634	0.1688
8.501	0
9.3559	0.0046
9.3559	0.0046
9.4277	0.0047
9.4515	0
9.4515	0
9.4707	0

Experimental geometry – CAM-B3LYP

Excitation Energy/eV	Oscillator Strength
3.7821	0
3.8188	0
3.8189	0
4.0948	0
4.0948	0
4.2761	0.0512
4.341	0
4.4964	0.0304
4.4964	0.0304
4.7061	0

4.7061	0
4.9894	0
4.9894	0
5.1115	0
5.1997	0
5.2792	0.0246
5.2792	0.0246
5.4611	0
5.4927	0.0785
5.4927	0.0785
5.5505	0
5.6484	0
5.8858	0.048
5.8859	0.048
6.0235	0.0462
6.0694	0
6.0694	0
6.2428	0
6.4474	0.0266
6.4476	0.0266
6.4946	0
6.4946	0
6.5924	0
6.636	0
6.636	0
6.7316	0.0042
6.8513	0
6.8513	0
6.9771	0.201
6.9771	0.201
7.4777	0.4753
7.5969	0
7.6233	0
7.6234	0
7.6868	0
7.6979	0.0052
7.698	0.0052
8.0824	0
8.1117	0
8.1117	0
8.1773	0
8.2392	0.1559
8.2392	0.1559
8.5397	0

9.2541	0.0073
9.2541	0.0073
9.3027	0.0043
9.3237	0
9.3237	0
9.3448	0

Appendix 3.3 Full spectra of $Fe(CO)_5$ – Two-photon absorption

CCSD optimized geometry with ANO-L basis set – QR-CCSD

Symmetry	Excitation Energy/eV	TPA Delta	Assignment
A1	4.33262	0.04862976	1E'
B2	4.33262	0.0486237	1E'
A2	4.6086	0	1A1"
A2	4.78249	1.61595321	1E"
B1	4.7825	1.61592515	1E"
B2	5.07684	0	1A2'
B1	5.11666	1.43892406	2E"
A2	5.11666	1.43892687	2E"
A1	5.14145	1.70752319	2E'
B2	5.14145	1.70753795	2E'
B1	5.17223	0	1A2"
B1	5.33067	24.47979547	3E"
A2	5.33068	24.47963744	3E"
B2	5.66098	0	2A2'
A1	5.68028	41.66526952	3E'
B2	5.68028	41.66265147	3E'
A1	5.68707	195.3120586	1A1'
A1	5.86409	29.34529249	4E'
B2	5.86409	29.34773643	4E'
A1	5.98313	67.8698668	2A1'
A1	6.04744	9.52689989	5E'
B2	6.04745	9.5270501	5E'
B2	6.2062	0	3A2'
A2	6.27135	0	2A1"
B1	6.34708	1.58130707	4E"
A2	6.34708	1.58135693	4E"
A1	6.40871	11.94023668	6E'
B2	6.40871	11.94007761	6E'
B1	6.74494	0	2A2"
A2	6.79837	0	3A1"

A2	6.83644	0.04909976	5E"
B1	6.83645	0.04922415	5E"
B1	6.87865	103.3520736	6E"
A2	6.87866	103.3512361	6E"
A2	6.92964	0	4A1"
A1	6.94288	23.03768119	7E'
B2	6.94288	23.0408464	7E'
A1	6.95048	49.42620151	3A1'
B1	7.16351	1.00546584	3A2"
B1	7.16817	0	7E"

Experimental geometry with ANO-L basis set – QR-CCSD

Symmetry	Excitation Energy/eV	TPA Delta	Assignment
A1	4.2966	0.03878653	1E'
B2	4.2966	0.03878677	1E'
A2	4.56544	0	1A1"
B1	4.74793	0.92098205	1E"
A2	4.74793	0.92098046	1E"
B2	4.96284	0	1A2'
A1	5.05745	0.85001303	2E'
B2	5.05745	0.85002511	2E'
B1	5.08533	1.80673568	2E"
A2	5.08533	1.80673421	2E"
B1	5.1197	0	1A2"
B1	5.29314	27.67576655	3E"
A2	5.29314	27.67586579	3E"
B2	5.60369	0	2A2'
A1	5.63387	65.99171453	3E'
B2	5.63387	65.99171453	3E'
A1	5.6378	177.6837805	1A1'
A1	5.78695	25.21253872	4E'
B2	5.78695	25.21254012	4E'
A1	5.91932	9.10800932	5E'
B2	5.91932	9.10810432	5E'
A1	5.93004	89.69867528	2A1'
B2	6.1913	0	3A2'
A2	6.20599	0	2A1"
B1	6.3131	1.56169304	4E"
A2	6.3131	1.56169296	4E"
A1	6.39552	11.59696942	6E'
B2	6.39552	11.59700376	6E'
B1	6.67507	0	2A2"
A2	6.75727	0	3A1"

B1	6.7621	110.7278793	5E"
A2	6.7621	110.7277412	5E"
A1	6.80763	49.59491206	3A1'
B2	6.81256	0	4A2'
A1	6.83729	133.2621991	3A1'
B1	6.84007	6.34254093	6E"
A2	6.84007	6.34283474	6E"
A2	6.92736	0	4A1"
B1	7.12112	0.53026236	3A2"
B1	7.1492	0	4A2"

Appendix 4.1 Cartesian coordinates from chapter 4

$Cr(CO)_6$ CCSD optimised geometry

Cr	0.000000	0.000000	0.000000
C	0.000000	0.000000	1.928104
C	0.000000	1.928104	0.000000
C	-1.928104	0.000000	0.000000
C	0.000000	0.000000	-1.928104
C	1.928104	0.000000	0.000000
C	0.000000	-1.928104	0.000000
O	0.000000	0.000000	3.075679
O	-3.075679	0.000000	0.000000
O	0.000000	-3.075679	0.000000
O	0.000000	3.075679	0.000000
O	0.000000	0.000000	-3.075679
O	3.075679	0.000000	0.000000

$Ni(CO)_4$ CCSD optimised geometry

Ni	0.000000	0.000000	0.000000
C	1.057505	1.057505	1.057505
C	-1.057505	-1.057505	1.057505
C	1.057505	-1.057505	-1.057505
C	-1.057505	1.057505	-1.057505
O	1.717400	1.717400	1.717400
O	-1.717400	1.717400	-1.717400
O	-1.717400	-1.717400	1.717400
O	1.717400	-1.717400	-1.717400

Appendix 4.2 Full spectra of $Cr(CO)_6$ and $Ni(CO)_4$ – One-photon absorption

$Cr(CO)_6$ - LR-CCSD with ANO basis set

Excitation Energy/eV	Oscilator Strength
4.38467	0.00000
4.38467	0.00000
4.40884	0.00000
4.43233	0.00000
4.43233	0.00000
4.43233	0.00000
4.94553	0.00000
4.94553	0.00000
4.94553	0.00000
4.99764	0.11159
4.99764	0.11159
4.99764	0.11159
5.17351	0.00000
5.17351	0.00000
5.24008	0.00000
5.38807	0.00000
5.38807	0.00000
5.38807	0.00000
5.47076	0.00000
5.47076	0.00000
5.47076	0.00000
5.70398	0.00000
5.70398	0.00000
5.70398	0.00000
5.86444	0.00000
5.86444	0.00000
6.05660	0.00000
6.05660	0.00000
6.05660	0.00000
6.12887	0.65520
6.12887	0.65520
6.12887	0.65520
6.23396	0.00000
6.23396	0.00000
6.23396	0.00000
7.24442	0.00000
7.24442	0.00000
7.24442	0.00000
7.46114	0.00000

7.46114	0.00000
7.86801	0.00000
8.02880	0.00000
10.03246	0.00000
10.03246	0.00000
10.03246	0.00000
10.06397	0.00113
10.06397	0.00113
10.06397	0.00113

$Ni(CO)_4$ – CC2 with ANO basis set

Excitation Energy/eV	Oscillator Strength
1.36177	0.49188896
1.36177	0.49188877
1.36177	0.49188938
1.89994	0
1.89994	0
1.89994	0
1.93236	0
1.93236	0
1.95563	0
1.9793	0.01514308
1.9793	0.01514312
1.9793	0.01514314
2.01229	0
2.01229	0
2.04718	0
2.04718	0
2.04718	0
2.08636	0
2.08636	0
2.08636	0

$Ni(CO)_4$ – LR-CCSD with ANO basis set

Excitation Energy/eV	Oscillator Strength
4.85394	0
4.85394	0
4.85394	0
4.88191	0
4.88191	0
5.18531	0
5.18531	0
5.18531	0
5.19843	0.03894604

5.19843	0.03894604
5.19843	0.03894605
5.54368	0
5.54368	0
5.54368	0
5.64043	0.09803678
5.64043	0.09803678
5.64043	0.09803678
6.06332	0
6.32145	0
6.32145	0

$Ni(CO)_4$ – CCR(3) with ANO basis set

Excitation Energy/eV
6.08874
6.08874
6.08874
6.10624
6.10624
6.3339
6.3339
6.3339
6.38731
6.38731
6.38731
6.65834
6.65834
6.65834
6.75149
6.75149
6.75149
6.75874
6.75874
6.81547

$Ni(CO)_4$ – LR-CCSD with ECP basis set

Excitation/eV	**Oscillator Strength**
3.6812	0
3.6812	0
3.6812	0
4.20977	0
4.20977	0
4.41575	0.05918535
4.41575	0.05918535

4.41575	0.05918535
4.44813	0
4.60292	0
4.60292	0
4.60292	0
4.63301	0
4.71853	0
4.71853	0
4.71853	0
5.11168	0
5.11168	0
5.11168	0
5.46756	0

$Ni(CO)_4$ – CCR(3) with ECP basis set

Excitation/eV
6.41837
6.71119
6.71119
6.71119
6.84063
6.84063
7.1737
7.40698
7.40698
7.40698
7.4338
7.4338
7.4338
7.61915
7.61915
7.61915
7.88169
7.88169
7.88169
8.10237

Appendix 4.3 Full spectra of $Cr(CO)_6$ and $Ni(CO)_4$ – Two-photon absorption

$Cr(CO)_6$ – CC2 with ANO basis set

Excitation/eV	Delta
4.04709	0.00000
4.04709	0.00000
4.04709	0.00000
4.05360	0.00000
4.05866	0.00000
4.05866	0.00000
4.15711	0.00000
4.15711	0.00000
4.15711	0.00000
4.76569	0.00000
4.76569	0.00000
4.82952	0.00000
4.82952	0.00000
4.82952	0.00000
4.85641	0.00000
4.85641	0.00000
4.85641	0.00000
5.01989	284.70386
5.01989	284.70359
5.01989	284.70462
5.88347	0.00000
5.88347	0.00000
5.88347	0.00000
6.11491	0.00000
6.11491	0.00000
6.23146	72.64154
6.23146	72.64135
6.23146	72.64166
6.45657	327.30896
6.45657	327.30827
6.45657	327.30998
6.48685	0.00000
6.48685	0.00000
6.48685	0.00000
6.61257	0.00000
6.63216	521.70308
6.63216	521.70572
8.54966	0.00000
8.54966	0.00000
8.54966	0.00000

$Cr(CO)_6$ – LR-CCSD with ANO basis set

Excitation/eV	Delta
4.38467	0.00000
4.38467	0.00000
4.40884	0.00000
4.43233	0.00000
4.43233	0.00000
4.43233	0.00000
4.94553	0.00000
4.94553	0.00000
4.94553	0.00000
4.99764	0.00000
4.99764	0.00000
4.99764	0.00000
5.17351	0.00000
5.17351	0.00000
5.38807	0.00000
5.38807	0.00000
5.38807	0.00000
5.47076	0.00000
5.47076	0.00000
5.47076	0.00000
5.70398	0.00000
5.70398	0.00000
5.70398	0.00000
5.86444	119.83761
5.86444	119.83991
6.05660	94.30350
6.05660	94.30399
6.05660	94.30333
6.12887	0.00000
6.12887	0.00000
6.12887	0.00000
6.23396	3.17141
6.23396	3.17141
6.23396	3.17142
7.46114	2395.57175
7.46114	85.95932
7.86801	0.00238
10.03246	0.00000
10.03246	0.00000
10.03246	0.00000

$Cr(CO)_6$ – CCR(3) with ANO basis set

Excitation/eV
0.00000
0.25252
4.33396
4.33396
4.36251
4.37477
4.37477
4.37477
4.86714
4.86714
4.86714
5.07096
5.07096
5.08970
5.08970
5.08970
5.28748
5.28748
5.28748
5.39698
5.39698
5.39698
5.46680
5.46680
5.46680
5.61434
5.61434
5.98612
5.98612
5.98612
6.04597
6.04597
6.04597
6.11137
6.11137
6.11137
7.03677
9.96988
9.96988
9.96988

$Cr(CO)_6$ – CC2 with ECP basis set

Excitation Energy/eV	Delta
5.79741	0.00000
3.71517	0.00000
3.71517	0.00000
3.71517	0.00000
3.71549	0.00000
3.73218	0.00000
3.73218	0.00000
3.82837	0.00000
3.82837	0.00000
3.82837	0.00000
4.50876	0.00000
4.50876	0.00000
4.57544	0.00000
4.57544	0.00000
4.57544	0.00000
4.59185	0.00000
4.59185	0.00000
4.59185	0.00000
4.84472	537.76058
4.84472	537.76205
4.84472	537.76097
4.95460	0.00000
4.95460	0.00000
4.95460	0.00000
5.68818	0.00000
5.68818	0.00000
5.68818	0.00000
5.79741	0.00000
6.05931	0.00000
6.13328	858.28327
6.13328	858.28560
6.13328	858.27873
6.17584	0.00000
6.17584	0.00000
6.17584	0.00000
6.30819	0.00000
6.30819	0.00000
6.30819	0.00000
7.99289	0.00000
7.99289	0.00000

$Cr(CO)_6$ – LR-CCSD with ECP basis set

Excitation Energy/eV	Delta
3.96172	0.00000
3.96172	0.00000
3.96546	0.00000
4.00805	0.00000
4.00805	0.00000
4.00805	0.00000
4.51829	0.00000
4.51829	0.00000
4.51829	0.00000
4.60927	0.00000
4.60927	0.00000
4.60927	0.00000
4.80782	0.00000
4.80782	0.00000
5.11709	0.00000
5.11709	0.00000
5.11709	0.00000
5.17223	0.03303
5.17223	0.03303
5.17223	0.03303
5.66375	0.00000
5.66375	0.00000
5.66375	0.00000
5.78892	126.30059
5.78892	126.30054
5.78892	126.30062
5.84725	0.00000
5.84725	0.00000
5.84725	0.00000
5.88777	47.61691
5.88777	47.61766
6.22991	0.00000
6.22991	0.00000
6.22991	0.00000
6.27045	2.79158
6.27045	2.79159
6.27045	2.79159
6.49369	0.00000
7.09488	2685.45461
7.09488	2685.46404

$Cr(CO)_6$ – CCR(3) with ECP basis set

Excitation/eV
3.99107
3.99107
4.00405
4.03168
4.03168
4.03168
4.56626
4.56626
4.56626
4.69503
4.69503
4.69503
4.78628
4.78628
5.01426
5.01426
5.01426
5.20006
5.20006
5.20006
5.29752
5.29752
5.29752
5.48710
5.48710
5.80525
5.80525
5.80525
5.95303
5.95303
5.95303
5.96110
5.96110
5.96110
6.35857
6.46574
6.46574
6.46574
6.70515
6.70515

$Ni(CO)_4$ – CC2 with ANO basis set

Excitation Energy/eV	Delta
1.36177	39.29176264
1.36177	0
1.36177	0
1.89994	0.06700193
1.89994	0
1.89994	0
1.93236	0
1.93236	0
1.95563	0
1.9793	0
1.9793	0
1.9793	0
2.01229	0
2.01229	0
2.04718	4.38740544
2.04718	0
2.04718	0
2.08636	499.261415
2.08636	0
2.08636	0.00012444

$Ni(CO)_4$ – LR-CCSD with ANO basis set

Excitation Energy/eV	Delta
4.85394	0.72170475
4.85394	0
4.85394	0
4.88191	1.02567566
4.88191	1.02567167
5.18531	0
5.18531	0
5.18531	0
5.19843	0
5.19843	0.18453471
5.19843	0.18444042
5.54368	33.12454631
5.54368	0
5.54368	0
5.64043	13.75095485
5.64043	27.16822978
5.64043	27.16722157
6.06332	0

6.32145	76.33423336
6.32145	76.33354926

$Ni(CO)_4$ – CC(R)3 with ANO basis set

Excitation Energy/eV
6.08874
6.08874
6.08874
6.10624
6.10624
6.3339
6.3339
6.3339
6.38731
6.38731
6.38731
6.65834
6.65834
6.65834
6.75149
6.75149
6.75149
6.75874
6.75874
6.81547

$Ni(CO)_4$ – LR-CCSD with ECP basis set

Excitation Energy/eV	**Delta**
3.6812	0
3.6812	0
3.6812	0
4.20977	2.208938
4.20977	2.20883823
4.41575	11.87888957
4.41575	11.87882039
4.41575	11.87887833
4.44813	0
4.60292	0
4.60292	0
4.60292	0
4.63301	0
4.71853	0
4.71853	0
4.71853	0

5.11168	1.97364415
5.11168	1.97361448
5.11168	1.97378653
5.46756	0

$Ni(CO)_4$ – CCR(3) with ECP basis set

Excitation Energy/eV

6.41837
6.71119
6.71119
6.71119
6.84063
6.84063
7.1737
7.40698
7.40698
7.40698
7.4338
7.4338
7.4338
7.61915
7.61915
7.61915
7.88169
7.88169
7.88169
8.10237

Appendix 5.1 Cartesian coordinates from chapter 5

$MnTc(CO)_{10}$ eclipsed minimum structure B3LYP and LanL2DZ basis set

1	43	0	0.000000	0.000000	1.364812
2	6	0	-1.837533	0.000000	-1.537140
3	6	0	0.000000	1.837533	-1.537140
4	6	0	0.000000	0.000000	-3.476270
5	6	0	-1.412567	1.412567	1.262209
6	6	0	0.000000	-1.837533	-1.537140
7	6	0	1.412567	1.412567	1.262209
8	6	0	1.837533	0.000000	-1.537140
9	6	0	1.412567	-1.412567	1.262209
10	6	0	0.000000	0.000000	3.304671
11	6	0	-1.412567	-1.412567	1.262209
12	8	0	0.000000	3.011456	-1.479643
13	8	0	2.241314	2.241314	1.221091
14	8	0	-2.241314	2.241314	1.221091

15	8	0	0.000000	0.000000	4.481675
16	8	0	-2.241314	-2.241314	1.221091
17	8	0	2.241314	-2.241314	1.221091
18	8	0	0.000000	-3.011456	-1.479643
19	8	0	3.011456	0.000000	-1.479643
20	8	0	-3.011456	0.000000	-1.479643
21	8	0	0.000000	0.000000	-4.651782
22	25	0	0.000000	0.000000	-1.679575

$MnTc(CO)_{10}$ eclipsed minimum structure B3LYP and SDD/6-311G* basis set

1	43	0	0.000000	0.000000	1.377227
2	6	0	-1.856889	0.000000	-1.539434
3	6	0	0.000000	1.856889	-1.539434
4	6	0	0.000000	0.000000	-3.501496
5	6	0	-1.418436	1.418436	1.265318
6	6	0	0.000000	-1.856889	-1.539434
7	6	0	1.418436	1.418436	1.265318
8	6	0	1.856889	0.000000	-1.539434
9	6	0	1.418436	-1.418436	1.265318
10	6	0	0.000000	0.000000	3.321907
11	6	0	-1.418436	-1.418436	1.265318
12	8	0	0.000000	2.998209	-1.484385
13	8	0	2.224156	2.224156	1.228014
14	8	0	-2.224156	2.224156	1.228014
15	8	0	0.000000	0.000000	4.466393
16	8	0	-2.224156	-2.224156	1.228014
17	8	0	2.224156	-2.224156	1.228014
18	8	0	0.000000	-2.998209	-1.484385
19	8	0	2.998209	0.000000	-1.484385
20	8	0	-2.998209	0.000000	-1.484385
21	8	0	0.000000	0.000000	-4.645357
22	25	0	0.000000	0.000000	-1.687129

$MnTc(CO)_{10}$ eclipsed minimum structure M062X and LanL2DZ basis set

1	43	0	0.000000	0.000000	1.340371
2	6	0	-1.863523	0.000000	-1.469076
3	6	0	0.000000	1.863523	-1.469076
4	6	0	0.000000	0.000000	-3.451609
5	6	0	-1.407096	1.407096	1.195221
6	6	0	0.000000	-1.863523	-1.469076
7	6	0	1.407096	1.407096	1.195221
8	6	0	1.863523	0.000000	-1.469076
9	6	0	1.407096	-1.407096	1.195221
10	6	0	0.000000	0.000000	3.268526
11	6	0	-1.407096	-1.407096	1.195221
12	8	0	0.000000	3.021821	-1.353211
13	8	0	2.226965	2.226965	1.095107
14	8	0	-2.226965	2.226965	1.095107

15	8	0	0.000000	0.000000	4.435535
16	8	0	-2.226965	-2.226965	1.095107
17	8	0	2.226965	-2.226965	1.095107
18	8	0	0.000000	-3.021821	-1.353211
19	8	0	3.021821	0.000000	-1.353211
20	8	0	-3.021821	0.000000	-1.353211
21	8	0	0.000000	0.000000	-4.614780
22	25	0	0.000000	0.000000	-1.640613

$MnTc(CO)_{10}$ eclipsed minimum structure M062X and SDD/6-311G* basis set

1	43	0	0.000000	0.000000	1.351611
2	6	0	-1.890725	0.000000	-1.458801
3	6	0	0.000000	1.890725	-1.458801
4	6	0	0.000000	0.000000	-3.473867
5	6	0	-1.410059	1.410059	1.185792
6	6	0	0.000000	-1.890725	-1.458801
7	6	0	1.410059	1.410059	1.185792
8	6	0	1.890725	0.000000	-1.458801
9	6	0	1.410059	-1.410059	1.185792
10	6	0	0.000000	0.000000	3.280641
11	6	0	-1.410059	-1.410059	1.185792
12	8	0	0.000000	3.016359	-1.332952
13	8	0	2.207668	2.207668	1.076740
14	8	0	-2.207668	2.207668	1.076740
15	8	0	0.000000	0.000000	4.417261
16	8	0	-2.207668	-2.207668	1.076740
17	8	0	2.207668	-2.207668	1.076740
18	8	0	0.000000	-3.016359	-1.332952
19	8	0	3.016359	0.000000	-1.332952
20	8	0	-3.016359	0.000000	-1.332952
21	8	0	0.000000	0.000000	-4.606864
22	25	0	0.000000	0.000000	-1.642301

$MnTc(CO)_{10}$ eclipsed minimum structure CAM-B3LYP and LanL2DZ basis set

1	43	0	0.000000	0.000000	1.327816
2	6	0	-1.825896	0.000000	-1.500746
3	6	0	0.000000	1.825896	-1.500746
4	6	0	0.000000	0.000000	-3.436579
5	6	0	-1.407371	1.407371	1.223855
6	6	0	0.000000	-1.825896	-1.500746
7	6	0	1.407371	1.407371	1.223855
8	6	0	1.825896	0.000000	-1.500746
9	6	0	1.407371	-1.407371	1.223855
10	6	0	0.000000	0.000000	3.264938
11	6	0	-1.407371	-1.407371	1.223855
12	8	0	0.000000	2.991993	-1.426065
13	8	0	2.230440	2.230440	1.171008
14	8	0	-2.230440	2.230440	1.171008

15	8	0	0.000000	0.000000	4.434323
16	8	0	-2.230440	-2.230440	1.171008
17	8	0	2.230440	-2.230440	1.171008
18	8	0	0.000000	-2.991993	-1.426065
19	8	0	2.991993	0.000000	-1.426065
20	8	0	-2.991993	0.000000	-1.426065
21	8	0	0.000000	0.000000	-4.604810
22	25	0	0.000000	0.000000	-1.648303

$MnTc(CO)_{10}$ eclipsed minimum structure CAM-B3LYP and SDD/6-311G* basis set

1	43	0	0.000000	0.000000	1.344216
2	6	0	-1.846679	0.000000	-1.502242
3	6	0	0.000000	1.846679	-1.502242
4	6	0	0.000000	0.000000	-3.463574
5	6	0	-1.413029	1.413029	1.226444
6	6	0	0.000000	-1.846679	-1.502242
7	6	0	1.413029	1.413029	1.226444
8	6	0	1.846679	0.000000	-1.502242
9	6	0	1.413029	-1.413029	1.226444
10	6	0	0.000000	0.000000	3.286082
11	6	0	-1.413029	-1.413029	1.226444
12	8	0	0.000000	2.981103	-1.428654
13	8	0	2.213913	2.213913	1.173594
14	8	0	-2.213913	2.213913	1.173594
15	8	0	0.000000	0.000000	4.424211
16	8	0	-2.213913	-2.213913	1.173594
17	8	0	2.213913	-2.213913	1.173594
18	8	0	0.000000	-2.981103	-1.428654
19	8	0	2.981103	0.000000	-1.428654
20	8	0	-2.981103	0.000000	-1.428654
21	8	0	0.000000	0.000000	-4.601258
22	25	0	0.000000	0.000000	-1.656647

$MnTc(CO)_{10}$ staggered transition state structure B3LYP with LanL2DZ basis set

1	43	0	0.000000	0.000000	1.417617
2	6	0	-1.840086	0.000000	-1.643621
3	6	0	0.000000	1.840086	-1.643621
4	6	0	0.000000	0.000000	-3.544195
5	6	0	-1.999423	0.000000	1.360816
6	6	0	0.000000	-1.840086	-1.643621
7	6	0	0.000000	1.999423	1.360816
8	6	0	1.840086	0.000000	-1.643621
9	6	0	1.999423	0.000000	1.360816
10	6	0	0.000000	0.000000	3.351035
11	6	0	0.000000	-1.999423	1.360816

12	8	0	0.000000	3.015092	-1.651548
13	8	0	0.000000	3.171577	1.394965
14	8	0	-3.171577	0.000000	1.394965
15	8	0	0.000000	0.000000	4.528261
16	8	0	0.000000	-3.171577	1.394965
17	8	0	3.171577	0.000000	1.394965
18	8	0	0.000000	-3.015092	-1.651548
19	8	0	3.015092	0.000000	-1.651548
20	8	0	-3.015092	0.000000	-1.651548
21	8	0	0.000000	0.000000	-4.719835
22	25	0	0.000000	0.000000	-1.751269

$MnTc(CO)_{10}$ staggered transition state structure B3LYP with SDD/6-311G* basis set

1	43	0	0.000000	0.000000	1.437119
2	6	0	-1.860467	0.000000	-1.643207
3	6	0	0.000000	1.860467	-1.643207
4	6	0	0.000000	0.000000	-3.561682
5	6	0	-2.007165	0.000000	1.364295
6	6	0	0.000000	-1.860467	-1.643207
7	6	0	0.000000	2.007165	1.364295
8	6	0	1.860467	0.000000	-1.643207
9	6	0	2.007165	0.000000	1.364295
10	6	0	0.000000	0.000000	3.375039
11	6	0	0.000000	-2.007165	1.364295
12	8	0	0.000000	3.002652	-1.653910
13	8	0	0.000000	3.146938	1.385636
14	8	0	-3.146938	0.000000	1.385636
15	8	0	0.000000	0.000000	4.519763
16	8	0	0.000000	-3.146938	1.385636
17	8	0	3.146938	0.000000	1.385636
18	8	0	0.000000	-3.002652	-1.653910
19	8	0	3.002652	0.000000	-1.653910
20	8	0	-3.002652	0.000000	-1.653910
21	8	0	0.000000	0.000000	-4.705748
22	25	0	0.000000	0.000000	-1.751685

$MnTc(CO)_{10}$ staggered transition state structure M062X with LanL2DZ basis set

1	43	0	0.000000	0.000000	1.393059
2	6	0	-1.867534	0.000000	-1.611368
3	6	0	0.000000	1.867534	-1.611368
4	6	0	0.000000	0.000000	-3.526675
5	6	0	-1.996061	0.000000	1.327718
6	6	0	0.000000	-1.867534	-1.611368
7	6	0	0.000000	1.996061	1.327718
8	6	0	1.867534	0.000000	-1.611368
9	6	0	1.996061	0.000000	1.327718

10	6	0	0.000000	0.000000	3.309066
11	6	0	0.000000	-1.996061	1.327718
12	8	0	0.000000	3.031408	-1.603007
13	8	0	0.000000	3.159015	1.358263
14	8	0	-3.159015	0.000000	1.358263
15	8	0	0.000000	0.000000	4.476758
16	8	0	0.000000	-3.159015	1.358263
17	8	0	3.159015	0.000000	1.358263
18	8	0	0.000000	-3.031408	-1.603007
19	8	0	3.031408	0.000000	-1.603007
20	8	0	-3.031408	0.000000	-1.603007
21	8	0	0.000000	0.000000	-4.690439
22	25	0	0.000000	0.000000	-1.724135

$MnTc(CO)_{10}$ staggered transition state structure M062X with SDD/6-311G* basis set

1	43	0	0.000000	0.000000	1.416366
2	6	0	-1.895776	0.000000	-1.597588
3	6	0	0.000000	1.895776	-1.597588
4	6	0	0.000000	0.000000	-3.539510
5	6	0	-1.997627	0.000000	1.319140
6	6	0	0.000000	-1.895776	-1.597588
7	6	0	0.000000	1.997627	1.319140
8	6	0	1.895776	0.000000	-1.597588
9	6	0	1.997627	0.000000	1.319140
10	6	0	0.000000	0.000000	3.333748
11	6	0	0.000000	-1.997627	1.319140
12	8	0	0.000000	3.036050	-1.581980
13	8	0	0.000000	3.139248	1.318664
14	8	0	-3.139248	0.000000	1.318664
15	8	0	0.000000	0.000000	4.479435
16	8	0	0.000000	-3.139248	1.318664
17	8	0	3.139248	0.000000	1.318664
18	8	0	0.000000	-3.036050	-1.581980
19	8	0	3.036050	0.000000	-1.581980
20	8	0	-3.036050	0.000000	-1.581980
21	8	0	0.000000	0.000000	-4.681342
22	25	0	0.000000	0.000000	-1.717578

$MnTc(CO)_{10}$ staggered transition state structure CAM-B3LYP with LanL2DZ basis set

1	43	0	0.000000	0.000000	1.382892
2	6	0	0.000000	1.829247	-1.605932
3	6	0	1.829247	0.000000	-1.605932
4	6	0	0.000000	0.000000	-3.494634
5	6	0	0.000000	1.992314	1.333906
6	6	0	-1.829247	0.000000	-1.605932
7	6	0	1.992314	0.000000	1.333906

8	6	0	0.000000	-1.829247	-1.605932
9	6	0	0.000000	-1.992314	1.333906
10	6	0	0.000000	0.000000	3.313434
11	6	0	-1.992314	0.000000	1.333906
12	8	0	2.997339	0.000000	-1.608084
13	8	0	3.156826	0.000000	1.369063
14	8	0	0.000000	3.156826	1.369063
15	8	0	0.000000	0.000000	4.483074
16	8	0	-3.156826	0.000000	1.369063
17	8	0	0.000000	-3.156826	1.369063
18	8	0	-2.997339	0.000000	-1.608084
19	8	0	0.000000	-2.997339	-1.608084
20	8	0	0.000000	2.997339	-1.608084
21	8	0	0.000000	0.000000	-4.663028
22	25	0	0.000000	0.000000	-1.710410

$MnTc(CO)_{10}$ staggered transition state structure CAM-B3LYP with SDD/6-311G* basis set

1	43	0	0.000000	0.000000	1.403923
2	6	0	0.000000	1.851036	-1.607968
3	6	0	1.851036	0.000000	-1.607968
4	6	0	0.000000	0.000000	-3.516001
5	6	0	0.000000	2.000011	1.333561
6	6	0	-1.851036	0.000000	-1.607968
7	6	0	2.000011	0.000000	1.333561
8	6	0	0.000000	-1.851036	-1.607968
9	6	0	0.000000	-2.000011	1.333561
10	6	0	0.000000	0.000000	3.338519
11	6	0	-2.000011	0.000000	1.333561
12	8	0	2.987330	0.000000	-1.614211
13	8	0	3.133648	0.000000	1.350191
14	8	0	0.000000	3.133648	1.350191
15	8	0	0.000000	0.000000	4.476918
16	8	0	-3.133648	0.000000	1.350191
17	8	0	0.000000	-3.133648	1.350191
18	8	0	-2.987330	0.000000	-1.614211
19	8	0	0.000000	-2.987330	-1.614211
20	8	0	0.000000	2.987330	-1.614211
21	8	0	0.000000	0.000000	-4.653943
22	25	0	0.000000	0.000000	-1.714128

$MnRe(CO)_{10}$ eclipsed minimum structure B3LYP and LanL2DZ basis set

1	25	0	0.000000	0.000000	-1.856400
2	6	0	-1.300161	1.300161	-1.716589
3	6	0	1.300161	1.300161	-1.716589
4	6	0	1.300161	-1.300161	-1.716589
5	6	0	-1.300161	-1.300161	-1.716589
6	6	0	0.000000	0.000000	-3.654673
7	6	0	0.000000	-1.994024	1.083689
8	6	0	-1.994024	0.000000	1.083689
9	6	0	0.000000	1.994024	1.083689
10	6	0	0.000000	0.000000	3.122223
11	6	0	1.994024	0.000000	1.083689
12	8	0	2.129699	2.129699	-1.655253
13	8	0	0.000000	3.167040	1.029382
14	8	0	2.129699	-2.129699	-1.655253
15	8	0	0.000000	0.000000	-4.829928
16	8	0	-2.129699	-2.129699	-1.655253
17	8	0	3.167040	0.000000	1.029382
18	8	0	0.000000	-3.167040	1.029382
19	8	0	-3.167040	0.000000	1.029382
20	8	0	-2.129699	2.129699	-1.655253
21	8	0	0.000000	0.000000	4.301595
22	75	0	0.000000	0.000000	1.187317

$MnRe(CO)_{10}$ eclipsed minimum structure B3LYP and SDD/6-311G* basis set

1	25	0	0.000000	0.000000	-1.878254
2	6	0	-1.313214	1.313214	-1.729356
3	6	0	1.313214	1.313214	-1.729356
4	6	0	1.313214	-1.313214	-1.729356
5	6	0	-1.313214	-1.313214	-1.729356
6	6	0	0.000000	0.000000	-3.694599
7	6	0	0.000000	-2.019898	1.088271
8	6	0	-2.019898	0.000000	1.088271
9	6	0	0.000000	2.019898	1.088271
10	6	0	0.000000	0.000000	3.159633
11	6	0	2.019898	0.000000	1.088271
12	8	0	2.119996	2.119996	-1.669928
13	8	0	0.000000	3.160179	1.037537
14	8	0	2.119996	-2.119996	-1.669928
15	8	0	0.000000	0.000000	-4.838307
16	8	0	-2.119996	-2.119996	-1.669928
17	8	0	3.160179	0.000000	1.037537
18	8	0	0.000000	-3.160179	1.037537
19	8	0	-3.160179	0.000000	1.037537
20	8	0	-2.119996	2.119996	-1.669928
21	8	0	0.000000	0.000000	4.306162
22	75	0	0.000000	0.000000	1.200611

$MnRe(CO)_{10}$ eclipsed minimum structure M062X and LanL2DZ basis set

1	25	0	0.000000	0.000000	-1.810582
2	6	0	-1.320317	1.320317	-1.644001
3	6	0	1.320317	1.320317	-1.644001
4	6	0	1.320317	-1.320317	-1.644001
5	6	0	-1.320317	-1.320317	-1.644001
6	6	0	0.000000	0.000000	-3.626675
7	6	0	0.000000	-1.981439	1.018821
8	6	0	-1.981439	0.000000	1.018821
9	6	0	0.000000	1.981439	1.018821
10	6	0	0.000000	0.000000	3.091836
11	6	0	1.981439	0.000000	1.018821
12	8	0	2.138265	2.138265	-1.523580
13	8	0	0.000000	3.141384	0.903075
14	8	0	2.138265	-2.138265	-1.523580
15	8	0	0.000000	0.000000	-4.789297
16	8	0	-2.138265	-2.138265	-1.523580
17	8	0	3.141384	0.000000	0.903075
18	8	0	0.000000	-3.141384	0.903075
19	8	0	-3.141384	0.000000	0.903075
20	8	0	-2.138265	2.138265	-1.523580
21	8	0	0.000000	0.000000	4.260910
22	75	0	0.000000	0.000000	1.167482

$MnRe(CO)_{10}$ eclipsed minimum structure M062X and SDD/6-311G* basis set

1	25	0	0.000000	0.000000	-1.827240
2	6	0	-1.337342	1.337342	-1.641483
3	6	0	1.337342	1.337342	-1.641483
4	6	0	1.337342	-1.337342	-1.641483
5	6	0	-1.337342	-1.337342	-1.641483
6	6	0	0.000000	0.000000	-3.661810
7	6	0	0.000000	-2.005204	1.009242
8	6	0	-2.005204	0.000000	1.009242
9	6	0	0.000000	2.005204	1.009242
10	6	0	0.000000	0.000000	3.125596
11	6	0	2.005204	0.000000	1.009242
12	8	0	2.132393	2.132393	-1.507736
13	8	0	0.000000	3.132722	0.882608
14	8	0	2.132393	-2.132393	-1.507736
15	8	0	0.000000	0.000000	-4.794559
16	8	0	-2.132393	-2.132393	-1.507736
17	8	0	3.132722	0.000000	0.882608
18	8	0	0.000000	-3.132722	0.882608
19	8	0	-3.132722	0.000000	0.882608
20	8	0	-2.132393	2.132393	-1.507736
21	8	0	0.000000	0.000000	4.263712
22	75	0	0.000000	0.000000	1.177639

$MnRe(CO)_{10}$ eclipsed minimum structure CAM-B3LYP and LanL2DZ basis set

1	25	0	0.000000	0.000000	-1.816988
2	6	0	-1.292307	1.292307	-1.674549
3	6	0	1.292307	1.292307	-1.674549
4	6	0	1.292307	-1.292307	-1.674549
5	6	0	-1.292307	-1.292307	-1.674549
6	6	0	0.000000	0.000000	-3.607036
7	6	0	0.000000	-1.986350	1.053796
8	6	0	-1.986350	0.000000	1.053796
9	6	0	0.000000	1.986350	1.053796
10	6	0	0.000000	0.000000	3.092559
11	6	0	1.986350	0.000000	1.053796
12	8	0	2.116346	2.116346	-1.599545
13	8	0	0.000000	3.151499	0.989410
14	8	0	2.116346	-2.116346	-1.599545
15	8	0	0.000000	0.000000	-4.774909
16	8	0	-2.116346	-2.116346	-1.599545
17	8	0	3.151499	0.000000	0.989410
18	8	0	0.000000	-3.151499	0.989410
19	8	0	-3.151499	0.000000	0.989410
20	8	0	-2.116346	2.116346	-1.599545
21	8	0	0.000000	0.000000	4.264479
22	75	0	0.000000	0.000000	1.160232

$MnRe(CO)_{10}$ eclipsed minimum structure CAM-B3LYP and SDD/6-311G* basis set

1	25	0	0.000000	0.000000	-1.841573
2	6	0	-1.305892	1.305892	-1.685337
3	6	0	1.305892	1.305892	-1.685337
4	6	0	1.305892	-1.305892	-1.685337
5	6	0	-1.305892	-1.305892	-1.685337
6	6	0	0.000000	0.000000	-3.649846
7	6	0	0.000000	-2.012974	1.056043
8	6	0	-2.012974	0.000000	1.056043
9	6	0	0.000000	2.012974	1.056043
10	6	0	0.000000	0.000000	3.130705
11	6	0	2.012974	0.000000	1.056043
12	8	0	2.107636	2.107636	-1.606226
13	8	0	0.000000	3.146193	0.990802
14	8	0	2.107636	-2.107636	-1.606226
15	8	0	0.000000	0.000000	-4.787321
16	8	0	-2.107636	-2.107636	-1.606226
17	8	0	3.146193	0.000000	0.990802
18	8	0	0.000000	-3.146193	0.990802
19	8	0	-3.146193	0.000000	0.990802
20	8	0	-2.107636	2.107636	-1.606226
21	8	0	0.000000	0.000000	4.270917
22	75	0	0.000000	0.000000	1.174427

$MnRe(CO)_{10}$ staggered transition state structure B3LYP with LanL2DZ basis set

1	25	0	0.000000	0.000000	-1.933219
2	6	0	1.840815	0.000000	-1.829029
3	6	0	0.000000	-1.840815	-1.829029
4	6	0	-1.840815	0.000000	-1.829029
5	6	0	0.000000	1.840815	-1.829029
6	6	0	0.000000	0.000000	-3.727955
7	6	0	0.000000	1.995436	1.173772
8	6	0	1.995436	0.000000	1.173772
9	6	0	0.000000	-1.995436	1.173772
10	6	0	0.000000	0.000000	3.162932
11	6	0	-1.995436	0.000000	1.173772
12	8	0	0.000000	-3.015265	-1.834472
13	8	0	0.000000	-3.169458	1.191999
14	8	0	-3.015265	0.000000	-1.834472
15	8	0	0.000000	0.000000	-4.903335
16	8	0	0.000000	3.015265	-1.834472
17	8	0	-3.169458	0.000000	1.191999
18	8	0	0.000000	3.169458	1.191999
19	8	0	3.169458	0.000000	1.191999
20	8	0	3.015265	0.000000	-1.834472
21	8	0	0.000000	0.000000	4.342516
22	75	0	0.000000	0.000000	1.233233

$MnRe(CO)_{10}$ staggered transition state structure B3LYP with SDD/6-311G* basis set

1	25	0	0.000000	0.000000	-1.950065
2	6	0	1.860212	0.000000	-1.839855
3	6	0	0.000000	-1.860212	-1.839855
4	6	0	-1.860212	0.000000	-1.839855
5	6	0	0.000000	1.860212	-1.839855
6	6	0	0.000000	0.000000	-3.761450
7	6	0	0.000000	2.021561	1.176141
8	6	0	2.021561	0.000000	1.176141
9	6	0	0.000000	-2.021561	1.176141
10	6	0	0.000000	0.000000	3.201346
11	6	0	-2.021561	0.000000	1.176141
12	8	0	0.000000	-3.002228	-1.844743
13	8	0	0.000000	-3.162764	1.183568
14	8	0	-3.002228	0.000000	-1.844743
15	8	0	0.000000	0.000000	-4.905315
16	8	0	0.000000	3.002228	-1.844743
17	8	0	-3.162764	0.000000	1.183568
18	8	0	0.000000	3.162764	1.183568
19	8	0	3.162764	0.000000	1.183568
20	8	0	3.002228	0.000000	-1.844743
21	8	0	0.000000	0.000000	4.348103

22	75	0	0.000000	0.000000	1.248756

$MnRe(CO)_{10}$ staggered transition state structure M062X with LanL2DZ basis set

1	25	0	0.000000	0.000000	-1.896352
2	6	0	1.870859	0.000000	-1.790727
3	6	0	0.000000	-1.870859	-1.790727
4	6	0	-1.870859	0.000000	-1.790727
5	6	0	0.000000	1.870859	-1.790727
6	6	0	0.000000	0.000000	-3.704403
7	6	0	0.000000	1.987283	1.143175
8	6	0	1.987283	0.000000	1.143175
9	6	0	0.000000	-1.987283	1.143175
10	6	0	0.000000	0.000000	3.129564
11	6	0	-1.987283	0.000000	1.143175
12	8	0	0.000000	-3.033615	-1.781779
13	8	0	0.000000	-3.152573	1.152661
14	8	0	-3.033615	0.000000	-1.781779
15	8	0	0.000000	0.000000	-4.867594
16	8	0	0.000000	3.033615	-1.781779
17	8	0	-3.152573	0.000000	1.152661
18	8	0	0.000000	3.152573	1.152661
19	8	0	3.152573	0.000000	1.152661
20	8	0	3.033615	0.000000	-1.781779
21	8	0	0.000000	0.000000	4.299217
22	75	0	0.000000	0.000000	1.214372

$MnRe(CO)_{10}$ staggered transition state structure M062X with SDD/6-311G* basis set

1	25	0	0.000000	0.000000	-1.903730
2	6	0	-1.896742	0.000000	-1.792052
3	6	0	0.000000	1.896742	-1.792052
4	6	0	1.896742	0.000000	-1.792052
5	6	0	0.000000	-1.896742	-1.792052
6	6	0	0.000000	0.000000	-3.727912
7	6	0	0.000000	-2.011431	1.137323
8	6	0	-2.011431	0.000000	1.137323
9	6	0	0.000000	2.011431	1.137323
10	6	0	0.000000	0.000000	3.165205
11	6	0	2.011431	0.000000	1.137323
12	8	0	0.000000	3.028423	-1.782870
13	8	0	0.000000	3.145688	1.127319
14	8	0	3.028423	0.000000	-1.782870
15	8	0	0.000000	0.000000	-4.861283
16	8	0	0.000000	-3.028423	-1.782870
17	8	0	3.145688	0.000000	1.127319
18	8	0	0.000000	-3.145688	1.127319
19	8	0	-3.145688	0.000000	1.127319

20	8	0	-3.028423	0.000000	-1.782870
21	8	0	0.000000	0.000000	4.303955
22	75	0	0.000000	0.000000	1.228257

$MnRe(CO)_{10}$ staggered transition state structure CAM-B3LYP with LanL2DZ basis set

1	25	0	0.000000	0.000000	-1.891132
2	6	0	1.830544	0.000000	-1.790458
3	6	0	0.000000	-1.830544	-1.790458
4	6	0	-1.830544	0.000000	-1.790458
5	6	0	0.000000	1.830544	-1.790458
6	6	0	0.000000	0.000000	-3.677429
7	6	0	0.000000	1.988390	1.149912
8	6	0	1.988390	0.000000	1.149912
9	6	0	0.000000	-1.988390	1.149912
10	6	0	0.000000	0.000000	3.128895
11	6	0	-1.988390	0.000000	1.149912
12	8	0	0.000000	-2.997917	-1.790889
13	8	0	0.000000	-3.154975	1.170257
14	8	0	-2.997917	0.000000	-1.790889
15	8	0	0.000000	0.000000	-4.845500
16	8	0	0.000000	2.997917	-1.790889
17	8	0	-3.154975	0.000000	1.170257
18	8	0	0.000000	3.154975	1.170257
19	8	0	3.154975	0.000000	1.170257
20	8	0	2.997917	0.000000	-1.790889
21	8	0	0.000000	0.000000	4.301074
22	75	0	0.000000	0.000000	1.202110

$MnRe(CO)_{10}$ staggered transition state structure CAM-B3LYP with SDD/6-311G* basis set

1	25	0	0.000000	0.000000	-1.908404
2	6	0	1.851190	0.000000	-1.800015
3	6	0	0.000000	-1.851190	-1.800015
4	6	0	-1.851190	0.000000	-1.800015
5	6	0	0.000000	1.851190	-1.800015
6	6	0	0.000000	0.000000	-3.712118
7	6	0	0.000000	2.015090	1.151057
8	6	0	2.015090	0.000000	1.151057
9	6	0	0.000000	-2.015090	1.151057
10	6	0	0.000000	0.000000	3.169357
11	6	0	-2.015090	0.000000	1.151057
12	8	0	0.000000	-2.987319	-1.800555
13	8	0	0.000000	-3.149993	1.156379
14	8	0	-2.987319	0.000000	-1.800555
15	8	0	0.000000	0.000000	-4.849928
16	8	0	0.000000	2.987319	-1.800555
17	8	0	-3.149993	0.000000	1.156379

18	8	0	0.000000	3.149993	1.156379
19	8	0	3.149993	0.000000	1.156379
20	8	0	2.987319	0.000000	-1.800555
21	8	0	0.000000	0.000000	4.309915
22	75	0	0.000000	0.000000	1.219672

$TcRe(CO)_{10}$ eclipsed minimum structure B3LYP and LanL2DZ basis set

1	43	0	0.000000	0.000000	-1.753048
2	6	0	1.989747	0.000000	1.242827
3	6	0	0.000000	1.989747	1.242827
4	6	0	0.000000	0.000000	3.310527
5	6	0	1.409987	1.409987	-1.630849
6	6	0	0.000000	-1.989747	1.242827
7	6	0	-1.409987	1.409987	-1.630849
8	6	0	-1.989747	0.000000	1.242827
9	6	0	-1.409987	-1.409987	-1.630849
10	6	0	0.000000	0.000000	-3.697943
11	6	0	1.409987	-1.409987	-1.630849
12	8	0	0.000000	3.163223	1.167964
13	8	0	-2.238900	2.238900	-1.571687
14	8	0	2.238900	2.238900	-1.571687
15	8	0	0.000000	0.000000	-4.875168
16	8	0	2.238900	-2.238900	-1.571687
17	8	0	-2.238900	-2.238900	-1.571687
18	8	0	0.000000	-3.163223	1.167964
19	8	0	-3.163223	0.000000	1.167964
20	8	0	3.163223	0.000000	1.167964
21	8	0	0.000000	0.000000	4.490357
22	75	0	0.000000	0.000000	1.373542

$TcRe(CO)_{10}$ eclipsed minimum structure B3LYP and SDD/6-311G* basis set

1	43	0	0.000000	0.000000	-1.770238
2	6	0	2.017170	0.000000	1.249733
3	6	0	0.000000	2.017170	1.249733
4	6	0	0.000000	0.000000	3.342661
5	6	0	1.416169	1.416169	-1.640549
6	6	0	0.000000	-2.017170	1.249733
7	6	0	-1.416169	1.416169	-1.640549
8	6	0	-2.017170	0.000000	1.249733
9	6	0	-1.416169	-1.416169	-1.640549
10	6	0	0.000000	0.000000	-3.719512
11	6	0	1.416169	-1.416169	-1.640549
12	8	0	0.000000	3.157640	1.182794
13	8	0	-2.222014	2.222014	-1.585836
14	8	0	2.222014	2.222014	-1.585836
15	8	0	0.000000	0.000000	-4.864129
16	8	0	2.222014	-2.222014	-1.585836
17	8	0	-2.222014	-2.222014	-1.585836

18	8	0	0.000000	-3.157640	1.182794
19	8	0	-3.157640	0.000000	1.182794
20	8	0	3.157640	0.000000	1.182794
21	8	0	0.000000	0.000000	4.489557
22	75	0	0.000000	0.000000	1.382065

$TcRe(CO)_{10}$ eclipsed minimum structure M062X and LanL2DZ basis set

1	43	0	0.000000	0.000000	-1.699630
2	6	0	1.979715	0.000000	1.168130
3	6	0	0.000000	1.979715	1.168130
4	6	0	0.000000	0.000000	3.258666
5	6	0	1.406871	1.406871	-1.545896
6	6	0	0.000000	-1.979715	1.168130
7	6	0	-1.406871	1.406871	-1.545896
8	6	0	-1.979715	0.000000	1.168130
9	6	0	-1.406871	-1.406871	-1.545896
10	6	0	0.000000	0.000000	-3.632845
11	6	0	1.406871	-1.406871	-1.545896
12	8	0	0.000000	3.138571	1.038330
13	8	0	-2.225330	2.225330	-1.430958
14	8	0	2.225330	2.225330	-1.430958
15	8	0	0.000000	0.000000	-4.799753
16	8	0	2.225330	-2.225330	-1.430958
17	8	0	-2.225330	-2.225330	-1.430958
18	8	0	0.000000	-3.138571	1.038330
19	8	0	-3.138571	0.000000	1.038330
20	8	0	3.138571	0.000000	1.038330
21	8	0	0.000000	0.000000	4.427940
22	75	0	0.000000	0.000000	1.332455

$TcRe(CO)_{10}$ eclipsed minimum structure M062X and SDD/6-311G* basis set

1	43	0	0.000000	0.000000	-1.715206
2	6	0	2.006131	0.000000	1.165534
3	6	0	0.000000	2.006131	1.165534
4	6	0	0.000000	0.000000	3.286311
5	6	0	1.410938	1.410938	-1.545262
6	6	0	0.000000	-2.006131	1.165534
7	6	0	-1.410938	1.410938	-1.545262
8	6	0	-2.006131	0.000000	1.165534
9	6	0	-1.410938	-1.410938	-1.545262
10	6	0	0.000000	0.000000	-3.647196
11	6	0	1.410938	-1.410938	-1.545262
12	8	0	0.000000	3.133133	1.036679
13	8	0	-2.207297	2.207297	-1.424936
14	8	0	2.207297	2.207297	-1.424936
15	8	0	0.000000	0.000000	-4.783702
16	8	0	2.207297	-2.207297	-1.424936
17	8	0	-2.207297	-2.207297	-1.424936

18	8	0	0.000000	-3.133133	1.036679
19	8	0	-3.133133	0.000000	1.036679
20	8	0	3.133133	0.000000	1.036679
21	8	0	0.000000	0.000000	4.424555
22	75	0	0.000000	0.000000	1.337735

$TcRe(CO)_{10}$ eclipsed minimum structure CAM-B3LYP and LanL2DZ basis set

1	43	0	0.000000	0.000000	-1.720690
2	6	0	1.981550	0.000000	1.211494
3	6	0	0.000000	1.981550	1.211494
4	6	0	0.000000	0.000000	3.281468
5	6	0	1.404370	1.404370	-1.592576
6	6	0	0.000000	-1.981550	1.211494
7	6	0	-1.404370	1.404370	-1.592576
8	6	0	-1.981550	0.000000	1.211494
9	6	0	-1.404370	-1.404370	-1.592576
10	6	0	0.000000	0.000000	-3.662296
11	6	0	1.404370	-1.404370	-1.592576
12	8	0	0.000000	3.146933	1.123523
13	8	0	-2.227403	2.227403	-1.517549
14	8	0	2.227403	2.227403	-1.517549
15	8	0	0.000000	0.000000	-4.831922
16	8	0	2.227403	-2.227403	-1.517549
17	8	0	-2.227403	-2.227403	-1.517549
18	8	0	0.000000	-3.146933	1.123523
19	8	0	-3.146933	0.000000	1.123523
20	8	0	3.146933	0.000000	1.123523
21	8	0	0.000000	0.000000	4.453804
22	75	0	0.000000	0.000000	1.347392

$TcRe(CO)_{10}$ eclipsed minimum structure CAM-B3LYP and SDD/6-311G* basis set

1	43	0	0.000000	0.000000	-1.739668
2	6	0	2.009708	0.000000	1.217909
3	6	0	0.000000	2.009708	1.217909
4	6	0	0.000000	0.000000	3.315104
5	6	0	1.410600	1.410600	-1.602155
6	6	0	0.000000	-2.009708	1.217909
7	6	0	-1.410600	1.410600	-1.602155
8	6	0	-2.009708	0.000000	1.217909
9	6	0	-1.410600	-1.410600	-1.602155
10	6	0	0.000000	0.000000	-3.685152
11	6	0	1.410600	-1.410600	-1.602155
12	8	0	0.000000	3.143114	1.136718
13	8	0	-2.211432	2.211432	-1.530978
14	8	0	2.211432	2.211432	-1.530978
15	8	0	0.000000	0.000000	-4.823481
16	8	0	2.211432	-2.211432	-1.530978

17	8	0	-2.211432	-2.211432	-1.530978
18	8	0	0.000000	-3.143114	1.136718
19	8	0	-3.143114	0.000000	1.136718
20	8	0	3.143114	0.000000	1.136718
21	8	0	0.000000	0.000000	4.455732
22	75	0	0.000000	0.000000	1.357415

$TcRe(CO)_{10}$ staggered transition state structure B3LYP with LanL2DZ basis set

1	6	0	-1.996274	0.000000	-1.734184
2	6	0	0.000000	1.996274	-1.734184
3	6	0	1.996274	0.000000	-1.734184
4	6	0	0.000000	-1.996274	-1.734184
5	6	0	0.000000	0.000000	-3.750519
6	6	0	0.000000	-1.992126	1.333646
7	6	0	-1.992126	0.000000	1.333646
8	6	0	0.000000	1.992126	1.333646
9	6	0	0.000000	0.000000	3.351345
10	6	0	1.992126	0.000000	1.333646
11	8	0	0.000000	3.169683	-1.746299
12	8	0	0.000000	3.167761	1.328490
13	8	0	3.169683	0.000000	-1.746299
14	8	0	0.000000	0.000000	-4.927903
15	8	0	0.000000	-3.169683	-1.746299
16	8	0	3.167761	0.000000	1.328490
17	8	0	0.000000	-3.167761	1.328490
18	8	0	-3.167761	0.000000	1.328490
19	8	0	-3.169683	0.000000	-1.746299
20	8	0	0.000000	0.000000	4.531264
21	75	0	0.000000	0.000000	1.419961
22	43	0	0.000000	0.000000	-1.812700

$TcRe(CO)_{10}$ staggered transition state structure B3LYP with SDD/6-311G* basis set

1	6	0	-2.004889	0.000000	-1.738135
2	6	0	0.000000	2.004889	-1.738135
3	6	0	2.004889	0.000000	-1.738135
4	6	0	0.000000	-2.004889	-1.738135
5	6	0	0.000000	0.000000	-3.772474
6	6	0	0.000000	-2.019820	1.336791
7	6	0	-2.019820	0.000000	1.336791
8	6	0	0.000000	2.019820	1.336791
9	6	0	0.000000	0.000000	3.379168
10	6	0	2.019820	0.000000	1.336791
11	8	0	0.000000	3.145608	-1.739482
12	8	0	0.000000	3.161981	1.332452
13	8	0	3.145608	0.000000	-1.739482
14	8	0	0.000000	0.000000	-4.917321
15	8	0	0.000000	-3.145608	-1.739482

16	8	0	3.161981	0.000000	1.332452
17	8	0	0.000000	-3.161981	1.332452
18	8	0	-3.161981	0.000000	1.332452
19	8	0	-3.145608	0.000000	-1.739482
20	8	0	0.000000	0.000000	4.526271
21	75	0	0.000000	0.000000	1.424540
22	43	0	0.000000	0.000000	-1.830117

$TcRe(CO)_{10}$ staggered transition state structure M062X with LanL2DZ basis set

1	6	0	-1.995165	0.000000	-1.688829
2	6	0	0.000000	1.995165	-1.688829
3	6	0	1.995165	0.000000	-1.688829
4	6	0	0.000000	-1.995165	-1.688829
5	6	0	0.000000	0.000000	-3.690195
6	6	0	0.000000	-1.985327	1.296010
7	6	0	-1.985327	0.000000	1.296010
8	6	0	0.000000	1.985327	1.296010
9	6	0	0.000000	0.000000	3.304904
10	6	0	1.985327	0.000000	1.296010
11	8	0	0.000000	3.158087	-1.696024
12	8	0	0.000000	3.151080	1.283577
13	8	0	3.158087	0.000000	-1.696024
14	8	0	0.000000	0.000000	-4.857755
15	8	0	0.000000	-3.158087	-1.696024
16	8	0	3.151080	0.000000	1.283577
17	8	0	0.000000	-3.151080	1.283577
18	8	0	-3.151080	0.000000	1.283577
19	8	0	-3.158087	0.000000	-1.696024
20	8	0	0.000000	0.000000	4.474697
21	75	0	0.000000	0.000000	1.387839
22	43	0	0.000000	0.000000	-1.769436

$TcRe(CO)_{10}$ staggered transition state structure M062X with LanL2DZ basis set

1	6	0	-2.001312	0.000000	-1.683792
2	6	0	0.000000	2.001312	-1.683792
3	6	0	2.001312	0.000000	-1.683792
4	6	0	0.000000	-2.001312	-1.683792
5	6	0	0.000000	0.000000	-3.699988
6	6	0	0.000000	-2.012363	1.291419
7	6	0	-2.012363	0.000000	1.291419
8	6	0	0.000000	2.012363	1.291419
9	6	0	0.000000	0.000000	3.325869
10	6	0	2.012363	0.000000	1.291419
11	8	0	0.000000	3.133607	-1.678602
12	8	0	0.000000	3.146233	1.275637
13	8	0	3.133607	0.000000	-1.678602
14	8	0	0.000000	0.000000	-4.837142
15	8	0	0.000000	-3.133607	-1.678602

16	8	0	3.146233	0.000000	1.275637
17	8	0	0.000000	-3.146233	1.275637
18	8	0	-3.146233	0.000000	1.275637
19	8	0	-3.133607	0.000000	-1.678602
20	8	0	0.000000	0.000000	4.464763
21	75	0	0.000000	0.000000	1.387971
22	43	0	0.000000	0.000000	-1.780518

$TcRe(CO)_{10}$ staggered transition state structure CAM-B3LYP with LanL2DZ basis set

1	6	0	-1.988946	0.000000	-1.700999
2	6	0	0.000000	1.988946	-1.700999
3	6	0	1.988946	0.000000	-1.700999
4	6	0	0.000000	-1.988946	-1.700999
5	6	0	0.000000	0.000000	-3.712056
6	6	0	0.000000	-1.984806	1.308751
7	6	0	-1.984806	0.000000	1.308751
8	6	0	0.000000	1.984806	1.308751
9	6	0	0.000000	0.000000	3.318294
10	6	0	1.984806	0.000000	1.308751
11	8	0	0.000000	3.154959	-1.706795
12	8	0	0.000000	3.153151	1.302945
13	8	0	3.154959	0.000000	-1.706795
14	8	0	0.000000	0.000000	-4.881888
15	8	0	0.000000	-3.154959	-1.706795
16	8	0	3.153151	0.000000	1.302945
17	8	0	0.000000	-3.153151	1.302945
18	8	0	-3.153151	0.000000	1.302945
19	8	0	-3.154959	0.000000	-1.706795
20	8	0	0.000000	0.000000	4.490824
21	75	0	0.000000	0.000000	1.390186
22	43	0	0.000000	0.000000	-1.777574

$TcRe(CO)_{10}$ staggered transition state structure CAM-B3LYP with SDD/6-311G* basis set

1	6	0	-1.997485	0.000000	-1.703333
2	6	0	0.000000	1.997485	-1.703333
3	6	0	1.997485	0.000000	-1.703333
4	6	0	0.000000	-1.997485	-1.703333
5	6	0	0.000000	0.000000	-3.734357
6	6	0	0.000000	-2.012785	1.309373
7	6	0	-2.012785	0.000000	1.309373
8	6	0	0.000000	2.012785	1.309373
9	6	0	0.000000	0.000000	3.348464
10	6	0	2.012785	0.000000	1.309373
11	8	0	0.000000	3.131989	-1.697071
12	8	0	0.000000	3.148753	1.299525
13	8	0	3.131989	0.000000	-1.697071

14	8	0	0.000000	0.000000	-4.872922
15	8	0	0.000000	-3.131989	-1.697071
16	8	0	3.148753	0.000000	1.299525
17	8	0	0.000000	-3.148753	1.299525
18	8	0	-3.148753	0.000000	1.299525
19	8	0	-3.131989	0.000000	-1.697071
20	8	0	0.000000	0.000000	4.489372
21	75	0	0.000000	0.000000	1.397143
22	43	0	0.000000	0.000000	-1.79594

Appendix 5.2 Full spectra of $MnTc(CO)_{10}$

TD B3LYP with LanL2DZ basis set

Excitation Energy/eV	Symmetry	Oscillator strength
3.2272	1E	f=0.0005
3.2272	1E	f=0.0005
3.5812	1B2	f=0.0000
3.6117	2E	f=0.0013
3.6117	2E	f=0.0013
3.6534	1A1	f=0.3910
3.7863	3E	f=0.0010
3.7863	3E	f=0.0010
4.1284	2B2	f=0.0000
4.1424	2B2	f=0.0000
4.2027	4E	f=0.0142
4.2027	4E	f=0.0142
4.2311	1B1	f=0.0000
4.2454	5E	f=0.0000
4.279	5E	f=0.0017
4.279	6E	f=0.0017
4.2916	6E	f=0.0000
4.3667	7E	f=0.0000
4.4065	7E	f=0.0261
4.448	8E	f=0.0031
4.448	8E	f=0.0031
4.5076	9E	f=0.0007
4.5076	9E	f=0.0007
4.5772	10E	f=0.0000
4.6212	2A1	f=0.0512
4.6245	2B1	f=0.0000
4.64	3B1	f=0.0000
4.6979	11E	f=0.0000
4.7096	11E	f=0.0000
4.7579	1A2	f=0.0000
4.7675	12E	f=0.0004

4.7675	13E	f=0.0004
4.7755	13E	f=0.0006
4.783	14E	f=0.0000
4.8096	15E	f=0.0001
4.8096	15E	f=0.0001
4.8308	16E	f=0.0301
4.8359	4B1	f=0.0000
4.8406	17E	f=0.0001
4.8406	17E	f=0.0001
4.8585	18E	f=0.0000
4.9047	19E	f=0.0000
4.9329	20E	f=0.0000
4.9561	21E	f=0.0005
4.9561	21E	f=0.0005
4.9884	22E	f=0.0000
4.9924	3A1	f=0.0335
5.0008	2A2	f=0.0000
5.0132	4A1	f=0.0036
5.0586	23E	f=0.0013
5.0586	23E	f=0.0013
5.0803	3A2	f=0.0000
5.1486	24E	f=0.0008
5.1486	24E	f=0.0008
5.1878	25E	f=0.0000
5.1878	25E	f=0.0000
5.1962	5B1	f=0.0000
5.2186	26E	f=0.0000
5.2517	27E	f=0.0031
5.2517	27E	f=0.0031

TD B3LYP with SDD/6-311G* basis set

Excitation Energy/eV	Symmetry	Oscillator strength
3.5142	1E	f=0.0002
3.5142	1E	f=0.0002
3.5803	2E	f=0.0018
3.5803	2E	f=0.0018
3.7836	1B2	f=0.0000
3.8028	1A1	f=0.4208
4.0233	3E	f=0.0006
4.0233	3E	f=0.0006
4.1515	2B2	f=0.0000
4.332	4E	f=0.0011
4.332	4E	f=0.0011
4.3964	1B1	f=0.0000
4.4063	3B2	f=0.0000

4.4089	5E	f=0.0143
4.4089	5E	f=0.0143
4.4703	6E	f=0.0000
4.5128	7E	f=0.0000
4.5485	8E	f=0.0060
4.5485	8E	f=0.0060
4.5833	9E	f=0.0000
4.6254	10E	f=0.0321
4.7307	11E	f=0.0000
4.7584	2A2	f=0.0307
4.7618	12E	f=0.0002
4.7618	12E	f=0.0002
4.7732	2B1	f=0.0000
4.7962	3B1	f=0.0000
4.8226	3A2	f=0.0000
4.8608	13E	f=0.0002
4.8608	13E	f=0.0002
4.8673	14E	f=0.0000
4.8715	15E	f=0.0000
4.9309	16E	f=0.0002
4.9437	17E	f=0.0000
5.0042	18E	f=0.0354
5.024	19E	f=0.0000
5.0346	4B1	f=0.0000
5.0369	20E	f=0.0001
5.0369	20E	f=0.0001
5.0586	4A2	f=0.0000
5.1206	21E	f=0.0001
5.1206	21E	f=0.0001
5.1403	5B1	f=0.0000
5.1462	2A1	f=0.0143
5.1701	22E	f=0.0000
5.1774	23E	f=0.0010
5.1774	23E	f=0.0010
5.1953	24E	f=0.0002
5.1953	24E	f=0.0002
5.2087	25E	f=0.0076
5.2684	6B1	f=0.0000
5.2702	5A2	f=0.0000
5.3443	6A2	f=0.0000
5.3458	26E	f=0.0001
5.3458	26E	f=0.0001
5.4144	27E	f=0.0019
5.4144	27E	f=0.0019
5.494	3A1	f=0.0073
5.5025	4B2	f=0.0000

5.5132	28E	f=0.0021

CAM-B3LYP with LanL2DZ basis set

Excitation Energy/eV	Symmetry	Oscillator strength
3.5908	1E	f=0.0009
3.5908	1E	f=0.0009
3.7386	1A1	f=0.4967
3.8088	2E	f=0.0007
3.8088	2E	f=0.0007
3.8165	1B2	f=0.0000
4.0288	3E	f=0.0011
4.0288	3E	f=0.0011
4.3692	2B2	f=0.0000
4.4461	1B1	f=0.0000
4.4896	3B2	f=0.0000
4.5157	4E	f=0.0266
4.5157	4E	f=0.0266
4.5199	5E	f=0.0000
4.5722	6E	f=0.0000
4.5722	6E	f=0.0000
4.6028	7E	f=0.0000
4.7297	8E	f=0.0042
4.7297	8E	f=0.0042
4.7378	9E	f=0.0000
4.837	10E	f=0.0000
4.9093	2B1	f=0.0000
4.9328	3B1	f=0.0000
4.9395	11E	f=0.0509
4.9529	12E	f=0.0003
4.9529	12E	f=0.0003
4.9584	1A2	f=0.0000
4.9694	2A1	f=0.0232
5.013	2A2	f=0.0000
5.039	13E	f=0.0000
5.0908	14E	f=0.0027
5.0908	14E	f=0.0027
5.1334	15E	f=0.0004
5.1841	16E	f=0.0000
5.2407	17E	f=0.0000
5.2407	17E	f=0.0000
5.2623	18E	f=0.0000
5.2908	19E	f=0.0000
5.2943	20E	f=0.0149
5.3403	3A2	f=0.0000
5.3557	21E	f=0.0000

5.3557	21E	f=0.0000
5.3665	22E	f=0.0001
5.3665	22E	f=0.0001
5.3702	3A1	f=0.0355
5.3741	4A2	f=0.0000
5.4347	4B1	f=0.0000
5.4556	23E	f=0.0010
5.4556	23E	f=0.0010
5.507	24E	f=0.0013
5.507	24E	f=0.0013
5.5502	5A2	f=0.0000
5.5996	25E	f=0.0000
5.6284	25E	f=0.0000
5.7499	6A2	f=0.0000
5.7668	26E	f=0.0009
5.7668	26E	f=0.0009
5.8218	4B2	f=0.0000
5.8396	27E	f=0.0010
5.8396	27E	f=0.0010

CAM-B3LYP with SDD/6-311G* basis set

Excitation Energy/eV	**Symmetry**	**Oscillator strength**
3.7277	1E	f=0.0003
3.7277	1E	f=0.0003
3.8758	1A1	f=0.5155
3.9015	2E	f=0.0015
3.9015	2E	f=0.0015
4.0185	1B2	f=0.0000
4.2624	3E	f=0.0007
4.2624	3E	f=0.0007
4.3533	2B2	f=0.0000
4.5886	1B1	f=0.0000
4.5926	4E	f=0.0013
4.5926	4E	f=0.0013
4.7356	5E	f=0.0217
4.7356	5E	f=0.0217
4.749	1A2	f=0.0000
4.793	3B2	f=0.0000
4.7967	6E	f=0.0000
4.8315	7E	f=0.0082
4.8315	7E	f=0.0082
4.8526	8E	f=0.0000
4.8994	9E	f=0.0000
4.9751	10E	f=0.0025
4.9751	10E	f=0.0025

5.0705	11E	f=0.0000
5.0825	2B1	f=0.0000
5.0986	3B1	f=0.0000
5.1097	2A1	f=0.0363
5.1687	12E	f=0.0210
5.1821	13E	f=0.0000
5.2014	14E	f=0.0000
5.2671	3A1	f=0.0048
5.3676	15E	f=0.0013
5.3676	15E	f=0.0013
5.3946	4B1	f=0.0000
5.4113	16E	f=0.0000
5.4415	16E	f=0.0218
5.4873	5B1	f=0.0000
5.5222	17E	f=0.0010
5.5222	17E	f=0.0010
5.5406	6B1	f=0.0000
5.5483	18E	f=0.0001
5.5483	18E	f=0.0001
5.5638	4A1	f=0.0188
5.6204	19E	f=0.0000
5.6204	19E	f=0.0000
5.6418	2A2	f=0.0000
5.7056	20E	f=0.0000
5.7056	20E	f=0.0000
5.7623	3A2	f=0.0000
5.7675	21E	f=0.0015
5.7675	21E	f=0.0015
5.8256	4B2	f=0.0000
5.8488	5A1	f=0.0114
5.8852	22E	f=0.0002
5.8852	22E	f=0.0002
5.9288	4A2	f=0.0000
5.9362	23E	f=0.0000
5.9877	5A2	f=0.0000
6.0041	5B2	f=0.0000
6.0243	6B2	f=0.0000

TD M062X with LanL2DZ basis set

Excitation Energy/eV	**Symmetry**	**Oscillator strength**
2.8074	1E	f=0.0000
2.8074	1E	f=0.0000
3.3257	1B2	f=0.0000
3.4854	2E	f=0.0031
3.4854	2E	f=0.0031

3.5987	1A2	f=0.0000
3.6917	3E	f=0.0028
3.6917	3E	f=0.0028
3.7492	1A1	f=0.4667
3.8561	2B2	f=0.0000
3.9619	4E	f=0.0001
3.9619	4E	f=0.0001
4.1248	5E	f=0.0000
4.1294	6E	f=0.0225
4.1294	6E	f=0.0225
4.2226	7E	f=0.0127
4.2226	7E	f=0.0127
4.3617	1B1	f=0.0000
4.4638	3B2	f=0.0000
4.6266	8E	f=0.0000
4.6616	2A1	f=0.0131
4.6633	9E	f=0.0000
4.7842	2B1	f=0.0000
4.8536	3A1	f=0.0280
4.8872	10E	f=0.0000
4.8952	11E	f=0.0045
4.8952	11E	f=0.0045
5.0111	12E	f=0.0000
5.0111	12E	f=0.0000
5.0833	13E	f=0.0000
5.0833	13E	f=0.0000
5.0924	3B1	f=0.0000
5.1345	14E	f=0.0000
5.192	15E	f=0.0000
5.216	4A1	f=0.0081
5.2546	5A1	f=0.0401
5.2683	16E	f=0.0001
5.2683	16E	f=0.0001
5.2706	4B1	f=0.0000
5.2757	5B1	f=0.0000
5.3669	17E	f=0.0032
5.3669	17E	f=0.0032
5.4025	18E	f=0.0000
5.4321	2A2	f=0.0000
5.5055	19E	f=0.0000
5.5055	19E	f=0.0000
5.5068	3A2	f=0.0000
5.5727	20E	f=0.0008
5.5727	20E	f=0.0008
5.5809	21E	f=0.0000
5.6287	22E	f=0.0497

5.6768	4B2	f=0.0000
5.7147	4A2	f=0.0000
5.7895	5B2	f=0.0000
5.7967	6B1	f=0.0000
5.8315	23E	f=0.0001
5.8315	23E	f=0.0001
5.8588	5A2	f=0.0000
5.8854	24E	f=0.0013
5.8854	24E	f=0.0013

TD M062X with SDD/6-311G* basis set

Excitation Energy/eV	Symmetry	Oscillator strength
2.5897	1E	f=0.0000
2.5897	1E	f=0.0000
3.2463	1A2	f=0.0000
3.3859	1B2	f=0.0000
3.5816	2E	f=0.0004
3.5816	2E	f=0.0004
3.784	3E	f=0.0043
3.784	3E	f=0.0043
3.8239	2B2	f=0.0000
3.9137	1A1	f=0.4695
3.9727	4E	f=0.0022
3.9727	4E	f=0.0022
4.2687	5E	f=0.0000
4.3371	6E	f=0.0232
4.3371	6E	f=0.0232
4.4339	7E	f=0.0126
4.4339	7E	f=0.0126
4.5199	1B1	f=0.0000
4.7861	2A1	f=0.0251
4.8017	3B2	f=0.0000
4.83	2B1	f=0.0000
4.9167	3A1	f=0.0038
5.0099	8E	f=0.0000
5.0206	9E	f=0.0000
5.0542	10E	f=0.0055
5.0542	10E	f=0.0055
5.0789	3B1	f=0.0000
5.1289	11E	f=0.0002
5.1289	11E	f=0.0002
5.1441	4B1	f=0.0000
5.3724	4A1	f=0.0086
5.419	12E	f=0.0000
5.4456	13E	f=0.0008

5.4456	13E	f=0.0008
5.4754	14E	f=0.0000
5.4773	5A1	f=0.0043
5.5043	15E	f=0.0398
5.5166	5B1	f=0.0000
5.5585	6B1	f=0.0000
5.5978	4B2	f=0.0000
5.6528	16E	f=0.0000
5.6528	16E	f=0.0000
5.6628	5B2	f=0.0000
5.6871	17E	f=0.0040
5.6871	17E	f=0.0040
5.7288	6A1	f=0.0009
5.755	18E	f=0.0001
5.755	18E	f=0.0001
5.7832	2A2	f=0.0000
5.7846	19E	f=0.0000
5.8072	20E	f=0.0582
5.816	21E	f=0.0014
5.816	21E	f=0.0014
5.9122	3A2	f=0.0000
5.9463	4A2	f=0.0000
6.0375	22E	f=0.0067
6.0375	22E	f=0.0067
6.095	23E	f=0.0000
6.095	23E	f=0.0000
6.1196	5A2	f=0.0000

Appendix 5.3 Full spectra of $MnRe(CO)_{10}$

TD B3LYP with LanL2DZ basis set

Excitation Energy/eV	Symmetry	Oscillator strength
3.2879	1E	f=0.0005
3.2879	1E	f=0.0005
3.6071	2E	f=0.0021
3.6071	2E	f=0.0021
3.689	1B2	f=0.0000
3.7197	1A1	f=0.3720
3.8902	3E	f=0.0004
3.8902	3E	f=0.0004
4.1218	4E	f=0.0000
4.1329	2B2	f=0.0000
4.1682	5E	f=0.0000

4.2142	3B2	f=0.0000
4.2699	6E	f=0.0000
4.2738	7E	f=0.0041
4.2738	7E	f=0.0041
4.3036	8E	f=0.0074
4.3036	8E	f=0.0074
4.3099	9E	f=0.0394
4.4032	1B1	f=0.0000
4.4135	10E	f=0.0024
4.4135	10E	f=0.0024
4.5611	11E	f=0.0000
4.5719	2B1	f=0.0000
4.6379	12E	f=0.0013
4.6379	12E	f=0.0013
4.6736	13E	f=0.0000
4.6885	14E	f=0.0000
4.6898	14E	f=0.0000
4.7066	15E	f=0.0002
4.7066	15E	f=0.0002
4.7403	2A1	f=0.0073
4.7831	16E	f=0.0002
4.7831	16E	f=0.0002
4.7947	1A2	f=0.0000
4.7994	17E	f=0.0000
4.8019	18E	f=0.0180
4.8236	19E	f=0.0000
4.8367	3A1	f=0.0102
4.8631	20E	f=0.0000
4.9371	21E	f=0.0004
4.9371	21E	f=0.0004
4.9527	2A2	f=0.0000
4.973	22E	f=0.0000
4.9977	4A1	f=0.0104
5.0053	3A2	f=0.0000
5.0235	4A2	f=0.0000
5.069	23E	f=0.0008
5.069	23E	f=0.0008
5.164	24E	f=0.0000
5.1661	25E	f=0.0001
5.1661	25E	f=0.0001
5.1737	3B1	f=0.0000
5.1785	26E	f=0.0003
5.1785	26E	f=0.0003
5.1885	27E	f=0.0044
5.1885	27E	f=0.0044
5.2559	4B1	f=0.0000

5.2789	28E	f=0.0000
5.3752	5A1	f=0.0024
5.4648	29E	f=0.0108

TD B3LYP with SDD/6-311G*

Excitation Energy/eV	Symmetry	Oscillator strength
3.478	1E	f=0.0002
3.478	1E	f=0.0002
3.5659	2E	f=0.0022
3.5659	2E	f=0.0022
3.802	1A1	f=0.3824
3.8393	1B2	f=0.0000
4.0855	3E	f=0.0002
4.0855	3E	f=0.0002
4.1405	2B2	f=0.0000
4.3026	4E	f=0.0000
4.3284	5E	f=0.0014
4.3284	5E	f=0.0014
4.3455	6E	f=0.0000
4.409	3B2	f=0.0000
4.4285	7E	f=0.0000
4.4642	8E	f=0.0081
4.4642	8E	f=0.0081
4.4767	9E	f=0.0405
4.5164	10E	f=0.0074
4.5164	10E	f=0.0074
4.5283	1B1	f=0.0000
4.6931	11E	f=0.0000
4.7222	2B1	f=0.0000
4.7464	12E	f=0.0000
4.7464	12E	f=0.0000
4.7802	3B1	f=0.0000
4.8239	1A2	f=0.0000
4.8377	13E	f=0.0000
4.8467	2A1	f=0.0144
4.862	2A2	f=0.0000
4.8757	14E	f=0.0011
4.8757	14E	f=0.0011
4.9239	15E	f=0.0001
4.9239	15E	f=0.0001
4.9297	16E	f=0.0000
4.9411	17E	f=0.0015
4.9615	18E	f=0.0280
4.9756	19E	f=0.0000
4.9763	19E	f=0.0000

5.0006	20E	f=0.0000
5.0668	21E	f=0.0008
5.0668	21E	f=0.0008
5.091	22E	f=0.0000
5.1227	3A1	f=0.0075
5.1923	23E	f=0.0005
5.1923	23E	f=0.0005
5.2219	3A2	f=0.0000
5.2271	4B1	f=0.0000
5.2442	4A2	f=0.0000
5.3069	24E	f=0.0000
5.3069	24E	f=0.0000
5.3637	25E	f=0.0047
5.3637	25E	f=0.0047
5.4154	26E	f=0.0000
5.4194	4A1	f=0.0078
5.4299	27E	f=0.0006
5.4299	27E	f=0.0006
5.4621	28E	f=0.0000
5.5064	29E	f=0.0000
5.5672	5A1	f=0.0057

CAM-B3LYP with LanL2DZ basis set

Excitation Energy/eV	Symmetry	Oscillator strength
3.652	1E	f=0.0008
3.652	1E	f=0.0008
3.8035	2E	f=0.0015
3.8035	2E	f=0.0015
3.8304	1A1	f=0.4624
3.9492	1B2	f=0.0000
4.1413	3E	f=0.0002
4.1413	3E	f=0.0002
4.3363	4E	f=0.0000
4.3713	2B2	f=0.0000
4.4313	5E	f=0.0000
4.5718	6E	f=0.0054
4.5718	6E	f=0.0054
4.575	3B2	f=0.0000
4.643	1B1	f=0.0000
4.6597	7E	f=0.0134
4.6597	7E	f=0.0134
4.6795	8E	f=0.0008
4.6795	8E	f=0.0008
4.6899	9E	f=0.0000
4.7341	10E	f=0.0000

4.7892	11E	f=0.0403
4.8206	2B1	f=0.0000
4.9565	12E	f=0.0001
4.9565	12E	f=0.0001
4.9567	3B1	f=0.0000
4.9686	1A2	f=0.0000
5.0237	13E	f=0.0049
5.0237	13E	f=0.0049
5.025	14E	f=0.0000
5.0319	15E	f=0.0000
5.135	2A1	f=0.0070
5.1642	3A1	f=0.0100
5.2165	2A2	f=0.0000
5.2673	16E	f=0.0000
5.2681	17E	f=0.0000
5.2913	18E	f=0.0238
5.3171	19E	f=0.0029
5.3171	19E	f=0.0029
5.3614	3A2	f=0.0000
5.3827	20E	f=0.0000
5.3827	20E	f=0.0000
5.4549	21E	f=0.0007
5.4549	21E	f=0.0007
5.4767	4B1	f=0.0000
5.5076	22E	f=0.0000
5.5741	23E	f=0.0000
5.5852	4A2	f=0.0000
5.7478	5A2	f=0.0000
5.7793	24E	f=0.0000
5.7889	25E	f=0.0001
5.7889	25E	f=0.0001
5.8368	26E	f=0.0079
5.8368	26E	f=0.0079
5.8606	27E	f=0.0000
5.8829	28E	f=0.0335
5.8829	28E	f=0.0335
5.8942	4A1	f=0.0139
5.9071	6A2	f=0.0000
5.9141	4A2	f=0.0000

CAM-B3LYP with SDD/6-311G* basis set

Excitation Energy/eV	**Symmetry**	**Oscillator strength**
3.7221	1E	f=0.0005
3.7221	1E	f=0.0005
3.8711	2E	f=0.0016

3.8711	2E	f=0.0016
3.9091	1A1	f=0.4705
4.1022	1B2	f=0.0000
4.3156	3E	f=0.0001
4.3156	3E	f=0.0001
4.3551	2B2	f=0.0000
4.5668	4E	f=0.0000
4.6137	5E	f=0.0006
4.6137	5E	f=0.0006
4.6507	6E	f=0.0000
4.7159	1B1	f=0.0000
4.7591	1A2	f=0.0000
4.7981	7E	f=0.0068
4.7981	7E	f=0.0068
4.8016	3B2	f=0.0000
4.8188	8E	f=0.0146
4.8188	8E	f=0.0146
4.8767	9E	f=0.0000
4.881	10E	f=0.0000
4.9702	11E	f=0.0016
4.9702	11E	f=0.0016
4.9745	12E	f=0.0419
4.9998	2B1	f=0.0000
5.1043	3B1	f=0.0000
5.1574	13E	f=0.0000
5.2028	14E	f=0.0000
5.2271	2A1	f=0.0202
5.2348	15E	f=0.0044
5.2348	15E	f=0.0044
5.2615	3A1	f=0.0030
5.4094	16E	f=0.0000
5.4122	17E	f=0.0000
5.434	18E	f=0.0238
5.4929	2A2	f=0.0000
5.5118	19E	f=0.0038
5.5118	19E	f=0.0038
5.5136	4B1	f=0.0000
5.5552	20E	f=0.0006
5.5552	20E	f=0.0006
5.6418	21E	f=0.0005
5.6418	21E	f=0.0005
5.6655	3A2	f=0.0000
5.7655	22E	f=0.0000
5.834	4A1	f=0.0027
5.8486	23E	f=0.0000
5.8699	4A2	f=0.0000

5.8705	24E	f=0.0001
5.8705	24E	f=0.0001
5.9656	5B1	f=0.0000
5.9903	5A2	f=0.0000
6.0107	5A1	f=0.0243
6.012	4B2	f=0.0000
6.013	25E	f=0.0258
6.013	25E	f=0.0258
6.0776	26E	f=0.0000
6.1041	27E	f=0.0003
6.1041	27E	f=0.0003

TD M062X with LanL2DZ

Excitation Energy/eV	**Symmetry**	**Oscillator strength**
2.7663	1E	f=0.0000
2.7663	1E	f=0.0000
3.4599	1B2	f=0.0000
3.5639	1A2	f=0.0000
3.5769	2E	f=0.0029
3.5769	2E	f=0.0029
3.7427	3E	f=0.0008
3.7427	3E	f=0.0008
3.8813	2B2	f=0.0000
3.8958	1A1	f=0.4336
3.954	4E	f=0.0000
3.954	4E	f=0.0000
4.1201	5E	f=0.0000
4.2477	6E	f=0.0088
4.2477	6E	f=0.0088
4.3763	7E	f=0.0181
4.3763	7E	f=0.0181
4.5233	8E	f=0.0000
4.5695	9E	f=0.0000
4.5839	3B2	f=0.0000
4.607	1B1	f=0.0000
4.6936	2A1	f=0.0018
4.7935	2B1	f=0.0000
4.8589	10E	f=0.0000
4.9531	11E	f=0.0020
4.9531	11E	f=0.0020
5.0292	12E	f=0.0001
5.0292	12E	f=0.0001
5.0486	3A1	f=0.0526
5.0517	12E	f=0.0000
5.1283	13E	f=0.0209

5.2297	14E	f=0.0000
5.2385	3B1	f=0.0000
5.2508	15E	f=0.0039
5.2508	15E	f=0.0039
5.2728	4B1	f=0.0000
5.3831	16E	f=0.0022
5.3831	16E	f=0.0022
5.4031	17E	f=0.0000
5.4042	2A2	f=0.0000
5.5174	3A2	f=0.0000
5.5398	18E	f=0.0000
5.5672	19E	f=0.0002
5.5672	19E	f=0.0002
5.608	20E	f=0.0316
5.7381	5B1	f=0.0000
5.7824	4B2	f=0.0000
5.802	21E	f=0.0042
5.802	21E	f=0.0042
5.8376	4A1	f=0.0307
5.8387	4A2	f=0.0000
5.8514	22E	f=0.0000
5.8798	5A2	f=0.0000
5.9142	23E	f=0.0043
5.9142	23E	f=0.0043
5.996	6B1	f=0.0000
6.0153	24E	f=0.0087
6.0153	24E	f=0.0087
6.1237	25E	f=0.0021
6.1334	6A2	f=0.0000

TD M062X with SDD/6-311G* basis set

Excitation Energy/eV	Symmetry	Oscillator strength
2.5773	1E	f=0.0000
2.5773	1E	f=0.0000
3.2376	1A2	f=0.0000
3.4374	1B2	f=0.0000
3.5713	2E	f=0.0003
3.5713	2E	f=0.0003
3.7869	3E	f=0.0036
3.7869	3E	f=0.0036
3.8955	2B2	f=0.0000
3.9882	1A1	f=0.4257
3.9985	4E	f=0.0004
3.9985	4E	f=0.0004
4.2702	5E	f=0.0000

4.4314	6E	f=0.0126
4.4314	6E	f=0.0126
4.5381	7E	f=0.0165
4.5381	7E	f=0.0165
4.6831	1B1	f=0.0000
4.7961	8E	f=0.0000
4.8132	9E	f=0.0000
4.8199	3B2	f=0.0000
4.8328	2A1	f=0.0115
4.992	10E	f=0.0000
5.0145	2B1	f=0.0000
5.0403	3A1	f=0.0204
5.1045	11E	f=0.0025
5.1045	11E	f=0.0025
5.1919	3B1	f=0.0000
5.2154	12E	f=0.0030
5.2154	12E	f=0.0030
5.2411	13E	f=0.0000
5.2943	14E	f=0.0569
5.4555	15E	f=0.0037
5.4555	15E	f=0.0037
5.4826	16E	f=0.0000
5.484	4A1	f=0.0003
5.5181	4B1	f=0.0000
5.6062	17E	f=0.0000
5.6404	18E	f=0.0012
5.6404	18E	f=0.0012
5.7355	2A2	f=0.0000
5.7482	19E	f=0.0000
5.7579	20E	f=0.0147
5.7996	21E	f=0.0002
5.7996	21E	f=0.0002
5.8248	5A1	f=0.0162
5.8374	3A2	f=0.0000
5.9108	6A1	f=0.0415
5.9408	22E	f=0.0002
5.9408	22E	f=0.0002
5.9464	4B2	f=0.0000
5.9579	5B1	f=0.0000
6.0712	23E	f=0.0124
6.0712	23E	f=0.0125
6.1381	24E	f=0.0005
6.1381	24E	f=0.0005
6.1432	4A2	f=0.0000
6.1508	25E	f=0.0000
6.1936	6B1	f=0.0000

6.2328	25E	f=0.0027

Appendix 5.3 Full spectra of $TcRe(CO)_{10}$

TD B3LYP with LanL2DZ basis set

Excitation Energy/eV	Symmetry	Oscillator strength
3.3123	1E	f=0.0001
3.3123	1E	f=0.0001
3.4347	2E	f=0.0004
3.4347	2E	f=0.0004
3.8387	1A1	f=0.3813
3.9776	1B2	f=0.0000
4.0091	1B1	f=0.0000
4.0854	3E	f=0.0073
4.0854	3E	f=0.0073
4.1124	4E	f=0.0000
4.1622	5E	f=0.0000
4.2355	6E	f=0.0000
4.2376	7E	f=0.0000
4.2819	8E	f=0.0061
4.2988	9E	f=0.0000
4.3522	10E	f=0.0000
4.4383	11E	f=0.0617
4.4444	12E	f=0.0017
4.4444	12E	f=0.0017
4.6174	2A1	f=0.0062
4.6183	2B1	f=0.0000
4.6184	13E	f=0.0000
4.6184	13E	f=0.0000
4.6615	14E	f=0.0003
4.6615	14E	f=0.0003
4.6721	2B2	f=0.0000
4.7154	15E	f=0.0001
4.7154	15E	f=0.0001
4.7401	16E	f=0.0001
4.7401	16E	f=0.0001
4.789	1A2	f=0.0000

4.8275	3B2	f=0.0000
4.9083	2A2	f=0.0000
4.9589	17E	f=0.0000
4.9784	18E	f=0.0002
4.9784	18E	f=0.0002
4.9976	19E	f=0.0000
5.0161	20E	f=0.0064
5.0281	3A2	f=0.0000
5.0314	4A2	f=0.0000
5.0417	21E	f=0.0000
5.0419	22E	f=0.0004
5.0419	22E	f=0.0004
5.0614	23E	f=0.0000
5.0821	5A2	f=0.0000
5.1254	6A2	f=0.0000
5.1274	24E	f=0.0001
5.1445	25E	f=0.0000
5.1599	26E	f=0.0000
5.1599	26E	f=0.0000
5.1688	27E	f=0.0001
5.1688	27E	f=0.0001
5.1951	28E	f=0.0000
5.2101	29E	f=0.0000
5.2551	30E	f=0.0151
5.2551	30E	f=0.0151
5.3146	31E	f=0.0000
5.3376	32E	f=0.0094
5.3376	32E	f=0.0094
5.3557	3B1	f=0.0000

TD B3LYP with SDD/6-311G* basis set

Excitation Energy/eV	**Symmetry**	**Oscillator strength**
3.5657	1E	f=0.0001
3.5657	1E	f=0.0001
3.7134	2E	f=0.0003
3.7134	2E	f=0.0003
4.0058	1A1	f=0.3999
4.2007	3E	f=0.0093
4.2007	3E	f=0.0093
4.2028	1B2	f=0.0000
4.3002	1B1	f=0.0000
4.3065	4E	f=0.0000
4.3524	5E	f=0.0000
4.4375	6E	f=0.0000
4.4763	7E	f=0.0203

4.4776	8E	f=0.0000
4.5187	9E	f=0.0000
4.5887	10E	f=0.0000
4.657	11E	f=0.0605
4.7578	12E	f=0.0008
4.7578	12E	f=0.0008
4.7848	2B1	f=0.0000
4.8031	13E	f=0.0003
4.8031	13E	f=0.0003
4.836	2B2	f=0.0000
4.8429	14E	f=0.0003
4.8429	14E	f=0.0003
4.8437	2A1	f=0.0000
4.9659	15E	f=0.0005
4.9659	15E	f=0.0005
5.0881	16E	f=0.0000
5.0881	16E	f=0.0000
5.094	1A2	f=0.0000
5.1184	3B2	f=0.0000
5.1768	17E	f=0.0000
5.2011	18E	f=0.0000
5.2143	19E	f=0.0001
5.2143	19E	f=0.0001
5.221	20E	f=0.0000
5.2419	21E	f=0.0051
5.2695	2A2	f=0.0000
5.2966	22E	f=0.0000
5.3236	23E	f=0.0000
5.3241	24E	f=0.0017
5.3241	24E	f=0.0017
5.3379	3A2	f=0.0000
5.3718	25E	f=0.0003
5.3932	26E	f=0.0001
5.3932	26E	f=0.0001
5.4033	4A2	f=0.0000
5.4102	5A2	f=0.0000
5.4559	27E	f=0.0057
5.4559	27E	f=0.0057
5.4624	28E	f=0.0000
5.4631	6A2	f=0.0000
5.4709	29E	f=0.0087
5.4709	29E	f=0.0087
5.4848	30E	f=0.0000
5.4948	3B1	f=0.0000
5.5888	3A1	f=0.0003
5.6097	31E	f=0.0129

5.6097	31E	f=0.0129

CAM-B3LYP with LanL2DZ basis set

Excitation Energy/eV	Symmetry	Oscillator strength
3.6704	1E	f=0.0001
3.6704	1E	f=0.0001
3.8168	2E	f=0.0005
3.8168	2E	f=0.0005
4.0098	1A1	f=0.4686
4.3036	3E	f=0.0000
4.3589	1B2	f=0.0000
4.3893	1B1	f=0.0000
4.4157	4E	f=0.0087
4.4157	4E	f=0.0087
4.4261	2B1	f=0.0000
4.4931	5E	f=0.0000
4.5602	6E	f=0.0000
4.659	7E	f=0.0000
4.738	8E	f=0.0180
4.7865	9E	f=0.0000
4.8382	10E	f=0.0000
4.8382	10E	f=0.0000
4.8998	11E	f=0.0570
4.903	3B1	f=0.0000
4.9451	12E	f=0.0009
4.9451	12E	f=0.0009
4.9972	2B2	f=0.0000
5.0562	2A1	f=0.0020
5.1282	13E	f=0.0000
5.1282	13E	f=0.0000
5.1866	14E	f=0.0003
5.1866	14E	f=0.0003
5.2116	1A2	f=0.0000
5.2561	3B2	f=0.0000
5.281	2A2	f=0.0000
5.3134	15E	f=0.0000
5.3134	15E	f=0.0000
5.3764	3A2	f=0.0000
5.4235	16E	f=0.0000
5.4257	17E	f=0.0000
5.4818	18E	f=0.0001
5.4818	18E	f=0.0001
5.5199	19E	f=0.0000
5.5461	20E	f=0.0000
5.5793	21E	f=0.0000

5.6032	22E	f=0.0005
5.6032	22E	f=0.0005
5.6069	4A2	f=0.0000
5.615	5A2	f=0.0000
5.7552	4B1	f=0.0000
5.786	23E	f=0.0267
5.786	23E	f=0.0267
5.8623	4B2	f=0.0000
5.8821	24E	f=0.0095
5.8821	24E	f=0.0095
5.9521	25E	f=0.0176
5.9569	26E	f=0.0000
5.9582	27E	f=0.0107
5.9582	27E	f=0.0107
5.9983	28E	f=0.0026
5.9983	28E	f=0.0026
6.0383	29E	f=0.0000
6.0519	30E	f=0.0024
6.0519	30E	f=0.0024

CAM-B3LYP with SDD/6-311G* basis set

Excitation Energy/eV	Symmetry	Oscillator strength
3.9491	1E	f=0.0002
3.9491	1E	f=0.0002
4.1129	2E	f=0.0003
4.1129	2E	f=0.0003
4.1807	1A1	f=0.4887
4.5312	3E	f=0.0107
4.5312	3E	f=0.0107
4.5367	4E	f=0.0000
4.6066	1B2	f=0.0000
4.6152	5E	f=0.0000
4.7089	1B1	f=0.0000
4.772	6E	f=0.0000
4.8287	7E	f=0.0000
4.8464	8E	f=0.0000
4.9267	9E	f=0.0333
5.0371	10E	f=0.0000
5.0778	11E	f=0.0000
5.0778	11E	f=0.0000
5.0822	2B1	f=0.0000
5.1323	12E	f=0.0523
5.1821	2B2	f=0.0000
5.2181	13E	f=0.0005
5.2181	13E	f=0.0005

5.2898	2A1	f=0.0005
5.3402	14E	f=0.0001
5.3402	14E	f=0.0001
5.4617	15E	f=0.0000
5.4617	15E	f=0.0000
5.4953	1A2	f=0.0000
5.5447	16E	f=0.0001
5.5447	16E	f=0.0001
5.5706	3B2	f=0.0000
5.6099	17E	f=0.0000
5.679	2A2	f=0.0000
5.7001	18E	f=0.0000
5.7756	19E	f=0.0000
5.8033	20E	f=0.0000
5.8579	21E	f=0.0008
5.8579	21E	f=0.0008
5.8763	3B1	f=0.0000
5.8801	22E	f=0.0000
5.9142	23E	f=0.0000
5.9268	24E	f=0.0013
5.9268	24E	f=0.0013
5.9454	3A2	f=0.0000
5.9853	3A1	f=0.0004
6.0008	25E	f=0.0359
6.0008	25E	f=0.0359
6.0204	4A2	f=0.0000
6.0961	26E	f=0.0000
6.0961	26E	f=0.0000
6.1424	4B2	f=0.0000
6.1786	27E	f=0.0001
6.1786	27E	f=0.0001
6.1877	4A1	f=0.0056
6.2185	4B1	f=0.0000
6.252	5A2	f=0.0000
6.2918	28E	f=0.0000
6.2918	28E	f=0.0000
6.303	29E	f=0.0113

TD M062X with LanL2DZ basis set

Excitation Energy/eV	Symmetry	Oscillator strength
3.758	1E	f=0.0002
3.758	1E	f=0.0002
3.9546	2E	f=0.0009
3.9546	2E	f=0.0009
4.1022	1A1	f=0.4064

4.485	3E	f=0.0000
4.4974	1B2	f=0.0000
4.5515	1B1	f=0.0000
4.5945	2B1	f=0.0000
4.6466	4E	f=0.0049
4.6466	4E	f=0.0049
4.6539	5E	f=0.0000
4.7095	6E	f=0.0000
4.9377	7E	f=0.0000
4.9756	8E	f=0.0097
4.9923	9E	f=0.0013
4.9923	9E	f=0.0013
5.0278	10E	f=0.0000
5.1107	2A1	f=0.0140
5.1276	11E	f=0.0007
5.1276	11E	f=0.0007
5.1612	12E	f=0.0970
5.1958	13E	f=0.0000
5.1958	13E	f=0.0000
5.279	2B2	f=0.0000
5.2865	3B1	f=0.0000
5.3659	2B2	f=0.0000
5.3903	14E	f=0.0015
5.3903	14E	f=0.0015
5.4215	1A2	f=0.0000
5.4708	2A2	f=0.0000
5.5399	15E	f=0.0000
5.5668	16E	f=0.0008
5.5668	16E	f=0.0008
5.5862	3A2	f=0.0000
5.624	17E	f=0.0000
5.624	17E	f=0.0000
5.6413	4B1	f=0.0000
5.7243	3B2	f=0.0000
5.7872	18E	f=0.0000
5.7901	19E	f=0.0000
5.7987	20E	f=0.0088
5.7987	20E	f=0.0088
5.8209	21E	f=0.0019
5.8209	21E	f=0.0019
5.8345	4A2	f=0.0000
5.86	5B1	f=0.0000
5.8832	5A2	f=0.0000
5.9431	22E	f=0.0063
5.9431	22E	f=0.0063
5.9452	4B2	f=0.0000

6.0474	5A2	f=0.0000
6.0476	23E	f=0.0002
6.0476	23E	f=0.0002
6.098	3A1	f=0.0068
6.1071	24E	f=0.0003
6.1071	24E	f=0.0003
6.1645	6A2	f=0.0000
6.1706	25E	f=0.0000
6.1893	25E	f=0.0102

TD M062X with SDD/6-311G* basis set

Excitation Energy/eV	Symmetry	Oscillator strength
4.0492	1E	f=0.0002
4.0492	1E	f=0.0002
4.2522	2E	f=0.0009
4.2522	2E	f=0.0009
4.2835	1A1	f=0.4283
4.7567	1B2	f=0.0000
4.7667	3E	f=0.0000
4.7738	4E	f=0.0059
4.7738	4E	f=0.0059
4.8233	5E	f=0.0000
4.8937	1B1	f=0.0000
5.001	6E	f=0.0000
5.0389	7E	f=0.0000
5.1465	8E	f=0.0000
5.1981	9E	f=0.0310
5.278	1A1	f=0.0070
5.3107	10E	f=0.0015
5.3107	10E	f=0.0015
5.3305	11E	f=0.0000
5.4195	12E	f=0.0001
5.4195	12E	f=0.0001
5.4247	13E	f=0.0902
5.4894	14E	f=0.0019
5.4894	14E	f=0.0019
5.5038	1B2	f=0.0000
5.5038	2B1	f=0.0000
5.6684	15E	f=0.0009
5.6684	15E	f=0.0009
5.6727	2B2	f=0.0000
5.7765	1A2	f=0.0000
5.7833	3B1	f=0.0000
5.7944	2A1	f=0.0003

5.8172	16E	f=0.0011
5.8172	16E	f=0.0011
5.839	2A2	f=0.0000
5.8977	3A2	f=0.0000
5.9485	17E	f=0.0023
5.9485	17E	f=0.0024
5.9798	4A2	f=0.0000
6.0285	18E	f=0.0034
6.0285	18E	f=0.0034
6.0395	19E	f=0.0000
6.0743	2A1	f=0.0001
6.1098	20E	f=0.0000
6.113	21E	f=0.0052
6.113	21E	f=0.0052
6.1293	3B2	f=0.0000
6.1422	4B2	f=0.0000
6.1827	22E	f=0.0029
6.1827	22E	f=0.0029
6.1877	23E	f=0.0011
6.1877	23E	f=0.0011
6.2033	24E	f=0.0000
6.2145	5A2	f=0.0000
6.297	6A2	f=0.0000
6.3041	5B2	f=0.0000
6.3281	25E	f=0.0157
6.3281	25E	f=0.0157
6.3283	3A1	f=0.0012
6.3933	4B1	f=0.0000

Appendix 6.1 Cartesian coordinates from chapter 6

C_{2V} symmetry $Cr(CO)_5$ structure

1	24	0	0.103916	0.072820	-0.000016
2	6	0	0.161383	0.113089	1.998608
3	6	0	2.005461	-0.348597	-0.000018
4	6	0	0.356747	2.004022	-0.000014
5	6	0	0.161380	0.113093	-1.998640
6	6	0	-1.706386	-1.195839	-0.000016
7	8	0	0.250128	0.175280	3.137265
8	8	0	3.125815	-0.615860	-0.000019
9	8	0	0.487877	3.148324	-0.000013
10	8	0	0.250124	0.175287	-3.137298
11	8	0	-2.632703	-1.845001	-0.000016

Appendix 7.1 Cartesian coordinates from chapter 7

D_{3h} $Mn(CO)_5$ conical intersection structure with CAS(7,8) active space and cc-pvdz basis set

1	25	0	0.000000	0.000000	0.000000
2	6	0	0.000000	2.005694	0.000000
3	6	0	1.736982	-1.002847	0.000000
4	6	0	0.000000	0.000000	1.998316
5	6	0	-1.736982	-1.002847	0.000000
6	6	0	0.000000	0.000000	-1.998316
7	8	0	0.000000	0.000000	3.114963
8	8	0	0.000000	3.122817	0.000000
9	8	0	-2.704439	-1.561409	0.000000
10	8	0	0.000000	0.000000	-3.114963
11	8	0	2.704439	-1.561409	0.000000

C_{4v} $Mn(CO)_5$ minimum structure with CAS(7,8) active space and cc-pvdz basis set

1	25	0	0.000000	0.000000	0.193849
2	6	0	0.000000	0.000000	-1.768625
3	6	0	0.000000	1.983332	0.445152
4	6	0	-1.983332	0.000000	0.445152
5	6	0	1.983332	0.000000	0.445152
6	6	0	0.000000	-1.983332	0.445152
7	8	0	0.000000	0.000000	-2.890125
8	8	0	0.000000	3.092589	0.568840
9	8	0	-3.092589	0.000000	0.568840
10	8	0	3.092589	0.000000	0.568840
11	8	0	0.000000	-3.092589	0.568840

C_{2v} $Mn(CO)_5$ transition state structure with CAS(7,8) active space and cc-pvdz basis set

1	25	0	0.000000	0.000000	0.101233
2	6	0	0.000000	1.989429	-0.020055
3	6	0	1.631260	0.000000	-1.057551
4	6	0	-1.631260	0.000000	-1.057551
5	6	0	0.000000	-1.989429	-0.020055
6	6	0	0.000000	0.000000	2.198808
7	8	0	0.000000	3.101270	-0.139713
8	8	0	2.557771	0.000000	-1.688787
9	8	0	-2.557771	0.000000	-1.688787
10	8	0	0.000000	-3.101270	-0.139713
11	8	0	0.000000	0.000000	3.307949

Appendix 8.1 Cartesian coordinates from chapter 8

T_d $Fe(CO)_4$ conical intersection geometry with CAS(8,10) basis set and LanL2DZ basis set

1	6	0	1.120609	1.120609	1.120609
2	6	0	-1.120609	-1.120609	1.120609
3	6	0	1.120609	-1.120609	-1.120609
4	6	0	-1.120609	1.120609	-1.120609
5	8	0	1.779780	1.779780	1.779780
6	8	0	-1.779780	1.779780	-1.779780
7	8	0	-1.779780	-1.779780	1.779780
8	8	0	1.779780	-1.779780	-1.779780
9	26	0	0.000000	0.000000	0.000000

C_{2v} $Fe(CO)_4$ minimum energy geometry with CAS(8,10) active space and LanL2DZ active space

1	26	0	0.000000	0.000000	0.273716
2	6	0	0.000000	1.373434	-1.059997
3	6	0	1.759443	0.000000	1.040477
4	6	0	0.000000	-1.373434	-1.059997
5	6	0	-1.759443	0.000000	1.040477
6	8	0	0.000000	2.234237	-1.810231
7	8	0	2.851152	0.000000	1.380083
8	8	0	0.000000	-2.234237	-1.810231
9	8	0	-2.851152	0.000000	1.380083

C_s $Fe(CO)_4$ transition state structure with M06L/cc-pVTZ

26	0.00011	0.07882	-0.34959
6	1.68526	-0.54705	-0.59916
6	0.0005	-0.74665	1.17823
6	-0.00196	1.87884	0.04725
6	-1.68381	-0.55007	-0.59971
8	2.73132	-0.98145	-0.78717
8	0.00089	-1.25423	2.2104
8	-2.72916	-0.98623	-0.78758
8	-0.0034	2.93945	0.48056